Effects of non-ionic surfactants and related compounds on the cooperative and molecular dynamics of their aqueous solutions

Dissertation
zur Erlangung des
Doktorgrades der Naturwissenschaften
(Dr. rer. nat.)
der Naturwissenschaftlichen Fakultät IV
Chemie und Pharmazie
der Universität Regensburg

vorgelegt von
Simon Schrödle
aus Donauwörth

Regensburg 2005

Promotionsgesuch eingereicht am:	12. Januar 2005
Tag des Kolloquiums:	2. Februar 2005
Die Arbeit wurde angeleitet von:	Apl. Prof. Dr. R. Buchner
Prüfungsausschuss:	Apl. Prof. Dr. R. Buchner Prof. Dr. W. Kunz Prof. Dr. O. Reiser Prof. Dr. G. Schmeer (Vorsitzender)

meinen Eltern

Contents

1 Introduction **1**
- 1.1 Basic aspects . . . 1
- 1.2 Aims of this study . . . 2
- 1.3 Systems investigated . . . 3

2 Theoretical background **5**
- 2.1 Basics of electrodynamics . . . 5
  - 2.1.1 Maxwell and constitutive equations . . . 5
  - 2.1.2 The electric displacement field . . . 6
  - 2.1.3 Wave equations . . . 7
- 2.2 Dielectric relaxation . . . 9
  - 2.2.1 Polarization . . . 9
  - 2.2.2 Response functions of the orientational polarization . . . 10
- 2.3 Empirical description of dielectric relaxation . . . 11
  - 2.3.1 Debye equation . . . 11
  - 2.3.2 Extensions of the Debye equation . . . 12
  - 2.3.3 Damped harmonic oscillator . . . 13
  - 2.3.4 Combination of models . . . 14
  - 2.3.5 Data processing . . . 14
- 2.4 Microscopic models of dielectric relaxation . . . 15
  - 2.4.1 Onsager equation . . . 15
  - 2.4.2 Cavell equation . . . 16
  - 2.4.3 Debye model of rotational diffusion . . . 17
  - 2.4.4 Microscopic and macroscopic relaxation time . . . 18
- 2.5 Temperature dependence of relaxation times . . . 18
  - 2.5.1 Arrhenius equation . . . 18

3 Experimental **19**
- 3.1 Measurement of dielectric properties . . . 19
  - 3.1.1 Low-frequency impedance spectroscopy . . . 19
  - 3.1.2 Time-domain reflectometry . . . 20
  - 3.1.3 Frequency-domain reflectometry . . . 22
  - 3.1.4 Interferometry . . . 26

3.1.5 Time-domain THz-pulse spectroscopy . . . 29
3.2 Further measurements . . . 32
3.2.1 Densitometry . . . 32
3.2.2 Refractive indices . . . 32
3.2.3 Viscosimetry . . . 32
3.2.4 Determination of liquid/liquid phase diagrams . . . 32
3.3 Calorimetric techniques . . . 32
3.3.1 Picker flow calorimetry . . . 32
3.3.2 Tian-Calvet calorimetry . . . 33

4 Investigation of model systems 35
4.1 1,4-Dioxane + water . . . 35
4.1.1 Introduction . . . 35
4.1.2 Materials . . . 36
4.1.3 VNA measurements and correction . . . 36
4.1.4 THz-TDS measurements . . . 37
4.1.5 Data processing . . . 41
4.1.6 Results and discussion . . . 46
4.2 Oligo(ethylene glycol) ethers + water . . . 57
4.2.1 Introduction . . . 57
4.2.2 Experiment and data processing . . . 58
4.2.3 Dielectric properties . . . 61
4.2.4 Results and discussion . . . 72
4.3 Pure triethylene glycol . . . 81
4.3.1 Introduction . . . 81
4.3.2 Experiment and data . . . 81
4.3.3 Results and discussion . . . 84

5 The non-ionic surfactant system C12E5 + water 89
5.1 The phase behavior of non-ionic surfactants . . . 89
5.2 Experimental and data analysis . . . 91
5.2.1 Materials . . . 91
5.2.2 Viscosimetry . . . 92
5.2.3 Dielectric measurements . . . 94
5.3 Results and discussion . . . 100

6 Dynamics of percolating microemulsions 109
6.1 Introduction . . . 109
6.2 Experimental section and data analysis . . . 111
6.3 Results and discussion . . . 113

7 Conclusions 123

A Determination of phase diagrams 137

B Thermodynamic properties of glycol ether solutions 147

C Dielectric relaxation parameters of water 159

Vorwort

Diese Doktorarbeit entstand in der Zeit von Oktober 2002 bis Dezember 2004 am Institut für Physikalische und Theoretische Chemie der naturwissenschaftlichen Fakultät IV – Chemie und Pharmazie – der Universität Regensburg.

An erster Stelle möchte ich mich bei Herrn Apl. Prof. Dr. Richard Buchner für die Erteilung des Themas und sein Interesse am Fortschreiten der Arbeit bedanken.

Weiterhin gilt mein Dank Herrn Prof. Dr. Werner Kunz für die großzügige, auch in schwierigen Zeiten nicht abreißende Unterstützung und zahlreichen Ratschläge.

Mein besonderer Dank gilt

- Herrn Prof. Dr. Glenn Hefter, Murdoch University, Western Australia, sowie der ganzen Hefter Family. Die dort gesammelten Erfahrungen sind von unschätzbarem Wert und die erlebte Gastfreundschaft hat mich tief beeindruckt.
- Herrn Prof. Dr. H.-P. Helm, Freiburger Materialforschungszentrum (FMF), Institut für molekulare und optische Physik, Freiburg, insbesondere Herrn Dipl. Phys. Bernd Fischer für die Zusammenarbeit auf dem Gebiet der THz-Spektroskopie von Flüssigkeiten.
- Herrn Prof. Dr. Gert Wolf und Herrn Dr. Jürgen Seidel, Institut für Physikalische Chemie, TU Bergakademie Freiberg, für die freundliche Aufnahme am Institut und die wertvollen Hinweise bei kalorimetrischen Messungen.
- Dem Verband der Chemischem Industrie e.V., Stiftung Stipendien-Fonds, für die Gewährung eines Doktorandenstipendiums.

Ohne diese Kooperationen und Zuwendungen wären große Teile dieser Arbeit nicht möglich gewesen.

Allen Mitarbeitern und Kollegen des Lehrstuhls danke ich für die freundschaftliche Atmosphäre und stete Hilfsbereitschaft.

Nicht zuletzt möchte ich allen Mitarbeitern der Werkstätten für die schnelle und gewissenhafte Erledigung der Aufträge meinen Dank aussprechen und meine besondere Hochachtung zum Ausdruck bringen.

Constants and symbols

Constants

Elementary charge	e_o	$= 1.60217739 \cdot 10^{-19}\,\mathrm{C}$
Electric field constant	ε_o	$= 8.854187816 \cdot 10^{-12}\,\mathrm{C^2(Jm)^{-1}}$
Avogadro's constant	N_A	$= 6.0221367 \cdot 10^{23}\,\mathrm{mol^{-1}}$
Speed of light	c	$= 2.99792458 \cdot 10^{8}\,\mathrm{m\,s^{-1}}$
Boltzmann's constant	k_B	$= 1.380658 \cdot 10^{-23}\,\mathrm{J\,K^{-1}}$
Permittivity of vacuum	μ_0	$= 4\pi \cdot 10^{-7}\,\mathrm{(Js)^2(C^2m)^{-1}}$
Planck's constant	h	$= 6.6260755 \cdot 10^{-34}\,\mathrm{Js}$

Symbols

$\vec{B}$	magnetic induction ($\mathrm{Vs\,m^{-2}}$)	$\vec{D}$	electric induction ($\mathrm{C\,m^{-2}}$)
ω	angular frequency ($\mathrm{s^{-1}}$)	$\vec{j}$	current density ($\mathrm{A\,m^{-2}}$)
$\vec{E}$	electric field strength ($\mathrm{V\,m^{-1}}$)	$\hat{\varepsilon}$	complex dielectric permittivity
$\vec{H}$	magnetic field strength ($\mathrm{A\,m^{-1}}$)	ε'	real part of $\hat{\varepsilon}$
$\vec{P}$	polarization ($\mathrm{C\,m^{-2}}$)	ε''	imaginary part of $\hat{\varepsilon}$
τ	relaxation time (s)	ε_∞	$\lim_{\nu\to\infty}(\varepsilon')$
η	viscosity (Pa s)	ε_s	$\lim_{\nu\to 0}(\varepsilon')$
T	temperature (K)	μ	dipole moment (C m)
t	time (s)	ν	frequency (Hz)
c	molarity ($\mathrm{mol\ dm^{-3}}$)	m	molality ($\mathrm{mol\ kg^{-1}}$)
κ	conductivity ($\mathrm{S\ m^{-1}}$)	ρ	density ($\mathrm{kg\,m^{-3}}$)

Acronyms

BN	benzonitrile	DMA	N,N-dimethylacetamide
DMF	N,N-dimethylformamide	PC	propylene carbonate
TDR	time-domain reflectometry	IF	interferometry
VNA	vector network analyzer	DRS	dielectric relaxation spectroscopy

Chapter 1

Introduction

1.1 Basic aspects

For a number of reasons, non-ionic surfactant solutions and microemulsions play an increasingly important role in industry, but are also of interest for basic research. Oligo(ethylene glycol) monoalkyl ethers are typical representatives for this kind of substances, with a general chemical structure $H(CH_2)_n$-$(OCH_2CH_2)_mOH$ that is simply denoted by C_nE_m. By choosing different length of the alkyl or glycol chain, the phase behavior of these compounds can be modulated in wide ranges. A variety of isotropic and liquid crystalline phases is known to exist, and transitions occur readily by changing the thermodynamic state of the system, e.g. composition, temperature or pressure.

It is obvious from the strong temperature dependence of the observed physico-chemical properties of non-ionic surfactant solutions that these mixtures are governed by a delicate balance of interaction forces between surfactant and water molecules. Especially in the case of aqueous solutions, the thermodynamic equilibrium properties of these systems and related microemulsions are determined to a large extend by cooperative interactions between molecules.

Besides their use as non-ionic surfactants, oligo(ethylene glycol) derivatives and related ethylene oxide polymers are widely employed in a variety of applications. These include protein crystallization[1–3], modification of surfaces for biocompatibility[4], control of particle aggregation[5] and the use in chemical synthesis[6]. Therefore, this study was extended to mono- and dimethyl ethers of oligo(ethylene glycol)s, both in pure liquid state and in aqueous solutions.

Despite a huge number of investigations in this field, including calorimetric[7], Raman[8] , UV[9], IR[10], NMR[11–13], and scattering[14,15] techniques, the molecular origin of the structural changes of these liquids is still not fully understood, mainly because of a very limited knowledge of the dynamic processes present in these systems.

Dielectric relaxation spectroscopy (DRS) is known to be a proper tool for the analysis of dynamics of various liquid systems, both homogeneous and multi-component colloidal ones. Concerning anionic and cationic surfactant systems, broad-band DRS techniques were already employed[16,17] and provided information on structure and dynamics which can be correlated with other methods.

In the case of aqueous solutions, DRS is very sensitive to changes within the cooperative dynamics of the hydrogen bond network that cannot be detected easily by other methods. We also want to address basic aspects such as dynamical and structural aspects of water, which are an important subject of ongoing experimental and theoretical work, due to the complexity of the chemistry found in aqueous solutions.
Although this investigation mainly focuses on surfactants and related model systems, dynamics of water near hydrophilic and hydrophobic surfaces is of major interest in the fields of biology and protein chemistry, with many implications for living organisms but also for artificial nanostructured systems.

1.2 Aims of this study

The general aim of this study is the application of dielectric spectroscopy on aqueous non-ionic surfactant and related systems. It is known from studies of ionic surfactant solutions[16,17] that this technique can provide information on micelle-specific processes and on the dynamics of water, both in the bulk phase and in bound state. For non-ionics, the situation is more complicated and even the dielectric response of binary mixtures of two interacting compounds is not well understood, nor are there data of sufficient accuracy and frequency coverage available in most cases.
For the analysis of the dielectric response of non-ionic surfactants, a systematic investigation of the effects of hydration of solutes with different degrees of internal freedom and solute-water interaction is essential, because dielectric spectra usually consist of broad bands that cannot always be easily identified without a closer knowledge of the dielectric properties of related (and preferably less complex) systems. We also want to investigate to what extent microheterogeneities are present in simple binary mixtures and their influence on H-bond rearrangement processes.
This should allow us to get a closer insight into the dynamics of water at the micellar interface, as well as of the hydrophilic oligo(ethylene glycol) units present in most of the non-ionic surfactants. Furthermore, quantitative information on the degree of hydration of the hydrophilic moieties can be obtained from the relaxation amplitudes as well as estimates for the effective dipole moment of water near hydrophilic surfaces.
Another important topic of modern physical chemistry is the effect of confinement on the properties of molecular entities, a question that can be readily approached by broad band dielectric measurements.
While most of the experiments are limited to binary systems, some ternary mixtures, namely non-ionic W/O microemulsions were investigated. These mixtures show very interesting charge transport[18–20] and structural[21] properties, but their dielectric properties in the percolation region remained unclear despite significant effort[22].
The study requires also the development and evaluation of suitable methods for the measurement of dielectric data. This includes the implementation of proper mathematical methods to calculate sample properties from the directly determined quantities, especially in the case of vector network analyzer (VNA) and low-frequency measurements, and the design of sample cells that can be used with small volumes of highly viscous liquids.

Furthermore, a new method for the determination of the stability regions of mesomorphic phases and similar liquid-liquid equilibria needs to be established, as the exact knowledge of the phase diagrams is essential. An automated instrument[23], much more precise than just the visual observation and characterized by a high sample throughput, is desired.

1.3 Systems investigated

An outline of all investigated binary systems is given in Fig. 1.1. 1,4-Dioxane, characterized by its ring structure, is the most rigid non-ionic compound studied here. It has a negligible overall dipole moment and no dielectric mode was found for 1,4-dioxane up to several 100 GHz.

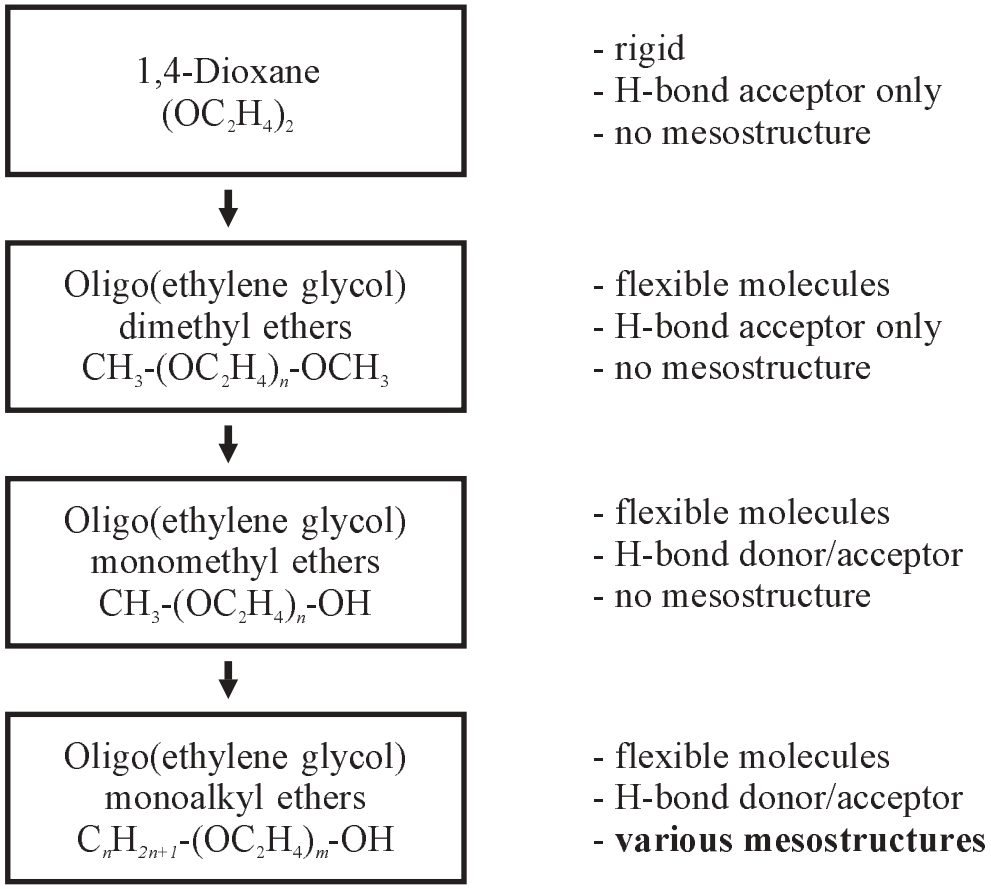

Figure 1.1: Investigated aqueous binary systems.

Oligo(ethylene glycol) dimethyl ethers are open-chain molecules with much higher degrees of conformational freedom, but, as there are only H-bond acceptor places present, no intermolecular H-bonds can be formed within these liquids. They are miscible with water and many organic solvents in any ratio and can dissolve large quantities of polar gases, what

makes them important chemicals for industrial applications. From the dimethyl ethers, it is only a short step to the monomethyl ethers. These are equipped with a free OH group, enabling them to form intermolecular H-bonds.
The C_nE_m, maybe the most important class of non-ionic surfactants, represent oligo(ethylene glycol) monoalkyl ethers. Although they differ from the oligo(ethylene glycol) monomethyl ethers only by the length of the hydrophobic alkyl side chain, a completely different physico-chemical behavior is observed, arising from the various mesostructures formed in aqueous solutions.
Ternary surfactant/oil/water systems can show even more complicated structures. As an example, $C_{12}E_5$ /water/*n*-octane microemulsions were investigated in the oil-rich region, because these mixtures are well characterized by other methods[24].
In some cases, D_2O was substituted for water in order to use the isotope effect for the interpretation of the relaxation behavior and for comparison with data from other methods that require isotope exchange (e.g. NMR spectroscopy or neutron scattering).

Chapter 2

Theoretical background

2.1 Basics of electrodynamics

2.1.1 Maxwell and constitutive equations

The theory of electromagnetic fields is based on the four Maxwell equations[25,26]. These four equations

$$\vec{\mathrm{rot}}\,\vec{H} = \vec{j} + \frac{\partial}{\partial t}\vec{D} \tag{2.1}$$

$$\vec{\mathrm{rot}}\,\vec{E} = -\frac{\partial}{\partial t}\vec{B} \tag{2.2}$$

$$\mathrm{div}\,\vec{D} = \rho_{el} \tag{2.3}$$

$$\mathrm{div}\,\vec{B} = 0. \tag{2.4}$$

express how electric charges (electric charge density, ρ_{el}) produce electric fields (electric field strength, $\vec{E}$; Gauss's law, Eq. 2.3), the absence of magnetic charges (Eq. 2.4), the generation of magnetic fields, $\vec{H}$ (magnetic field strength), by currents (extended Ampère's law, Eq. 2.1), and how changing magnetic fields produce electric fields (Faraday's law of induction, Eq. 2.2). $\vec{B}$ and $\vec{D}$ account for the magnetic and electric induction, also called magnetic flux density or electric displacement field, respectively.
Together with the Newton equation

$$m\frac{\partial^2}{\partial t^2}\vec{r} = q(\vec{E} + \vec{v} \times \vec{B}), \tag{2.5}$$

a full set of linear partial differential equations is obtained which enables us, at least in principle, to calculate all kinds of electromagnetic phenomena.
Now we want to constrain ourselves to homogenous, non-dispersive, isotropic materials at

low fields (linear regime) and introduce the constitutive equations

$$\vec{D} = \varepsilon\varepsilon_0\vec{E} \tag{2.6}$$

$$\vec{j} = \kappa\vec{E} \tag{2.7}$$

$$\vec{B} = \mu\mu_0\vec{H}, \tag{2.8}$$

where the $\vec{D}$ and $\vec{H}$ fields are related to $\vec{E}$ and $\vec{B}$ by time- and field strength-independent scalars (material properties): the relative electrical permittivity, ε, specific conductivity, κ, and relative magnetic permeability, μ. ε_0 and μ_0 are the absolute permittivity of vacuum and the permeability of vacuum, respectively.

2.1.2 The electric displacement field

The constitutive equations (2.6-2.8) are valid only for the special case of a time-independent field response.
Considering the dynamic case, with an electric field $\vec{E}$ that harmonically oscillates with the amplitude $\vec{E}_0$ and angular frequency $\omega = 2\pi\nu$,

$$\vec{E}(t) = \vec{E}_0\cos(\omega t), \tag{2.9}$$

most condensed systems show above a certain frequency, typically of the order of 1 MHz to 1 GHz, a significant phase delay, $\delta(\omega)$, between the electric field and the electric displacement field so that

$$\vec{D}(t) = \vec{D}_0\cos(\omega t - \delta(\omega)). \tag{2.10}$$

Eq. 2.10 can be written as

$$\vec{D}(t) = \vec{D}_0\cos(\delta(\omega))\cos(\omega t) + \vec{D}_0\sin(\delta(\omega))\sin(\omega t), \tag{2.11}$$

and by introducing

$$\vec{D}_0\cos(\delta(\omega)) = \varepsilon'(\omega)\varepsilon_0\vec{E}_0 \tag{2.12}$$

$$\vec{D}_0\sin(\delta(\omega)) = \varepsilon''(\omega)\varepsilon_0\vec{E}_0 \tag{2.13}$$

the electric displacement field can be expressed as

$$\vec{D}(t) = \varepsilon'(\omega)\varepsilon_0\vec{E}_0\cos(\omega t) + \varepsilon''(\omega)\varepsilon_0\vec{E}_0\sin(\omega t), \tag{2.14}$$

with a phase shift

$$\tan(\delta(\omega)) = \frac{\varepsilon''(\omega)}{\varepsilon'(\omega)}. \tag{2.15}$$

Hence, the relation between $\vec{D}(t)$ and $\vec{E}(t)$ is not longer characterized by an amplitude $\vec{D}_0$ and a phase shift $\delta(\omega)$, but by the real and imaginary part of the complex permittivity,

$$\hat{\varepsilon}(\omega) = \varepsilon'(\omega) - \mathrm{i}\varepsilon''(\omega). \tag{2.16}$$

The dispersive part of the electric displacement field, $\varepsilon'(\omega)\varepsilon_0\vec{E}_0\cos(\omega t)$, is described by the real part and the imaginary part is the dissipative contribution, $\varepsilon''(\omega)\varepsilon_0\vec{E}_0\sin(\omega t)$. Note that the latter is phase shifted by $\pi/2$ with respect to the driving electric field.

To simplify the mathematical treatment, complex field vectors $\hat{\vec{E}}(t)$ and $\hat{\vec{D}}(t)$ can be introduced:

$$\hat{\vec{E}}(t) = \vec{E}_0\cos(\omega t) + \mathrm{i}\vec{E}_0\sin(\omega t) = \vec{E}_0\exp(\mathrm{i}\omega t) \tag{2.17}$$

$$\hat{\vec{D}}(t) = \vec{D}_0\cos(\omega t - \delta) + \mathrm{i}\vec{D}_0\sin(\omega t - \delta) = \vec{D}_0\exp[\mathrm{i}(\omega t - \delta)]. \tag{2.18}$$

Thus, for the non-static case, the constitutive equations (2.6) to (2.8) have to be rewritten as[27]

$$\hat{\vec{D}}(t) = \hat{\varepsilon}(\omega)\varepsilon_0\hat{\vec{E}}(t) \tag{2.19}$$

$$\hat{\vec{j}}(t) = \hat{\kappa}(\omega)\hat{\vec{E}}(t) \tag{2.20}$$

$$\hat{\vec{B}}(t) = \hat{\mu}(\omega)\mu_0\hat{\vec{H}}(t), \tag{2.21}$$

with the complex conductivity $\hat{\kappa}(\omega)$, and the complex relative magnetic permeability, $\hat{\mu}$. Thus, Eqs. (2.19)-(2.21) are suitable for the description of the frequency-dependent linear dielectric response of dissipative systems.

2.1.3 Wave equations

The Maxwell equation (2.1) for harmonic fields

$$\hat{\vec{E}}(t) = \vec{E}_0\cos(\mathrm{i}\omega t) \tag{2.22}$$

$$\hat{\vec{H}}(t) = \vec{H}_0\cos(\mathrm{i}\omega t) \tag{2.23}$$

can be transformed with the help of the complex constitutive equations (2.19) - (2.21) into

$$\vec{\mathrm{rot}}\,\vec{H}_0 = (\hat{\kappa}(\omega) + \mathrm{i}\omega\hat{\varepsilon}(\omega)\varepsilon_0)\vec{E}_0. \tag{2.24}$$

In a similar way, the equation

$$\vec{\mathrm{rot}}\,\vec{E}_0 = -\mathrm{i}\omega\hat{\mu}(\omega)\mu_0\vec{H}_0 \tag{2.25}$$

is obtained from the Maxwell equation (2.2).

By application of the rotation operator on Eq.(2.24) and by using the Legendre vectorial identity,

$$\vec{\mathrm{rot}}\,\vec{\mathrm{rot}}\,\vec{H}_0 = \vec{\mathrm{grad}}\,\mathrm{div}\,\vec{H}_0 - \triangle\vec{H}_0 = \vec{\mathrm{grad}}\,(0) - \triangle\vec{H}_0 = -\triangle\vec{H}_0, \tag{2.26}$$

and Eq.(2.25), the reduced form of the wave equation of the magnetic field can be obtained:

$$\triangle \vec{H}_0 + \hat{k}^2 \vec{H}_0 = 0 \tag{2.27}$$

The propagation constant $\hat{k}$ is given by

$$\hat{k}^2 = k_0^2 \left(\hat{\mu}(\omega)\hat{\varepsilon}(\omega) + \frac{\hat{\mu}(\omega)\hat{\kappa}(\omega)}{\mathrm{i}\omega\varepsilon_0} \right). \tag{2.28}$$

The propagation constant of the vacuum, k_0, is defined by

$$k_0 = \omega\sqrt{\varepsilon_0\mu_0} = \frac{2\pi}{\lambda_0} \tag{2.29}$$

$$c_0 = \frac{1}{\sqrt{\varepsilon_0\mu_0}}, \tag{2.30}$$

where c_0 is the speed of light and λ_0 the wavelength of a monochromatic wave in vacuum. For a source-free medium ($\operatorname{div} \vec{E} = 0$) a reduced wave equation for $\vec{E}$ can be obtained, Eq. 2.31.

$$\triangle \hat{\vec{E}}_0 + \hat{k}^2 \hat{\vec{E}}_0 = 0 \tag{2.31}$$

In the case of non-magnetizable substances ($\hat{\mu} = 1$), the complex propagation constant, Eq.(2.28), can be written as

$$\hat{k}^2 = k_0^2 \left(\hat{\varepsilon}(\omega) + \frac{\hat{\kappa}(\omega)}{\mathrm{i}\omega\varepsilon_0} \right) \equiv k_0^2 \hat{\eta}(\omega), \tag{2.32}$$

where $\hat{\eta}$ is the generalized complex permittivity, $\hat{\eta} = \eta' - \mathrm{i}\eta''$.
Its real part is given by

$$\eta'(\omega) = \varepsilon'(\omega) - \frac{\kappa''(\omega)}{\omega\varepsilon_0} \tag{2.33}$$

and the imaginary part by

$$\eta''(\omega) = \varepsilon''(\omega) + \frac{\kappa'(\omega)}{\omega\varepsilon_0}. \tag{2.34}$$

Equations (2.32) to (2.34) show that the dielectric properties and the conductivity of the system cannot be measured separately. In electrolyte systems, the theory[28] suggests some dispersion of the complex conductivity, $\hat{\kappa}$. However, at microwave frequencies this effect can be neglected[29], especially at the low electrolyte concentrations of the materials covered by this study.
Therefore we assume

$$\kappa'(\omega) = \kappa \tag{2.35}$$

and

$$\kappa''(\omega) = 0. \tag{2.36}$$

Finally, the complex dielectric permittivity is calculated from the (measured) generalized complex permittivity and the experimentally accessible conductivity by

$$\varepsilon'(\omega) = \eta'(\omega) \tag{2.37}$$

and

$$\varepsilon''(\omega) = \eta''(\omega) - \frac{\kappa}{\omega\varepsilon_0}. \tag{2.38}$$

2.2 Dielectric relaxation

2.2.1 Polarization

The electric displacement field $\hat{\vec{D}}$ can be split into two contributions,

$$\hat{\vec{D}} = \hat{\varepsilon}\varepsilon_0\hat{\vec{E}} = \varepsilon_0\hat{\vec{E}} + \hat{\vec{P}}, \tag{2.39}$$

with

$$\hat{\vec{P}} = (\hat{\varepsilon} - 1)\varepsilon_0\hat{\vec{E}}, \tag{2.40}$$

where $\hat{\vec{P}}$ is the so-called polarization and describes the effect of an electric field on the medium, while $\varepsilon_0\hat{\vec{E}}$ is also present in vacuum.
The macroscopical definition of $\hat{\vec{P}}$[27] can be microscopically rewritten as a sum of the orientational and induced polarization,

$$\hat{\vec{P}} = \hat{\vec{P}}_\mu + \hat{\vec{P}}_\alpha, \tag{2.41}$$

with

$$\hat{\vec{P}}_\mu = \sum_k \rho_k \langle\vec{\mu}_k\rangle \tag{2.42}$$

and

$$\hat{\vec{P}}_\alpha = \sum_k \rho_k \alpha_k (\hat{\vec{E}}_i)_k, \tag{2.43}$$

respectively. The orientational polarization defined by Eq.(2.42) results from the reorientation of molecular dipoles of species k with dipole moment $\vec{\mu}_k$ and number densities, ρ_k, when an external electric field is applied.
The molecular polarizability, α_k, gives rise to an electron and atomic polarization caused by the inner field, $(\hat{\vec{E}}_i)_k$, acting at the position of the particle. Thus, the field leads to the formation of induced dipole moments and so to the induced polarization.
The time scale of these processes is in the region of $\sim 1\,\mathrm{MHz}$-$\sim 10\,\mathrm{THz}$. Thus measurements of the frequency dependent complex permittivity can provide insights into the dynamics of liquids.

$\hat{\vec{P}}_\alpha$ is rather constant in the microwave range and its frequency dependence leads to information about the intramolecular dynamics of the system. It consists of two contributions, one in the infrared (atomic polarization) and the other in the ultraviolet range (electron polarization). The absorption peaks are in most cases sharper compared to those at microwave frequencies[30].

Because of the different time scales of $\hat{\vec{P}}_\mu$ and $\hat{\vec{P}}_\alpha$, both polarization effects can be separated[31] and an infinite frequency permittivity, ε_∞, can be introduced:

$$\hat{\vec{P}}_\mu = \varepsilon_0(\hat{\varepsilon} - \varepsilon_\infty)\hat{\vec{E}} \tag{2.44}$$

$$\hat{\vec{P}}_\alpha = \varepsilon_0(\varepsilon_\infty - 1)\hat{\vec{E}} \tag{2.45}$$

2.2.2 Response functions of the orientational polarization

At sufficiently high frequencies, the polarization cannot reach its maximum value any more, as the molecular dipoles are not able to follow the field variation without delay.

Assuming a linear medium, a relation between $\hat{\vec{E}}$ and $\hat{\vec{P}}$ can be then established by the help of the response functions.

A linear medium is characterized by the applicability of the superposition principle. I.e. if one field $\vec{E}_1$ produces a polarization $\vec{P}_1$ and another field $\vec{E}_2$ a polarization $\vec{P}_2$, then the field $\vec{E}_1 + \vec{E}_2$ leads to a polarization $\vec{P}_1 + \vec{P}_2$.

Let us now assume an isotropic linear dielectric material which is exposed to a field $\vec{E}$ causing a polarization, $\vec{P}$. At time $t = 0$, the field is switched off and the time evolution of the polarization is studied.

If we consider that the induced polarization, $\vec{P}_\alpha$, follows the change of the applied field without decay, then the corresponding polarization can be written as

$$\hat{\vec{P}}_\mu(t) = \hat{\vec{P}}_\mu(0) \cdot F_P^{or}(t) \quad \text{with} \quad F_P^{or}(0) = 1, \quad F_P^{or}(\infty) = 0. \tag{2.46}$$

$F_P^{or}(t)$ is the step response function defined as

$$F_P^{or}(t) = \frac{\langle \vec{P}_\mu(0) \cdot \vec{P}_\mu(t) \rangle}{\langle \vec{P}_\mu(0) \cdot \vec{P}_\mu(0) \rangle}. \tag{2.47}$$

One of the methods used in this work, the time domain reflectometry (TDR), is based on this principle[32].

In the case of a harmonic field of the form $\hat{\vec{E}}(t) = \hat{\vec{E}}_0 \exp(-\mathrm{i}\omega t)$ the polarization can be defined as

$$\hat{\vec{P}}_\mu(\omega, t) = \varepsilon_0(\varepsilon - \varepsilon_\infty)\hat{\vec{E}}(t) \int_0^\infty \exp(-\mathrm{i}\omega t') f_P^{or}(t') \mathrm{d}t' \tag{2.48}$$

with

$$\int_0^\infty \exp(-\mathrm{i}\omega t')f_P^{or}(t')\mathrm{d}t' = \mathcal{L}_{\mathrm{i}\omega}[f_P^{or}(t')] \tag{2.49}$$

where $\mathcal{L}_{iw}[f_P^{or}(t')]$ is the Laplace transformed pulse response function of the orientational polarization. This can be obtained from the negative derivative of the normalized step response function

$$f_P^{or}(t') = -\frac{\partial F_P^{or}(t-t')}{\partial(t-t')} \quad \text{normalized with} \quad \int_0^\infty f_P^{or}(t')\mathrm{d}t' = 1. \tag{2.50}$$

Thus, the complex permittivity, $\hat{\varepsilon}(\omega)$, can be then calculated by[27]

$$\hat{\varepsilon}(\omega) = \varepsilon'(\omega) - \mathrm{i}\varepsilon''(\omega) = \varepsilon_\infty + (\varepsilon - \varepsilon_\infty)\cdot\mathcal{L}_{\mathrm{i}\omega}[f_P^{or}(t')] \tag{2.51}$$

2.3 Empirical description of dielectric relaxation

For the description of dielectric relaxation phenomena, a number of different equations have been developed over time. As the majority of the spectra represent a sum of various relaxation processes the best description of the spectra can be achieved by a combination of various equations.

2.3.1 Debye equation

The Debye equation[33] represents the simplest way of describing dielectric spectra of liquid. It is assumed that the decrease of the polarization in the absence of an outer electric field is directly proportional to the polarization itself[34]. Therefore, it can be expressed by a time law of the first order,

$$\frac{\partial}{\partial t}\vec{P}_\mu(t) = -\frac{1}{\tau}\vec{P}_\mu(t), \tag{2.52}$$

where τ represents the relaxation time and describes the dynamics of the system. From the solution of the differential equation,

$$\vec{P}_\mu(t) = \vec{P}_\mu(0)\exp\left(-\frac{t}{\tau}\right), \tag{2.53}$$

the step response function, $F_P^{or}(t) = \exp(-t/\tau)$, can be obtained. By application of Eq.(2.50), the pulse response function,

$$f_P^{or}(t) = \frac{1}{\tau}\exp\left(-\frac{t}{\tau}\right), \tag{2.54}$$

can be easily calculated.

Using a Fourier transform, the complex dielectric permittivity is obtained from the pulse response function according to Eq.(2.51):

$$\hat{\varepsilon}(\omega) = \varepsilon_\infty + (\varepsilon - \varepsilon_\infty) \cdot \mathcal{L}_{\mathrm{i}\omega} \left[\frac{1}{\tau} \exp\left(-\frac{t}{\tau} \right) \right] \tag{2.55}$$

Finally, the Debye equation can be written as

$$\hat{\varepsilon}(\omega) = \varepsilon_\infty + \frac{\varepsilon - \varepsilon_\infty}{1 + \mathrm{i}\omega\tau}, \tag{2.56}$$

which can be split into the real

$$\varepsilon'(\omega) = \varepsilon_\infty + \frac{\varepsilon - \varepsilon_\infty}{1 + \omega^2\tau^2} \tag{2.57}$$

and imaginary part

$$\varepsilon''(\omega) = \omega\tau \frac{\varepsilon - \varepsilon_\infty}{1 + \omega^2\tau^2}. \tag{2.58}$$

The dispersion curve, $\varepsilon' = \varepsilon'(\ln(\omega))$, is a monotonically decreasing point-symmetric function and the absorption curve, $\varepsilon' = \varepsilon'(\ln(\omega))$, an axis-symmetric band reaching its maximum at $\omega = 1/\tau$.

2.3.2 Extensions of the Debye equation

Equations (2.57) and (2.58) are not always appropriate. However, the assumption of a continuous relaxation time distribution, $g(\tau)$, can be used[27]. Due to practical reasons, the logarithmic representation, $G(\ln\tau)$, is preferred. The complex permittivity can then be written as

$$\hat{\varepsilon}(\omega) = \varepsilon_\infty + (\varepsilon - \varepsilon_\infty) \int_0^\infty \frac{G(\ln\tau)}{(1 + \mathrm{i}\omega\tau)} \mathrm{d}\ln\tau \quad \text{with} \quad \int_0^\infty G(\ln\tau)\mathrm{d}\ln\tau = 1. \tag{2.59}$$

Unfortunately, $G(\ln\tau)$ cannot be extracted from the data in an straightforward way. Therefore empirical parameters are used which account for the broadness and shape of the relaxation time distribution.

Cole-Cole equation

Compared with the Debye equation, the Cole-Cole equation[35,36]

$$\hat{\varepsilon}(\omega) = \varepsilon_\infty + \frac{\varepsilon - \varepsilon_\infty}{1 + (\mathrm{i}\omega\tau_0)^{1-\alpha}}. \tag{2.60}$$

contains an additional empirical parameter, $\alpha \in [0..1]$, which describes a symmetric relaxation time distribution at the principal relaxation time, τ_0. This kind of distribution results in flatter dispersion curves and broadened absorption spectra.
For $\alpha = 0$, the Cole-Cole equation turns into the Debye equation.

Cole-Davidson equation

When an asymmetric relaxation time distribution is present the Cole-Davidson equation[37,38] with a parameter $\beta \in [0..1]$,

$$\hat{\varepsilon}(\omega) = \varepsilon_\infty + \frac{\varepsilon - \varepsilon_\infty}{(1 + \mathrm{i}\omega\tau_0)^\beta}, \tag{2.61}$$

is used. The Cole-Davidson equation describes asymmetric dispersions and absorption curves. For $\beta = 1$, this equation turns into the Debye form.

Havriliak-Negami equation

When both parameters $\alpha \in [0..1]$ and $\beta \in [0..1]$ are combined, another way for the description of a broad asymmetric relaxation time distribution is obtained[39]:

$$\hat{\varepsilon}(\omega) = \varepsilon_\infty + \frac{\varepsilon - \varepsilon_\infty}{(1 + (\mathrm{i}\omega\tau_0)^{1-\alpha})^\beta} \tag{2.62}$$

Both the dispersion and absorption curves are asymmetric. For $\alpha = 0$ and $\beta = 1$ this equation turns into the Debye equation.

2.3.3 Damped harmonic oscillator

Besides the dielectric response arising from dipole orientational relaxation, resonance phenomena can lead to a dielectric dispersion. As a first approximation of such processes, a damped harmonic oscillator model can be used.
Assuming an harmonic oscillator which is subject to a damping force and driven by a harmonically oscillating field $E(t) = E_0 e^{\mathrm{i}\omega t}$. When the damping force is linearly dependent upon the velocity $\frac{\partial}{\partial t}x(t)$, the time-dependent motion $x(t)$ of an effective charge q can be obtained from the solution of the differential equation

$$m\frac{\partial^2}{\partial t^2}x(t) + m\gamma\frac{\partial}{\partial t}x(t) + kx(t) = qE(t) = qE_0 e^{\mathrm{i}\omega t}, \tag{2.63}$$

derived from Newton's equation, Eq. 2.5. With a characteristic frequency $\omega_0 = \sqrt{k/m}$ and a damping constant $\gamma = 1/\tau_\mathrm{D}$, Eq. 2.63 can be written as

$$\frac{\partial^2}{\partial t^2}x(t) + \tau_\mathrm{D}^{-1}\frac{\partial}{\partial t}x(t) + \omega_0^2 x(t) = \frac{qE_0}{m}e^{\mathrm{i}\omega t} = Ce^{\mathrm{i}\omega t}, \tag{2.64}$$

where τ_D is the characteristic damping time and $C = \frac{qE_0}{m}$ a constant.
It can be shown that

$$x(t) = \frac{C}{\omega_0^2 - \omega^2 + \mathrm{i}\omega\tau_\mathrm{D}^{-1}}e^{\mathrm{i}\omega t} \tag{2.65}$$

is a solution of Eq. 2.64. Now we consider the polarisation at time t, which is defined as the total overall dipole moment per unit volume, $P(t) = \rho q x(t)$, where ρ is the number density of the effective charges q.

From an extension of Eq. 2.44 to a polarisation caused by a resonance type dielectric dispersion, the complex permittivity can be expressed by Eq. 2.66.

$$\hat{\varepsilon}(\omega) - \varepsilon_\infty = \frac{P(t)}{\varepsilon_0 E(t)} = \frac{\rho q x(t)}{\varepsilon_0 E_0 e^{\mathrm{i}\omega t}} \tag{2.66}$$

Using Eq. 2.65, $\hat{\varepsilon}(\omega)$ is given as

$$\hat{\varepsilon}(\omega) - \varepsilon_\infty = \frac{P(t)}{\varepsilon_0 E(t)} = \frac{\rho q^2}{\varepsilon_0 m} \frac{1}{(\omega_0^2 - \omega^2 + \mathrm{i}\omega\tau_\mathrm{D}^{-1})}. \tag{2.67}$$

For a static field (Eq. 2.6),

$$\varepsilon = \hat{\varepsilon}(0) = \varepsilon_\infty + \frac{\rho q^2}{\varepsilon_0 m \omega_0^2} \tag{2.68}$$

is obtained. Therefore, we get the frequency dependent complex permittivity of the system:

$$\hat{\varepsilon}(\omega) = \varepsilon_\infty + \frac{(\varepsilon - \varepsilon_\infty)\,\omega_0^2}{(\omega_0^2 - \omega^2) + \mathrm{i}\omega\tau_\mathrm{D}^{-1}}. \tag{2.69}$$

2.3.4 Combination of models

In most of the systems the complex permittivity spectrum is composed of more than one relaxation process. So it is possible to write Eq.(2.59) as superimposition of n separate processes:

$$\hat{\varepsilon}(\omega) = \varepsilon_\infty + \sum_{j=1}^{n} (\varepsilon_j - \varepsilon_{\infty,j}) \int_0^\infty \frac{G_j(\ln \tau_j)}{1 + \mathrm{i}\omega\tau_j} \mathrm{d} \ln \tau_j \tag{2.70}$$

Each of the processes is treated separately and has its own relaxation time, τ_j, and dispersion amplitude, S_j:

$$\varepsilon - \varepsilon_\infty = \sum_{j=1}^{n} (\varepsilon_j - \varepsilon_{\infty,j}) = \sum_{j=1}^{n} S_j \tag{2.71}$$

$$\varepsilon_{\infty,j} = \varepsilon_{j+1} \tag{2.72}$$

2.3.5 Data processing

After the measurement of the complex dielectric permittivity spectra $\hat{\varepsilon}(\nu_i)$ at spot frequencies ν_i a frequency-continuous description has to be found. This is achieved by a relaxation model comprising one or more of the empirical terms given above.
The choice of the relaxation model follows some basic rules. The parameters obtained must be physically reasonable and the variance of the fit, χ_r^2, (Eq.(2.73)) should be small. Furthermore, the number of the relaxation processes should be reasonably small and the relaxation models should not change within one concentration or temperature series, except

for specific physical reasons. Additionally, it is desirable to find a physical interpretation for the relaxation processes.
For many systems, more than one relaxation model with similar χ^2_r can be used. The model also depends on the measured frequency range and also the precision of the data, the density of the spot frequency and the empirical conductivity correction, which is not always exactly identical with the measured Ohmic conductivity. For the evaluation of the data the MWFIT program based on the method of Levenberg and Marquardt[40] was used. For the purpose of this study, the program was extended by a term describing a damped harmonic oscillator. It determines the best set of relaxation parameters of the chosen relaxation model for the experimentally obtained ε' and ε'' data. The quality of the fit is described by the variance

$$\chi^2_r = \frac{1}{2\,m - n} \sum_{i=1}^{m} \left[(\varepsilon'_i - \varepsilon'_{i,\mathrm{calc}})^2 + (\varepsilon''_i - \varepsilon''_{i,\mathrm{calc}})^2 \right]. \tag{2.73}$$

In Eq.(2.73) m represents the number of value triples, n the number of fit parameters, $\hat{\varepsilon}_i$ the experimental and $\hat{\varepsilon}_{i,\mathrm{calc}}$ the calculated dielectric permittivity.

2.4 Microscopic models of dielectric relaxation

2.4.1 Onsager equation

The Onsager model[27,41] describes dielectric polarization of dipole mixtures. It uses a continuum description of the material which provides an environment for the dipole reorientation. Specific interactions and the anisotropy of the surrounding field are not taken into account.
From this picture, Onsager deduced Eq. 2.74 for the interpretation of dielectric properties.

$$\varepsilon_0(\varepsilon - 1)\vec{E} = \vec{E}_h \cdot \sum_j \frac{\rho_j}{1 - \alpha_j f_j} \left(\alpha_j + \frac{1}{3k_B T} \cdot \frac{\mu^2_{eff,j}}{1 - \alpha_j f_j} \right) \tag{2.74}$$

Here, ρ_j represents the charge density, α_j the polarizability, f_j the reaction field factor of the species j and $\mu_{eff,j}$ the effective dipole moment of species j.
$\vec{E}_h$ stands for the cavity field which can be calculated by

$$\vec{E}_h = \frac{3\varepsilon}{2\varepsilon + 1}\vec{E} \tag{2.75}$$

under the conditions of a sphere-like cavity in a continuum dielectric material of permittivity ε.
A combination of Eq.(2.75) and Eq.(2.74) leads to the general form of the Onsager equation,

$$\frac{(\varepsilon - 1)(2\varepsilon + 1)\varepsilon_0}{3\varepsilon} = \sum_j \frac{\rho_j}{1 - \alpha_j f_j} \left(\alpha_j + \frac{1}{3k_B T} \cdot \frac{\mu^2_{eff,j}}{1 - \alpha_j f_j} \right). \tag{2.76}$$

Furthermore, for a simple dipolar liquid, Eq.(2.76) can be converted to

$$\frac{(\varepsilon - \varepsilon_\infty)(2\varepsilon + \varepsilon_\infty)}{\varepsilon(\varepsilon_\infty + 2)^2} = \frac{\rho \mu_{eff}^2}{9\varepsilon_0 k_B T}. \tag{2.77}$$

Statistical mechanics provides a possibility of taking into account the influence of specific intermolecular interactions. In this way molecular characteristics can be interpreted in terms of macroscopic properties. The theory[42,43] is based on a model of a dipole whose orientation correlates with its neighbors and results in the Kirkwood-Fröhlich equation,

$$\frac{(\varepsilon - \varepsilon_\infty)(2\varepsilon + \varepsilon_\infty)}{\varepsilon(\varepsilon_\infty + 2)^2} = \frac{\rho \mu^2}{9\varepsilon_0 k_B T} \cdot g, \tag{2.78}$$

where g is the Kirkwood factor, representing the interactions between the particles. If the orientation between the neighbors is preferentially parallel, a value $g > 1$ is found whereas $g < 1$ indicates an antiparallel orientation correlation.

2.4.2 Cavell equation

The Cavell equation[44] represents the extension of the Onsager equation (2.76) to systems with more dispersion steps, caused by different dipolar species. According to this theory, the dispersion amplitude, $S_j = \varepsilon_j - \varepsilon_{j+1}$, of a relaxation process j can be obtained from the concentration c_j of the species, its effective dipole moment, $\mu_{eff,j}$ and polarizability, α_j, by

$$\frac{2\varepsilon + 1}{\varepsilon} \cdot (\varepsilon_j - \varepsilon_{\infty,j}) = \frac{N_A c_j}{k_B T \varepsilon_0} \cdot \frac{\mu_{eff,j}^2}{(1 - f_j \alpha_j)^2}, \tag{2.79}$$

where f_j is a reaction field factor. For a sphere-like cavity of radius a_j, this factor is given as[27]

$$f_j = \frac{1}{4\pi\varepsilon_0 a_j^3} \cdot \frac{2\varepsilon - 2}{2\varepsilon + 1}. \tag{2.80}$$

For the evaluation of dispersion amplitudes Eq.(2.79) is used in the following form

$$c_j = \frac{(\varepsilon_j - \varepsilon_{\infty,j})\varepsilon_0(2\varepsilon + 1)}{\varepsilon} \cdot \frac{(1 - \alpha_j f_j)^2}{\mu_j^2} \cdot \frac{k_B T}{N_A} \tag{2.81}$$

However, since spherical cavities cannot always be assumed, Eq. 2.79 was extended for ellipsoidal particles with half-axes $a_j > b_j > c_j$[27,45]:

$$\frac{\varepsilon + A_j(1 - \varepsilon)}{\varepsilon} \cdot \Delta\varepsilon_j = \frac{N_A c_j}{3 k_B T \varepsilon_0} \cdot \frac{\mu_{eff,j}^2}{(1 - f_j \alpha_j)^2} \tag{2.82}$$

where

$$f_j = \frac{3}{4\pi\varepsilon_0 a_j b_j c_j} \cdot \frac{A_j(1 - A_j)(\varepsilon - 1)}{\varepsilon + (1 - \varepsilon)A_j} \tag{2.83}$$

and

$$A_j = \frac{a_j b_j c_j}{2} \int_0^\infty \frac{\mathrm{d}s}{(s+a_j^2)^{3/2}(s+b_j^2)^{1/2}(c+c_j^2)^{1/2}}. \tag{2.84}$$

2.4.3 Debye model of rotational diffusion

Debye tried to predict the relaxation time of a simple system consisting of an aggregation of sphere-like inelastic dipoles which do not interact with each other. Microscopically, colliding dipolar particles cause a reorientation of the dipole. Thus, this mechanism is regarded as a diffusion of dipole orientation.
However, the picture only holds as long as the moment of inertia and the dipole-dipole interaction can be neglected. Therefore, the applicability of this theory is limited to non-associated systems.
Within these limitations and by describing the inner field with a Lorentz field, Debye obtained the dipole correlation function,

$$\gamma(t) = \exp\left(-\frac{t}{\tau_s}\right), \tag{2.85}$$

where the relaxation time, τ_s, can be calculated from the friction factor, ζ,

$$\tau_s = \frac{\zeta}{2k_B T}. \tag{2.86}$$

Using hydrodynamic laws for the rotation of a sphere in viscous media, namely the Stokes-Debye-Einstein equation,

$$\tau_s = \frac{3V\eta}{k_B T} \tag{2.87}$$

is obtained, where V represents the volume of the sphere and η the dynamic viscosity of the environment of the sphere (the so-called microscopic viscosity). However the application of this theory has its drawbacks as the relation between macroscopic and microscopic viscosity is not clear.
This problem can be solved by introducing various parameters into the equation[46] that lead to the term

$$\tau_s = \frac{3V\eta}{k_B T} f_{stick} C + \tau_s^0. \tag{2.88}$$

The shape factor, f_{stick}, describes the deviation of the shape of the molecule from the ideal form of a sphere. For a sphere with *stick* boundary conditions of rotational diffusion $f_{stick} = 1$. The friction parameter, C, represents a correction of the macroscopic viscosity and its value in the case of *stick* conditions is $C = 1$. For *slip* motion, $C = 1 - f_{stick}^{-2/3}$.
τ_s^0 is an empirical value which can be interpreted as a correlation time of the free rotor.

2.4.4 Microscopic and macroscopic relaxation time

The relation between the experimentally measurable relaxation time, τ, and the microscopic relaxation time, τ_s, plays an important role in the interpretation of the dielectric spectra and there are various theoretical approaches that address this problem.
Debye suggested the expression[47]

$$\tau = \frac{\varepsilon + 2}{\varepsilon_\infty + 2} \cdot \tau_s, \tag{2.89}$$

derived under the assumption of a Lorentz field as inner field. However, this approach is not accurate enough for polar dielectrics and so it can be used for non-polar systems only. For the case of pure rotational diffusion Powles and Glarum combined the macroscopic and microscopic relaxation time[48,49] in the following manner

$$\tau = \frac{3\varepsilon}{2\varepsilon + \varepsilon_\infty} \cdot \tau_s \tag{2.90}$$

Using the *corresponding macro-micro correlation theorem* of statistical mechanics[50–52], a generalized form

$$\tau = \frac{3\varepsilon}{2\varepsilon + \varepsilon_\infty} \cdot \frac{g}{\dot{g}} \cdot \tau_s \tag{2.91}$$

can be obtained, where g is the Kirkwood correlation factor and $\dot{g}$ the dynamic correlation factor. When $g/\dot{g} = 1$, expression (2.91) turns into the Powles-Glarum equation (2.90).

2.5 Temperature dependence of relaxation times

2.5.1 Arrhenius equation

The Arrhenius equation[53] represents one of the oldest methods for the description of the temperature dependence of rate constants in the fields of chemical kinetics and of relaxation times.

$$\ln(\tau/\mathrm{s}) = \ln(\tau_0/\mathrm{s}) + \frac{E_a}{RT} \tag{2.92}$$

$$= a_0 + a_1/T \qquad \text{where} \qquad E_a = a_1 \cdot R \tag{2.93}$$

This approach is based on the idea that particles are pushed by thermal fluctuations to a transition between two stable energetic levels which are separated by a temperature dependent potential barrier, E_a, the activation energy. The frequency factor, τ_0, accounts for the shortest possible relaxation time.

Chapter 3

Experimental

3.1 Measurement of dielectric properties

3.1.1 Low-frequency impedance spectroscopy

The low-frequency dielectric response of liquids was measured with a complex voltage divider setup, Fig. 3.1. A gold plated coaxial capacitor cell (WTW, Germany) was filled with the sample ($\sim 30\,\mathrm{mL}$), thermostated by a circulating thermostat T (FP45-HP, Julabo, Germany) and connected in series to a switchable resistor, R, and a vector voltmeter (ZPV with E1 detector unit, Rhode&Schwarz, Germany) to measure the (complex) voltage ratio $\hat{r}_{\mathrm{ba}} = \hat{U}_{\mathrm{b}}/\hat{U}_{\mathrm{a}}$. From this ratio, the complex admittance of the cell, $\hat{Y}$, was calculated by Eq. 3.1.

$$\hat{Y} = \frac{\hat{r}_{\mathrm{ba}} - 1}{R} \tag{3.1}$$

The value of R can be set to $50\,\Omega$, $1000\,\Omega$ or $10\,\mathrm{k}\Omega$ to optimize the signal-to-noise ratio and to use the full resolution of the vector voltmeter.
An alternating voltage of $\sim 400\,mV_{\mathrm{PP}}$ from a signal generator (SG; SMH/SMG01, generously provided by Rhode&Schwarz, Germany) was applied to the resistor network. The frequency can be varied from $< 1\,\mathrm{kHz}$ to $\sim 10\,\mathrm{MHz}$.
The basic accuracy of the ZPV vector voltmeter is $\sim 2\%$ and some additional errors may be introduced by non-idealities of the setup. Thus, a careful calibration was performed before each series of measurement, using two substances of known dielectric properties, namely air and a solvent/water. For each spot frequency and setting of the resistor, R, an effective cell constant, $k(\nu, R)$, was determined from the difference of the complex admittance of the filled relative to the empty cell, $\hat{Y}_{\mathrm{cal}}$ and $\hat{Y}_{\mathrm{air}}$, respectively.

$$k = \frac{\mathrm{Im}(\hat{Y}_{\mathrm{cal}} - \hat{Y}_{\mathrm{air}})}{2\pi\nu\,\varepsilon_0\,\mathrm{Re}\,(\hat{\varepsilon}_{\mathrm{cal}} - \hat{\varepsilon}_{\mathrm{air}})} \tag{3.2}$$

Then, the dielectric properties of a sample, $\hat{\varepsilon}_{\mathrm{sap}}(\nu)$, can be calculated as

$$\hat{\varepsilon}_{\mathrm{sap}} = \hat{\varepsilon}_{\mathrm{air}} + \frac{1}{\mathrm{i}\,2\pi\nu\varepsilon_0 k}(\hat{Y}_{\mathrm{sap}} - \hat{Y}_{\mathrm{air}}) \tag{3.3}$$

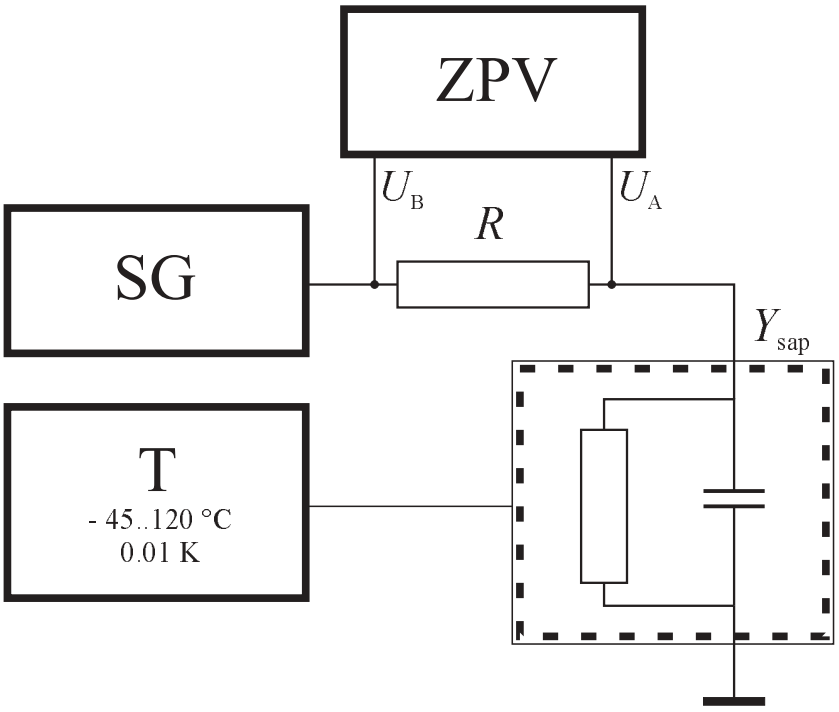

Figure 3.1: Block diagram of the setup for low-frequency dielectric measurements.

3.1.2 Time-domain reflectometry

Time domain reflectometry (TDR) was used to determine the dielectric properties of liquids up to several GHz. These can be obtained from reflection coefficient measurements on cells of the 'cut-off' variety[54].

Theory

The TDR experiment employs a fast rising voltage pulse, $V_0(t)$, which is applied to the sample. The shape of $V_0(t)$ is then compared with the transients of the signal reflected by the sample cell, $V_r(t)$.
An application of a Fourier transform to the time-dependent intensities of the signals results in

$$v_0(\omega) = \mathcal{L}_{\mathrm{i}\omega}\left[\frac{\mathrm{d}}{\mathrm{d}t}V_0(t)\right] = \int_0^\infty \frac{\mathrm{d}}{\mathrm{d}t}V_0(t)\cdot\exp(\mathrm{i}\omega t)\mathrm{d}t \tag{3.4}$$

$$v_r(\omega) = \mathcal{L}_{\mathrm{i}\omega}\left[\frac{\mathrm{d}}{\mathrm{d}t}V_r(t)\right] = \int_0^\infty \frac{\mathrm{d}}{\mathrm{d}t}V_r(t)\cdot\exp(\mathrm{i}\omega t)\mathrm{d}t, \tag{3.5}$$

where $v_0(\omega)$ and $v_r(\omega)$ represent the intensities in the frequency domain.

These can be used to calculate the absolute reflection coefficient of the cell, $\hat{\rho}(\omega)$, Eq. 3.6.

$$\hat{\rho}(\omega) = \frac{c_0}{\mathrm{i}\omega g l} \cdot \frac{v_0(\omega) - v_r(\omega)}{v_0(\omega) + v_r(\omega)} \tag{3.6}$$

l is the electrical pin-length and g the ratio between the wave resistance of the empty cell and the feeding line.
Within some approximations, the generalized complex dielectric permittivity, $\hat{\eta}(\omega)$, can be obtained from $\hat{\rho}(\omega)$ as

$$\hat{\eta}(\omega) = \hat{\rho}(\omega) \cdot \hat{z} \cot \hat{z} \tag{3.7}$$

where

$$\hat{z} = \frac{\omega l}{c_0} \sqrt{\hat{\eta}(\omega)}. \tag{3.8}$$

However, the signal intensity of the incident wave cannot be easily obtained from the measurement. Therefore, a sample of known (and preferably similar) dielectric properties is used, and a relative reflection coefficient,

$$\hat{\rho}_{xr}(\omega) = \frac{c}{\mathrm{i}\omega g l} \cdot \frac{\mathcal{L}_{\mathrm{i}\omega}\left[\frac{\mathrm{d}}{\mathrm{d}t} V_{rr}(t)\right] - \mathcal{L}_{\mathrm{i}\omega}\left[\frac{\mathrm{d}}{\mathrm{d}t} V_{rx}(t)\right]}{\mathcal{L}_{\mathrm{i}\omega}\left[\frac{\mathrm{d}}{\mathrm{d}t} V_{rr}(t)\right] + \mathcal{L}_{\mathrm{i}\omega}\left[\frac{\mathrm{d}}{\mathrm{d}t} V_{rx}(t)\right]}, \tag{3.9}$$

is determined instead of the absolute one. In Eq. 3.9, $V_{rx}(t)$ and $V_{rr}(t)$ represent the relative time dependent reflection intensities of the sample and the reference[55,56]. It can be shown that this coefficient can be expressed as

$$\hat{\rho}_{xr} = \frac{\hat{\eta}_x \cdot \hat{z}_r \cot(\hat{z}_r) - \hat{\eta}_r \cdot \hat{z}_x \cot(\hat{z}_x)}{\hat{z}_r \cot(\hat{z}_r) \hat{z}_x \cot(\hat{z}_x) + g^2 \cdot \hat{\eta}_x \hat{\eta}_r (\omega l / c)^2} \tag{3.10}$$

with

$$\hat{z}_x = \frac{\omega l}{c} \sqrt{\hat{\eta}_x} \quad \text{and} \quad \hat{z}_r = \frac{\omega l}{c} \sqrt{\hat{\eta}_r}. \tag{3.11}$$

In order to obtain the complex dielectric permittivity of the sample, some approximations have to be used as no closed solution of Eq.(3.10) exists. For a numerical solution, a Newton-Raphson procedure was employed and the term $\hat{z} \cdot \cot \hat{z}$ expanded into a Taylor series[57].

Instrumentation

An overview of the experimental setup presently used is given in Fig. 3.2. The time-domain reflectometer is composed of a sampling scope (TEK 11802; Tektronix) and two sampling heads (SD24), which generate a square wave signal with a frequency of 200 kHz and very fast rise time (typ. 17.5 ps). Each of the sampling heads has two independent channels which are used for the measurement of two cells of the cut-off variety. One trace is used for the actual sample measurement, the other as a time reference to account for drifts of the time base. Traces were recorded with a resolution of 5120 points and averaged over 256 single measurements, to reduce random noise. Several cells are available to optimize the signal-to-noise ratio depending on frequency range and sample properties. Further details were already described elsewhere.[54,58].

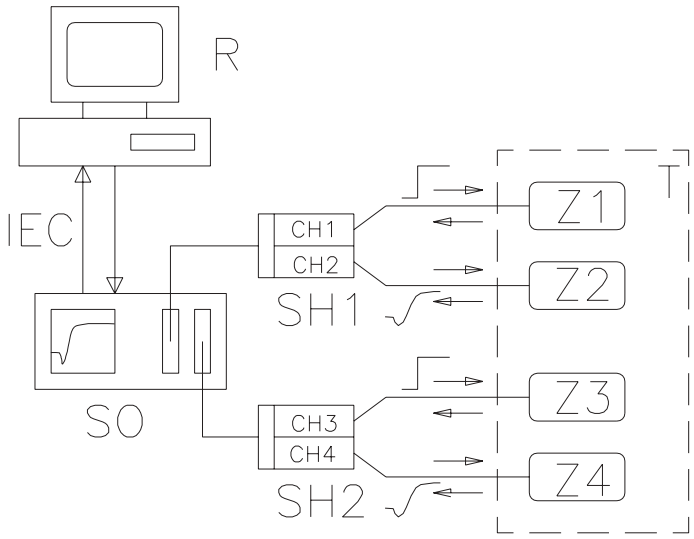

Figure 3.2: Diagram[54] describing the time-domain reflectometer used in our group: **SO** digital sampling scope; **SH1,SH2** SD-24 sampling heads; **Z1-Z4** cutoff cells; **T** precision thermostat; **R** personal computer with access to other computers for data analysis.

3.1.3 Frequency-domain reflectometry

Data acquisition

Dielectric experiments up to 20 GHz were performed with a Hewlett Packard HP85070B coaxial probe and a HP8720D vector network analyzer (VNA) at the institute of Prof. Glenn Hefter, Murdoch University (Western Australia). The network analyzer is used to determine the relative complex reflection coefficient $\hat{\Gamma}_a$ at the probehead/sample interface. $\hat{\Gamma}_a$ is related to the normalized aperture impedance of the probe head, $\hat{Y}$, by

$$\hat{\Gamma}_a = \frac{1-\hat{Y}}{1+\hat{Y}}. \tag{3.12}$$

Some modifications of the former experimental setup[59] were required due to the limited amount of sample material available. The probe head was placed inside of a thermostated holder, Fig. 3.3, equipped with a calibrated temperature sensor. With the new design, a sample volume of ~ 3 mL is sufficient for the measurement, compared with $25-30$ mL necessary for the old procedure. Additionally, problems arising from air bubbles and impurities of the surface of the mercury short are avoided, as the probe surface is located at the bottom of the sample containment.

A simplified coaxial aperture opening model[60,61] was used to calculate the complex dielectric properties $\hat{\varepsilon}_m$ from the normalized aperture impedance of the probe head, $\hat{Y}$, by

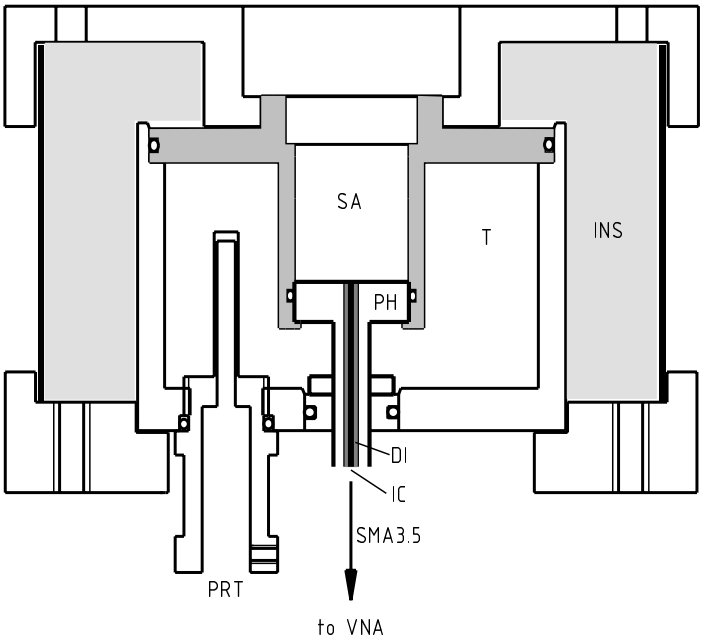

Figure 3.3: VNA cut-off cell for liquid samples. **PH** represents the HP85070B coaxial probe head, **SA** the sample space, **T** is the mantle filled with thermostating liquid, **PRT** the opening for a platinum resistance temperature probe, **INS** insulating rubber foam. **IC** is the inner conductor of the probe head, surrounded by dielectric material **DI**, characterized by dielectric properties $\hat{\varepsilon}_\mathrm{c}$.

numerical solution of Eq. 3.13,

$$\hat{Y} = \frac{\mathrm{i}\hat{k}_\mathrm{m}^2}{\pi\hat{k}_\mathrm{c}\ln(b/a)}\left[\mathrm{i}\left(I_1 - \frac{\hat{k}_\mathrm{m}^2 I_3}{2} + \frac{\hat{k}_\mathrm{m}^4 I_5}{24} - \frac{\hat{k}_\mathrm{m}^6 I_7}{720} + ...\right) + \left(I_2\hat{k}_\mathrm{m} - \frac{\hat{k}_\mathrm{m}^3 I_4}{6} + \frac{\hat{k}_\mathrm{m}^5 I_6}{120} - ...\right)\right], \tag{3.13}$$

where $\hat{k}_\mathrm{c} = \omega\sqrt{\hat{\varepsilon}_\mathrm{c}\varepsilon_0\mu_0}$ is the propagation constant within the dielectric material of the coaxial probe head and $\hat{k}_\mathrm{m} = \omega\sqrt{\hat{\varepsilon}_\mathrm{m}\varepsilon_0\mu_0}$ that of the sample, respectively. The first 28 probe constants, I_i, calculated from a theoretical approach and further optimized,[61] were used.

For the measurement of the reflection coefficient $\hat{\Gamma}_\mathrm{a}$, a standard VNA three point calibration was employed, Eq. 3.14, to correct for signal distortions between the reference plane of the probe head and that of the VNA instrument.

$$\hat{\Gamma}_\mathrm{a} = \frac{\hat{\Gamma}_\mathrm{m} - \hat{e}_\mathrm{d}}{\hat{e}_\mathrm{s}(\hat{\Gamma}_\mathrm{m} - \hat{e}_\mathrm{d}) + \hat{e}_\mathrm{r}}. \tag{3.14}$$

Three reference measurements of the (uncorrected) reflection coefficient $\hat{\Gamma}_\mathrm{m}$ were used to determine the complex, frequency-dependent correction constants $\hat{e}_\mathrm{d}$, $\hat{e}_\mathrm{r}$ and $\hat{e}_\mathrm{s}$ by forward application of Eq. 3.13. The references include air, short and a liquid, namely,

N,N-dimethylacetamide (DMA; measurement 1) or N,N-dimethylformamide (DMF; measurement 2).

Data correction

By use of this procedure, rather accurate spectra of non-conducting liquids can be obtained for materials with dielectric properties similar to that of the calibration standard. As the dielectric constant of water + 1,4 dioxane varies from 2.2 to 78, significant errors were observed at both ends of the composition range, Fig. 3.4. Whereas the permittivities were found up to 10 % higher at low values of ε, these were too low at high water concentrations ($\varepsilon > 40$).

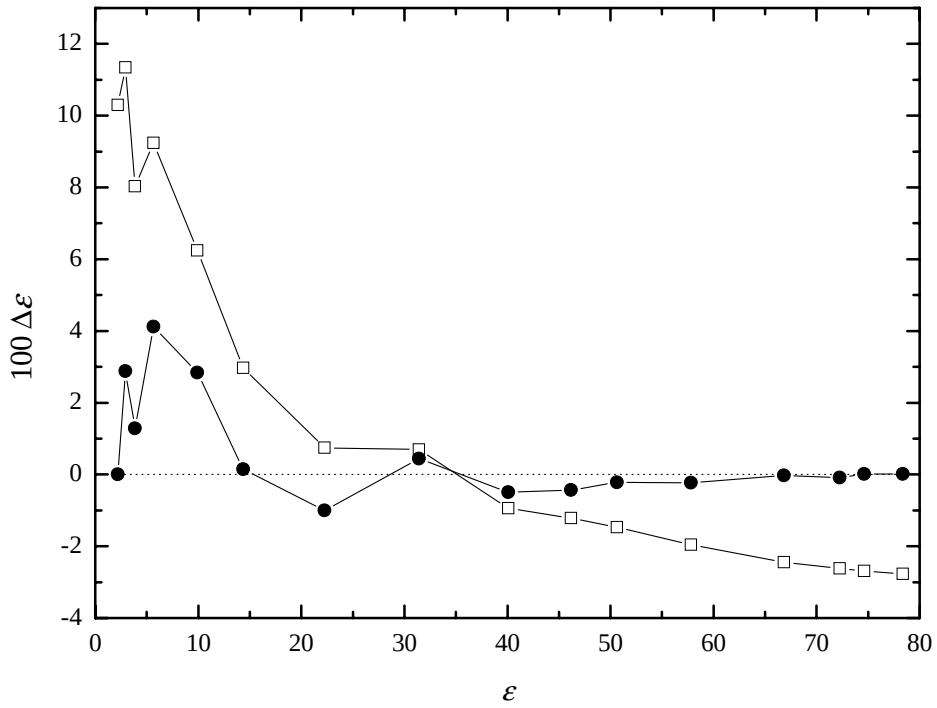

Figure 3.4: Relative error of the static dielectric constant, $\Delta\varepsilon = (\varepsilon - \varepsilon_{\mathrm{ref}})/\varepsilon_{\mathrm{ref}}$, determined on various 1,4-dioxane + water mixtures (uncorrected data: □, 1-1 Pade-correction: •). The accuracy of the reference value, $\varepsilon_{\mathrm{ref}}$, calculated from various literature data and precision measurements, is estimated to be in the order of 0.5 %.

Therefore, we applied a further correction to the measured ε_{m}, comprising a complex Padé approximation method, Eq. 3.15.

$$\varepsilon_{\mathrm{m}}^{\mathrm{corr}} = P_{n/m}\left[\varepsilon_{\mathrm{m}}\right] = \frac{A_0 + A_1\varepsilon_{\mathrm{m}} + ... + A_n(\varepsilon_{\mathrm{m}})^n}{1 + B_1\varepsilon_{\mathrm{m}} + ... + B_m(\varepsilon_{\mathrm{m}})^m} \tag{3.15}$$

The approximation constants, $A_n(\omega)$ and $B_m(\omega)$, can be calculated either analytically or by a complex linear fit algorithm[57] from a set of measurements of substances with known

dielectric properties, namely 1,4-dioxane (DX), benzonitrile (BN), propylene carbonate (PC), water(W) and air.

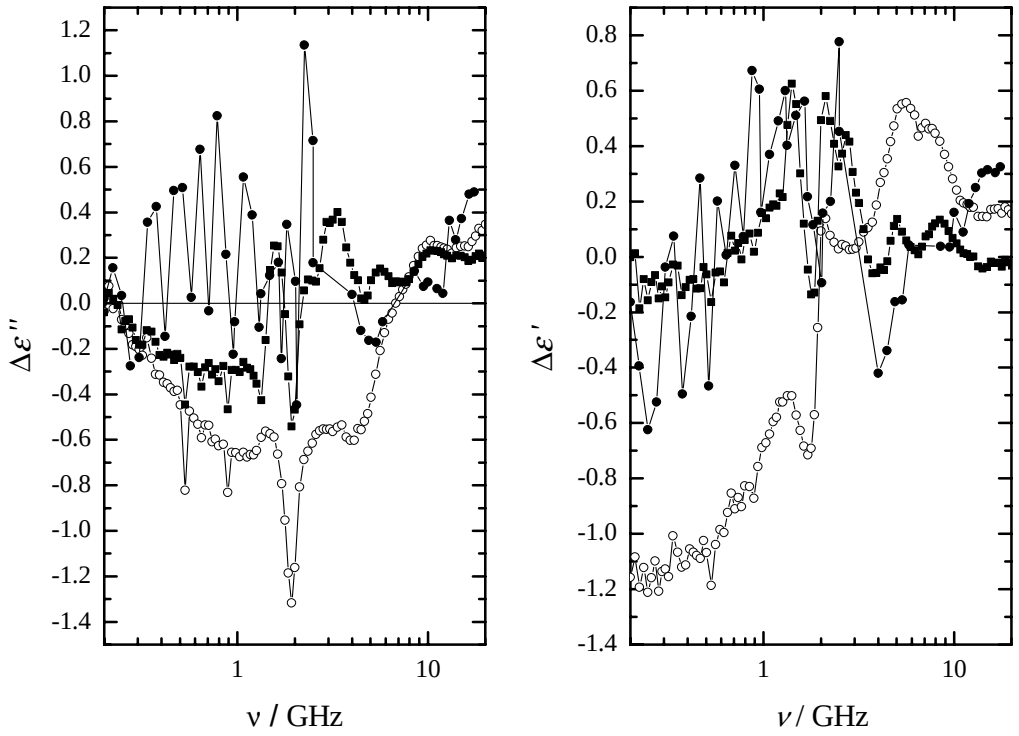

Figure 3.5: Frequency-dependent deviations of the complex permittivity of propylene carbonate at 298.15 K from the well establish reference relaxation model. (○) represent raw data obtained from VNA measurements with references AIR/SHORT/DMA. (■) are data after 1-1 Padé correction with AIR/DMA/Water as reference. The difference of the reference data, obtained by interferometry and TDR experiments, from the fit model (●) is also shown.

Fig. 3.5 shows spectra obtained with propylene carbonate as a sample liquid. For the uncorrected data, significant systematic, frequency dependent deviations were found. With a Padé correction applied, the errors lay within the scatter of the precision interferometry and TDR data which were used for the fit.
Therefore, the Padé correction is a simple and quite effective method to improve the accuracy of data obtained from VNA-R measurements, especially for samples of low permittivity.

3.1.4 Interferometry

Waveguide interferometers based on the principle of travelling waves were used for the determination of dielectric properties, especially at frequencies $> 20\,\mathrm{GHz}$.
For each frequency, several steps are required to get both attenuation coefficient and medium wavelength from a single data set. After setting up all the auxiliary devices, the first step of the procedure requires to establish a fully destructive interference at a probe position z_0' by means of attenuators and a phase shifter.
Assuming harmonically oscillating fields, the time-dependent electric field propagating through the reference beam is given by

$$\hat{E}_1(t) = E_0 \exp(\mathrm{i}\omega t) \tag{3.16}$$

Let now z_0 be the absolute optical path length of the sample liquid and x the relative distance from the interference minimum, $x = z_0 - z_0'$.
Thus, we assume for the sample beam,

$$\hat{E}_2(t,x) = E_0 \exp(-\alpha x) \exp\left[\mathrm{i}(\omega t + \pi - \beta x)\right]. \tag{3.17}$$

The term π of the second exponential term results from the condition of fully destructive interference, which requires a phase shift of $\Delta\varphi$ of the interfering waves,

$$\Delta\varphi = (2n+1)\pi \quad \text{mit } n \in \mathbb{Z}. \tag{3.18}$$

At the receiver, the sum of the fields propagating through the sample and reference beam,

$$\hat{E}(t,x) = \hat{E}_1(t) + \hat{E}_2(t,x) = \hat{E}_0 \exp(\mathrm{i}\omega t)\left[1 + \exp(-\alpha x)\exp(\mathrm{i}(\pi - \beta x))\right], \tag{3.19}$$

can be detected.
The power P of the signal reaching the receiver can be calculated from the square of the amplitude of the electric field,

$$P = \hat{E} \cdot \hat{E}^* = E_0^2 \cdot I(x) \tag{3.20}$$

where $I(x)$ is the interference function,

$$\begin{aligned} I(x) &= \left[1 + \exp(-\alpha x)\exp(\mathrm{i}(\pi - \beta x))\right] \cdot \left[1 + \exp(-\alpha x)\exp(\mathrm{i}(\pi - \beta x))\right] && (3.21)\\ &= 1 + \exp(-2\alpha x) + \exp(-\alpha x) \cdot 2\cos(-\pi + \beta x). && (3.22) \end{aligned}$$

The quantity actually measured by the experiment is the relative attenuation of the signal on a logarithmic scale, $A(x)$, Eq. 3.23.

$$A(x) = 10\,\mathrm{lg}\,\frac{P(x)}{P_{\mathrm{ref}}}. \tag{3.23}$$

P_{ref} is usually not known and the measured attenuation is normalized by A_0 corresponding to $P_0 = E_0^2$:

$$\begin{aligned} A_{\mathrm{rel}}(x) &= A(x) - A_0 \\ &= 10\lg\frac{P(x)}{P_{\mathrm{ref}}} - 10\lg\frac{P_0}{P_{\mathrm{ref}}} \\ &= 10\lg\frac{P(x)}{P_0} \\ &= 10\lg\frac{E_0^2\cdot I(x)}{E_0^2} \end{aligned} \tag{3.24}$$

Therefore, the power attenuation coefficient, α_{dB} in dB/m, and the wavelength of the radiation within the sample, $\lambda_{\mathrm{M}} = 2\pi/\beta$ can be obtained from a fit of the recorded interference data $A(z_0 - z_0')$ by the expression[62]

$$\begin{aligned} A(z_0 - z_0') = A_0 + 10\lg\{&1 + \exp\left[-2p\alpha_{\mathrm{dB}}(z_0 - z_0')\right] \\ &- 2\cos\left(\frac{2\pi}{\lambda_M}(z_0 - z_0')\right)\cdot\exp\left[-2p\alpha_{\mathrm{dB}}(z_0 - z_0')\right]\Big\} \end{aligned} \tag{3.25}$$

with the conversion constant

$$p = \left(20\lg\mathrm{e}\cdot\frac{dB}{Np}\right)^{-1}. \tag{3.26}$$

Instrumentation

For the measurements double-beam interferometers with a measuring cell of variable pathlength in the sample beam were used. The apparatus of the Buchner group (for details see[62]) is composed of a set of four rectangular waveguide interferometers working on the transmission principle, each with waveguides fitted to a particular microwave frequency band: X-band $8.5 \leq \nu/\mathrm{GHz} \leq 12$, Ku-band $12.5 \leq \nu/\mathrm{GHz} \leq 18$, A-band $27 \leq \nu/\mathrm{GHz} \leq 40$ and E-band $60 \leq \nu/\mathrm{GHz} \leq 89$. Within slight variations, all instruments follow the construction of the E-band instrument, Fig. 3.6. For all bands, a frequency stabilized signal source whose output is split by a directional coupler, feeds both the measuring and reference branch. In the measuring branch, a phase shifter and a sample cell are placed. The cell is composed of a piece of wave guide filled with the sample liquid and a probe with variable, motor-controlled position. The reference branch comprises a precision phase shifter and attenuators. The relative amplitude of the recombined beams is then measured by a precision attenuation measurement receiver, equipped with proper mixers for frequency conversion.

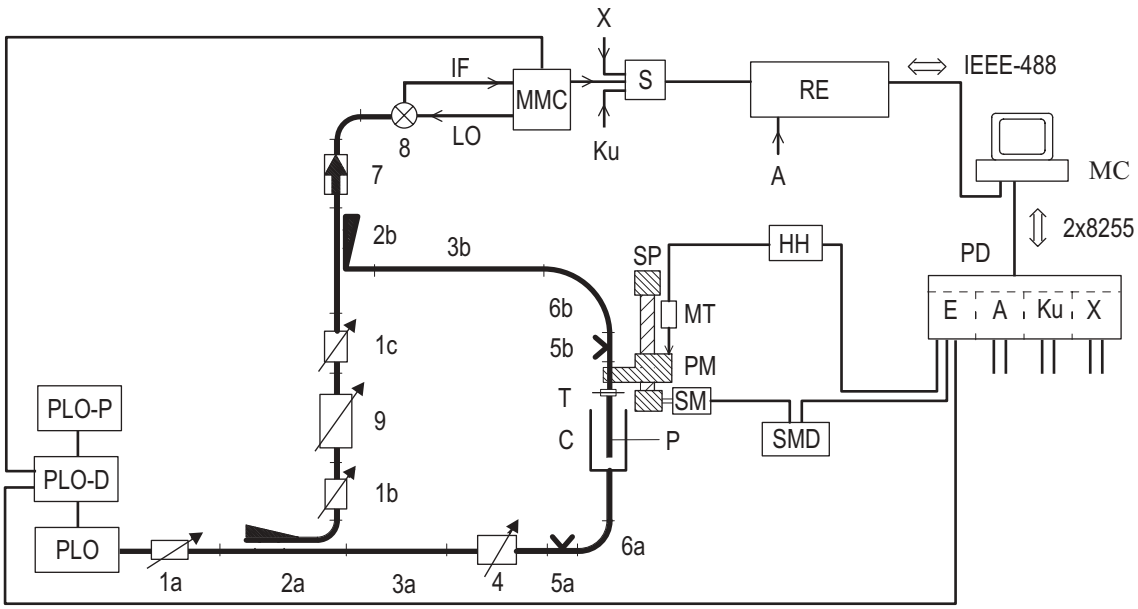

Figure 3.6: Block diagram of the E-band device[62]: **1a**, **b**, **c** represent variable attenuators; **2a**, **b** directional couplers; **3a**, **b** waveguide sections; **4** precision phase shifter; **5a**, **b** E/H tuners; **6a**, **b** flexible waveguides; **7** isolator; **8** harmonic mixer; **9** variable precision attenuator; **C** cell, **HH** bidirectional counter; **MC** microcomputer; **MMC** millimeter-wave to microwave converter; **MT** digital length gauge; **P** probe; **PD** parallel interface unit; **PLO** phase locked oscillators; **PLO-D** PLO-control unit; **PLO-P** PLO-power supply; **PM** probe mount; **RE** precision receiver; **S** electromechanical switch; **SM** stepping motor; **SMD** stepping motor control unit; **SP** spindle and spindle mount; **T** tapered transmission; double lines represent waveguides, thick lines semi-rigid microwave cables and normal lines symbolize data transfer connections (analog or digital).

3.1.5 Time-domain THz-pulse spectroscopy

A standard THz time-domain spectrometer setup in a *1f-2f-2f-2f-1f* geometry, as previously described in literature[63,64], Fig. 3.7, was used in cooperation with the group of Prof. Helm at the University of Freiburg (Germany). Pulses of $\sim 15-20$ fs duration from a Ti:sappire oscillator ($\sim$ 260 mW, 80 MHz repetition rate, $\sim$ 800 nm center wavelength; Femtolasers, Wien, Austria) pumped by a frequency-doubled Nd:YVO_4 solid state laser (4 W, 532 nm; VERDI, Coherent, USA) were used to excite a gallium arsenide (GaAs) dipole antenna, biased with a voltage $\sim$ 35 V applied between strips of 30 μm distance. The estimated power incident on the transmitter chip is $\sim$ 20 mW. Another part of the femtosecond (fs) laser pulse is used to gate a dipole receiver (silicon on saphire, H structure with 5 μm gap). The photocurrent is measured by means of a lock-in amplifier and a chopper wheel operating at $\sim$ 330 Hz.

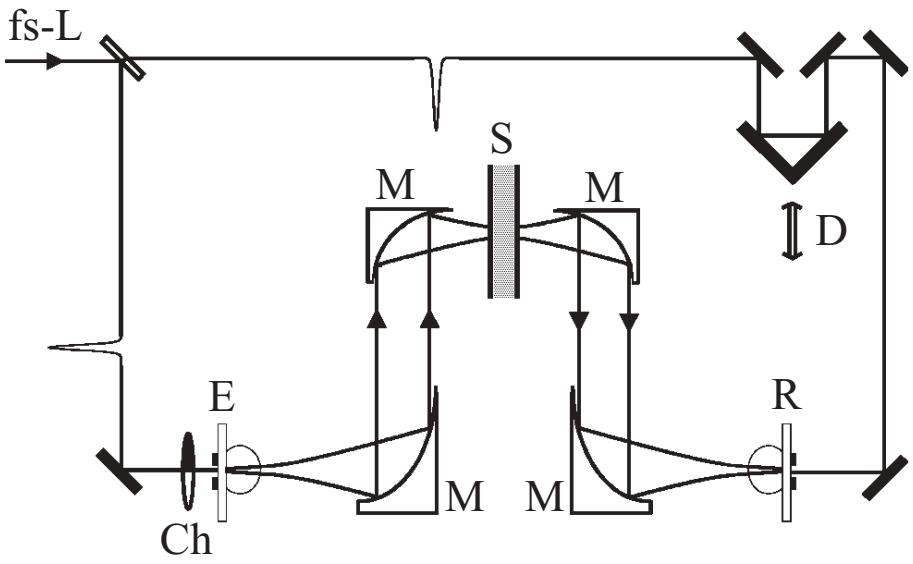

Figure 3.7: THz-TDS setup. **fs-L** represents the fs-laser, **Ch** the chopper wheel, **M** are parabolic mirrors, **S** is the liquid sample placed between two windows, **E** emitter antenna, **R** is the receiver antenna. **D** is a delay line placed within the gate beam.

With a delay line placed in the gate beam, the temporal profile of the electric field strength of the THz pulse was recorded over 140 ps with time steps of 67 fs. Thus, the spectral resolution is $\sim$ 30 GHz over a useful bandwidth from 200 GHz to 4 THz ($7-130\,\mathrm{cm}^{-1}$). The whole THz beam path is located within a box filled with dry nitrogen (N_2) to avoid absorption induced by rotational transitions of water molecules.
A spherical silicon (Si) lens and two off-axis parabolic mirrors were used to focus the THz beam to a spot of $\sim$ 3 mm diameter, with another two mirrors and a Si lens guiding the signal to the gated ultrafast antenna receiver.
The liquid samples were placed in the focus of the THz beam between two parallel windows made from ram-extruded PTFE (Dyneon, Germany), each 3 mm thick, Fig. 3.8. The pathlength was set by a metal spacer made from carbon steel and gold plated. Perfluoroelastomer seals (Kalrez 4079, DuPont Dow, USA) were used throughout, as 1,4-dioxane

readily attacks all other common elastomer materials. The cell (Fig. 3.8) was placed between two thermostated metal blocks and the temperature monitored by means of a calibrated platinum resistance temperature probe connected to a precision thermometer (TWS Donauwörth, 15 mK accuracy, 1 mK resolution; sensor accuracy ~ 20 mK).

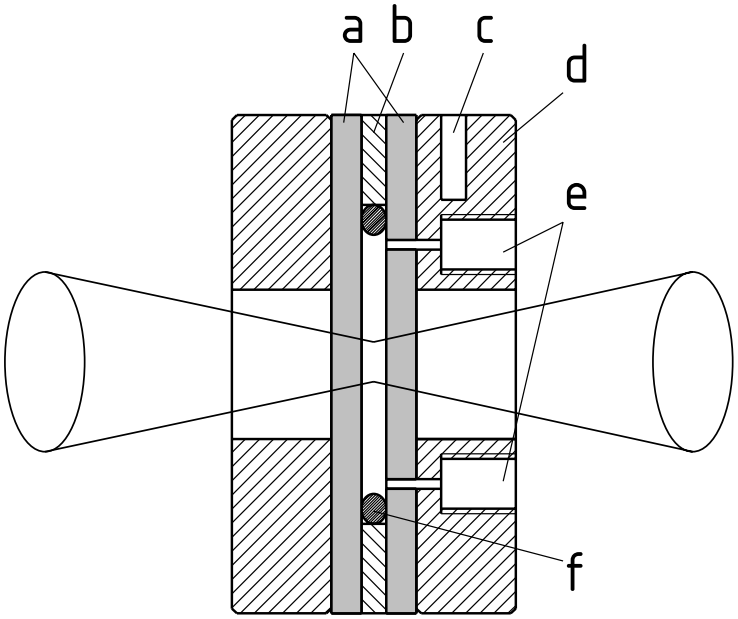

Figure 3.8: THz cell for liquid samples. (a) windows (PTFE), (b) precision spacer (carbon steel, gold plated), (c) platinum resistance thermometer, (d) cell body, (e) sample inlet/outlet (connected to PTFE tubing), (f) O-ring seal.

Immediately after the time domain spectrum of the empty cell (reference pulse, $E_{\mathrm{r}}(t)$) was obtained, the cell was filled with the sample from outside of the N_2-filled box through PTFE (Teflon) tubing. After some thermal equilibration, the sample transmission data (sample pulse, $E_{\mathrm{s}}(t)$) were recorded. The time-domain data were transformed into the frequency domain by the Fourier integral,

$$\hat{E}_{\mathrm{r,s}}(\nu) = \frac{1}{2\pi} \int_{-\infty}^{+\infty} e^{-\mathrm{i}\,2\pi\nu t} E_{\mathrm{r,s}}(t) dt. \tag{3.27}$$

From the (complex) ratio $R(\nu)$ of the Fourier transforms of the sample pulse and the reference pulse,

$$\hat{R}(\nu) = \hat{E}_{\mathrm{s}}(\nu)/\hat{E}_{\mathrm{r}}(\nu) = A(\nu) \cdot e^{\mathrm{i}\,\Delta\phi(\nu)}, \tag{3.28}$$

the refractive index of the sample is determined by the phase $\Delta\phi$ of $\hat{R}$ as $n_{\mathrm{s}} = n_{\mathrm{air}} + c\,\Delta\phi/2\pi\nu d$, where d is the thickness of the sample, $n_{\mathrm{air}} = 1.00027$ the refractive index of air and c the speed of light. Assuming a weakly absorbing sample, the absorption coefficient

is calculated from the amplitude, A, of $\hat{R}$ as $\alpha_s = -2\ln(f \cdot A)/d$, where

$$f = \frac{(n_w + n_s)^2}{n_s \cdot (n_w + 1)^2} \tag{3.29}$$

accounts for the reflection losses at the sample/PTFE interfaces. The refractive index of the PTFE window material was assumed to be $n_w = 1.433$[65] over the frequency range studied.
From the calculated values of $n_s(\nu)$ and $\alpha_s(\nu)$ the complex frequency-dependent dielectric response of the sample liquid, $\varepsilon(\nu)$, can be obtained by Eq. 3.30,

$$\hat{\varepsilon}(\nu) = [n_s(\nu) - \mathrm{i}k(\nu)]^2, \tag{3.30}$$

where $k(\nu) = c\,\alpha_s/4\pi\nu$.

Note: The determination of the optical thickness d of the sample is carried out by analysis of the temporal shape of a THz pulse transmitted through the empty cell. Please refer to the water + 1,4-dioxane section for a detailed description of the procedure.

3.2 Further measurements

3.2.1 Densitometry

Solution densities, ρ, were determined by vibrating tube densimetry (Anton Paar DMA602/ mPDS4000 system) and are accurate to $\sim 5 \cdot 10^{-3}\,\mathrm{kg\,m^{-3}}$. The temperature was kept constant to $\pm 4\,\mathrm{mK}$ with a circulating thermostat (Julabo F33 SD). The densimeter was calibrated using water and air as references. The density of water at 298.15 K was taken as $997.047\,\mathrm{kg\,m^{-3}}$ consistent with the IAPWS-IF97 value[66], and that of air was calculated from generally accepted equations[67]. At least two independent density measurements were performed with each solution.

3.2.2 Refractive indices

Refractive indices were measured with a Zeiss Jena refractometer, Abbé type, using the sodium D line. Values are accurate to 0.00015 and with a precision of 0.00005. The temperature was kept constant by a circulation thermostat and is estimated to be accurate to $\pm 0.15\,^{\circ}\mathrm{C}$. The instrument was calibrated using suitable reference liquids (water, 2-propanol, *n*-dodecane) or glass standards.

3.2.3 Viscosimetry

Dynamic viscosities were determined using a rotational viscosimeter RV-DVIII+ (Brookfield, UK).
The instrument was calibrated using *n*-decanol as reference liquid (η=11.75 mPa s[68,69]). All measurements described here were done with a cone of 0.5° slope, $r_0 = 24\,\mathrm{mm}$. The estimated accuracy of the instrument is 1% relative to the reference liquid. The temperature was stable to $\pm 0.1\,\mathrm{K}$ with an accuracy of 0.5 K.

3.2.4 Determination of liquid/liquid phase diagrams

Liquid/liquid phase diagrams were measured using an automated, high precision apparatus. All details and a careful evaluation of the instrument have already been published[23]. A reprint is attached as Appendix A to this thesis.

3.3 Calorimetric techniques

3.3.1 Picker flow calorimetry

Isobaric volumetric heat capacities were measured relative to water using a Picker flow calorimeter (Sodev, Sherbrooke, Canada) at the institute of Prof. Glenn Hefter, Murdoch University (Western Australia). The instrument consists of a specific heat unit, model CP-Cpr, a thermal detector, model DT-C, and a temperature control/program unit, model CT-L. A peristaltic pump (Gilson Minipulse 3) was used to control the flow

rate ($\sim 0.5\,\mathrm{mL\,min^{-1}}$). The output voltage from the detector was digitized by a voltmeter (Agilent 34401A) connected to a computer. From each measurement, two independent values were determined for the relative volumetric heat capacity $\Delta\sigma/\sigma^0 = (\sigma - \sigma^0)/\sigma^0$, where σ and σ^0 are the heat capacities per unit volume of the sample and reference liquid respectively[70]. The values of c_p, the isobaric specific heat capacity, were calculated from these values using the expression[71]

$$c_\mathrm{p} = c_\mathrm{p}^0 \cdot (1 + \Delta\sigma/\sigma^0) \cdot \rho^0/\rho. \tag{3.31}$$

The calorimeter was calibrated electrically at the end of each series of measurements. Water was used as a reference liquid, assuming $c_\mathrm{p}^0 = 4181.3\,\mathrm{J \cdot K^{-1} \cdot kg^{-1}}$ according to the IAPWS-95 formulation[72]. No correction was made for heat losses[70].

3.3.2 Tian-Calvet calorimetry

A Tian-Calvet type heat-conduction microcalorimeter (MicroDSC II, Setaram, France) was utilized to measure the heat capacities of the pure organic materials with an accuracy sufficient for the determination of thermodynamic excess quantities. Specially designed batch cells (sample volume $\sim 0.8\,\mathrm{mL}$) made from stainless steel with a perfluoroelastomer O-ring seal (Kalrez 4079) were used. A discontinuous step method was employed with heating/cooling rates of $0.1\,\mathrm{K/min}$ and an isothermal delay of $3600\,\mathrm{s}$[73,74]. The power difference needed to heat or cool the reference and sample cells between 297.65 and 298.65 K (1 K step) were determined by integration of the heat flow signals. An internal reference (*n*-Heptane; $c_\mathrm{p} = 2244.4\,\mathrm{J \cdot K^{-1} \cdot kg^{-1}}$) was used[75]. Heat capacities were calculated from two independent experiments, each consisting of several heating and cooling cycles. The reproducibility of the c_p values was usually better than 0.1%, the overall uncertainty of the measurement estimated from calibration and test experiments is assumed to be $\sim 0.3\%$. No allowances were made for sample vaporization and gas phase corrections as the vapor volume was kept below 10% of the total cell volume and all substances have quite low vapor pressures at the measurement temperature[76].

We thank Dr. Jürgen Seidel and Prof. Gert Wolf (TU Bergakademie Freiberg) for providing access to their calorimeter and for valuable hints.

Chapter 4

Investigation of model systems

4.1 1,4-Dioxane + water

4.1.1 Introduction

1,4-Dioxane is miscible with water and is therefore a very popular solvent system for various studies of reaction kinetics or conductivity, as a large range of dielectric constants ($\varepsilon = 2 - 78$ at 298.15 K) can easily be attained. It is also a polar solvent mixture of high industrial importance and used in many chemical reactions and other applications.
Despite of the miscibility with water, it offers a substantial non-interacting surface area (C_2H_4 segments), which enables us to study the effect of small hydrophobic inclusions on water dynamics.
Since dioxane molecules cannot form hydrogen bonds with themselves, no associated dioxane aggregates can be formed. Additionally, 1,4-dioxane in its predominant chair conformation does not have an overall dipole moment, resulting in a very low dielectric constant ($\varepsilon = 2.21$ at 298.15 K). Therefore, dielectric spectroscopy is a well suited tool to study the dynamics of these liquids, as all significant contributions to the dielectric spectra arise from water molecules, either interacting only with other water molecules arranged to clusters or with dioxane oxygen sites.
Further understanding of the microdynamics and intermolecular interactions of this system can be obtained by linking thermodynamic data, especially the excess volumes[77], excess heats of mixing[78], molar excess heat capacities[77] and viscosity, to structural and dynamic information determined by X-ray diffraction, NMR[79] and spectroscopic techniques, with DRS extending low-frequency Raman scattering[80] and IR spectroscopy[81].
Furthermore, intermolecular resonance modes, which can be observed in the THz region at low water concentrations in 1,4-dioxane, can lead to a better understanding of water dynamics at interfaces or inside hydrophobic cavities, a matter of outstanding importance from a biological point of view, but also for basic research.
Due to a lack of commercial instruments and technical difficulties associated with the study of the dielectric response of liquids in the high-GHz and THz region ($1.5-120\,\mathrm{cm}^{-1}$), former studies suffer from insufficient frequency coverage[82] or a scarcity of spot frequencies, at which the complex dielectric constant was measured[83–85].

This study uses different techniques for obtaining complex dielectric spectra, namely, VNA-reflectometry (VNA-R), waveguide interferometry (IF) and time-domain THz pulse spectrometry (THz-TDS). This enables us to cover the whole frequency band of interest with regard to hydrogen bond dynamics.

4.1.2 Materials

1,4-Dioxane (Merck, Germany; analytical grade) for the preparation of aqueous mixtures was refluxed over solid calcium hydride and then distilled under dry nitrogen atmosphere[86]. The water content of the purified material (mole fraction $\geq$ 0.9997, g.c.) was always found to be below 30 ppm (coulometric Karl Fischer apparatus).

For the measurements of the THz spectra of pure 1,4-dioxane, material of UV spectroscopic grade (Fluka, Switzerland) was extensively dried by refluxing and stirring over calcium hydride for 14 days and subsequently distilled within the same, specially equipped apparatus ($H_2O < 15$ ppm).

Deuterium oxide (euriso-top, Saclay, France; isotope enrichment $\geq$ 99.9 %) was used without further purification.

1,4-Dioxane-D_8 purchased from Cambridge Isotope Laboratories (Andover, USA; isotope enrichment 99.2 %) was dried over 4 Å molecular sieves (fully dehydrated by heating in a quartz tube to 300-350 °C at a pressure $\leq 10^{-7}$ mbar for several days).

The mixtures were prepared gravimetrically on an analytical balance without buoyancy corrections. Concentrations are thus accurate to four significant figures. Water, deionized and purified with a Millipore Milli-Q system (finally passed through a 0.22 μm filter) was used throughout the experiments. Densities of these and related glycol ether + water mixtures were reported elsewhere[77].

4.1.3 VNA measurements and correction

VNA measurements were performed and permittivities calculated from the raw data as already described, see Chap. 3.1.3. Two sets of data were recorded, one with air, a liquid mercury short and N,N-dimethylacetamide as reflectivity standards, the other with N,N-dimethylformamide substituted for DMA.
A careful evaluation showed that best results were obtained by using a DX/BN/DMA $P_{1/1}$ and DX/BN/DMF $P_{1/1}$ approximation for the AIR/SHORT/DMA (1) and AIR/SHORT/DMF (2) measurements for a static permittivity of the sample, $\varepsilon \lesssim 40$, for the others, DX/DMA/W $P_{1/1}$ and DX/DMF/W $P_{1/1}$. The two corrected spectra, $\hat{\varepsilon}^{\,\mathrm{corr},1}(\nu)$ and $\hat{\varepsilon}^{\,\mathrm{corr},2}(\nu)$, were always found in very good agreement and then averaged.

4.1.4 THz-TDS measurements

THz-TDS measurements were all performed by the group of Prof. Helm, Department of Molecular and Optical Physics, University of Freiburg, Germany. All technical details can be found in the experimental section, Chap. 3.1.5. The existing THz setup was equipped with a cell, developed in Regensburg and suitable for the determination of complex dielectric properties of liquid samples. The accuracy of the measurement is affected by several parameters. One limiting factor is, of course, the stability of the laser system with regard to power output and noise as well as the phase stability of the THz antenna/receiver setup. To account for these drift effects, each sample measurement was windowed by two measurements of the empty (i.e. nitrogen filled) cell. In all cases, ~ 8 traces of the delay-time dependent photocurrent $I(t)$, which is directly related to the electric field strength $E(t)$, were recorded and averaged. Then, the reference (empty cell) and sample data were transformed into the frequency domain by means of a fast Fourier transform (FFT) algorithm and the resulting dielectric spectra $\hat{\varepsilon}(\nu)$ checked for drifts by comparison of reference measurement before and after the sample measurement. In most cases both spectra were found to be in good agreement and then averaged. The fluctuations, especially of the real part of the complex permittivity, caused by phase instabilities of the experimental setup (e.g. due to thermal expansion of the optical table), can be estimated to be in the order of $\sim 0.02 - 0.05$ absolute units of ε'.

For the determination of absolute values for the refractive index and absorption, the knowledge of the exact path length of the sample is essential. Common mechanical ways for the determination of the liquid path length, x (Fig. 4.2), cannot be easily employed here. Moreover, it is desirable to monitor the sample thickness of the cell mounted in the experimental setup at the time of the measurement, as it might change due to temperature drifts and other influences, like a phase change of the PTFE window material that takes place at a temperature not far from ambient conditions. A systematic deviation of the optical path length from the mechanical distance of the windows might also arise from the non-normal incidence of the THz beam, because the cell is placed in the focus generated by a parabolic mirror.

Fortunately, artifacts from reflections caused by the optical properties of the two cell windows of thickness d and refractive index n_{W} separated by a distance x can be used for the determination of the effective pathlength within the sample. Figure 4.1 shows a typical trace recorded with a 1.6 mm spacer between PTFE windows, each 3 mm thick. The corresponding optical pathways are given in Fig. 4.2. Note that for reflection (b) and (c) two possible ways contribute to the observed signals, by reflection within either the left (b', c') or right (b, c) window. From the very weak signal (e) around 77 ps it is obvious that higher order reflections (involving 4 or higher even numbers of single reflections) can be neglected.

Very instructive is the phase change of the signal: as a phase jump of the reflected relative to the incident signal only occurs for a reflection at the optically more dense material, a total phase change of 0 is found in cases (a; $\pi + \pi$), (b/b'; $0 + 0$) and (d; $0 + 0$), whereas a phase change of π can be found in case (c/c', $0 + \pi/\pi + 0$).

Using the equation $\Delta x = v\,\Delta t = c/n\,\Delta t$, where c is the speed of light, n the refractive

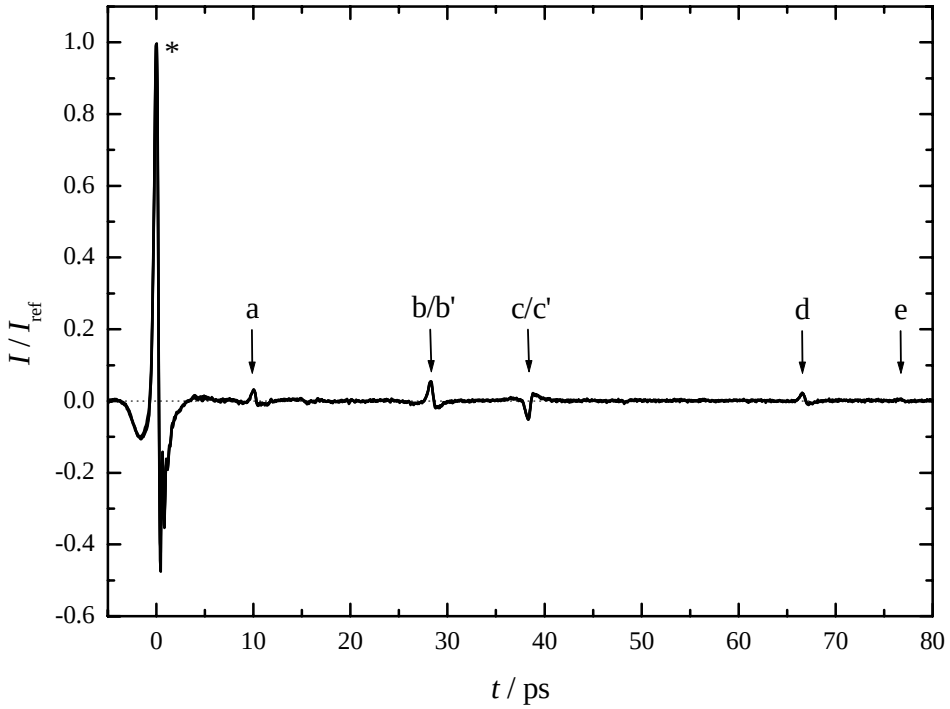

Figure 4.1: Temporal shape of the THz pulse ($\star$) and echoes (a-e) transmitted through an empty cell.

index of air (~ 1) or the window material ($n_{\mathrm{W}} = 1.433$[65]), respectively, the path length difference relative to the not reflected signal, $\star$ ($t = 0$), can be calculated:

$$x = \frac{c}{2}\, t_a = \frac{c}{2}\,(t_c - t_b), \tag{4.1}$$

$$d = \frac{c}{2\, n_{\mathrm{W}}}\, t_b = \frac{c}{2\, n_{\mathrm{W}}}\,(t_d - t_c). \tag{4.2}$$

On the other hand, Eq. 4.2 can also be used to calculate the refractive index n_{W}, when d is known from a discrete measurement by a precision micrometer. For the window material used, $n_{\mathrm{W}} = 1.424$ was found, 0.009 less than the accepted literature value for PTFE[65].
Two different spacers were used for the measurements, in order to optimize the signal-to-noise ratio. The effective path length obtained from several traces recorded with the empty cell was $x = 1.508\,\mathrm{mm}$ and $x = 2.308\,\mathrm{mm}$, respectively, with errors in the order of $0.002\,\mathrm{mm}$.
Figure 4.3 (upper diagram) shows the time-domain (raw) data of representative samples together with their power spectra (lower diagram), obtained by a discrete Fourier transform. At higher water contents, the average refractive index and the absorbance of the sample increases, shifting the transmitted pulse (a-c) to higher times and diminishing its amplitude. From the power spectra (lower diagram), the useful bandwidth of the spectra can be estimated: 0.2- $>3\,\mathrm{THz}$ for samples (a) and (b), $\sim$0.2-2 THz for sample (c).

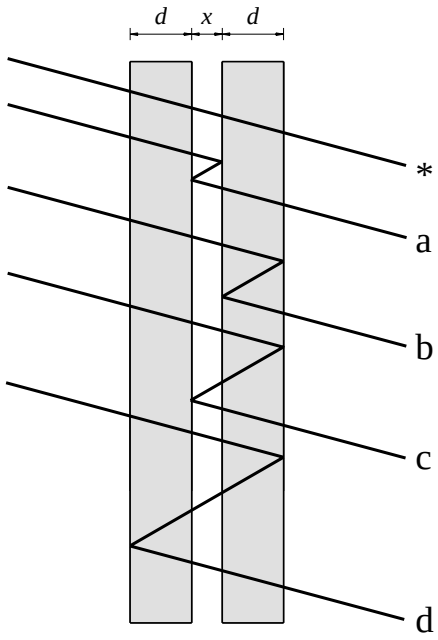

Figure 4.2: THz pulse ($\star$) and first-order echoes (a-d) transmitted through an empty cell.

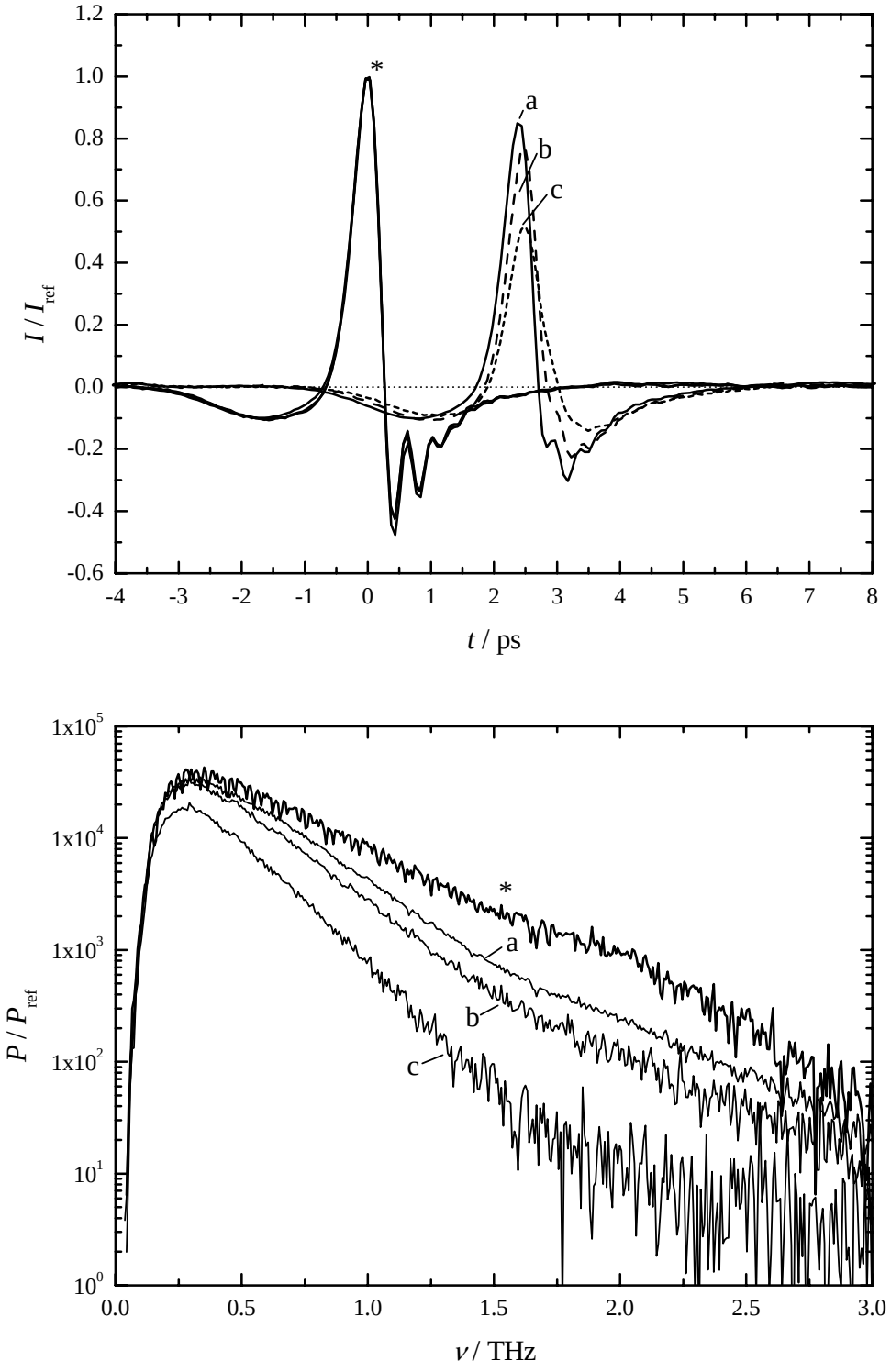

Figure 4.3: Effect of the sample dielectric properties on the temporal shape (upper diagram) and power spectrum (lower diagram) of the THz pulse. The signals are records from a PTFE windowed cell with path length 1.508 mm, filled with dry nitrogen ($\star$) or water + 1,4-dioxane mixtures at different weight fractions of water, w_1 (a: $w_1 = 0$; b: $w_1 = 0.025$; c: $w_1 = 0.05$).

4.1.5 Data processing

For a dielectric relaxation study, it is quite advantageous that 1,4-dioxane in its pure liquid state has a very low dielectric absorption, orders of magnitude below that of water. Values of $\varepsilon'' = 0.003$ at 25 GHz[83] and 0.0173 (20 °C)[85] at 142 GHz were reported in literature. Therefore, the decomposition of the usually broad bandshapes of the dielectric modes is not additionally complicated by the dielectric response of the bulk solvent. Nevertheless, the selection of a suitable relaxation model still remains a critical issue. Mashimo et al.[82] used a single Cole-Cole equation (Eq. 2.60) for the description of the dielectric behavior of 1,4-dioxane+water mixtures up to 10 GHz. This model fails at higher frequencies, Figs. 4.4 and 4.6, because of the asymmetric band shape of the dielectric spectra. Therefore, great care must be taken for the interpretation of results derived from studies, where the main dispersion step is not fully covered by the experiment. Especially the infinite-frequency limit of the permittivity, ε_∞, obtained from the simple Cole-Cole fit is not necessarily the physically correct one and may lead to strange effects of the calculated relaxation strength[82].

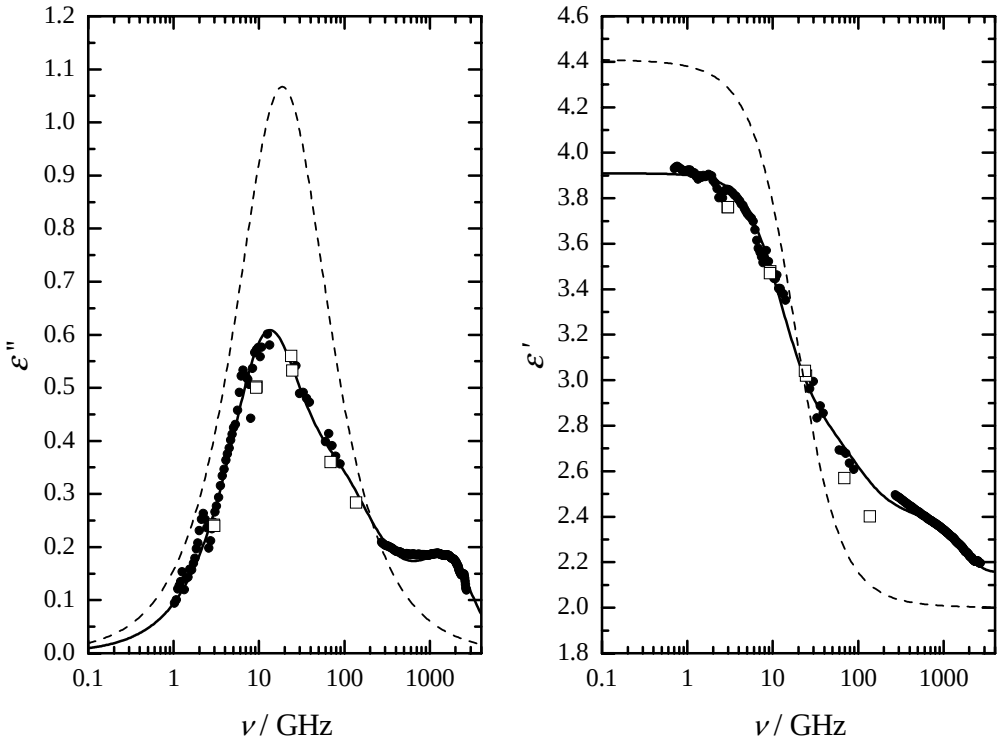

Figure 4.4: Complex dielectric data of a water + 1,4-dioxane mixture, $x_{DX} = 0.8$, at 298.15 K. (•) this study, (□) Smyth et al.[83,84], (dashed line) Mashimo et al.[82].

A comparison of our measurements with literature data, Fig. 4.4, shows very good agreement with the results published by the group of Smyth[83,84]. The TDR results reported by Mashimo et al.[82] do not fit into the exisiting body of data, not even within the frequency range of 0.1-10 GHz covered by their TDR measurements.

It is known from a Fourier transform interferometric study in the far-infrared region of the dielectric spectrum ($0.1 - 4\,\mathrm{THz}; 3 - 120\,\mathrm{cm}^{-1}$)[87] and the THz-TDS measurements presented here that a maximum of the loss curve of pure dioxane can be found around 2.6 THz, Fig. 4.10. Furthermore, the real part of the dielectric spectrum, $\varepsilon'(\nu)$, shows a minimum $\sim 2.6\,\mathrm{THz}$. Therefore, we assume in accordance with Davies et al.[87] that the dynamic process observed for pure dioxane is of resonance origin.

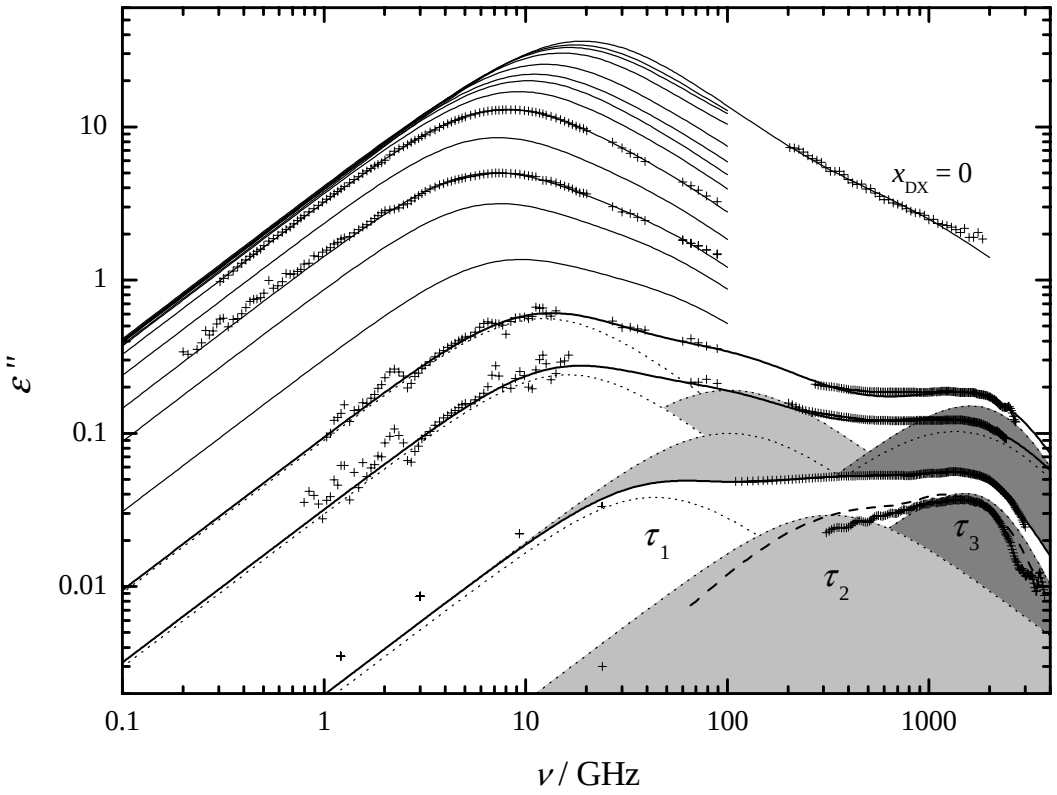

Figure 4.5: Dielectric loss spectra, $\varepsilon''(\nu)$, of water + 1,4-dioxane mixtures as measured by VNA-R, IF and THz-TDS. The concentrations correspond to the values given in Table 4.2, starting from pure water ($x_{\mathrm{DX}} = 0$). The dotted lines show the contribution from the two Debye (τ_1, τ_2) and the damped harmonic oscillator (τ_3) modes. Dashed line: 1,4-dioxane, lit.[87]

An evaluation of possible bandshape functions showed that the dioxane spectra can be reasonably well described by a damped harmonic oscillator model (DHO), Eq. 2.69. For dilute solutions of water in 1,4-dioxane (i.e. up to a water mass fraction of 0.05), a combination of two Debye type equations, Eq. 2.56, with an additional oscillator term, proved to be sufficient for a reasonably accurate description of the data obtained. The values calculated from the spectra are given in Tab. 4.1.
At higher concentrations of water, where no data in the THz range could be measured, the complex dielectric spectra are broadened towards high frequencies, Fig. 4.6. It was found

Table 4.1: Angular frequency and characteristic damping time, ω_0 (in THz) and τ_D (in ps), obtained for water + 1,4-dioxane mixtures using a Debye+Debye+DHO fit model.

x_2	$x_{O,2}$	ε_3	ω_0	τ_D	ε_∞
0.80000	0.88889	2.45	14.54	0.0350*	2.203
0.88889	0.94118	2.33	19.28	0.0202	2.157
0.97558	0.98764	2.21	13.24	0.0486	2.156

*value kept constant during fit procedure.

that either a Cole-Davidson equation, or a sum of two Debye terms can be utilized for the description of data up to 89 GHz. The two Debye model was already used at the time of early studies up to $\sim 70\,\mathrm{Ghz}$[83,84], although the complex permittivity was only determined at 4 spot frequencies and therefore the five parameters required for a fit comprising two Debye equations are not well defined.

Except for the water-rich end, both fits are of comparable quality, but approaching high dioxane concentrations, relaxation time distribution parameters, β, of the Cole-Davidson equation ~ 0.5 indicate that the liquid dynamics is governed by quite different timescales of dielectric relaxation. Thus, it is not likely to assume a single physical origin for the largely stretched dynamics observed.

Therefore, all spectra were analyzed using a two Debye relaxation model, with an additional vibrational contribution at high dioxane mole fractions. The relaxation parameters and the frequency band of the measurements are summarized in Tab. 4.2.

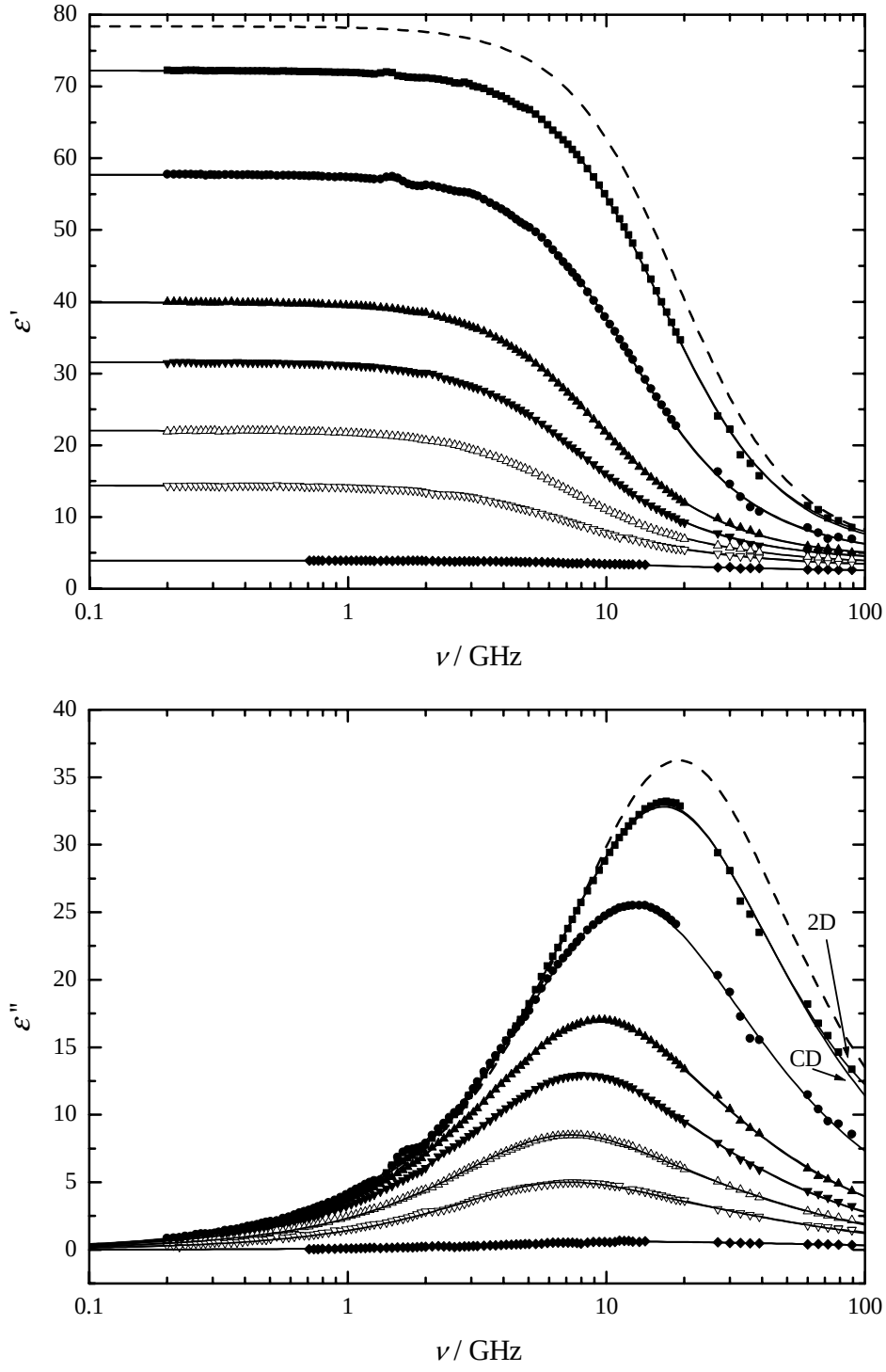

Figure 4.6: Dielectric permittivity and loss spectra, $\varepsilon'(\nu)$ and $\varepsilon''(\nu)$, of water + 1,4-dioxane mixtures at 298.3 K measured by VNA-reflectometry and interferometry. The dashed lines show data for pure water[57]. The lines represent fits by a sum of two Debye terms (2D) and a single Cole-Davidson equation (CD), which give very similar results in most cases. Dioxane mole fractions are 0.016 (■), 0.063 (●), 0.143 (▲), 0.200 (▼), 0.286 (△), 0.400 (▽) and 0.800 (♦), respectively.

Table 4.2: Relaxation parameters, ε_j, τ_j (in ps), and reduced error function χ^2_r for water + 1,4-dioxane mixtures at 298.15 K.

x_2	$x_{O,2}$	ε^1	ε_1	τ_1	ε_2	τ_2	$\varepsilon_3/\varepsilon_\infty$	$10^3\,\chi^2_r$
1,4-dioxane + H_2O								
0.1-2000 GHz[2]								
0	0	78.368	78.17	8.32	5.87	0.260	3.40	48.5
0.2-89 GHz								
0.00990	0.01961	74.606	74.62	9.11	6.58	0.454	1.84	96.5
0.01639	0.03226	72.253	72.19	9.68	6.93	0.600	1.58	58.8
0.03226	0.06250	66.854	66.84	10.7	6.79	0.753	2.57	26.0
0.06250	0.11765	57.825	57.69	13.0	7.50	2.25	4.50	47.7
0.09091	0.16667	50.640	50.53	14.8	7.71	2.94	4.43	17.3
0.11111	0.20000	46.181	45.98	15.9	6.98	3.20	4.48	5.42
0.14286	0.25000	40.099	39.90	17.6	7.02	3.64	4.32	5.93
0.20000	0.33333	31.428	31.57	20.4	6.54	4.12	4.06	5.93
0.28571	0.44444	22.254	22.03	22.9	5.91	4.49	3.59	3.78
0.40000	0.57143	14.352	14.37	24.0	5.03	4.35	3.19	5.22
0.50000	0.66667	9.8960	10.18	23.3	4.42	4.27	2.95	4.80
0.66667	0.80000	5.6594	5.893	19.1	3.48	3.48	2.64	2.20
0.5-3000 GHz								
0.80000	0.88889	3.8635	3.913	13.8	2.87	2.34	2.45	(0.360)
0.88889	0.94118	2.9280	3.012	9.85	2.53	1.56	2.33	(0.227)
1.2-3500 GHz[3]								
0.97558	0.98764	2.2677	2.345	3.64	2.27	0.486	2.21	–
1	1	2.2095	–	–	–	–	2.21	–
1,4-dioxane + D_2O								
0.2-89 GHz								
0.06250	0.11765	–	57.56	16.7	8.57	3.94	4.61	24.9
0.11111	0.20000	–	45.99	19.9	7.15	4.04	4.41	8.42
0.28571	0.44444	–	22.05	26.9	5.46	3.93	3.42	4.06
0.66667	0.80000	–	5.884	21.9	3.51	3.79	2.64	0.752

[1] interpolated[88–98].

[2] fitted using interpolated data from Rønne et al.[99,100].

[3] fitted using data (1.2-147 GHz) from Crossley et al.[101]

4.1.6 Results and discussion

Before going into details of the dielectric properties of 1,4-dioxane + water mixtures, it is worthwhile to get a closer understanding of the thermodynamic features of these systems. Especially the thermodynamic excess mixing properties can provide information about the energetic and structural changes upon addition of dioxane to water.
For comparison with other related mixtures of oligomeric compounds that will be addressed later on, it is helpful to introduce a new measure of composition, as mole fraction itself is not fully satisfactory. It was found that the mole fraction of oxygen atoms from the non-ionic solute,

$$x_{\mathrm{O},2} = \frac{n_{\mathrm{O},2} \cdot x_2}{n_{\mathrm{O},2} \cdot x_2 + x_1} = \frac{n_{\mathrm{O},2} \cdot x_2}{1 + x_2 \cdot (n_{\mathrm{O},2} - 1)} \tag{4.3}$$

can be advantageously used, where (1) denotes water and (2) the organic compound containing $n_{\mathrm{O},2}$ oxygen atoms. For example, in case of 1,4-dioxane, $n_{\mathrm{O},2} = 2$.

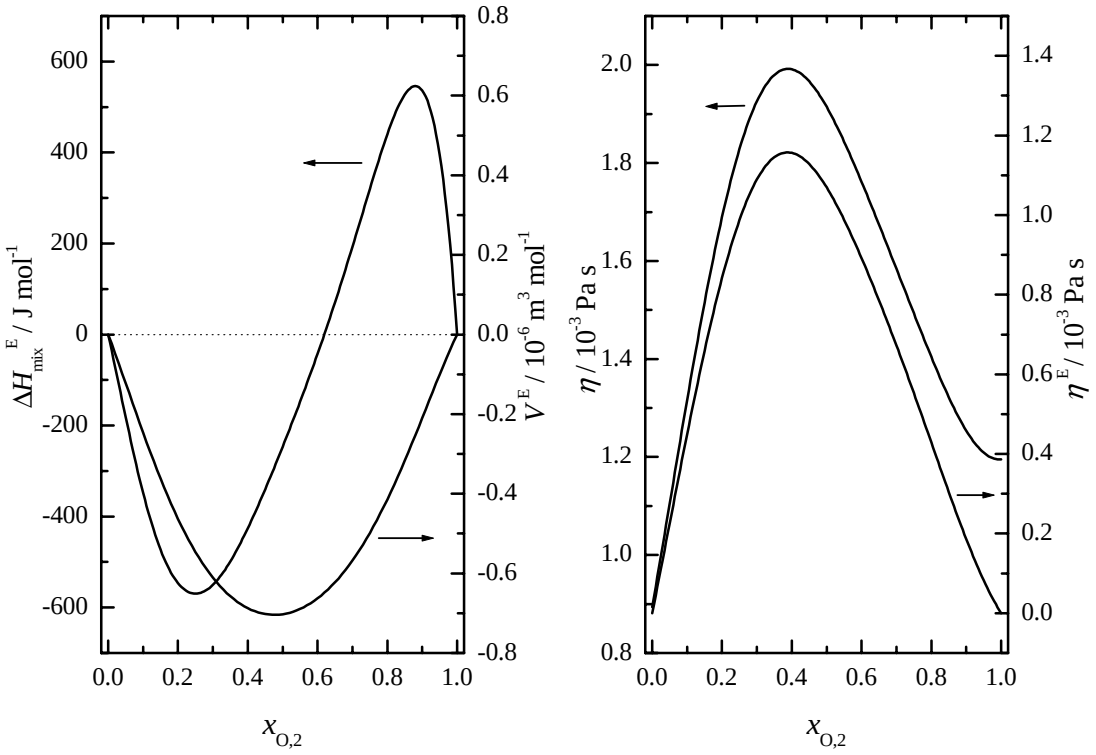

Figure 4.7: Thermodynamic properties of water + 1,4-dioxane mixtures at 298.15 K: excess heat of mixing, $\Delta H_{\mathrm{mix}}^{\mathrm{E}}$ [102–105], excess molar volume, V^{E} [77,106] (left diagram), viscosity and excess molar viscosity, η and η^{E} [107–109] (right diagram).

The excess molar heat of mixing of water + 1,4-dioxane was determined by several investigators[102–105]. A careful evaluation of these data shows that they are in agreement within an accuracy limit of $\sim 3\%$. Figure 4.7 (left diagram) gives a fit curve of selected literature data. The heat of mixing is found exothermic in the water-rich region, with a pronounced minimum around a molar fraction $x_{\mathrm{O},2} \approx 0.25$. With increasing dioxane content of the

mixture, at $x_{O,2} \approx 0.6$, an endothermic effect is observed upon addition of dioxane. From these measurements, together with the knowledge of the activity coefficients, it is also possible to calculate molar excess entropies of the systems, which are strongly negative over the whole concentration range[78,102] and a minimum value was observed around $x_{O,2} \approx 0.45$. At a similar concentration, the excess molar volume and the molar excess viscosities, η^E, show a minimum and maximum value, respectively, see Fig.4.7 (right diagram).
Thus, it is obvious from the thermodynamic properties of the mixtures that these represent a more dense state compared with the pure liquids, and that the various degrees of freedom, like rotational and translational motions, are restricted. This can also be interpreted in terms of a structure enhancement within the mixture, but thermodynamics cannot discriminate between the contributions from water-ether or water-water interactions, nor are they sensitive to the dynamics of the hydrogen-bond network.
Usually, this structural effect is attributed to a strengthening of the hydrogen bond network near non-interacting surfaces, the so-called hydrophobic effect[110]. This hypothesis was convoluted with various other ideas, like the formation of a stable dioxane-water complex[111], higher aggregates formed by water molecules bridging between two ether molecules[103] up to the presence of micelle-like clusters[82], but no clear evidence for such aggregates was given, nor are they the only possible explanations for the given experimental results.

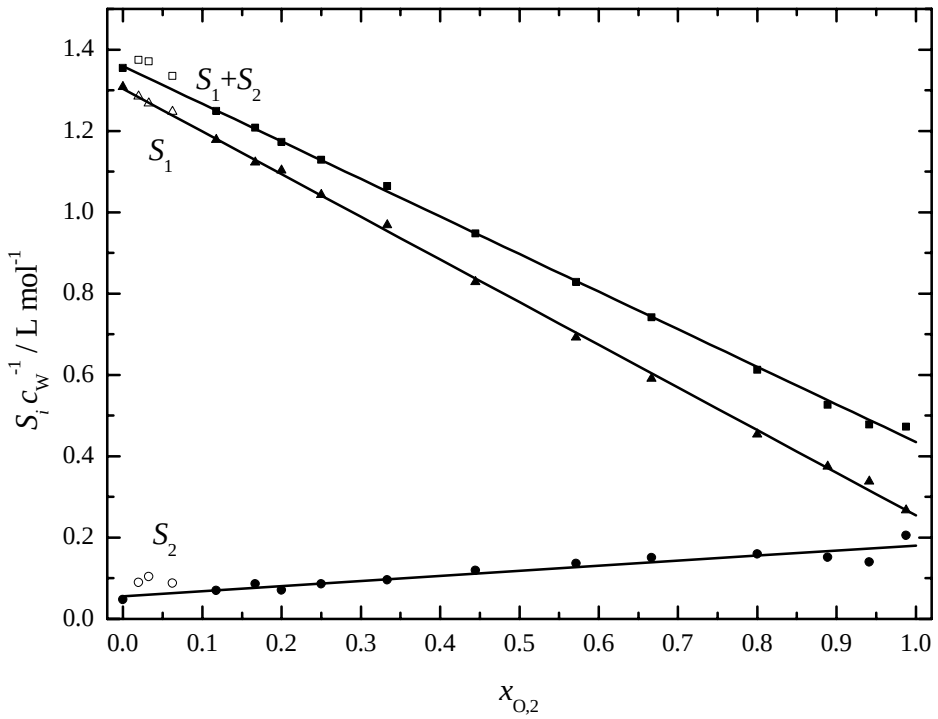

Figure 4.8: Normalized amplitudes of the two Debye processes found in water + 1,4-dioxane mixtures at 298.15 K. Open symbols are data not used for the calculation of the (fitted) lines.

Now we want to focus on results from dielectric studies, mainly the more recent paper of Mashimo et. al.[82]. The authors postulate the existence of a water cluster percolation

point around $x_{O,2} = 0.3$ from the non-linear decrease of the normalized relaxation strength calculated from his measurements. A comparison of these data with interferometric results from literature[83–85] and our VNA-R and IF measurements indicates severe problems with regard to data accuracy that may explain why we were not able to reproduce this finding. In contrast to Mashimo et al.[82], we observe an almost linear decrease of the normalized relaxation strength of the major dielectric relaxation region, Fig. 4.8, up to very high molar fractions of dioxane. Thus, there is no evidence of a breakdown of the water structure in general or of a percolation threshold at molar fractions below $x_{O,2} \approx 0.8$. Otherwise significant effects on the relaxation amplitudes should be observable. The linear decrease also holds for the normalized amplitudes of both Debye terms separately. The separation of the whole dielectric response into separate contributions becomes more difficult at higher dioxane concentrations, because of the low total amplitude. At the same time, the water concentrations are small, thus larger errors of the individual normalized amplitudes have to be assumed that might explain the larger scatter at $x_{O,2} > 0.85$.

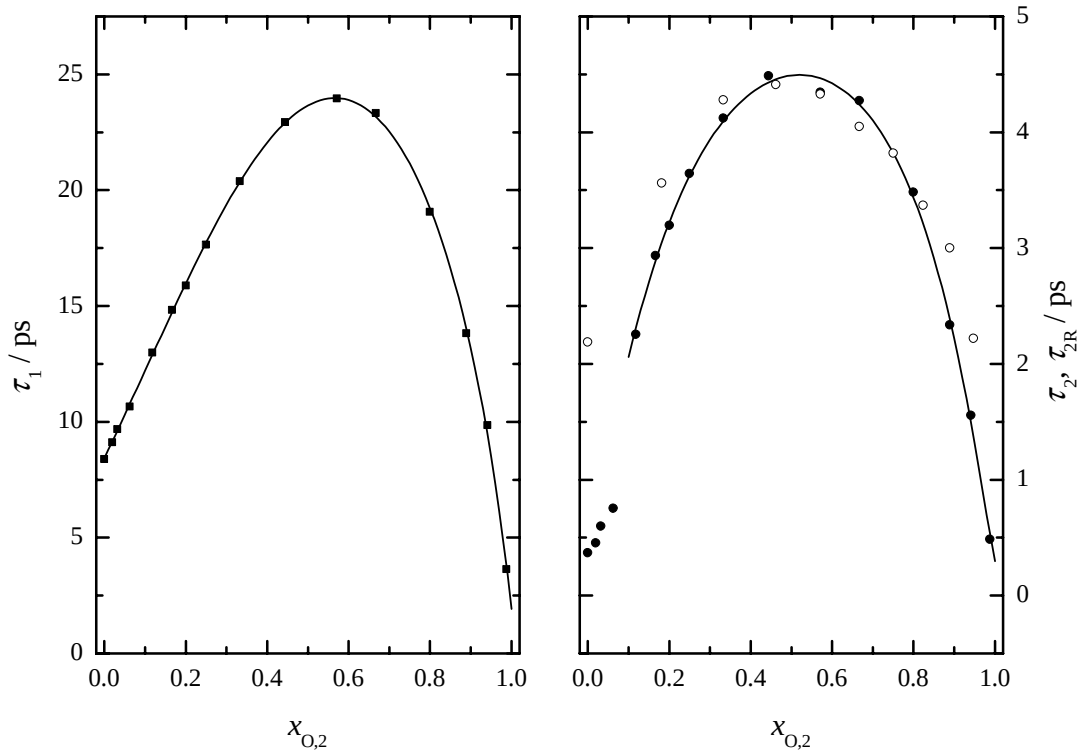

Figure 4.9: Relaxation times, τ_1 (■) and τ_2 (•), of the two Debye processes found in water + 1,4-dioxane mixtures at 298.15 K. τ_{2R} (○) is the rotational correlation time of D_2O in 1,4-dioxane-D_8[79].

The interpretation of dielectric relaxation processes in terms of the microscopic dynamics is always a difficult task and great care must be taken. However, in the case of water + 1,4-dioxane mixtures, two processes of the Debye type could be identified. Fig. 4.9 shows the relaxation times obtained from measurements by a fit procedure already described, Chap. 2.3.5. Starting from pure water, $x_{O,2} = 0$, a linear increase of the relaxation time τ_1 is observed.

For pure water, whose dielectric spectrum can be well described by a single Debye term up to 90 GHz, this process is usually assigned to a cooperative relaxation mode of water clusters comprising 10-40 molecules. This interpretation is strongly supported by molecular dynamics simulations[112,113]. It can be assumed that the relaxation process (S_1, τ_1) observed in 1,4-dioxane + water mixtures is of similar origin, with dioxane molecules modifying the size distribution and environment of the water clusters. Both factors have large effects on the macroscopic relaxation time, τ_1. Even at molar fractions $x_{O,2} = 0.9$, where 9 out of 10 hydrogen bond acceptor sites are part of a dioxane molecule, the cooperative relaxation (τ_1) is still slower than in pure water.

Very instructive is also a comparison of the τ_1 values found for 1,4-dioxane + water mixtures with D_2O substituted for H_2O. Especially at lower concentrations, the ratio of the relaxation times is very similar to that of pure light and heavy water (~ 1.27; found 1.28 at $x_{O,2} = 0.12$ and 1.25 at $x_{O,2} = 0.2$). This fact further supports our interpretation of the (S_1, τ_1) process.

In literature, water-dioxane interactions up to the formation of more or less stable hydrates were often held responsible for the structural properties of these mixtures. In contrast to this, we cannot find evidence for any such species. In fact, the water-ether oxygen hydrogen bond is weak compared with water-water hydrogen bond[103] and large local energy fluctuations up to 60 kJ/mol present in liquid water[112,113] are in variance with the formation of stable associates in liquid mixtures.

Furthermore, the interpretation of τ_1 as a cooperative relaxation mode within water clusters up to high molar fractions of dioxane gets strong support from recent molecular dynamics studies of closely related systems[114,115] that postulate water aggregates even in highly concentrated polyethyleneoxide solutions.

Low-frequency Raman data published by Tominaga et al.[80] also support this idea, as the band observed around 190 cm^{-1} (S-band), which is attributed to a stretching-like vibrational mode of H-bonded water molecules, shows a rapid increase of both characteristic frequency and damping constant with addition of dioxane to water. This can only be explained be a strengthening of water-water hydrogen bonds. If a significant amount of dioxane-water hydrogen bonds were formed and this process were associated with the destruction of the clustered water structure, a shift of the S-band to lower frequencies should take place as a result of the weaker ether oxygen-water hydrogen bond and the higher mass of the dioxane molecule. The same reasoning applies to the large increase of the damping constant, which indicates stronger coupling of the oscillator to the environment.

Now we want to focus on the second relaxation process (S_2, τ_2). The normalized amplitude, $S_2\, c_W^{-1}$ is characterized by a slow increase towards higher dioxane content of the mixture, contributing to about half of the total dielectric loss of very dilute solutions of water in dioxane, Fig. 4.8.

In pure water, the relaxation behavior differs from a single Debye term at high frequencies and this deviation can be fitted well by a second Debye-like contribution. But this contribution is relatively small and a more accurate determination of the actual amplitude and relaxation time of this process requires, due to vibrational contributions in the far-infrared range of the dielectric spectrum, the knowledge of the dielectric properties from MHz frequencies up to infrared radiation. Unfortunately, these data are not established accurately

enough at present time and we do not want to go into all details of fast dynamics in liquid water here, as our study of the FIR response mainly focuses on dilute solutions of water in dioxane. On the water rich side, no data above 89 GHz were measured because of lacking experimental facilities and the large experimental difficulties associated with the precise determination of dielectric properties of high-loss liquids in the high-GHz and THz region. Below a mole fraction $x_{O,2} = 0.1$, the two Debye fit employed for the description of our spectra resulted in relaxation times $\tau_2 < 1$ ps, therefore these values have to be handled with care and were not used for further analysis as the data are limited to 89 GHz, except for pure water, where FIR data were available. From $x_{O,2} \approx 0.1$ on, the relaxation times τ_2 show a rapid increase, thus the decomposition of the spectra leads to more reliable results, Fig. 4.9. Around a mole fraction $x_{O,2} = 0.5$, where half of the hydrogen bond acceptor sites are part of a dioxane molecule, the relaxation time τ_2 shows a broad maximum.

It is not easy to assign the fast process (S_2, τ_2) to the microscopic dynamics of the liquid mixture. With a characteristic time ~ 4 ps, it is likely that it reflects the relaxation of a rather small dipole. Furthermore, as the normalized amplitude is increasing with the addition of dioxane, there is evidence that water molecules which are not part of a water cluster or at the surface of such a cluster, therefore forming not more than one hydrogen bond to an other water molecule, might be responsible for the dispersion region observed. This idea gets support from NMR results[79], which can provide us with the rotational correlation time, τ_{2R}, of water molecules in dioxane solution at various concentrations, Fig. 4.9. Here, large similarities with respect to the overall behavior can be found.

But care must be taken comparing dielectric relaxation times with times obtained by NMR studies. It can be shown by electrodynamics theory[27] that a ratio of $\tau_2/\tau_{2R} = 3$ should be observed, at least approximately for rotational diffusion of the dipole. Furthermore, the calculation of NMR correlation times incorporates several approximations, which are not straightforward in mixtures of polar liquids. So, we only want to point out the similarities, keeping in mind that the NMR experiment provides information about the dynamics of the single molecule.

From a chemical point of view, we have to reconsider the dielectric response from water molecules which are not part of a larger water cluster and are not sharing several hydrogen bonds with other water molecules. In addition to water molecules at a water cluster surface this includes molecules which are either free within a dioxane-rich microregion of the mixture or form hydrogen bonds with dioxane oxygen sites. Otherwise, and without a very rapid dynamic equilibrium between cluster formation and water molecules interacting with dioxane, macroscopic phase separation would occur. Due to this fast and continuous reorganisation of the liquid structure, we only observe a single Debye step, S_2/τ_2, comprising the dynamics of single water molecules, which might be determined mainly by the rotation of OH groups or of the water dipole around a hydrogen bond.

Let us know focus on the dynamics > 100 GHz. It is known from literature that the dielectric properties of liquids in the THz and far infrared (FIR) range is particularly appropriate for revealing information about the motions of water molecules dissolved in organic solvents either as monomers or associated to clusters of various size[116,117]. Furthermore, THz data proved to be helpful for the investigation of confined water pools within an apolar medium[118,119].

The THz complex dielectric spectra of pure 1,4-dioxane ($M_{\mathrm{H8}} = 88.11\,\mathrm{g\,mol^{-1}}$) as determined by THz-TDS experiments is given in Fig. 4.10, together with the spectrum of fully deuterated dioxane, 1,4-dioxane-D8 ($M_{\mathrm{D8}} = 96.16\,\mathrm{g\,mol^{-1}}$).

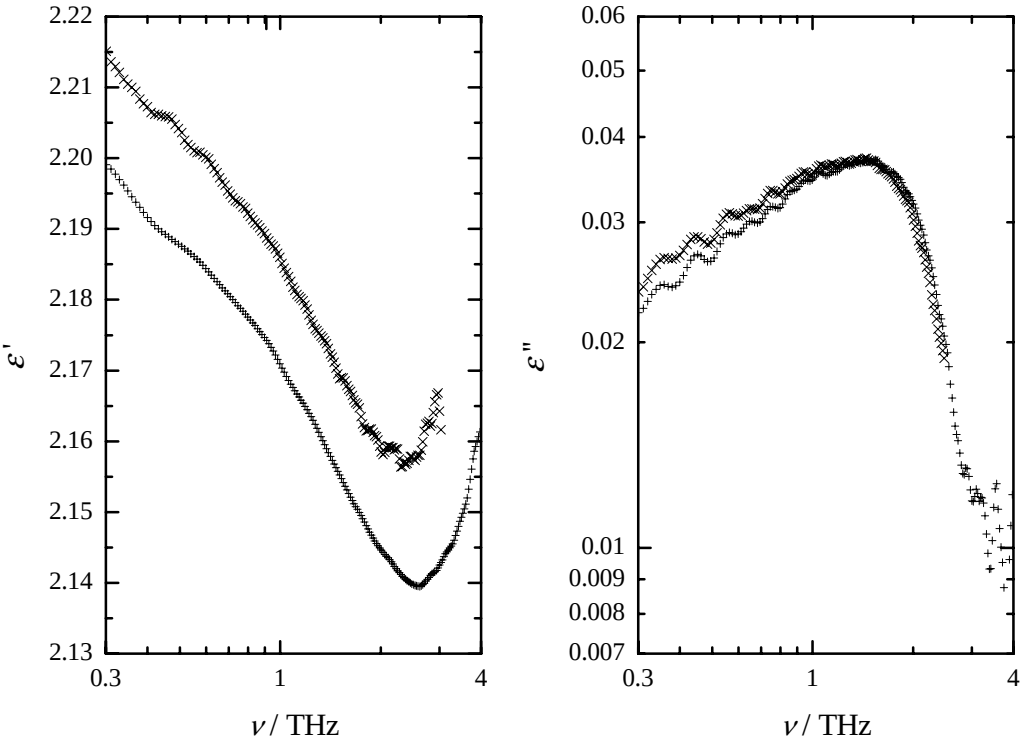

Figure 4.10: Complex dielectric permittivity of pure 1,4-dioxane (+) and 1,4-dioxane-D_8 ($\times$) as measured by THz-TDS at $\sim 298\,\mathrm{K}$.

The spectra show a maximum of the dielectric loss, $\varepsilon''(\nu)$, at frequencies around 1.5 THz, whereas a minimum of the dielectric permittivity is observed at $\sim 2.5\,\mathrm{THz}$. As will be shown below, isotopic substitution leads to a slowing down of the dynamics, without any major changes of the shape, Fig. 4.10.

The molecular origin of the dielectric loss observed in pure liquid dioxane was assigned to collisional interactions by Davies et al.[87]. We want to follow his argumentation and can provide further evidence of this process by taking into account the dielectric spectrum of 1,4-dioxane-D_8, which is presented here for the first time. Within a first approximation, the collisional frequency will be proportional to the mean molecular velocity, v, determined by the thermal energy of an molecule and its mass, m, especially for molecules that only differ by the isotopes. Since $v^2 \sim \frac{3}{2}\frac{k_{\mathrm{b}}T}{m}$, the maximum of the dielectric loss of 1,4-dioxane-D8 should be shifted to lower frequencies by a factor of $r = \sqrt{M_{\mathrm{D8}}/M_{\mathrm{H8}}} = 0.957$. A ratio of the maximum frequencies of ε'', $r_{\mathrm{obs},\varepsilon''} = 0.95$ was determined by graphical evaluation of the spectra. The same applies to the frequencies, where the absorption coefficient, α (Eq. 3.30), reaches its maximum. These maxima can be estimated with higher accuracy, Fig. 4.11, and $r_{\mathrm{obs},\alpha} = 0.96$ was found, calculated from $\nu_{\mathrm{max,H8}} = 1.98\,\mathrm{THz}$ (lit. 2.1 ± 0.1[87]) and $\nu_{\mathrm{max,D8}} = 1.90\,\mathrm{THz}$.

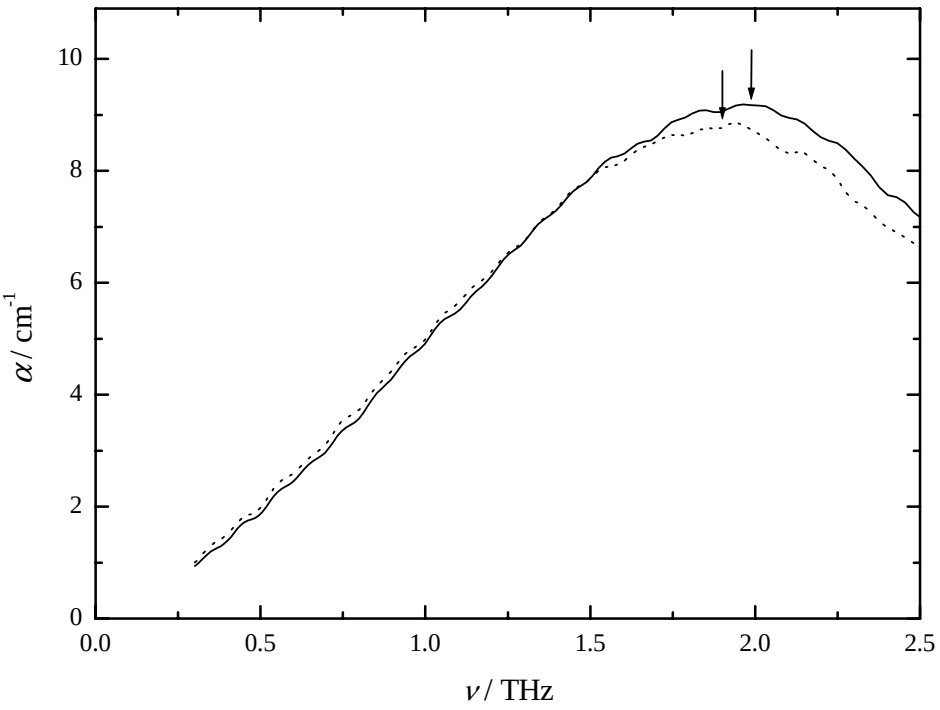

Figure 4.11: Absorption coefficient, α, of liquid 1,4-dioxane (full line) and 1,4-dioxane-D8 (dotted line) as measured by THz-TDS at $\sim 298\,\mathrm{K}$.

Predictions of band intensities are quite difficult to carry out [120] because of the many factors that have to be taken into consideration, like the anisotropic polarizability of the particles, the angular distribution of the molecular collisions and the cancellation of the generated moments within the condensed phase. Nevertheless, a qualitative discussion of the findings is possible.

Within a simplified model, the dielectric loss arises from induced dipole moments generated by mainly bimolecular collision interactions. These microscopic processes result in a translational-vibrational mode, whose amplitude is mainly determined by the size of the effective collision-induced dipole moments and the field surrounding these dipolar states.

By addition of a strongly dipolar liquid (e.g. water) to a macroscopically non-dipolar liquid comprising suitable interaction sites, like the oxygen atoms of a dioxane molecules, the intermolecular interaction can give rise to a polarization of the non-polar molecule which is much stronger than those induced by collisions.

In the case studied here, the addition of water leads to an increase of the dielectric loss in the THz range over almost two orders of magnitude, see Fig. 4.12. Interestingly, the shape of the spectra and the characteristic frequency of the resonant dielectric contribution remains almost unchanged within the experimental error, so does the position of the minimum of the $\varepsilon'(\nu)$ spectrum, Fig. 4.13.

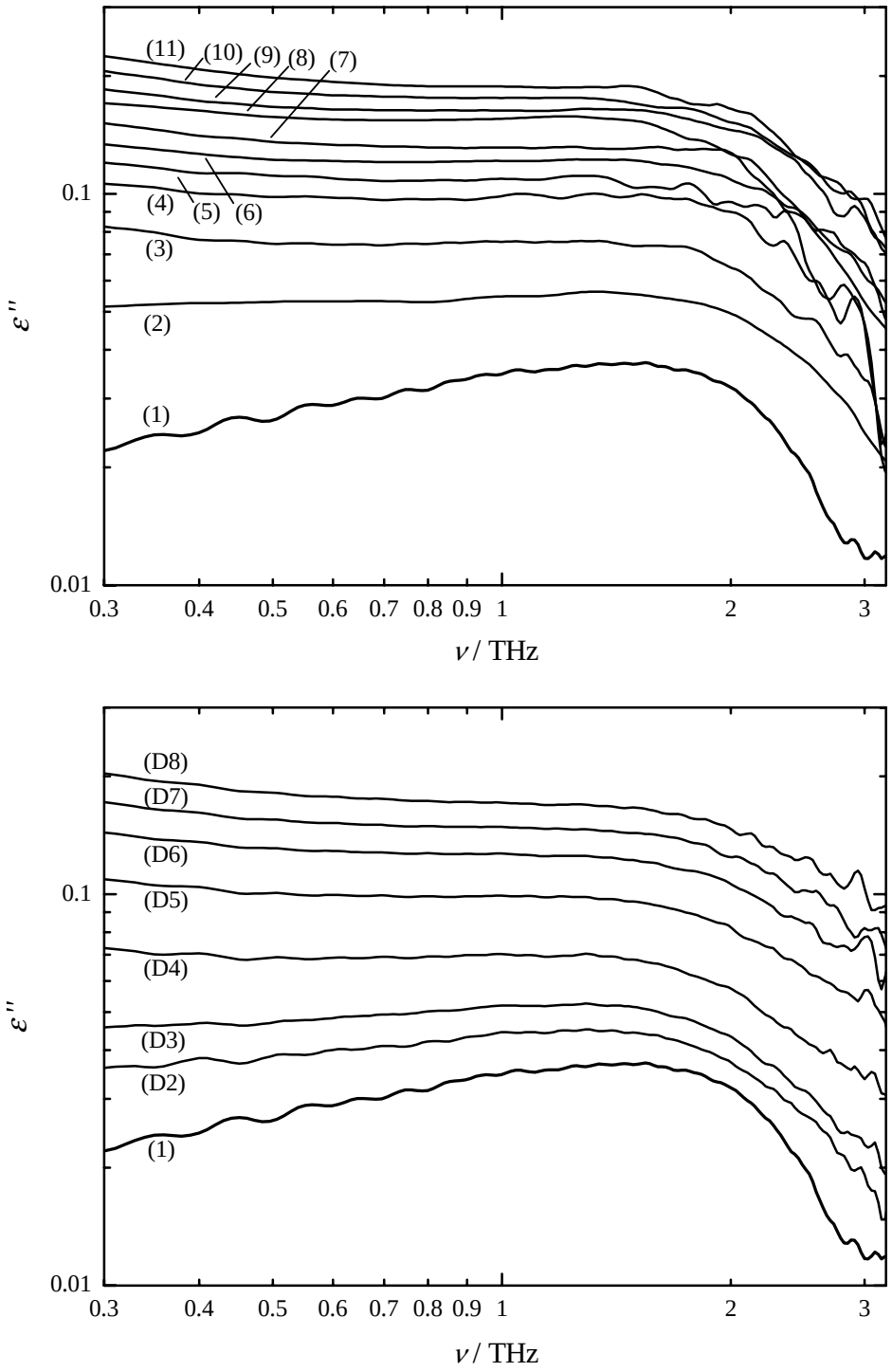

Figure 4.12: Dielectric loss spectra, $\varepsilon''(\nu)$, of 1,4-dioxane + water/deuterium oxide (D) mixtures at 298.3 K measured by THz-TDS. The concentrations corresponding to the numbers are given in Table 4.3.

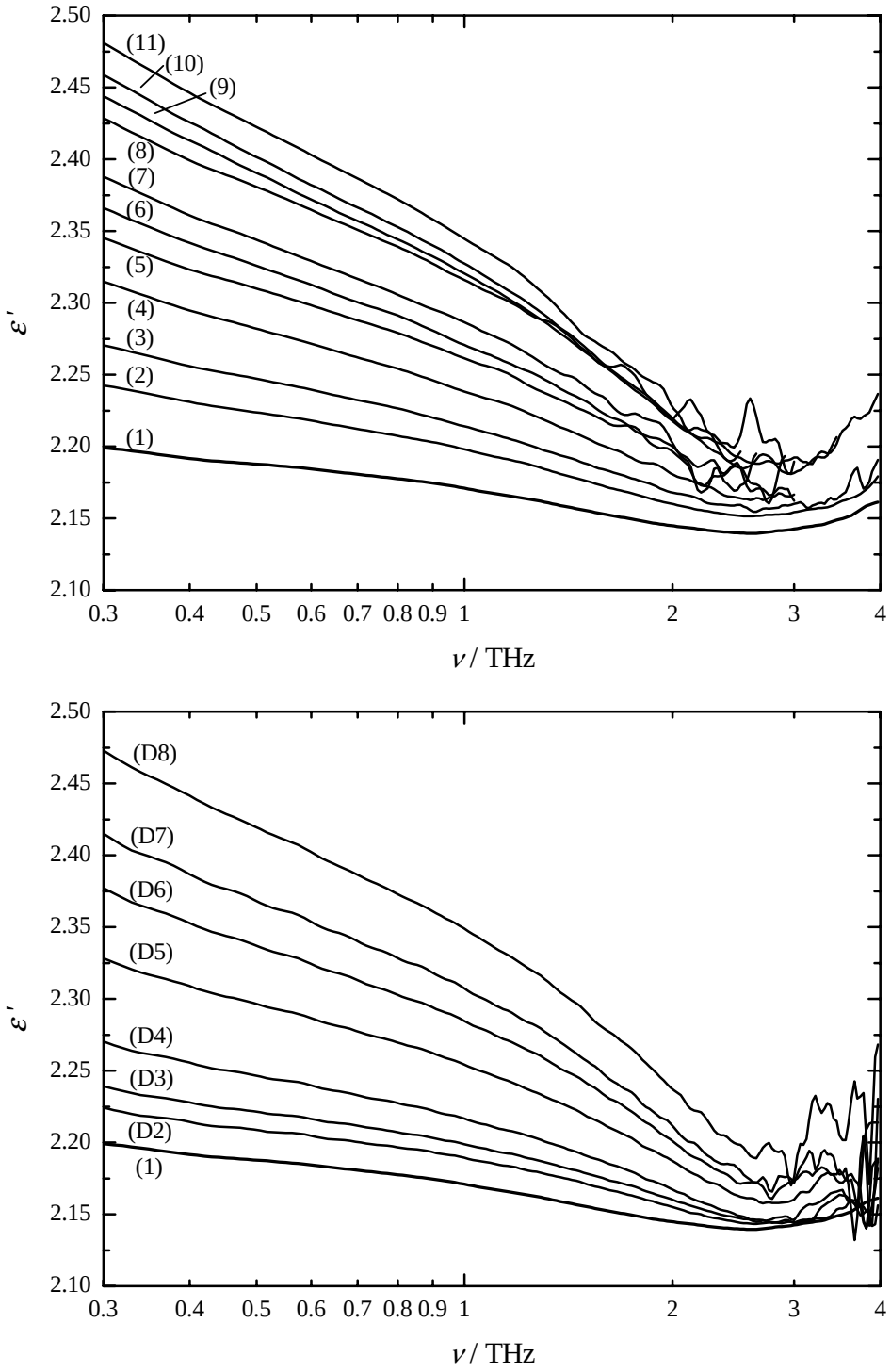

Figure 4.13: Dielectric permittivity spectra, $\varepsilon'(\nu)$, of 1,4-dioxane + water/deuterium oxide (D) mixtures at 298.3 K measured by THz-TDS. The concentrations corresponding to the numbers are given in Table 4.3.

Table 4.3: Concentration of water (H_2O) and heavy water (D_2O) of water + 1,4-dioxane mixtures studied by THz-TDS experiments. w_1 is the mass fraction of water.

id	$100\,w_1$ (H_2O)	$x_{O,2}$ (H_2O)	$100\,w_1$ (D_2O)	$x_{O,2}$ (D_2O)
1	0	1	0	1
2	0.509	0.9876	0.228	0.9950
3	0.893	0.9784	0.416	0.9909
4	1.606	0.9616	0.970	0.9789
5	2.030	0.9518	1.956	0.9580
6	2.513	0.9407	3.010	0.9361
7	2.982	0.9301	3.974	0.9166
8	3.554	0.9174	4.964	0.8970
9	3.947	0.9087	–	–
10	4.484	0.8971	–	–
11	5.140	0.8830	–	–

This interpretation is corroborated by the data of dilute solutions of heavy water in 1,4-dioxane, Figs. 4.13, 4.12 (lower diagrams): although the Debye relaxation modes, τ_1 and τ_2, show a considerable shift of the relaxation times towards lower frequencies, the shape and peak position of the THz spectra is not affected significantly within the accuracy of the THz-TDS experiments. Thus, it is unlikely that the rate of formation and the stability of hydrogen bond affects the dynamics of the liquid in the THz range.

Further information about the nature of the THz resonance process can be obtained from its relaxation strength. Fig. 4.14 shows the overall relaxation strength of water + 1,4-dioxane mixtures, together with the amount not covered by the two Debye relaxation steps. To account for the varying water content, both amplitudes are normalized by the analytical water concentration. The usual assumption $\varepsilon_\infty = 1.1\,n_D$ was used to handle additional dispersion effects at frequencies not covered by the relaxation model here.

The overall dielectric response shows an almost linear decrease starting form pure liquid water up to molar fraction as high as $x_{O,2} \approx 0.9$. This is in agreement with the former interpretation that cooperative relaxation of water clusters within water-rich domains of the mixture has to be assumed even at low water concentrations.

The normalized amplitude of the cluster relaxation is affected by changes of the environment of the relaxing cluster accompanied with different geometrical constrains compared to pure water and the size of the cluster. At concentrations above $x_{O,2} \approx 0.9$, a rapid decrease of both the normalized overall amplitude and the relaxation times is observed, indicating a breakdown of the cooperative relaxation mechanism.

The amplitude not covered by the two Debye terms, $\Delta\varepsilon_3$, shows only a slight decrease with increasing water concentration. The evaluation of this amplitude in terms of an amount of non-clustered water within dioxane microregions of the liquid is not straightforward,

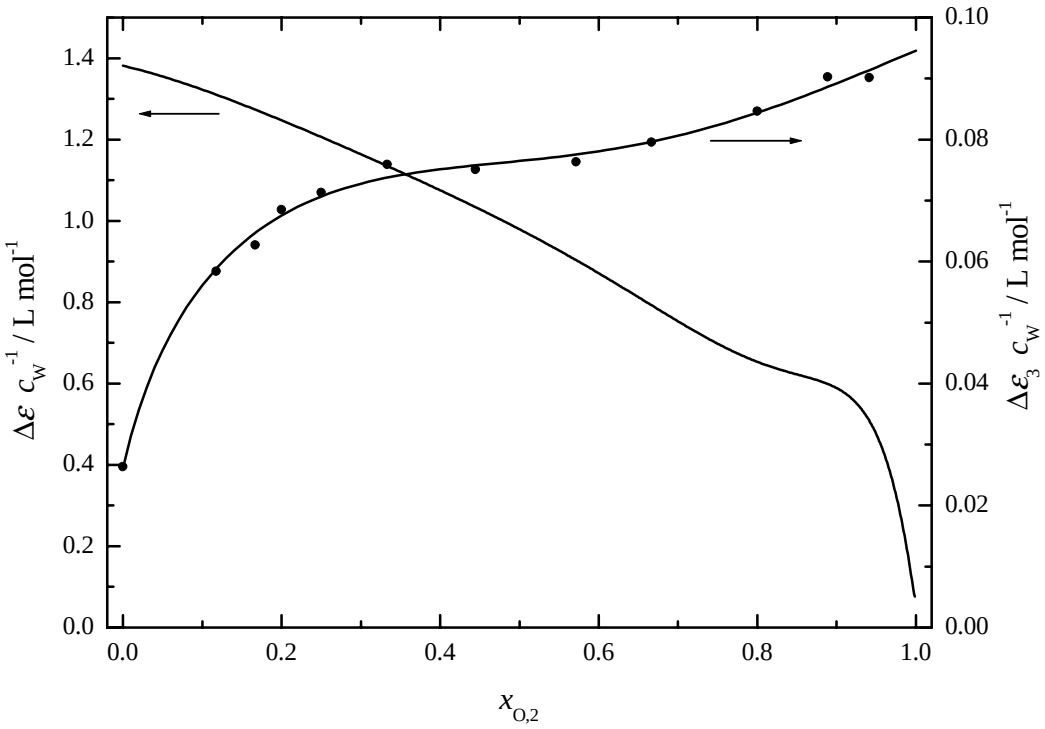

Figure 4.14: Relaxation strength, $\Delta\varepsilon = \varepsilon - 1.1\, n_D^2$, of water + 1,4-dioxane mixtures, compared with the relaxation strength not covered by the two Debye terms, $\Delta\varepsilon_3 = \varepsilon_3 - 1.1\, n_D^2$. All values are normalized by the water concentration, c_w, and at 298.15 K. Refractive indices, n_D^{25}, were interpolated from selected literature values[121–123].

and requires careful theoretical studies, e.g. molecular dynamics simulations. Assuming dioxane regions which are large compared to the correlation length of interactions in the liquid, it might be inferred from the normalized amplitude $\Delta\varepsilon_3$ that the fraction of non-clustered water is rather constant over a broad range of concentrations and somewhat increasing from $x_{O,2} \approx 0.8$ on. Within this picture, the THz resonance mode acts as a probe for water molecules within dioxane rich domains.

To summarize: Our investigation of mixtures of water + 1,4-dioxane revealed a cooperative relaxation behavior of water clusters even at high dioxane concentrations. This indicates a largely microheterogeneous structure, where water-rich domains of significant size are present. These are trapped within dioxane-rich regions and therefore restricted in their rotational and translations motions, causing largely increased relaxation times compared to pure water. In contrast to former studies by other investigators that suffer from insufficient frequency coverage, we cannot find evidence for stable dioxane-water aggregates or a percolation threshold at low dioxane concentration. Furthermore, THz-TDS measurements showed an enhancement of a dioxane collisional mode at ~ 2 THz by addition of water, which gives evidence for the presence of water in dioxane-rich domains. This assumption is further corroborated by the peculiarities of the (S_2, τ_2) mode, which is assumed to be caused by water molecules near dioxane-rich domains of the mixtures.

4.2 Oligo(ethylene glycol) ethers + water

4.2.1 Introduction

As already pointed out in the introduction, oligo(ethylene glycol) methyl ethers are suitable models for the hydrophilic moieties of C_nE_m non-ionic surfactants. Due to hydrogen bonding, they are miscible with water at any ratio. These interactions have major influence on the microdynamics of glycol ether + water mixtures, which attracted considerable attention during the last few years[124–129], mainly because of the high importance of oligo(ethylene glycol) derivatives both in industry and science, see Chap. 1.1.
The dielectric properties of pure water that up to 100 GHz can be well described by a single relaxation time, τ_W (~ 8.3 ps at 298.15 K), are heavily altered by the presence of non-ionic solutes.
It is generally accepted that this major Debye relaxation process is not caused by a rotational diffusion or fluctuation process of single molecules or local H-bonds but that it is connected with a cooperative rearrangement of H-bonds within a relaxation cluster[112,113].
The origin of additional relaxation modes at higher frequencies is still not fully clear and beyond the scope of this work, as we want to focus on the dynamics of hydrogen bond networks here.
The timescale of such rearrangement processes in pure water and binary mixtures of water with H-bonding liquids is determined by several factors. One is the microscopic time needed for the formation of a single hydrogen bond. However, it is not only the strength of the interactions, determined by the charge density around a water or organic (C-O-C or C-O-H) H-bond acceptor place and geometrical factors, but more complicated changes of the liquid structure have to be taken into account.
As already pointed out in literature[130,131], the availability of hydrogen bond acceptor sites is important for the dynamics of the H-bond rearrangement. A convenient measure is the number density, ρ_O, of hydrogen bond acceptor sites,

$$\rho_O = \frac{(c_1 + n_{O,2}\, c_2)}{c_W}, \tag{4.4}$$

where $n_{O,2}$ is the number of acceptor sites per organic molecule. c_1, c_2, and c_W are the molar concentrations of water, the organic solute and pure water (55.33 mol L^{-1} at 298.15 K), respectively.
The reduced density is a helpful parameter for the correlation of relaxation times of various systems[130], but it is mainly limited to lower concentrations of the organic species and to the comparison of similar compounds. These limitations and the lack of general rules point out the importance of further work. Using homologous series of oligo(ethylene glycol) monomethyl and dimethyl ethers, this study wants to investigate cooperative relaxation phenomena in the dilute region, but in concentrated solution as well. There, the relaxation behavior is governed by the organic compound and effects of the chainlike glycol ether molecules on the dynamics of the mixtures can be studied.

4.2.2 Experiment and data processing

Materials

Ethylene glycol monomethyl ether (C_1E_1OH; Fluka; 0.999 mole fraction; $H_2O \leq 300$ ppm), ethylene glycol dimethyl ether ($C_1E_1C_1$; Sigma; 0.9994 mole fraction; $H_2O \leq 80$ ppm) and triethylene glycol monomethyl ether (C_1E_3OH; Fluka; 0.997 mole fraction; $H_2O \leq 300$ ppm) were used as received. Diethylene glycol dimethyl ether (Merck, for synthesis) was heated with solid CaH_2, then fractionally distilled at atmospheric pressure using a 25 cm column, giving a product with a purity of 0.999 mole fraction; $H_2O \leq 60$ ppm. Triethylene glycol dimethyl ether ($C_1E_3C_1$; Merck, for synthesis) was distilled at ∼1 mbar using a 65 cm column. The fraction used for measurements had a purity of 0.998 mole fraction; $H_2O \leq$ 500 ppm.

Pentaethylene glycol monomethyl ether (C_1E_5OH) was prepared from diethylene glycol and 1-(2-chloro-ethoxy)-2-(2-methoxy-ethoxy)-ethane as follows. Using stirring throughout, a stochiometric amount of sodium metal (12.7 g) and 0.1 g of powdered, anhydrous sodium iodide (NaI) were added to 233.5 g diethylene glycol (dried by distillation). The mixture was heated to 120 °C until all the sodium dissolved. Then 100.5 g of 1-(2-chloro-ethoxy)-2-(2-methoxy-ethoxy)-ethane (prepared from triethylene glycol monomethyl ether and thionyl chloride[132], fractionated at ∼ 0.1 mbar) was added dropwise and the resulting mixture heated to 120 °C for several hours. After standing overnight at room temperature, sodium chloride was removed by filtration and washed with methanol. The filtrate was evaporated and the excess diethylene glycol removed by distillation at ∼ 0.03 mbar using a 25 cm column. Phosphoric acid (∼ 20% w/w, 25 mL) was added to the residue and the aqueous phase extracted with dichloromethane (4 × 100 mL). The combined extracts were evaporated and the residue was fractionated at 0.02 mbar. The middle fraction was further purified using a short-path molecular distillation apparatus at ∼ $3 \cdot 10^{-5}$ mbar. Pentaethylene glycol monomethyl ether (58 g) with a final purity of 0.994 mole fraction ($H_2O \leq 500$ ppm, $n_D^{25} = 1.4481$) was collected.

Pentaethylene glycol dimethyl ether ($C_1E_5C_1$) was prepared in a similar way from ethylene glycol monomethyl ether and 1,2-bis-(2-chloro-ethoxy)-ethane: 69 g sodium was cut into small pieces and added under stiring to 500 g ethylene glycol monomethyl ether (C_1E_1OH; destilled from CaH_2). This mixture was heated to 100 °C until the sodium dissolved. Anhydrous NaI (1 g, finely powdered) and 281 g 1,2-bis-(2-chloro-ethoxy)-ethane (dropwise) were added, and heating (100 °C) continued for 3 days. After evaporation of excess C_1E_1OH the remainder was dissolved in water and extracted with dichloromethane (4 × 100 mL). The organic layers were combined, dried over anhydrous sodium sulfate and evaporated. The residue was then distilled at 0.04 mbar. The fraction boiling between 95-119 °C was heated with 100 mL of ∼5% hydrochloric acid for a few hours to decompose byproducts (acetals), washed with *n*-pentane (3 × 50 mL) and the water evaporated at atmospheric pressure. 300 mL dichloromethane was added to the residue. After stirring over anhydrous potassium carbonate for several hours the dichloromethane was removed under vacuum. The raw product was fractionated over 40 cm column at 0.03 mbar and the center fraction (b.p. ∼105 °C) was further distilled at ∼0.008 mbar using a Fischer Spaltrohr apparatus (60 theoretical plates at 1013 mbar). The pentaethylene glycol dimethyl ether (73 g) so

obtained had a purity of 0.997 mole fraction ($H_2O \leq 500$ ppm; $n_D^{25} = 1.4376$).
The structures of the pentaethylene glycol ethers were confirmed by n.m.r. spectroscopy (^{1}H, ^{13}C and ^{13}C-DEPT 135°).
Note that all reactions were carried out with anhydrous reagents under a dry nitrogen atmosphere. All distillations employed vacuum-jacketed Vigreux colums.
Aqueous mixtures were prepared gravimetrically on an analytical balance without buoyancy corrections. Concentrations are thus accurate to four significant figures. Water, deionized and purified with a Millipore Milli-Q system (with a final pass through a 0.22 μm filter) was used throughout. All pure liquids were carefully degassed at low pressure prior to mixture preparation.

Thermodynamic properties

The thermodynamic properties of several oligomeric ethylene glycol mono- and dimethyl ethers as well as of their cyclic analogues, 1,4-dioxane and crown ethers, were extensively studied, especially with respect to apparent and molar excess volumes and heat capacities. All details were already discussed elsewere[77]. A preprint of the paper is attached as Appendix B to this thesis.

Refractive indices

Refractive indices of the mixtures water (1) + ethers $C_1E_nC_1$ (2) needed for the calculation of dielectric relaxation amplitudes were obtained from literature for $1 \leq n \leq 3$[133–135] where available, otherwise determined with an Abbé-type refractometer, see Chap. 3.2.2. For $n = 4$ only one reference could be found[136]. As these data did not follow the behavior expected from the other ethers, we redetermined the refractive index at some concentrations and all values of n_D^{25} given by McGee[136] were found to be ~ 0.003 too high, except for the value of pure water. Therefore, a correction $n_D^{25,\mathrm{corr}} = n_D^{25,\mathrm{McGee}} - 0.00275$ was applied, taking into account the difference of the n_D^{25} of the pure compound ($n_D^{25} = 1.43045$ measured and in close agreement with literature values[137,138], compared with $n_D^{25} = 1.4332$ given by McGee[136]). To our knowledge, no literature data are available for $C_1E_5C_1$.
The experimental values were fitted to fourth order polynomials, with coefficients given in Table 4.4.

Table 4.4: Refractive indices, n_{D}^{25}, of water (1) + ethylene glycol dimethyl ethers (2) mixtures as a function of mass fraction, w_2, at 298.15 K. Given are the coefficients a_i of the fits $n_{\mathrm{D}}^{25} = \sum_{i=0}^{4} a_i w_2^i$, and the values of the pure compounds, $n_{\mathrm{D},2}^{25}$.

n	$n_{\mathrm{D},2}^{25}$	a_0	a_1	a_2	a_3	a_4
1	1.3773[133]	1.332503	0.076842	0.070084	-0.176526	0.074546
2	1.40576[134]	1.332593	0.092744	0.086010	-0.175838	0.070268
3	1.4209[135]	1.332478	0.100080	0.086247	-0.151236	0.053235
4	1.43043[137]	1.332558	0.108179	0.070438	-0.109964	0.029059
5	1.4376[77]	1.332558	0.106039	0.106933	-0.169301	0.061307

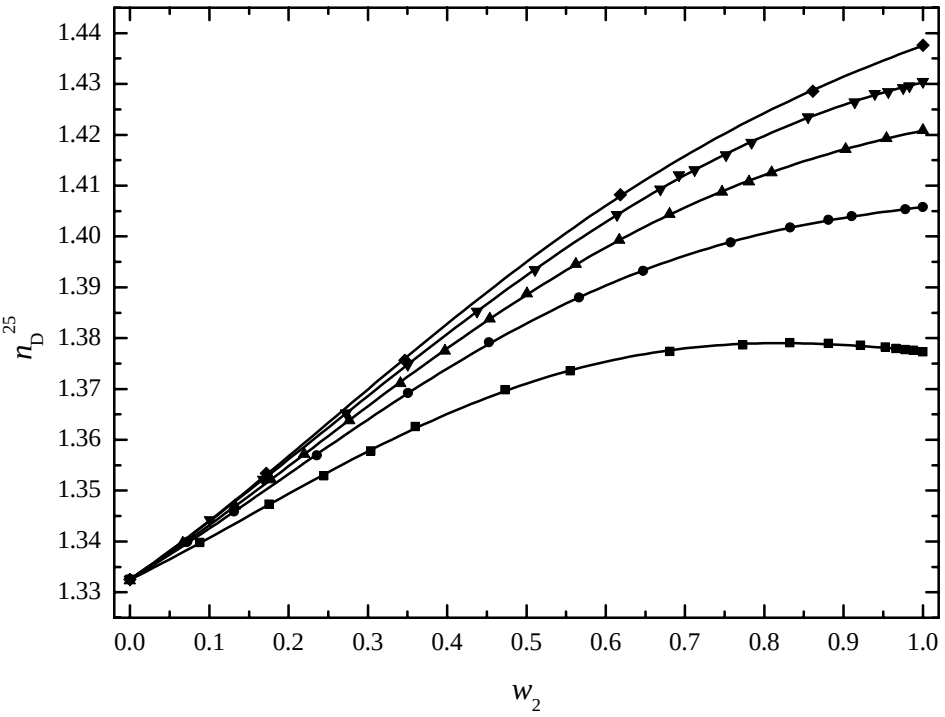

Figure 4.15: Refractive indices, n_{D}^{25}, of mixtures water (1) + oligoethylene glycol dimethyl ethers $C_1E_nC_1$ (2). w_2 represents the weight fraction of ether, with $n = 1$ (■), $n = 2$ (•), $n = 3$ (▲), $n = 4$ (▼) and $n = 5$ (♦).

4.2.3 Dielectric properties

Pure glycol ethers

TDR, VNA-R and IF experiments were performed with the pure liquid oligo(ethylene glycol) dimethyl ethers $C_1E_nC_1$ at 298.15 K covering a frequency range $0.2 \leq \nu/\mathrm{GHz} \leq 89$, see Fig. 4.16. For $n = 3$, the relaxation behavior has already been discussed elsewhere[139] and it was pointed out that a sum of three Debye equations is the most useful description within the frequency range of the measurement. The same model can be applied for $n = 5$; however, the complex permittivity of ethylene glycol dimethyl ether ($n = 1$) is best described by two Debye equations, Tab. 4.5. This may well be related to the reduced flexibility of this molecule, as the CH_2-O-CH_2 chain fragment responsible for the so-called crankshaft motion is only present for $n \geq 2$.

Table 4.5: Relaxation parameters, ε_j, τ_j (in ps), and the value of the reduced error function χ^2_r for pure liquid ethers $C_1E_nC_1$ at 298.15 K. Superposition of two (2D) or three (3D) Debye-type equations. Static dielectric constants, ε, were determined with a low-frequency impedance measurement setup, see Chap. 3.1.1.

n	model	ε	ε_1	τ_1	ε_2	τ_2	ε_3	τ_3	ε_∞	$10^3\,\chi^2_\mathrm{r}$
0.1-100 GHz; 298.15 K										
1	2D	7.07	7.08	-	-	5.21	3.96	1.94	2.28	0.679
3	3D	7.84	7.78	44.92	6.91	10.52	3.43	2.02	2.52	0.541
5	3D	7.90	7.91	49.05	6.55	15.41	3.57	2.56	2.60	0.830

The complex dielectric properties of oligo(ethylene glycol) monomethyl ethers were determined by VNA reflectometry only, because of the limited material and instrument time available for the experiments. Therefore, a lower accuracy of the measurement has to be assumed. The description of the data by a Cole-Cole term, Eq. 2.60, is not fully satisfactory at higher concentrations because the shape of the dielectric permittivity would suggest a more asymmetric band shape, broadened towards higher frequencies, see Fig. 4.16 (lower diagrams). Due to the limited frequency coverage a fit comprising more sophisticated relaxation models was not feasible. Thus, we want to use these data for a general discussion of the dynamics of their aqueous solutions only, whereas a more precise analysis of the dynamics of the pure monomethyl ether compounds remains as a subject of further studies.

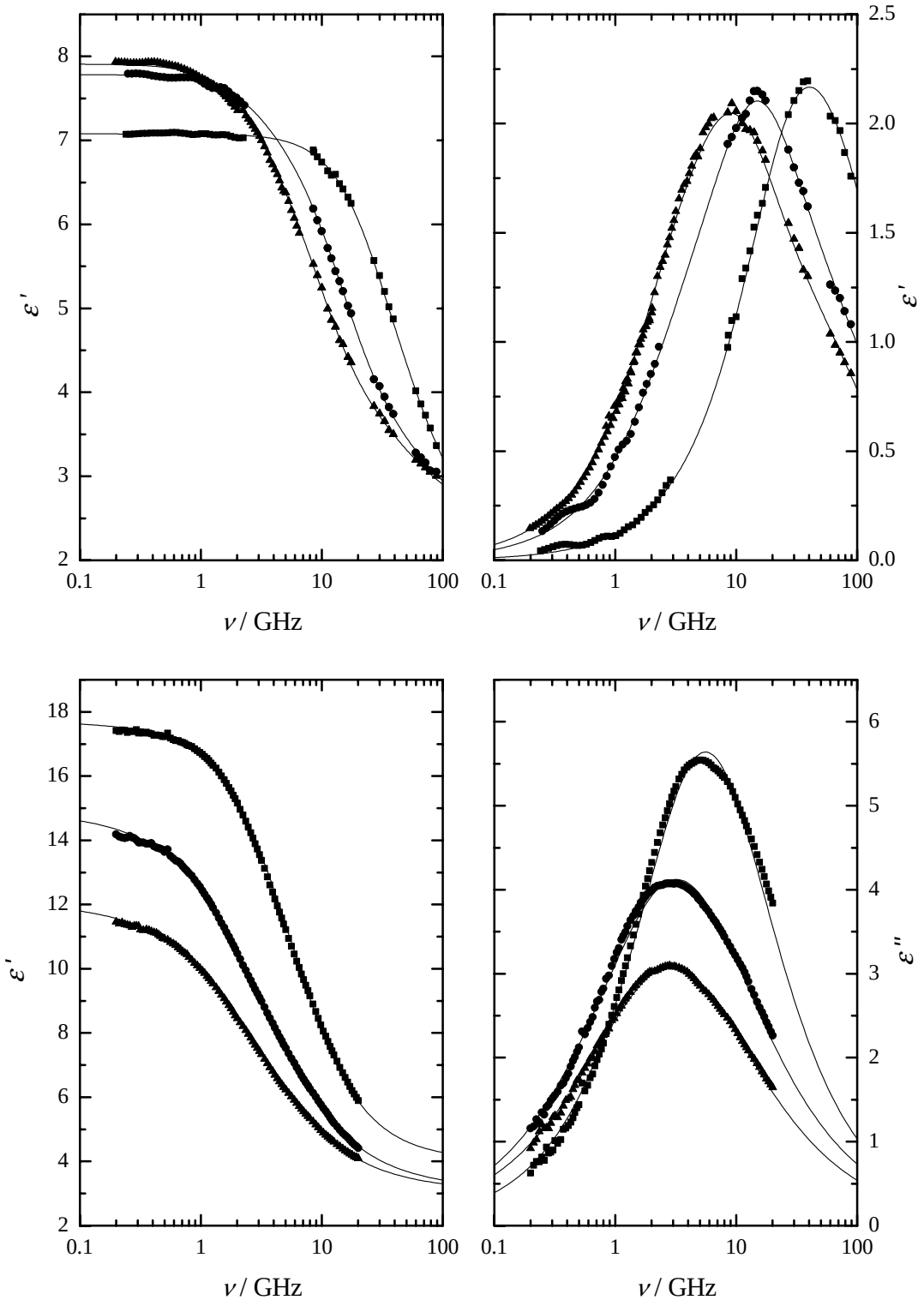

Figure 4.16: Dielectric permittivity, $\varepsilon'(\nu)$, and loss, $\varepsilon''(\nu)$, of pure oligo(ethylene glycol) dimethyl ethers ($C_1E_nC_1$, upper diagrams) and oligo(ethylene glycol) monomethyl ethers (C_1E_nOH, lower diagrams), with $n = 1$ (■), $n = 3$ (●), and $n = 5$ (▲). All values at 298.15 K.

Mixtures water + $C_1E_nC_1$

Complex dielectric spectra of mixtures water (1) + $C_1E_nC_1$ (2) were obtained by VNA-R over a frequency range $0.2 \leq \nu/\text{GHz} \leq 20$. The raw data measured using an air/short/ DMA and air/short/DMF calibration of the experimental setup were refined using the Pade $P_{1/1}$ approximation algorithm, see Chap. 3.1.3. The pure ethers $C_1E_nC_1$, BN and DMA/DMF were used as reference liquids for $\varepsilon \lesssim 40$, otherwise BN/DMA, DMF/water.

For $C_1E_1C_1$ lower relaxations times were found. Thus the frequency range for the aqueous solutions was extended to 89 GHz by A- and E-band interferometry. The statistical weights of the interferometric points were doubled to achieve a smoother data point density within the frequency range studied.
The data indicate an asymmetric shape of the dielectric loss spectra, $\varepsilon''(\nu)$, Fig. 4.17.

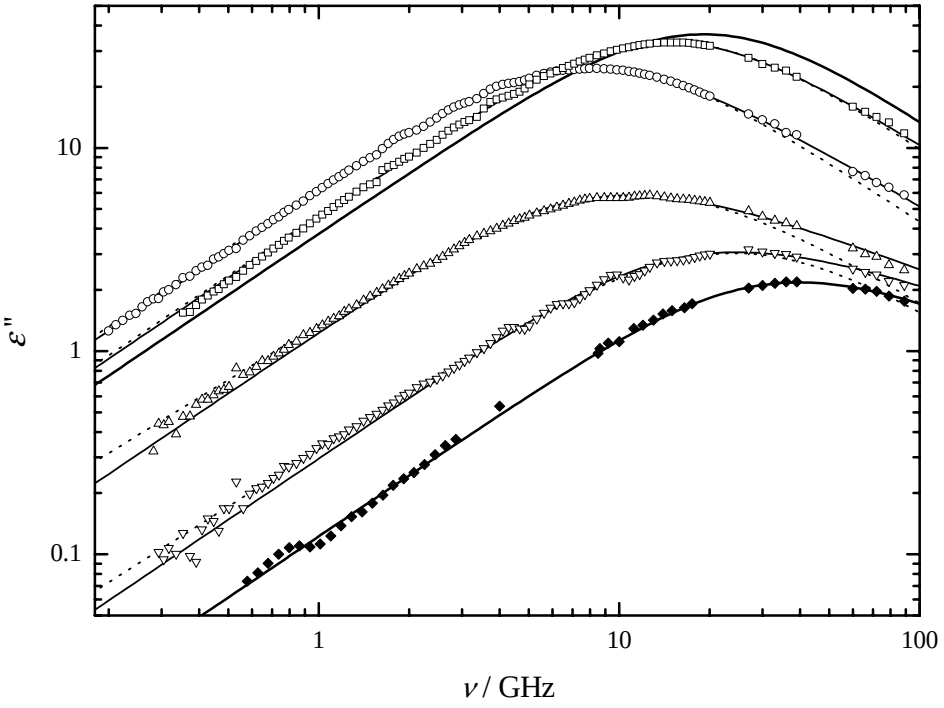

Figure 4.17: Dielectric loss spectra, $\varepsilon''(\nu)$, of mixtures water (1) + $C_1E_1C_1$. Full lines indicate Cole-Davidson fits, compared with Cole-Cole fits (dotted lines), at different concentrations: (black line) $x_{O,2} = 0$, (□) $x_{O,2} = 0.038$, (○) $x_{O,2} = 0.167$, (△) $x_{O,2} = 0.667$, (▽) $x_{O,2} = 0.889$, and (♦) $x_{O,2} = 1$.

Therefore, a Cole-Davidson term, Equ. 2.61, can be advantageously used for a proper description of the measured complex permittivity values. The relaxation parameters calculated are all summarized in Tab. 4.6. This table also includes results from a fit of the VNR-R data (0.2-20 GHz) alone, using a Cole-Cole equation for comparison with data obtained for the aqueous mixtures of the higher ether homologues, where waveguide interferometry data are not available. The difference of both relaxation models are indicated in

Table 4.6: Cole-Davidson and Cole-Cole relaxation parameters, ε, τ (in ps), α/β and reduced error function χ^2_r for water (1) + $C_1E_1C_1$ (2) at 298.15 K.

x_2	$x_{O,2}$	ε	τ	α, β	ε_∞	$10^3\,\chi^2_r$
0.2-89 GHz; 298.15 K; Cole-Davidson						
0[57]	0	78.17	8.31	1.00	5.73	46.7
0.01316	0.02597	74.31	10.4	0.96	4.79	121
0.01961	0.03846	72.50	11.5	0.94	4.63	92.4
0.03846	0.07407	67.62	14.7	0.90	4.40	79.5
0.04762	0.09091	65.44	16.2	0.89	4.24	77.4
0.06250	0.11765	62.08	18.2	0.89	4.11	47.6
0.07692	0.14286	59.10	20.3	0.88	4.14	30.9
0.09091	0.16667	56.30	22.1	0.87	3.98	29.5
0.11111	0.20000	52.76	23.6	0.88	4.12	17.9
0.14286	0.25000	47.08	25.8	0.86	3.96	15.0
0.20000	0.33333	38.78	27.3	0.84	3.60	9.94
0.33333	0.50000	25.58	26.7	0.71	2.60	3.70
0.50000	0.66667	16.94	22.4	0.58	1.69	5.06
0.66667	0.80000	12.23	16.0	0.52	1.26	4.39
0.80000	0.88889	9.702	10.6	0.53	1.31	3.09
1	1	7.075	5.598	0.65	1.74	0.669
0.2-20 GHz; 298.15 K; Cole-Cole						
0.01316	0.02597	74.43	9.94	0.0090	5.49	17.5
0.01961	0.03846	72.61	10.8	0.011	5.50	32.7
0.03846	0.07407	67.78	13.2	0.018	5.56	48.4
0.04762	0.09091	65.59	14.4	0.019	5.62	50.8
0.06250	0.11765	62.25	16.3	0.019	5.65	45.7
0.07692	0.14286	59.25	17.9	0.019	5.64	36.6
0.09091	0.16667	56.43	19.3	0.019	5.62	28.6
0.11111	0.20000	52.90	20.9	0.019	5.55	20.3
0.14286	0.25000	47.21	22.5	0.020	5.36	12.4
0.20000	0.33333	38.96	23.0	0.029	5.01	8.50
0.33333	0.50000	25.78	19.5	0.054	4.48	7.61
0.50000	0.66667	17.12	13.8	0.082	3.86	3.27
0.66667	0.80000	12.33	9.27	0.080	3.43	2.30
0.80000	0.88889	9.751	6.63	0.059	3.10	2.02

Fig. 4.17. Up to 20 GHz, Cole-Cole and Cole-Davidson models give comparable results. At higher frequencies, significant deviations due to the asymmetric bandshape were observed. In principle, asymmetric bandshapes of the dielectric functions have to be expected for the higher oligomers as well. Therefore, the empirical Cole-Davidson equation or a similar relaxation model comprising two or more Debye terms which account for the additional contributions at higher frequencies should be employed here. Unfortunately, no data at frequencies > 20 GHz were available for analysis, except for the pure substances. This causes instabilities of the fit procedure when asymmetric relaxation models are used due to an insufficient frequency coverage of the high-frequency wing of the dispersion region. However, we want to mainly discuss cooperative relaxation phenomena for the aqueous mixtures of the higher homologues, which give rise to a major relaxation step located within the frequency range of the VNA-R measurements, Fig. 4.18. Therefore, a single Cole-Cole term was used for processing all water + glycol ether mixtures and the results given in Tab. 4.7 and 4.8 for $C_1E_3C_1$ and $C_1E_5C_1$ provide a good description of the measured dielectric properties at least up to 20 GHz, especially for the more diluted solutions, Fig. 4.18.

Table 4.7: Cole-Cole relaxation parameters, ε, τ (in ps), α and reduced error function χ^2_r for water (1) + $C_1E_3C_1$ (2) at 298.15 K.

id	x_2	$x_{O,2}$	ε	τ	α	ε_∞	$10^3\,\chi^2_r$
0.2-20 GHz; 298.15 K							
1	0.01316	0.05063	71.50	11.1	0.040	4.41	21.5
2	0.01961	0.07407	68.72	12.6	0.053	4.41	31.4
3	0.03846	0.13793	61.21	17.7	0.073	4.37	25.6
4	0.04762	0.16667	57.60	20.3	0.079	4.41	18.4
5	0.06250	0.21053	53.75	24.4	0.085	4.64	13.5
6	0.07692	0.25000	49.76	28.0	0.089	4.63	13.9
7	0.09091	0.28571	46.53	31.1	0.092	4.66	11.4
8	0.11111	0.33333	42.47	34.6	0.096	4.63	12.8
9	0.14286	0.40000	37.10	37.9	0.10	4.48	10.9
10	0.20000	0.50000	29.42	38.8	0.10	4.40	28.3
11	0.33333	0.66667	19.97	32.9	0.12	3.97	21.3
12	0.50000	0.80000	14.36	24.4	0.16	3.36	4.47
13	0.66667	0.88889	11.40	18.6	0.15	3.26	1.24
14	0.79356	0.93894	9.840	15.3	0.15	3.08	1.23

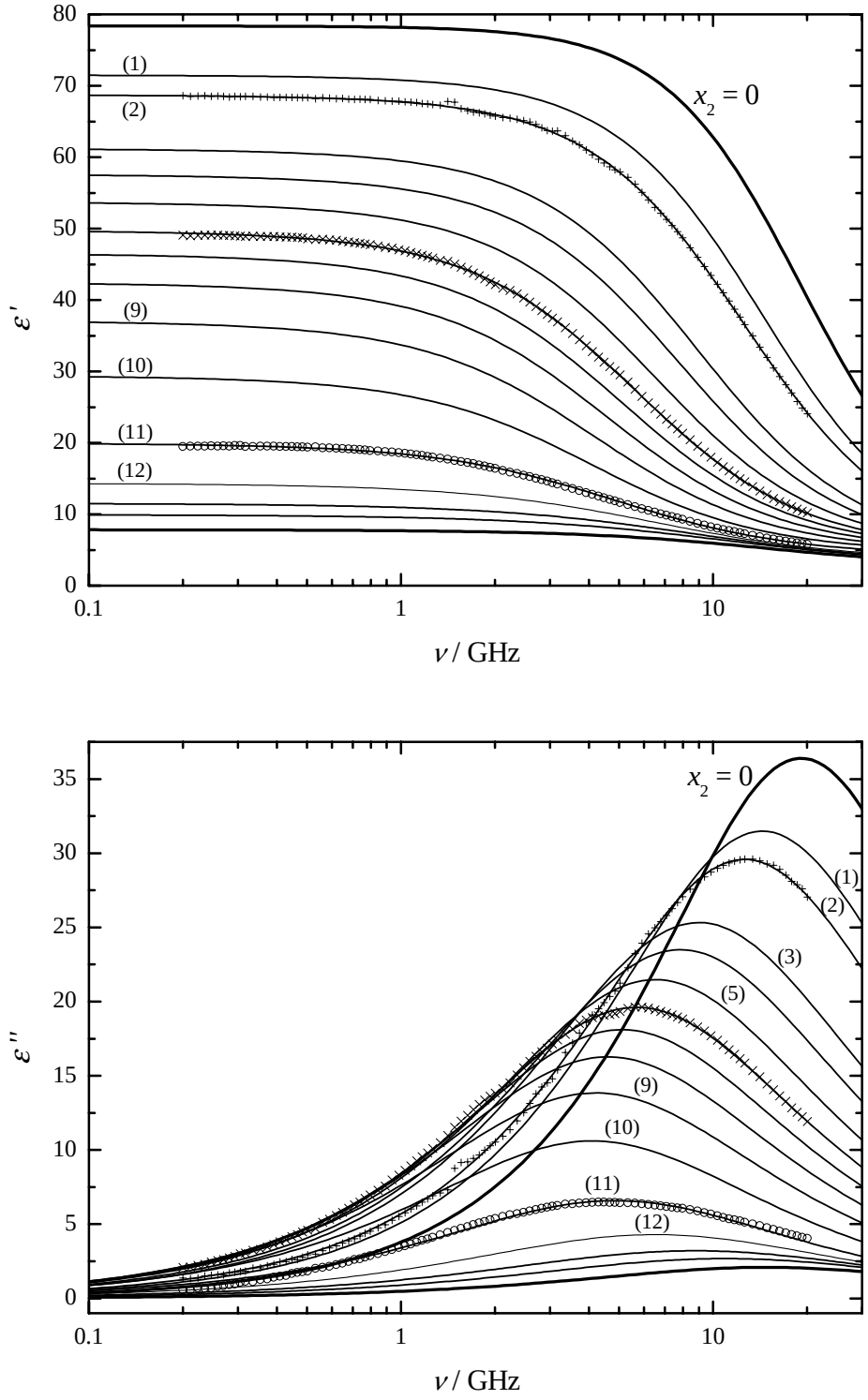

Figure 4.18: Complex dielectric permittivity spectra, $\varepsilon'(\nu)$ and $\varepsilon''(\nu)$, of mixtures water (1) + $C_1E_3C_1$. Thick lines indicate pure substances, the other represent Cole-Cole fit of the data obtained at concentrations given in Tab. 4.7. For mixtures no. 2 (+), 6 (×) and 11 (∘) experimental results are also shown.

Table 4.8: Cole-Cole relaxation parameters, ε, τ (in ps), α and reduced error function χ^2_r for water (1) + $C_1E_5C_1$ (2) at 298.15 K.

x_2	$x_{O,2}$	ε	τ	α	ε_∞	$10^3\,\chi^2_r$
0.2-20 GHz; 298.15 K						
0.00662	0.03846	73.05	10.1	0.037	4.25	18.7
0.00990	0.05660	70.69	11.2	0.048	4.16	29.3
0.01961	0.10714	64.58	14.8	0.072	4.31	20.8
0.03846	0.19355	55.39	22.9	0.096	4.52	5.51
0.06250	0.28571	46.68	33.3	0.11	4.54	4.86
0.09091	0.37500	39.17	42.9	0.12	4.43	2.51
0.16667	0.54545	27.24	49.8	0.15	3.91	2.93
0.33333	0.75000	16.74	39.8	0.18	3.48	4.22
0.50000	0.85714	12.56	30.4	0.19	3.17	1.81
0.66667	0.92308	10.35	24.2	0.19	2.94	0.848

The complex dielectric spectra of mixtures water + $C_1E_5C_1$ are very similar to those of the solutions containing $C_1E_3C_1$, Fig. 4.18. For $C_1E_5C_1$, higher relaxation times were found, which will be subject to further discussion below. From the Cole-Cole fits, not only relaxation amplitudes and times are obtained, but also a so-called shape or distribution parameter, α. For a relaxation behavior featuring a single relaxation time, $\alpha = 0$ can be calculated (Debye case). Higher values reflect a broader, symmetric distribution of relaxation times. Fig. 4.19 summarizes all distribution parameters calculated from the spectra. For all oligomers, these show a steep increase starting from pure water and level off at higher $x_{O,2}$ mole fractions. For $C_1E_1C_1$ a pronounced plateau value is found between $x_{O,2} \approx 0.1..0.2$. Here we have to keep in mind that due to the lower relaxation times found for this homologue the difference in the statistical weight of the dielectric spectra at frequencies lower and higher than the frequency of the maximum of the dielectric loss has to be taken into account. Unfortunately, the Cole-Cole description of the spectra is of lower quality at high ether concentrations. Thus the α values given in this concentration region ($x_{O,2} > 0.5$) are less accurate and show larger scatter, Fig. 4.19.

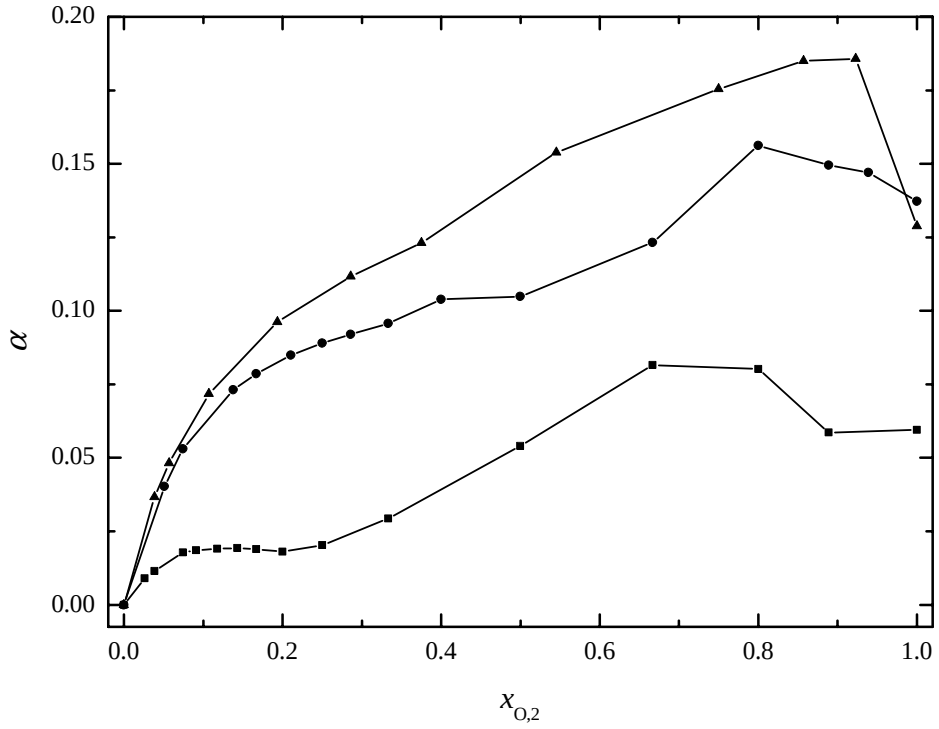

Figure 4.19: Concentration depencence of the distribution parameter, α, obtained from the fit of a Cole-Cole term to the complex dielectric loss spectra, $\hat{\varepsilon}(\nu)$, over a frequency range $0.2 \leq \nu/\mathrm{GHz} \leq 20$ of mixtures water (1) + ethers $C_1E_nC_1$ (2). $n = 1$ (■), $n = 3$ (●), and $n = 5$ (▲).

Mixtures water + C_1E_nOH

Dielectric data over of mixtures water (1) + C_1E_nOH (2) were determined from VNA reflectometry measurements. Reference liquids included BN, DMA/DMF and water, depending on the dielectric properties of the sample. Air and a mercury short were used as second and third standard for all measurements. The data were not corrected against additional internal references, therefore larger errors have to be assumed regarding the absolute permittivity values at the low-permittivity side. However, as the pure monomethyl ethers have relatively high permittivities compared with the corresponding dimethyl ethers, these deviations are not so severe ($\varepsilon > 15$, Fig. 3.4).
All spectra were fitted using a Cole-Cole relaxation model. A description by a Cole-Davidson term or sums of two or more Debye is possible, but leads to numerically instable values due to a lack of data in the high-frequency region (> 20 GHz).

Table 4.9: Cole-Cole relaxation parameters, ε, τ (in ps), α and reduced error function χ^2_r for water (1) + C_1E_1OH (2) at 298.15 K.

x_2	$x_{O,2}$	ε	τ	α	ε_∞	$10^3\,\chi^2_r$
0.2-20 GHz; 298.15 K						
0.01316	0.02597	76.04	9.58	0.0067	5.63	16.5
0.01961	0.03846	74.97	10.3	0.0096	5.83	24.8
0.03846	0.07407	71.90	12.3	0.012	6.35	57.0
0.04762	0.09091	70.47	13.4	0.012	6.56	68.3
0.06250	0.11765	68.23	15.0	0.011	6.69	82.4
0.07692	0.14286	66.22	16.5	0.012	6.58	90.3
0.09091	0.16667	64.31	17.9	0.012	6.56	92.5
0.14286	0.25000	56.88	21.9	0.030	5.39	21.5
0.20000	0.33333	51.03	26.5	0.033	5.34	21.1
0.33333	0.50000	40.73	33.1	0.048	4.98	25.7
0.50000	0.66667	32.21	36.0	0.072	4.65	29.6
0.66667	0.80000	25.68	37.0	0.091	4.39	26.4
0.80000	0.88889	22.06	34.5	0.11	4.23	23.4
1	1	17.71	28.6	0.12	3.99	15.0

The data obtained for the mixtures water (1) + ether C_1E_nOH (2) are all summarized in Tab. 4.9-4.11. The sudden increase of the distribution parameters, α, around $x_{O,2} \approx 0.2$ can be attributed to the chance of the reference system from water/short/air to DMA,DMF/short/air that causes these artifacts. Densities and other thermodynamic data of the solutions were already published elsewhere[77].

Table 4.10: Cole-Cole relaxation parameters, ε, τ (in ps), α and reduced error function χ^2_r for water (1) + C_1E_5OH (2) at 298.15 K.

x_2	$x_{O,2}$	ε	τ	α	ε_∞	$10^3\,\chi^2_r$
0.2-20 GHz; 298.15 K						
0.00662	0.03846	73.92	9.89	0.037	4.08	20.6
0.00990	0.05660	71.94	10.8	0.051	3.79	25.5
0.01961	0.10714	66.71	14.1	0.079	3.85	26.7
0.03846	0.19355	58.74	21.9	0.11	4.02	13.1
0.06250	0.28571	51.15	33.8	0.13	4.24	12.6
0.09091	0.37500	44.52	48.5	0.14	4.34	4.62
0.16667	0.54545	33.48	77.0	0.17	4.13	2.37
0.33333	0.75000	23.10	94.0	0.23	3.55	2.62
0.50000	0.85714	18.24	87.8	0.25	3.28	1.89
0.66667	0.92308	15.40	75.8	0.26	3.14	1.78
1	1	12.08	54.5	0.24	3.05	1.71

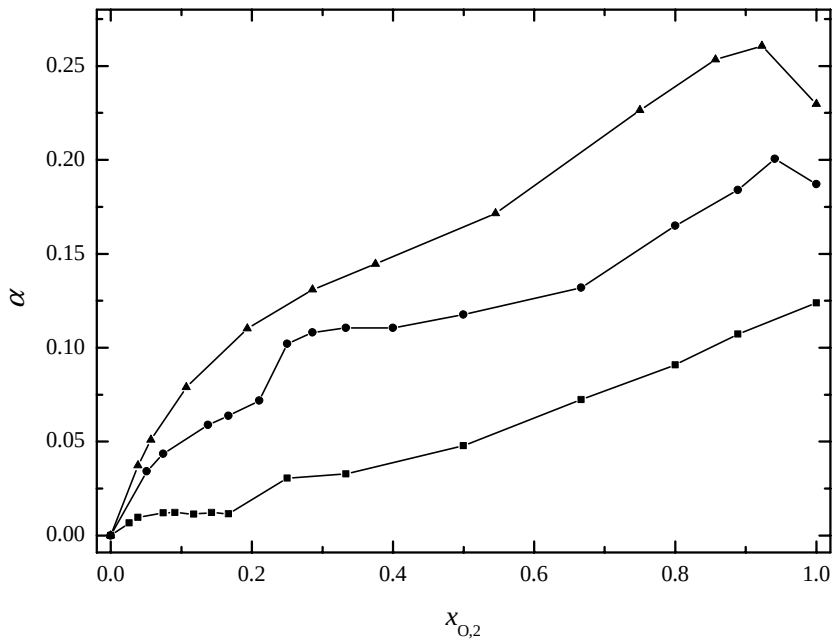

Figure 4.20: Distribution parameter, α, obtained from Cole-Cole fits of complex dielectric spectra of mixutures water + C_1E_nOH (2). $n = 1$ (■), $n = 3$ (●), and $n = 5$ (▲).

Table 4.11: Cole-Cole relaxation parameters, ε, τ (in ps), α and reduced error function χ^2_r for water (1) + C_1E_3OH (2) at 298.15 K.

x_2	$x_{O,2}$	ε	τ	α	ε_∞	$10^3\,\chi^2_r$
0.2-20 GHz; 298.15 K						
0.01316	0.05063	73.17	10.7	0.034	4.95	29.6
0.01961	0.07407	70.98	12.1	0.043	5.11	46.0
0.03846	0.13793	65.19	16.9	0.059	5.51	68.1
0.04762	0.16667	62.78	19.3	0.064	5.54	68.4
0.06250	0.21053	59.14	23.5	0.072	5.44	64.9
0.07692	0.25000	55.41	26.9	0.10	4.40	23.9
0.09091	0.28571	52.76	31.2	0.11	4.41	16.0
0.11111	0.33333	49.26	36.8	0.11	4.55	20.4
0.14286	0.40000	44.58	44.7	0.11	4.74	48.9
0.20000	0.50000	38.11	58.0	0.12	4.55	28.1
0.33333	0.66667	28.84	69.7	0.13	4.28	44.1
0.50000	0.80000	22.95	69.9	0.17	3.85	41.0
0.66667	0.88889	18.97	67.3	0.18	3.66	15.0
0.80000	0.94118	16.82	61.5	0.20	3.46	9.78
1	1	14.92	49.6	0.22	3.10	5.65

4.2.4 Results and discussion

Like for the 1,4-dioxane + water mixtures, we want to start the discussion of the results of the DRS experiments of the glycol ether compounds from the viewpoint of their thermodynamic properties. Oligo(ethylene glycol) dimethyl ethers, $C_1E_nC_1$, differ from dioxane by their higher degree of conformational freedom, and it is known from Raman spectroscopic investigations that the populations of the conformers are changing in aqueous environments[140]. Whereas a single dioxane molecule is characterized by an almost spherical shape, glycol ether oligomers consist of chain-like molecules. These can promote interactions over much longer distances by their interacting groups (i.e. CH_2-O-CH_2), which are connected by covalent bonds. Therefore it should be possible to distinguish localized effects from those involving larger aggregates.

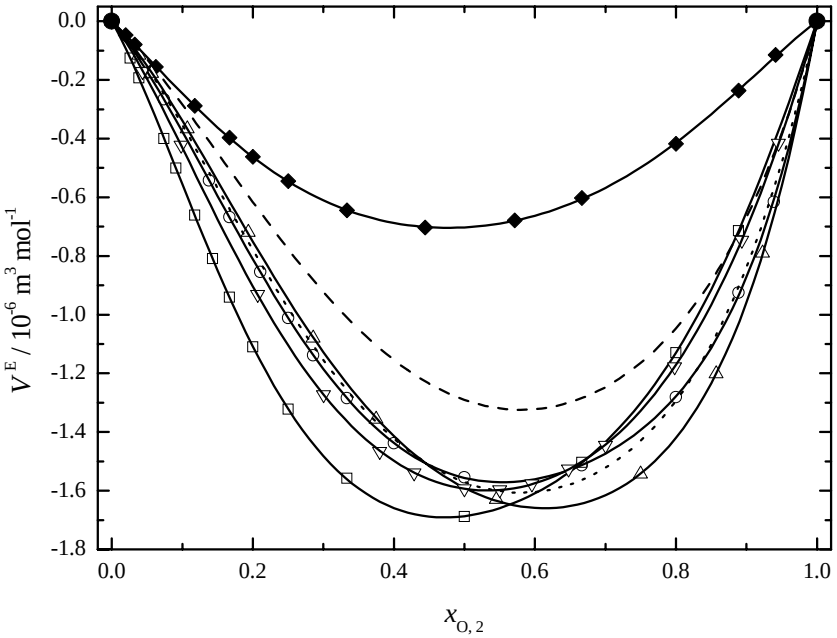

Figure 4.21: Molar excess volumes, V^E of mixtures water (1)+1,4-dioxane (⧫), 12-crown-4[141] (dashed line), $C_1E_1C_1$ (□), $C_1E_2C_1$ (▽), $C_1E_3C_1$ (○), $C_1E_4C_1$[142] (dotted line) and $C_1E_5C_1$ (△).

The importance of chain length and flexibility of the ether molecule for the properties of their aqueous mixtures is clearly revealed by the excess volumes, Fig. 4.21. Whereas 1,4-dioxane shows a rather small negative excess molar volume, these of the $C_1E_nC_1$ compounds are all very similar and much more negative. Because of the higher degree of conformational freedom of open chain ethers, these can more easily occupy void space of the water structure and can give rise to large thermodynamic effects, e.g. excess heat capacities[77]. The same applies to higher analogues of 1,4-dioxane, the crown ethers (*cyclo*-$(CH_2CH_2O)_n$), which gain flexibility by their larger ring diameter, finally resembling the properties of the dimethyl ethers for large n[77].

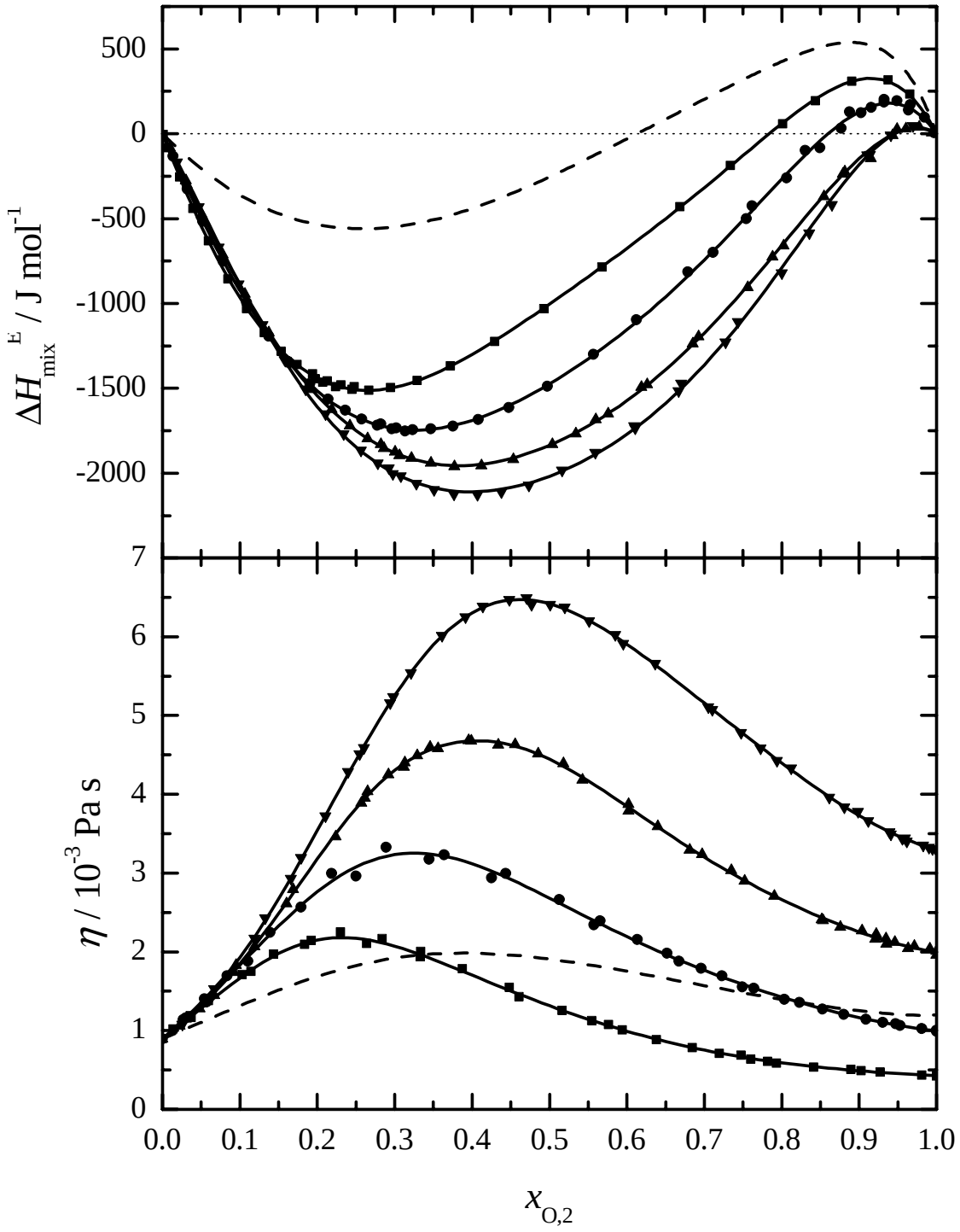

Figure 4.22: Thermodynamic properties of mixtures of water(1) + glycol ethers (2): Molar excess heats of mixing, ΔH^{E}_{mix} [143] and viscosities, η, of (■) $C_1E_1C_1$ [133,144,145], (●) $C_1E_2C_1$ [134,145], (▲) $C_1E_3C_1$ [135,145], and (▼) $C_1E_4C_1$ [136,145]. The dashed lines show the corresponding properties of water(1) + 1,4-dioxane mixtures. All values at 298.15 K

Fig. 4.22 (upper diagram) shows the excess heat of mixing found for mixtures water + $C_1E_nC_1$. Up to a molar fraction $x_{O,2} \approx 0.15$ very similar exothermic effects can be observed for ethers of different chain length. Thus it can be assumed that within this concentration regime the ethers affect interactions on lengthscales short compared with the structural features of the liquid. At higher concentrations, an important role is played by the chain length, but the overall increase of the exothermic effect is moderate, keeping in mind the linearly increasing molecular weight of the solute. In contrast to 1,4-dioxane + water mixtures, a positive heat of mixing is only observed at high ether contents and it seems likely that this endothermic region mainly arises from the predominant presence of the more hydrophobic methoxy headgroups compared with the -CH_2CH_2O- chain segments.

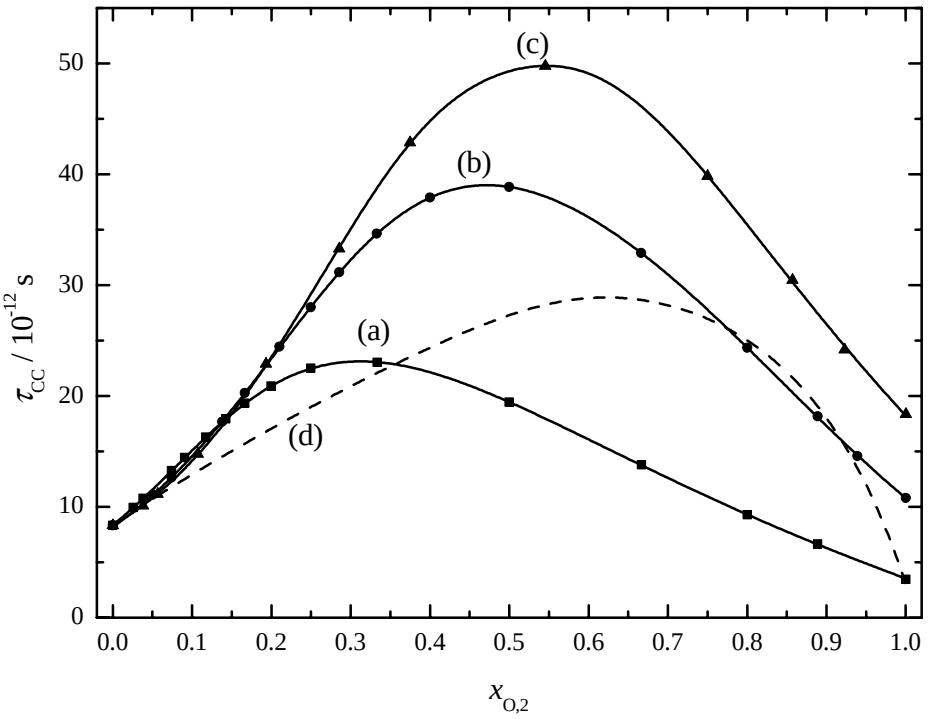

Figure 4.23: Cole-Cole relaxation times, τ_{CC}, of mixtures water(1) + $C_1E_nC_1$ (2). (■, a) $n = 1$, (•, b) $n = 3$, (▲, c) $n = 5$. For comparison, the Cole-Davidson relaxation times for water (1) + 1,4-dioxane are also shown (dashed line, d). All values at 298.15 K.

A comparison of the macroscopic viscosity with relaxation times calculated from dielectric spectra can be very instructive. For simple liquids consisting of non-interacting spheres, the Debye model of rotational diffusion, Eq. 2.88, predicts a direct relation between both quantities. But for the compounds discussed here, none of the underlying assumptions are fulfilled, although a comparison of viscosities of mixtures water (1) + ethers $C_1E_nC_1$ (2), Fig. 4.22 (lower diagram), with Cole-Cole relaxation times, Fig. 4.23, suggests a close correlation, in contrast to 1,4-dioxane + water mixtures, where the position of the peak maximum differs significantly. Therefore care must be taken with the interpretation of the macroscopic viscosity, as many factors influence this quantity. During the last years,

some progress was made in deriving thermodynamic properties from molecular dynamics simulations, especially that of water + $C_1E_1C_1$ mixtures[124–128] as well as of higher (polydisperse) ether homologues ($n \approx 10$)[129]. The numerical studies point out the peculiarities of these systems but a better modelling at least with respect to some thermodynamic equilibrium properties is still required. Unfortunately, the calculation of the time dependent dipole moment autocorrelation function, which would allow the calculation of the complex dielectric spectrum, $\hat{\varepsilon}(\nu)$, is not so straightforward to carry out[114].

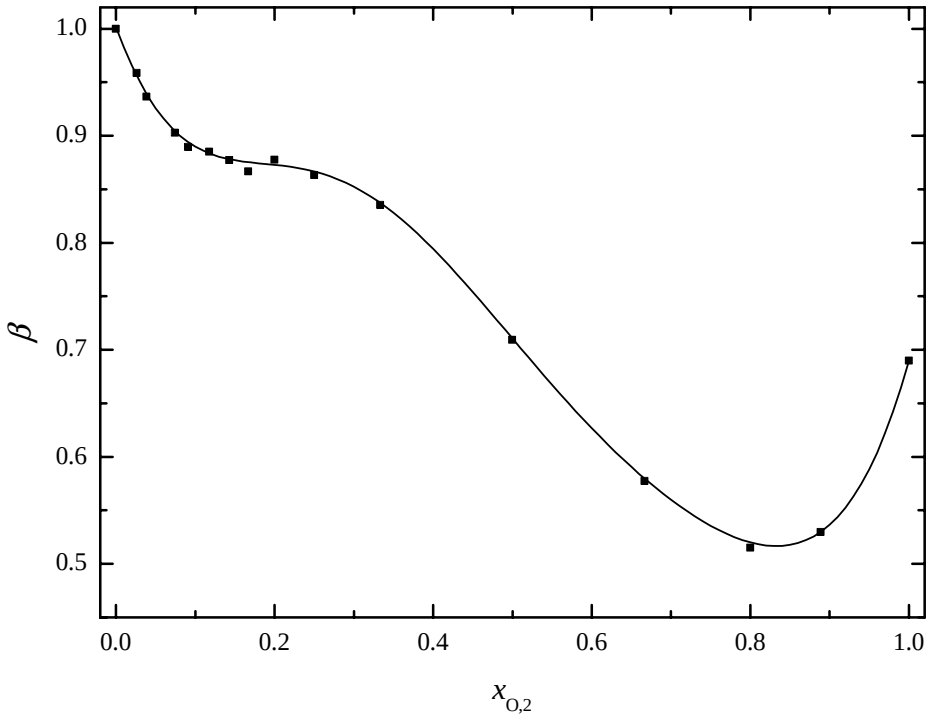

Figure 4.24: Distribution parameter, β, obtained from a Cole-Davidson fit of the dielectric spectra of mixtures water (1) + $C_1E_1C_1$ (2).

Here we have to reconsider the origin of the major dielectric dispersion step observed in pure water that is a relaxation process involving several water molecules, the so-called cooperative relaxation of a water cluster. These clusters must not be understood in terms of stable aggregates but only reflect the correlation length of dipole relaxation within an associated liquid, consisting of many local-order rearrangement processes which are fast compared to the macroscopic dielectric relaxation time. These elementary steps involve the breaking and formation of hydrogen bonds, with a time constant affected by several factors. One is, as already pointed out by other investigators[130,131,146], the inverse hydrogen bond acceptor number density, ρ_O^{-1}.

Taking into account the dynamic nature of the organic solute, it is not only the concentration of H-bond acceptor sites that determines the rate constant of the cooperative relaxation process, but also the mobility of these groups. The H-bond acceptor groups that are part of the same chain molecule cannot move independently, but require a change of the conforma-

tion of the ether molecule. It is also known from spectroscopic investigations[140,147–149] and molecular dynamics simulations[128] that only some of the possible conformers are favorably present in aqueous mixtures. From the dielectric spectra of the pure oligo(ethylene glycol) dimethyl ethers and of oligo(ethylene glycols)[139] the characteristic time needed for a rearrangement of a hydrogen-bond acceptor segment can be estimated to be at least 10 ps, much longer than the time needed for an elementary relaxation step in pure water, which is < 1 ps due to the close vicinity of a fifth neighbor[113]. One might now argue that the motions of -CH_2OCH_2- segments could be much faster in aqueous solution compared with the neat substance and therefore not be held responsible for the slowing down of the water relaxation dynamics observed, but there is clear evidence from Raman spectroscopic investigations that oligoethylene glycol ethers do not tend to form closely packed structures. On the contrary, these molecules take rather disordered conformations in pure liquid state, whereas the conformational order increases on addition of water to such a system[150]. On the timescale of water dielectric relaxation, the ether chains are rather stiff molecules and therefore significantly slow down the cooperative relaxation of water-rich clusters.

Up to a molar fraction $x_{O,2} \approx 0.15 - 0.2$ the relaxation times grow almost uniformly for all members of the homologous series of dimethyl ethers, Fig. 4.23. Thus, it can be assumed that within this concentration region the relaxing cluster is large compared with the size of an ether molecule incorporated in the hydrogen bond network structure. The ether affects only the relaxation time by providing non-interacting inner surfaces and by filling void spaces of the water structure. This will slow down the average rate of hydrogen bond reformation, leading to an increase of the macroscopic relaxation time which just depends on the fraction of oxygen sites provided by ether molecules. Especially for water + $C_1E_1C_1$ mixtures, there is also evidence for this interpretation from the shape parameters, α and β, of the dielectric spectra, Fig. 4.20 and 4.24. These undergo a characteristic change around $x_{O,2} \approx 0.2$ which indicates a change of the relaxation mechanism or a crossover of length scales, respectively. For the higher homologues of $C_1E_nC_1$, $n \geq 3$, the distribution parameter, α, reaches much larger values, maybe due to the -CH_2OCH_2- chain segments which are not present for $n = 1$ and cause an additional broadening at the low frequency side of the dielectric spectrum. The increase of the β parameter for $x_{O,2} \gtrsim 0.85$ can be mainly attributed to the effects of $C_1E_1C_1$ bulk regions, which govern the overall relaxation behavior at high ether concentrations.

At higher concentrations of the ethers, at least two effects on the water relaxation dynamics have to be considered. One is, as already mentioned, the flexibility of the ether chain and the correlation of H-bond acceptor site rearrangements due to their covalent linkage by -C_2H_4- bridges. On the other hand, we have to address a change in the characteristic number of water molecules incorporated in the cooperative dielectric relaxation mechanism. It is reasonable to assume a significant decrease of this number due to the predominant presence of H-bond acceptor places from ether molecules, which interrupt, from a certain threshold on, the propagation of the H-bond network restructuring. Thus, the lack of strong interactions between water and ether molecules and the comparatively strong water-water interactions lead to large fluctuations of the local density of water molecules, an idea supported by recent molecular dynamics simulations[114,151].

Further evidence for this microscopic view is found by comparison of the results with

dielectric data of mixtures water + oligo(ethylene glycol) monomethyl ethers (C_1E_nOH). Most interesting here are the relaxation times, τ, obtained from Cole-Cole fits, Fig. 4.26 (lower diagram). In contrast to the dimethyl ether compounds, the maximum of the relaxation time is found at mole fractions $x_{O,2} \approx 0.8$, independent of the chain length of the ether. We argue that this difference arises from the stronger interactions of water with hydroxyl (COH) compared to ether (COC) oxygen sites and from the ability of the former to act as a H-bond donor molecule. Thus the existence of regions of high water content becomes unfavorable with increasing ether concentrations. Additionally, self-association of the ethers is possible, which is also obvious from thermodynamic data[77].

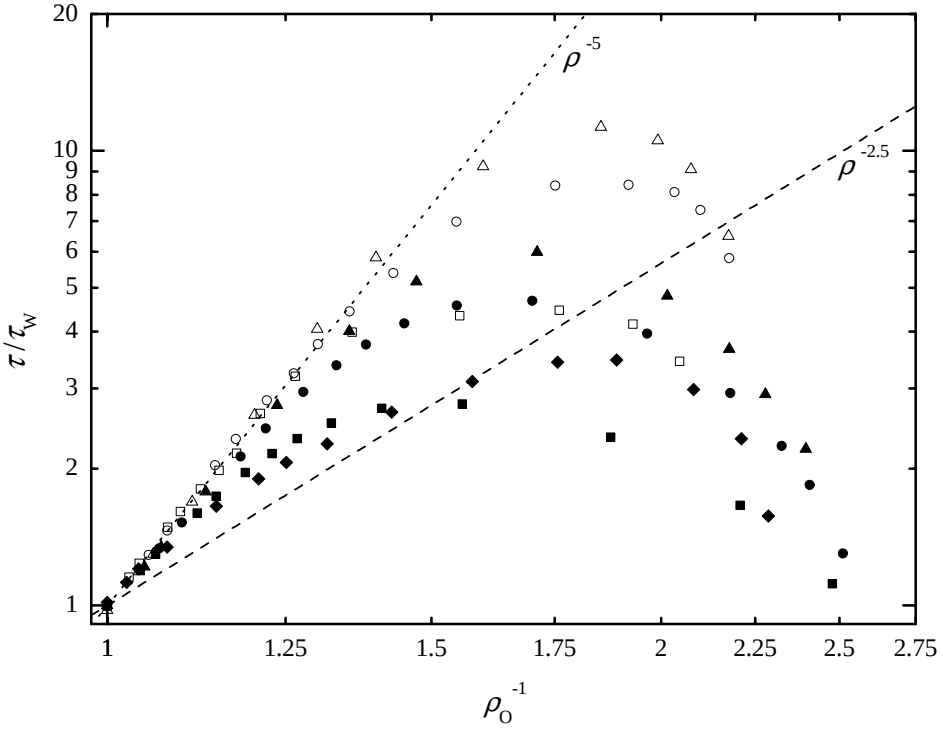

Figure 4.25: Bilogarithmic plot of the relaxation time ratio τ/τ_W as a function of the inverse relative H-bond acceptor number density, ρ_O^{-1}, for mixtures water(1) + glycol ethers C_1E_nOH (2, open symbols) and $C_1E_nC_1$ (2, full symbols) at 298.15 K, with (■) $n = 1$, (●) $n = 3$, (▲) $n = 5$. Also shown are data for 1,4-dioxane (⧫).

These effects might also explain the deviations from linear behavior and the different exponents, k, of the reduced function $\tau/\tau_W = \rho_O^{-k}$, where $k = 2.5$ was found for a variety of monohydric alcohols[146] and $k = 5$ for the oligomeric monomethyl ethers studied here, Fig. 4.25. Mixtures of water + 1,4-dioxane and the dimethyl ethers show deviations

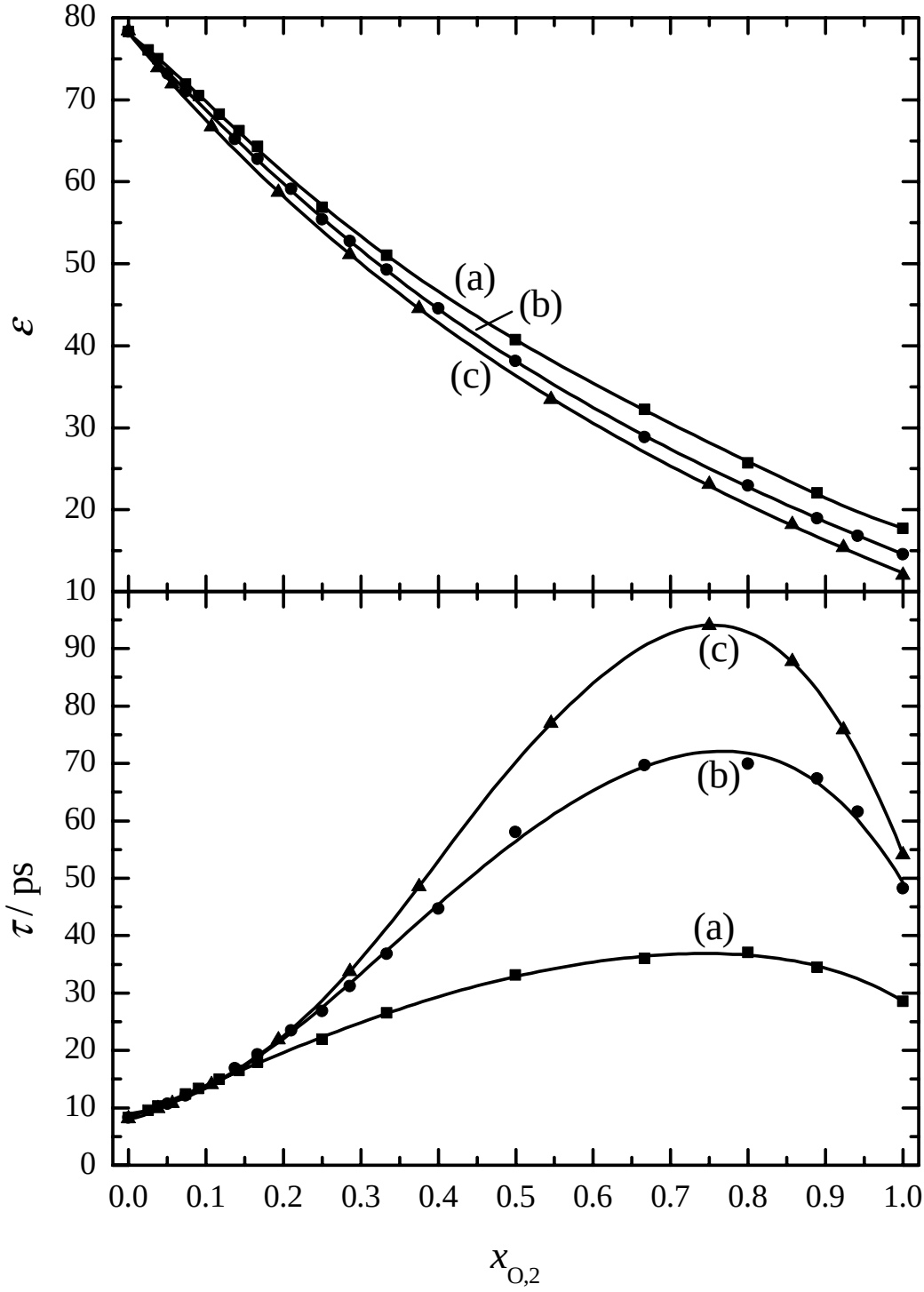

Figure 4.26: Static dielectric constant, ε, and Cole-Cole relaxation times, τ_{CC}, for mixtures water(1)+ glycol ether C_1E_nOH (2) at 298.15 K, with (■, a) $n = 1$, (●, b) $n = 3$, (▲, c) $n = 5$.

from linear behavior already at low concentrations. While the underlying model assumes a uniform hydrogen bond acceptor density even at the molecular level, we infer from the thermodynamic and dielectric data the presence of relatively large local fluctuations of the water number density (i.e. the existence of regions of high water content, on a length scale larger than several molecules), especially for 1,4-dioxane and oligo(ethylene glycol) dimethyl ether + water mixtures.
The analysis of the relaxation strength, which could provide further insight into this topic has some inherent difficulties, especially in the case of interacting, non-spherical molecules. Assuming a binary mixture, where both components are microscopically separated and show the same dielectric response as in the pure liquid (bulk) state we can define an excess relaxation strength

$$\Delta\varepsilon - \Delta\varepsilon^{\mathrm{id}} = \varepsilon - 1.05(n_{\mathrm{D}}^{25})^2 - c_1/c_1^0\,\Delta\varepsilon_1^0 - c_2/c_2^0\,\Delta\varepsilon_2^0, \tag{4.5}$$

where $\Delta\varepsilon_i^0 = \varepsilon_i - 1.05(n_{\mathrm{D},i}^{25})^2$ is the relaxation strength and c_i the concentration of the component i. c_i^0, ε_i and $n_{\mathrm{D},i}^{25}$ are the concentrations, static permittivities and refractive indices of the pure substances, respectively.
The absolute and excess relaxation strength obtained from the dielectric spectra of water + $C_1E_nC_1$ mixtures are given in Fig. 4.27. The behavior of the lowest member of the homologous series of dimethyl ethers, $C_1E_1C_1$, significantly differs from the higher ones, but the overall trend remains similar for all mixtures studied. Below a mole fraction $x_{\mathrm{O},2} \approx 0.5$ positive values of the excess relaxation strength were found. This may be caused by a stronger correlation of water dipoles or by additional contributions from glycol ether molecules. Molecular dynamics simulations carried out by Bedrov et al.[124] showed that polarisation effects due to interactions of water dipoles with induced dipole moments in $C_1E_1C_1$ do not play an important role. Therefore, we assume that an enhanced orientational correlation of water dipoles within the relaxing cluster and the stronger cavity field compared with the pure organic liquid, caused by water-rich regions in vicinity of ether dipoles, is mainly responsible for the excess relaxation amplitude effect observed. At higher ether concentrations, an almost ideal behavior is found in agreement with a microheterogeneous structure model, except for $C_1E_1C_1$. For this compound, changes in the distribution of the conformers caused by the addition of water have to be taken into account[128,140] and result in larger dipolar effects compared with molecules featuring longer chain length.
Finally we conclude that the mono- and dimethyl ethers differ significantly in their relaxation behavior, both in pure liquid state and in aqueous solutions. While the dimethyl ethers revealed a highly microheterogeneous structure, like for the 1,4-dioxane + water mixtures, the monomethyl ethers show stronger interactions with water due to their hydroxyl group. These interactions lead to a strong coupling of the water and glycol ether relaxation at higher concentrations as it is obvious from the long relaxation times observed. The large fluctuation of the local water concentration in case of the dimethyl ethers also explains the difficulties associated with simple models for the correlation of relaxation times comprising the H-bond acceptor density.

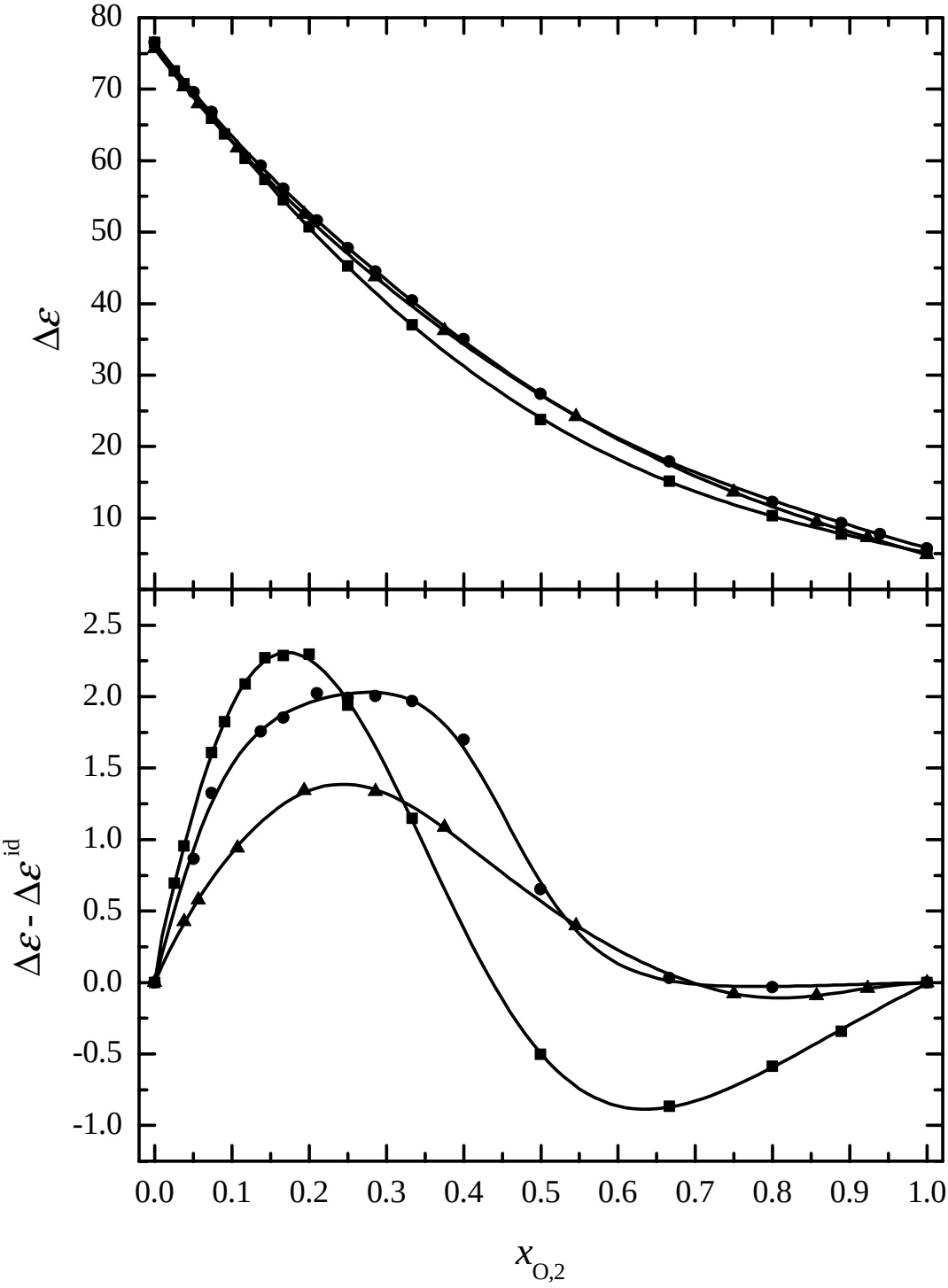

Figure 4.27: Relaxation strength, $\Delta\varepsilon$, and excess relaxation strength, $\Delta\varepsilon - \Delta\varepsilon^{\mathrm{id}}$ for mixtures water(1) + glycol ether $C_1E_nC_1$ (2) at 298.15 K, with (■) $n = 1$, (●) $n = 3$, (▲) $n = 5$.

4.3 Pure triethylene glycol

4.3.1 Introduction

Oligo(ethylene glycol)s have been extensively studied with various experimental methods, including DRS techniques[139]. They are not only of great industrial importance, but can also serve as model systems to investigate the properties of the hydrophilic parts of nonionic surfactants.

Due to the hydroxyl groups at both ends of the flexible chain molecule, oligo(ethylene glycol)s are significantly associated in their pure liquid state. In a previous paper[139] it was found that these interactions give rise to a cooperative H-bond reformation process, which is characterized by relaxation times $\sim 300\,\mathrm{ps}$. On shorter timescales, a relaxation process reflecting the "crankshaft motion"of free C-O-C groups was observed.

Thus, as the relaxation processes arise from different physical mechanisms, an investigation of the energy barriers (activation energies) involved should be helpful to get further insights into the dynamics of associated liquids.

4.3.2 Experiment and data

For a former study[23], a polydisperse material of average molecular mass $174\,\mathrm{g\,mol^{-1}}$ was used. This caused some problems with the analysis of the dielectric spectra, because several compounds of various molecular weight contribute to the dielectric spectra. Therefore, pure triethylene glycol was used this time. The material obtained from Fluka (no. 90390, purity 99.9 %, $H_2O\approx 0.06\,\%$) did not require any further purification.

Dielectric data of pure triethylene glycol were determined in 10 K steps from 278.15 K to 338.15 K by means of waveguide IF (8.5-89 GHz at 298.15 K, otherwise 13-89 GHz), VNA-reflectometry and TDR measurements. Air, a mercury short and DMA/DMF were used as references for the VNA calibration and all data were corrected with a Pade $P_{1/1}$ approximation (air, BN, DMA/DMF). The corrected data obtained from DMA and DMF measurement series were found in close agreement and averaged.

The combined spectra, both real ($\varepsilon'(\nu)$) and imaginary part ($\varepsilon''(\nu)$) of the complex dielectric permittivity, are presented in Fig. 4.28. These spectra can also be used for an evaluation of systematic errors involved in the measurement of the dielectric properties using various techniques. The VNA-R results, especially the ε'' values, were found somewhat higher than those determined by waveguide interferometry at $\nu \gtrsim 8\,\mathrm{GHz}$. As interferometry is regarded to be a rather accurate method, this deviation might be ascribed to imperfections of the VNA probe model, which was optimized for samples of higher permittivity. Larger deviations exist for the TDR data $\varepsilon''(\nu)$ for $\nu \gtrsim 1\,\mathrm{GHz}$, which are presumably of similar origin, namely, the cut-off cell reflectivity model. However, the overall errors are relatively small and the data can thus be assumed to be well-established due to the use of experiments based on completely different instruments and techniques.

For the analysis, the complex dielectric spectra were fitted by a relaxation model comprising four Debye equations (4D model) up to a temperature of 328.15 K, see Tab. 4.12. At 338.15 K, a sum of three Debye equations provides an accurate description of the spectrum,

whereas no convergence of the fit could be achieved with the 4D model.
A more detailed discussion of other models can be found elsewhere[139,152].

Table 4.12: Relaxation parameters, ε_j, τ_j (in ps), and reduced error function χ^2_r for pure triethylene glycol. Superposition of four (278.15-328.15 K) or three (338.15 K) Debye-type equations.

T/K	$\varepsilon^\star$	ε_1	τ_1	ε_2	τ_2	ε_3	τ_3	ε_4	τ_4	ε_∞	$10^3\,\chi^2_r$
278.15	25.66	25.80	789	10.9	200	5.91	29.5	3.90	2.72	3.27	1.480
288.15	24.30	24.25	495	12.3	162	6.25	25.9	3.98	2.58	3.23	1.747
298.15	23.03	23.02	301	12.3	112	6.22	20.6	3.97	2.02	3.11	(11.67)
308.15	21.84	21.84	194	11.7	78.5	6.46	17.9	3.98	1.65	3.06	1.011
318.15	20.73	20.87	124	10.6	51.4	6.48	15.0	3.98	1.38	2.99	1.675
328.15	19.68	19.87	82.6	9.42	36.3	6.74	13.9	4.01	1.61	3.07	2.217
338.15	–	19.10	59.2	8.66	17.4	–	–	4.30	2.22	3.19	5.081

* interpolated[153].

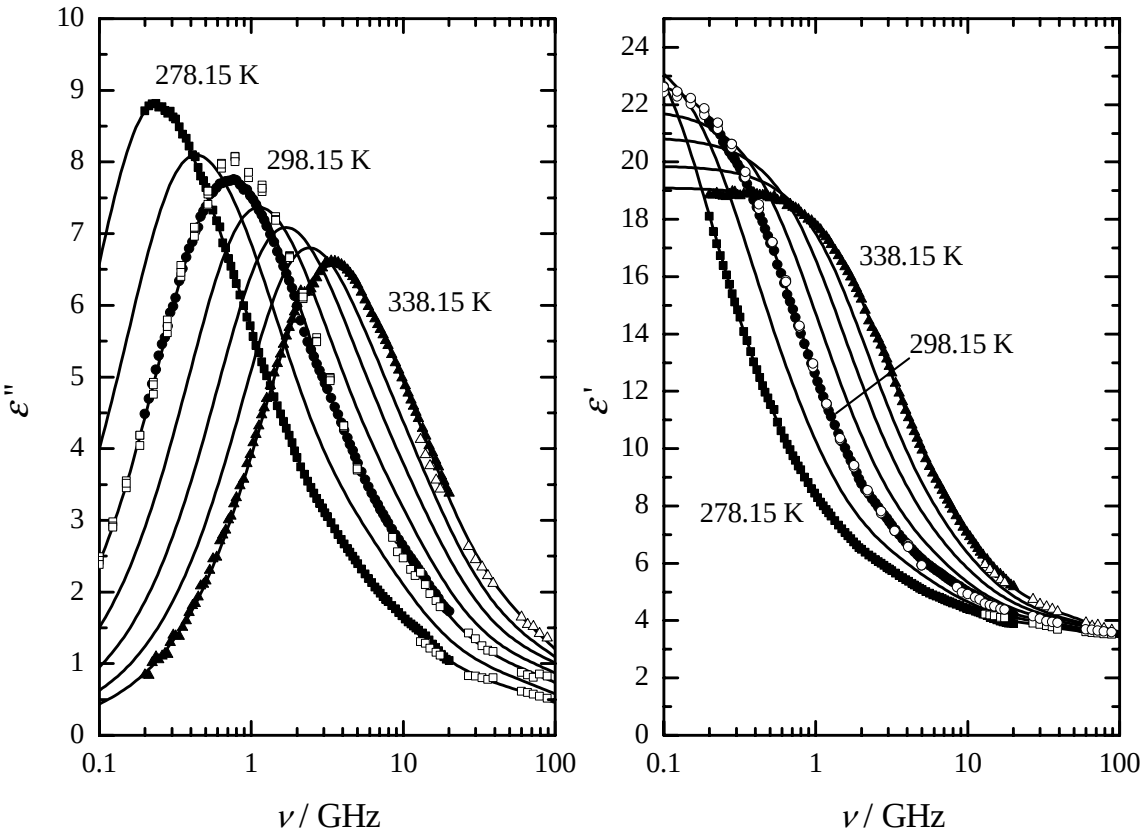

Figure 4.28: Complex dielectric permittivity spectra of pure triethylene glycol. Full symbols: VNA data, open symbols: IF data (IF+TDR at 298.15 K). Lines show fits using a superposition of three (338.15 K) and four (other temperatures) Debye equations.

4.3.3 Results and discussion

The effect of chain length on the dynamics of oligo(ethylene glycol)s in their pure liquid state was already discussed in detail elsewhere[139]. It was found that the 4D model allows a self-consistent assignment of the resolved dispersion steps to the inter- and intramolecular dynamics of the samples. The two modes at lower frequencies (τ_1, τ_2) could be attributed to cooperative intermolecular interactions and the dynamics of ether oxygens involved as acceptors in hydrogen bonds, whereas the modes (S_3, τ_3) and (S_4, τ_4) were assigned to "crankshaft-like"motions of C-O-C groups and the reorientation of OH-groups not incorporated into hydrogen bonding.

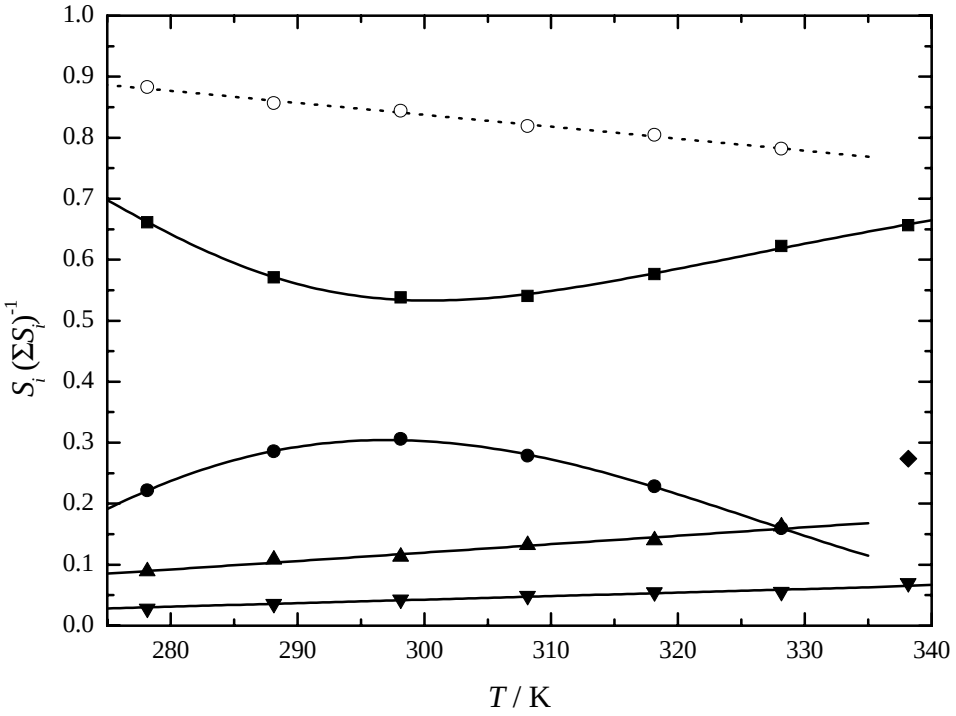

Figure 4.29: Temperature dependence of the normalized relaxation amplitudes of the Debye contribution i (■: $i = 1$; ●: $i = 2$; ▲: $i = 3$; ▼: $i = 4$), of pure triethylene glycol. At 338.15 K, values from a 3D fit are shown ($i = 2$: ♦). Symbols (∘, dotted line) represents the normalized sum of the amplitudes S_1 and S_2.

With increasing temperature, one would expect some changes in the relative contribution of the relaxation modes to the overall dielectric response. Namely, the amount of hydrogen bonding should decrease and the density of non-interacting dipolar groups is expected to increase. The evaluation of our measurements revealed normalized relaxation amplitudes that exactly fit into this picture. Fig. 4.29 clearly shows that the sum contribution of the processes (S_1, τ_1) and (S_2, τ_2) decreases almost linearly with increasing temperature. As these processes were assigned to H-bond interaction, a weakening of the H-bond network might be concluded. The analysis of the individual processes, which show minimum and maximum values, respectively, at around 300 K, is not straightforward. The values of the

relaxation times, τ_1 and τ_2, which differ only by a factor < 3, suggest a rather strong coupling of both dynamic modes. Additionally, mathematical artifacts of the fitting procedure might also have significant effects on the results. For the same reason, the data at 338.15 K were left out of consideration, as the low amplitude of the (S_2, τ_2) did not allow a separation of the spectrum by the 4D model.

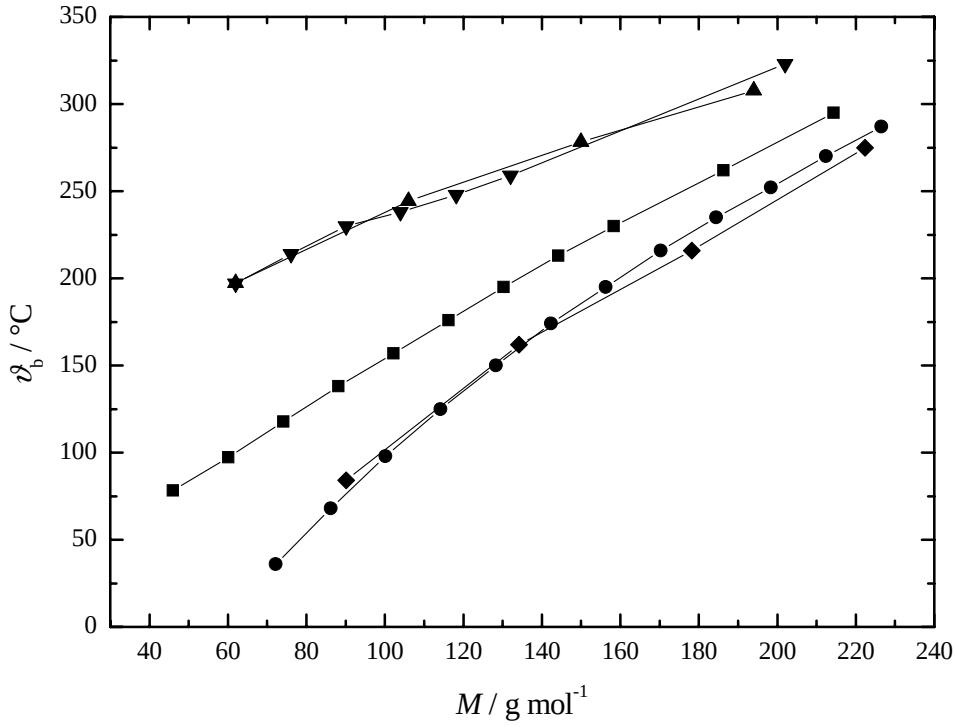

Figure 4.30: Boiling points, ϑ_b, of various homologous series of oligo(ethylene glycol)s (▲), terminal n-diols (▼), n-alkanols (■), n-alkanes (•), and oligo(ethylene glycol) dimethyl ethers (◆)[154–157]. All values at 1013.25 hPa.

On the other hand, the reduced H-bond interactions with increasing temperatures allows a larger number of dipolar groups (both C-O-C and -C-O-H segments) to contribute to the dielectric response of "free"groups, the (τ_3) and (S_4, τ_4) modes.
Moreover, the relatively small changes of the contributions are in line with the strong association of these liquids even at elevated temperatures, which is obvious from their high boiling points compared with related compounds, Fig. 4.30.

Table 4.13: Arrhenius parameters for relaxation processes (S_i; τ_i), $i = 1..4$, of pure triethylene glycol. Fits include τ_i data from 278.15-328.15 K (338.15 K for $i = 1$).

i	$\frac{E_a}{\mathrm{kJ\,mol^{-1}}}$	$\ln(\tau_0/\mathrm{s})$
1	34.5 ± 0.4	-35.84 ± 0.17
2	26.6 ± 1.7	-33.71 ± 0.67
3	12.0 ± 0.6	-29.43 ± 0.23
4	10.3 ± 2.0	-31.06 ± 0.81

Further insights into the dynamics of liquid oligo(ethylene glycol)s can be obtained from the relaxation times, Fig. 4.31, as these provide information on the energy barriers (activation energies) of the physical processes involved. Several methods can be used for the calculation of activation energies, which are all based on different assumptions concerning the reaction mechanism. Here, the well-known Arrhenius equation, Eq. 2.93, was employed. While we want to leave the frequency factors, τ_0, which cannot be interpreted in an straightforward way, out of consideration, the activation energy parameter, E_a, reveals similar values for the first and second process, whereas those of the (S_3, τ_3) and (S_4, τ_4) modes were found significantly smaller. This observation points out the high strength of H-bond interactions compared with the energy barriers needed for reorientation of non-bonded chain segments or of free C-O-H groups at the end of a glycol molecule chain. Some estimates of a gauche-gauche conformational transition of oligo(ethylene glycol) chain segments can be obtained from semiempirical calculations[152] as well as from NMR experiments[158] and were found in the order of $17-18\,\mathrm{kJ\,mol^{-1}}$, not far from a weighted average of the the activation energies of the τ_2 and τ_3 processes ($\sim 23\,\mathrm{kJ\,mol^{-1}}$).
Thus we want to conclude that the four Debye model is applicable for the description of the relaxation behavior of triethylene glycol over a wide temperature range. The two contributions at lower frequencies, characterized by relaxation times, τ_1 and τ_2, seem to be closely coupled, as it is also reasonable from their physical origin. The sum of the relative amplitude of these modes decreases with increasing temperature, and the (S_2, τ_2) process almost vanishes at temperatures $T \gtrsim 335\,K$. In contrast to this, the amount of free, i. e. not hydrogen-bonded groups shows an increase with temperature, reflecting a change in the dynamics of the liquids from intermolecular to intramolecular motions, which are characterized by lower activation energies compared with those incorporating H-bond interactions.

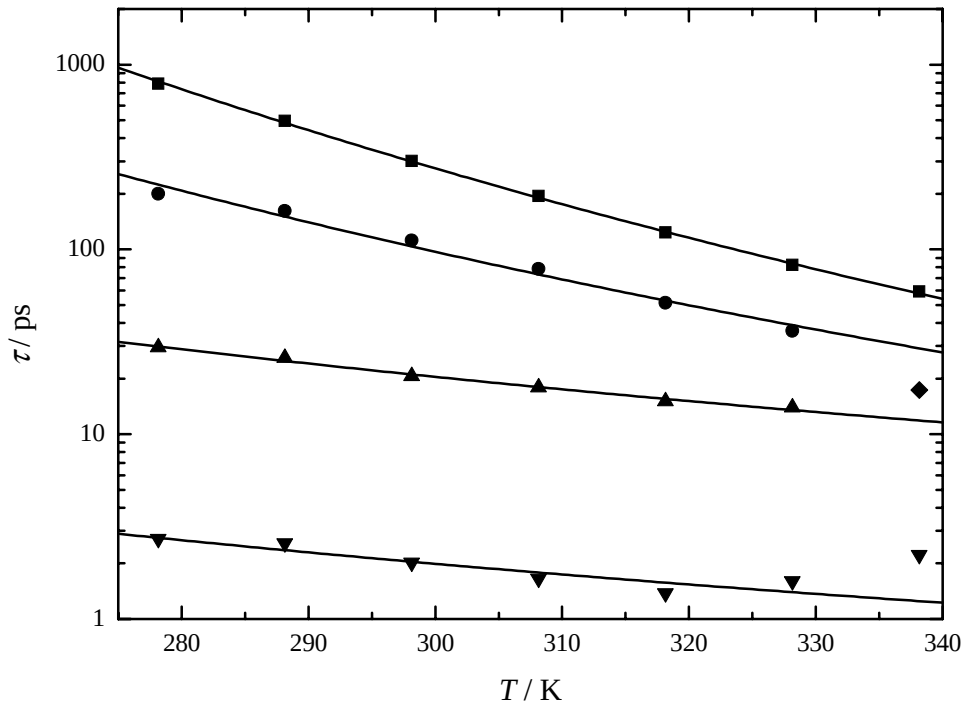

Figure 4.31: Temperature dependence of the relaxation times, τ_i (■: $i = 1$; ●: $i = 2$; ▲: $i = 3$; ▼: $i = 4$), of pure triethylene glycol. At 338.15 K, values from a 3D fit are shown ($i = 2$: ♦).

Chapter 5

The non-ionic surfactant system C12E5 + water

5.1 The phase behavior of non-ionic surfactants

For non-ionic surfactant systems, a large variety of phases, both isotropic and liquid-crystalline, have been observed[159–161]. These phases reflect the various ways, how polar and apolar regions can be separated by interfacial regions, which contain surfactant molecules. In a simple micellar solution, discrete polar regions exist, whereas in lamellar phases, the polar and apolar layers extend in two dimensions. Additionally, these aggregates can form higher ordered structures, like bilayers or vesicles. This self-organization process has large implications for biology and life sciences.
The phase diagram of the $C_{12}E_5$ + water binary system studied here is shown in Fig. 5.1[161]. According to the notation of Tiddy[162], L_1, L_2 and L_3 denote micellar, reverse micellar and dilute micellar isotropic liquid phases. L_α is the lamellar phase, V and H are cubic and hexagonal liquid crystalline phases, respectively. The region, where isolated surfactant monomers exist in aqueous solution (critical micellar concentration, cmc) is located at very low surfactant content ($\sim 3 \cdot 10^{-5}$ volume fraction[161]) and is therefore not shown in Fig. 5.1.

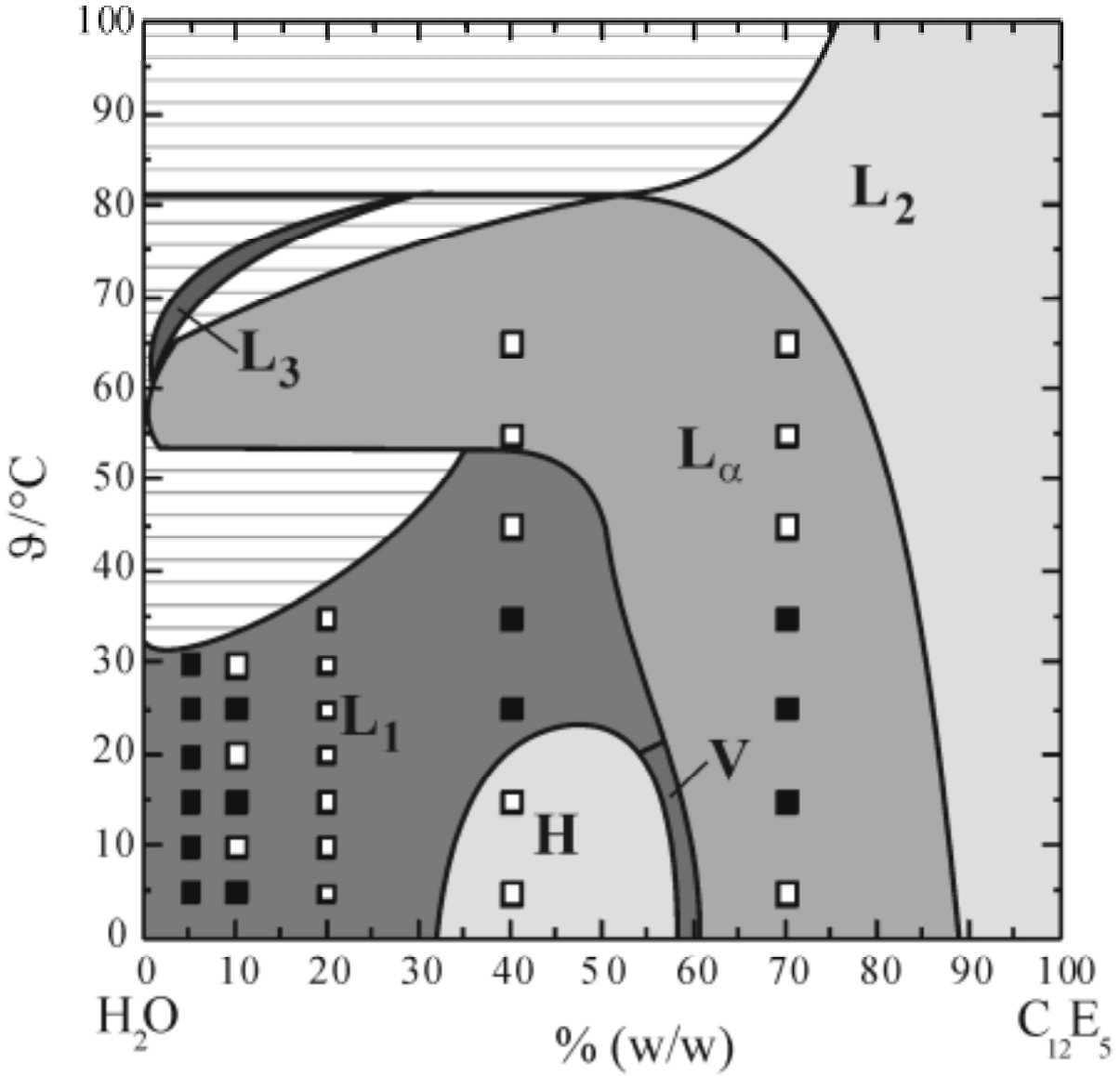

Figure 5.1: Phase diagram of the system water + $C_{12}E_5$. Black squares (■) indicate points of measurement VNA+IF, at thermodynamic conditions (□) only VNA data were obtained (see text)[161].

5.2 Experimental and data analysis

5.2.1 Materials

For all experiments, $C_{12}E_5$ with a purity of $> 99.8\,\%$ (GC) from Nikkol, Japan was used. All solutions were prepared from degassed materials 2-3 days before use and kept at the temperature of measurement for equilibration. Some of the higher concentrated solutions had to be stored for several days and were therefore kept under nitrogen in the dark.
Note that the surfactant, both in the pure liquid state and in aqueous solution shows significant degradation especially when exposed to air. Decomposition manifests in large changes of the cloud point (decrease of several K).
Recovery of the pure surfactant from used solutions is possible by liquid/liquid extraction with methylene chloride, careful drying with anhydrous sodium sulfate and purification using a high-vacuum molecular distillation apparatus at $\sim 10^{-6}$ mbar.
The densities of the binary mixtures necessary for the calculation of molar concentrations could not be determined for all mixtures and at all temperatures studied due to the high price of the material. Additionally, most of the samples show high viscosity which makes these measurements very tedious because of the inclusion of small air bubbles. Fortunately, the density of the pure surfactant (ρ_2^0) is known from literature[163] between 25 and 50 °C and is well described within the required accuracy by

$$\rho_2^0(T) = [991.66 - 0.99 \cdot (T/\mathrm{K} - 273.15)]\ \mathrm{kg\,m^{-3}}. \tag{5.1}$$

Below $\sim 25\,^\circ$C, pure $C_{12}E_5$ is a waxy solid, therefore the density values were extrapolated using the given equation.
Assuming ideal mixing behavior, the densities, ρ, of binary water/$C_{12}E_5$ mixtures were then calculated by Eq. 5.2,

$$\rho = \frac{1}{\frac{1}{\rho_1^0} + w\,(\frac{1}{\rho_2^0} - \frac{1}{\rho_1^0})}, \tag{5.2}$$

where ρ_1^0 is the density of pure water[66] and w the weight fraction of the surfactant. To check the applicability of this method, densities of two solutions containing 10% $C_{12}E_5$ in light and heavy water were determined with high accuracy at 298.15 K. The measured values (996.08 and $1091.88\,\mathrm{kg\,m^{-3}}$) were found somewhat higher but in close agreement with those calculated by use of Eq. 5.2, 993.94 and $1088.95\,\mathrm{kg\,m^{-3}}$, respectively. The small deviation of $\sim 0.25\%$ indicates a small negative molar excess volume for both solutions which can be neglected for the intended purpose.

5.2.2 Viscosimetry

During the experiments, an interesting behavior of the dynamic viscosity of $C_{12}E_5$ solutions was observed. The L_1 and L_2 phases are liquids of low viscosity, whereas the lamellar L_α phase has a viscosity which is several orders of magnitude higher. The hexagonal liquid crystalline phase is a waxy, semi-solid substance.
The measurements given here where performed on solutions of 5 % $C_{12}E_5$ in water, with a rotational viscosimeter, see Chap. 3.2.3. A cone of 0.8 ° slope (CP40) was used. The shear rate was first increased to the maximum speed and then decreased with proper time steps between subsequent readings. As already described for similar compounds in the literature[164,165], with increasing temperature the viscosity increases, Fig. 5.2. This is attributed to a temperature dependent change of the micelle shape and intermicellar interactions. At lower temperatures (and concentrations), the isotropic aqueous solutions consist of almost spherical micelles that grow to rodlike aggregates at higher temperatures. From a certain length on, micelles interconnect and form a three dimensional network structure[166]. This structure is governed by fast dynamics and resembles aqueous polymer solutions[165], although the latter consist of chains of covalently bound monomers.
In order to get some information about the characteristic time of the network formation process, viscosity measurements were performed up to relatively high shear rates ($1300 - 1800\,s^{-1}$), Fig. 5.3. Within the limits of the experiment, no shear rate dependence of the dynamic viscosity could be found. Therefore, the (mechanical) relaxation time is below the ms timescale, at least for the concentration discussed here. The slight decrease of the viscosity during the experiment observed at higher temperatures (Fig. 5.3) can be attributed to artifacts arising from small air bubbles generated by the fast rotation of the cone, which become more important at higher viscosities.

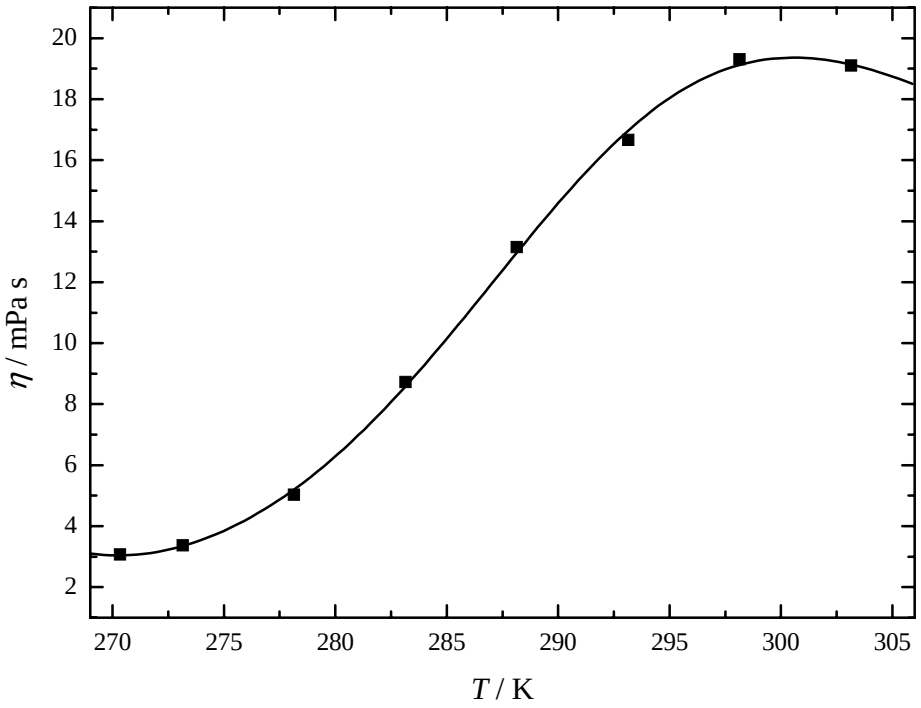

Figure 5.2: Viscosity, η, of an aqueous $C_{12}E_5$ solution as a function of temperature, T.

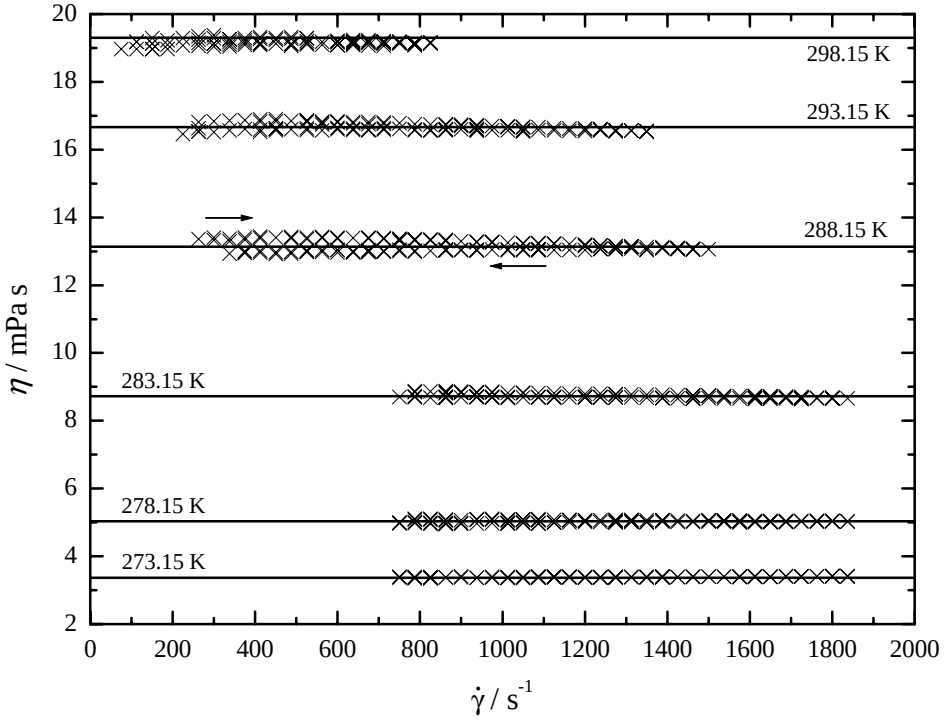

Figure 5.3: Viscosity, η, of an aqueous $C_{12}E_5$ solution as a function of shear rate, $\dot{\gamma}$, at different temperatures.

5.2.3 Dielectric measurements

Using VNA, TDR and IF techniques, the frequency dependent complex dielectric permittivity was determined at various thermodynamic state points of the binary $C_{12}E_5$ + water system, Fig. 5.1. Several experimental problems are associated with these measurements, namely, the high viscosity of the surfactant solutions and the volatility of water at elevated temperatures. As the TDR and IF instruments are designed for liquids of low viscosity, elaborated filling procedures are needed to provide a properly filled cell. Additionally, a single IF measurement at e.g. five spot frequencies within one waveguide band takes at least 2 hours, leading to a significant concentration change due to water loss at temperatures $> 40\,^{\circ}\mathrm{C}$. Thus, no data of sufficient reproducibility and accuracy could be obtained within this region of the phase diagram.

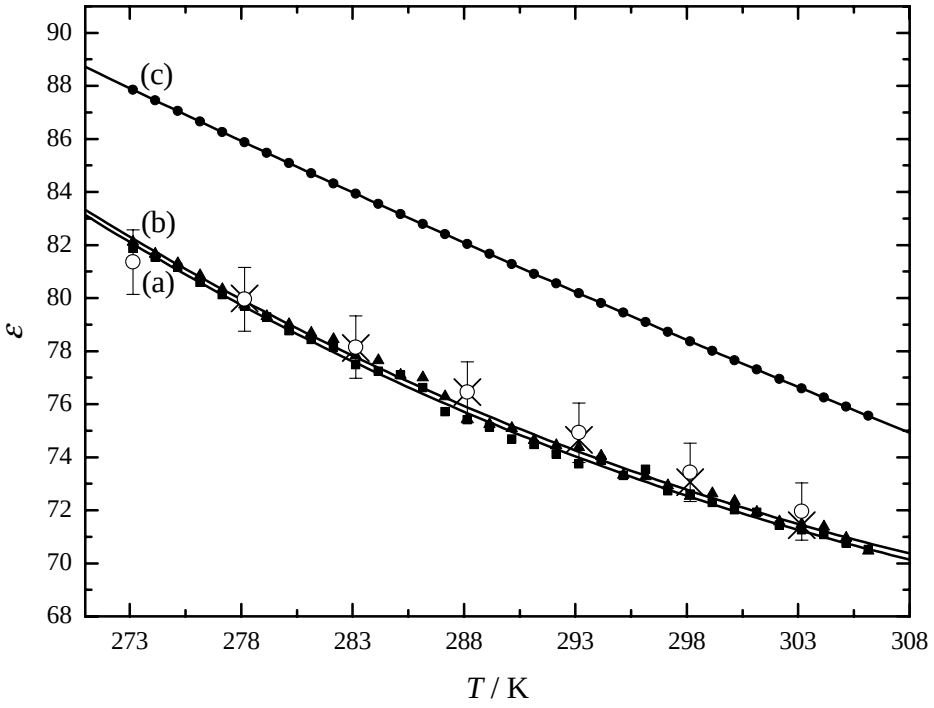

Figure 5.4: Static dielectric permittivity, ε, of aqueous $C_{12}E_5$ solutions (0 mmol KCl; ■, a) and (2.5 mmol KCl; ▲, b), at a surfactant weight fraction $w = 0.05$. Also shown are the values for pure water, (•, c)[167].(×) are values extrapolated from VNA+IF and (∘) from TDR+IF measurements for comparison. Error bars indicate 1.5 % of the measured value.

Most of the measurements performed are limited to 200 MHz at the low frequency side of the spectrum. To rule out any additional relaxation region that might arise from a Maxwell-Wagner related effect below this point, the static permittivity of an aqueous $C_{12}E_5$ solution (5% w/w) was determined with an impedance spectrometer, see Chap. 3.1.1, and compared with results extrapolated from VNA, TDR and IF measurements, Fig. 5.4. Within the accuracy limits of the instruments, no evidence could be found for

any additional low-frequency contributions to the dielectric spectrum.
Relaxation processes in microheterogeneous materials can be caused by charge transport phenomena. Thus small amounts of potassium chloride were added to the solution, but the static permittivity remained unchanged. The insignificantly higher results can be explained by systematic errors of the impedance spectrometer and contributions from electrode polarization effects at the low frequencies used (1-400 kHz).
For the analysis of the dielectric spectra, we want to focus on the samples with a weight fraction $w \leq 0.20$ first. When $C_{12}E_5$ is added to pure water the dielectric spectra show a distinct broadening towards lower frequencies and can be decomposed into two contributions, both described by a Debye-type relaxation process. Fig. 5.5, which shows normalized dielectric loss spectra, $f^{\mathrm{T}}\,\varepsilon''(\nu)$, for better comparison of the spectra, clearly supports this relaxation model.

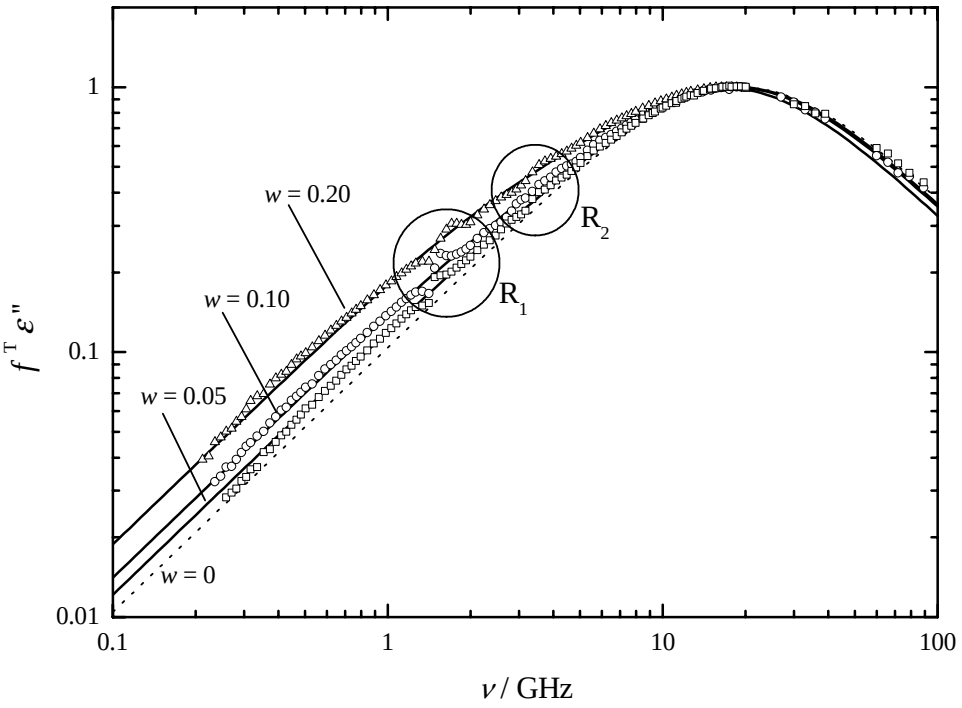

Figure 5.5: Normalized dielectric loss, $f^{\mathrm{T}}\varepsilon''$, of aqueous $C_{12}E_5$ solutions at different weight fractions, w. The dotted line shows data of pure water. All values at 298.15 K.

For a quantitative interpretation of the dielectric spectra, accuracy of the data is a crucial factor, because of the small difference of sample spectra compared with pure water, Fig. 5.6. Commercial instruments which are only available for the VNA-R technique at microwave frequencies, provide an accuracy of ε' and ε'' in the order of several percent[168], which is not satisfactory for the purpose of this study. Thus, the use of well established reference materials is of high importance, especially with regard to the liquid standard and the short[169].
Within two small frequency bands of the VNA measurements, characteristic signatures,

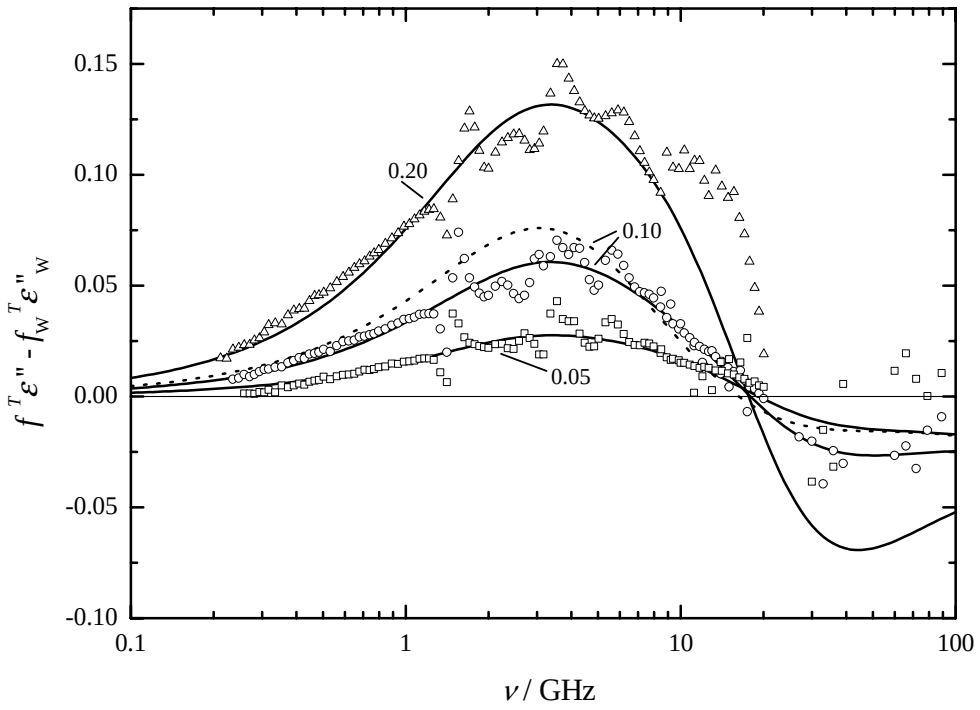

Figure 5.6: Difference dielectric loss spectra of aqueous $C_{12}E_5$ solutions and pure water. Full lines indicate values calculated from fitted curves, after rescaling to a maximum value of the dielectric loss $\varepsilon''(\nu)_{\max} = 1$. The actually measured data at various weight fractions of surfactant, w, are also shown (□: $w = 0.05$, ○: $w = 0.10$, △: $w = 0.20$). The dotted line represents results for the D_2O solution, $w = 0.10$.

R_1 and R_2, arising from reflections at the sample/air interface were noticed, Fig. 5.5. These are more pronounced for samples of higher permittivities, especially for the calibration measurement using pure water as a reference. Although the Padé correction method enables us to get rid of most of these distortions, they cannot be fully eliminated.

Further improvement of the accuracy of the measurements might be possible by using a non-conductive material of high loss for the sample cell, instead of stainless steel. The material of choice is a graphite filled PTFE compound, which also shows a sufficiently high thermal conductivity to ensure proper temperature control of the liquid under test. However, this subject requires further testing.

Unfortunately, more accurate measurements by waveguide interferometry below 27 GHz were not possible due to the limited amount of material available and the high viscosities of the solutions. However, for some samples ($w = 0.05$, $w = 0.10$, $w = 0.40$, $w = 0.70$ at 298.15 K) the VNA-R results were checked for systematic deviations by comparison with TDR, X (only for $w = 0.05$) and Ku-band interferometric data.

As all values obtained by different methods were found in good agreement within the experimental error ($\sim 1 - 2\,\%$), the data were fitted by well-established procedures, see Chap. 2.3.5. The relaxation parameters for the samples with $w \leq 0.2$ are all summarized

Table 5.1: Relaxation parameters, ε_j, τ_j (in ps), and reduced error function χ^2_r of water + $C_{12}E_5$ mixtures. Superposition of two Debye-type equations.

w	T/K	ρ/kg m^{-3}	ε_1	τ_1	ε_2	τ_2	ε_∞	$10^3\,\chi^2_r$
0.05	278.15	999.3	79.98	72.2	77.22	14.8	6.07	52.0
0.05	283.15	998.8	78.13	67.3	75.80	12.6	5.90	29.3
0.05	288.15	998.0	76.42	63.7	74.26	11.0	5.86	56.2
0.05	293.15	996.9	74.67	58.8	72.83	9.64	5.90	39.8
0.05	298.15	995.5	73.09	51.9	71.31	8.42	5.71	96.9
0.05	303.15	993.9	71.60	47.7	70.04	7.55	5.79	50.1
0.10	278.15	998.6	74.29	75.1	69.54	15.1	5.99	38.2
0.10	283.15	997.9	72.56	68.9	68.47	12.9	5.97	18.3
0.10	288.15	996.8	71.08	59.8	67.00	11.2	5.84	63.8
0.10	293.15	995.5	69.42	55.3	65.86	9.81	5.76	22.9
0.10	298.15	993.9	67.95	48.6	64.47	8.59	5.57	64.7
0.10	303.15	992.2	66.52	46.9	63.57	7.70	5.40	26.3
0.20	278.15	997.3	63.90	85.7	56.64	16.2	6.27	34.5
0.20	283.15	996.1	62.51	76.8	55.89	13.9	6.19	34.0
0.20	288.15	994.6	61.28	68.1	55.04	12.0	6.02	39.9
0.20	293.15	992.8	59.86	61.8	54.16	10.6	6.06	36.3
0.20	298.15	990.9	58.62	55.0	53.21	9.29	5.94	43.8
0.20	303.15	988.7	57.28	49.5	52.12	8.35	5.90	34.6
0.20	308.15	986.4	55.76	43.7	50.70	7.32	5.88	39.1

Table 5.2: Relaxation parameters, ε_j, τ_j (in ps), and reduced error function χ^2_r of heavy water + $C_{12}E_5$ binary mixtures. Superposition of two Debye-type equations.

w	T/K	ρ/kg m^{-3}	ε_1	τ_1	ε_2	τ_2	ε_∞	$10^3\,\chi^2_r$
0.10	278.15	1092.5	72.94	83.0	66.50	19.9	5.79	38.8
0.10	283.15	1092.2	71.24	73.7	65.78	16.9	5.88	21.3
0.10	288.15	1091.4	69.69	60.6	64.04	14.2	5.44	64.3
0.10	293.15	1090.4	68.05	54.7	63.18	12.4	5.49	24.7
0.10	298.15	1088.9	66.63	46.0	61.52	10.6	5.19	76.4
0.10	303.15	1087.2	65.19	44.3	60.97	9.51	5.00	28.1

in Tab. 5.1. The data of samples prepared from $C_{12}E_5$ and heavy water (D_2O) are listed in Tab. 5.2.
At the higher concentrations, $w = 0.40$ and $w = 0.70$, the relaxation model comprising two Debye-type equations is not sufficient for an adequate description of the complex dielectric spectra. Therefore, we investigated other relaxation models, namely combinations of a Cole-Davidson + Debye term, a sum of three Debye equations (3D) and a Cole-Cole + Debye model (CC+D). While no stable fits could be obtained with models incorporating a Cole-Davidson equation, the 3D and CC+D models can be used for a proper description of the complex dielectric spectra. In contrast to the 3D model, which did not always result in physically reasonable values (especially the relaxation times τ_1 were often found very large), the CC+D model is quite useful and could be successfully applied to all spectra of samples with a $C_{12}E_5$ weight fraction of $w = 0.40$ and $w = 0.70$.

Table 5.3: Relaxation parameters, ε_j, τ_j (in ps), distribution parameter, α, and reduced error function χ^2_r of water + $C_{12}E_5$ mixtures. Superposition of a Cole-Cole ($j = 1$) and a Debye ($j = 2$) term.

w	T/K	ε_1	τ_1	α	ε_2	τ_2	ε_∞	$10^3\,\chi^2_r$
0.40	278.15	47.5	44.75	0.19	23.8	19.07	4.72	2.89
0.40	288.15	45.5	28.36	0.22	21.5	14.17	4.22	1.74
0.40	298.15	43.7	21.19	0.24	21.4	10.67	3.87	10.1
0.40	308.15	40.7	19.86	0.21	23.2	7.90	4.51	4.46
0.40	318.15	38.4	18.42	0.21	24.5	6.68	5.25	1.85
0.40	328.15	32.7	20.37	0.15	24.0	5.54	7.36	2.54
0.70	278.15	22.6	92.37	0.23	4.8	30.41	3.45	2.48
0.70	288.15	20.6	56.15	0.23	5.1	21.97	3.47	3.09
0.70	298.15	19.3	35.53	0.23	5.1	16.38	3.40	3.52
0.70	308.15	17.9	28.08	0.23	6.3	12.66	3.62	7.01
0.70	318.15	17.0	24.10	0.21	7.3	10.12	4.16	2.22
0.70	328.15	16.6	19.56	0.19	7.9	8.28	4.17	2.38
0.70	338.15	15.7	16.59	0.15	7.5	6.88	4.64	3.63

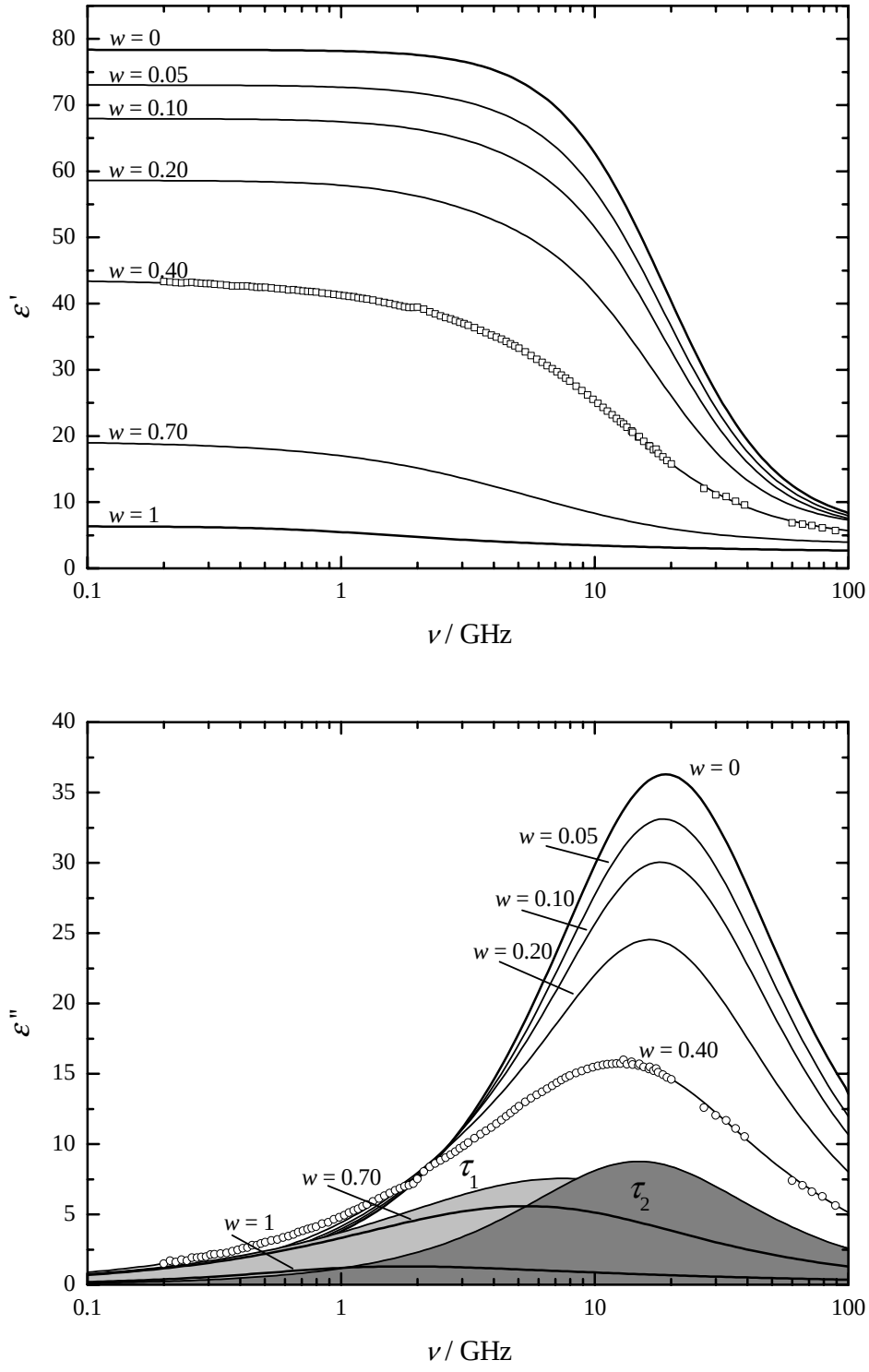

Figure 5.7: Real an imaginary part, ε' and ε'', of the complex dielectric permittivity as a function of the frequency, ν. All data were obtained at 298.15 K from aqueous $C_{12}E_5$ solutions of surfactant weight fraction w. Data of neat $C_{12}E_5$ are from a supercooled liquid sample.

5.3 Results and discussion

In literature, measurements of the static and low-frequency dielectric permittivity were frequently used for the investigation of surfactant-based systems, such as micellar solutions, microemulsions[170] and liquid crystalline mesophases, and for studies of colloidal dispersions[171], including biological materials[172]. The interpretation of these data is mainly based on mixture theories to predict the dielectric properties from a microscopic model. While interfacial polarization effects present at relatively low frequencies can be used for an analysis of the data[173,174] of samples with at least one conductive phase, these are not present in the case of non-ionic surfactant solutions which show no significant dielectric loss up to several MHz. Furthermore, an evaluation of non-ionic systems by means of static mixture models requires an exact knowledge of the structure and the geometrical features as well as assumptions for the dielectric properties of the microregions, which consist of at least 3 phases: oil core, interface region and bulk water. So it seems that static and low frequency (i.e. data at $\nu < 100\,\mathrm{MHz}$) dielectric permittivities are not very helpful for the investigation of non-ionic surfactant systems, as these properties are not sensitive enough to variations in the water-surfactant interaction. Additionally, static models cannot be regarded as adequate for a more detailed description of surfactant systems, which are governed by delicate dynamic effects on a broad timescale, a fact that is clearly revealed by the numerous and often conflicting models proposed in literature.

As this study wants to gain further insights into the cooperative dynamics associated with the hydrogen bond interactions in aqueous solutions, we want to discuss the dielectric properties of these liquids at microwave frequencies now. Former dielectric studies on ionic surfactant systems[17] as well as on binary mixtures of water + various oligomeric models of the hydrophilic moieties of non-ionic surfactant revealed specific information about the cooperative dynamics of H-bond network rearrangement processes, which is largely affected by the presence of the organic compounds. In the case of aqueous solutions of $C_{12}E_5$ we want to use these characteristic changes in water relaxation dynamics to distinguish between water located at different sites within the microstructure of the system.

The terms "bound"and "free"water are often used in the literature to describe the presence of water participating in different kinds of interactions[175]. This is somewhat misleading, as the interaction strength of water with the hydrophilic part of a non-ionic surfactant molecule is likely to be smaller compared with that of a water-water hydrogen bond. Therefore, a rapid exchange of water molecules between both states has to be assumed and there are other factors, which are even more important for the structural and dynamic properties of strongly associated liquids. It was already pointed out for the mixtures of water with oligomeric model compounds, which do not show micellar aggregation that the availability (i.e. the concentration and microscopic mobility) of an interaction site incorporated in the cooperative relaxation of a water-rich cluster determines the dynamics of the hydrogen bond network reformation over a broad concentration range.

Let us now focus on the results of this study at the lower surfactant concentrations. There, micellar hydration can be expected to be rather constant as long as the surfactant concentration is low and interfacial regions are separated by distances long enough to allow an undisturbed relaxation of water like in the bulk liquid state. It was already pointed

out that these solutions can be very well described by a superposition of two Debye equations. The contribution at low frequencies (S_1, τ_1) increases with increasing surfactant weight fraction, w, whereas the amplitude of the second Debye term (S_2, τ_2) decreases. The relaxation time of the second process is very similar to that of pure water and obeys the same temperature dependence, see Fig. 5.8. Therefore, the same mechanism as in pure water is supposed to cause this process. This assumption is further confirmed by the results obtained for a solution of 10% $C_{12}E_5$ in heavy water (D_2O). Heavy water in its pure liquid state shows a considerably larger relaxation time, τ_w, compared with light water[57] and the same applies to the (S_2, τ_2) process found for the surfactant solution. Furthermore, a very similar ratio $\tau_2/\tau_w \approx 1.03$ was found, see Fig. 5.8. This indicates large water-continuous domains. Within these regions, the cooperative relaxation mode of water is almost unaltered by the presence of surfactant micelles. The concentration of monomeric surfactant molecules present in bulk water domains is very low ($\sim$ CMC) and cannot cause any significant contribution to the dielectric spectra.

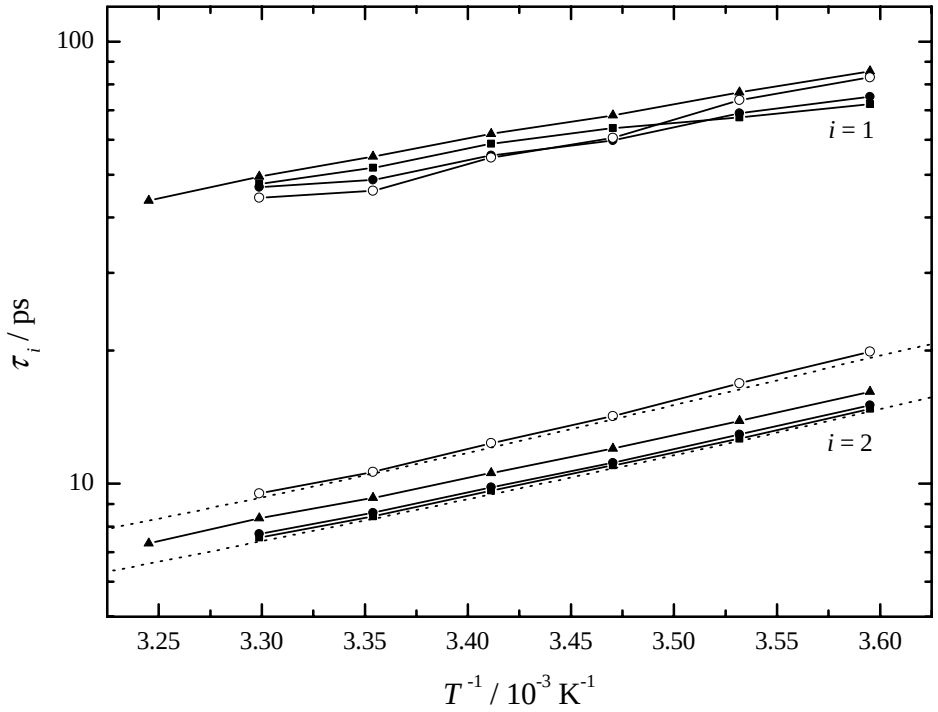

Figure 5.8: Relaxation times, τ_1 and τ_2, calculated by fitting a sum of two Debye-type equations to the complex dielectric spectra of aqueous $C_{12}E_5$ solutions of weight fraction w, shown as a function of the reciprocal absolute temperature, $1/T$ (■: $w = 0.05$, ●: $w = 0.10$, ○: $w = 0.10$ (D_2O), ▲: $w = 0.20$). The dotted lines represent the relaxation times, τ_w, observed for the cooperative mode of pure liquid water (D_2O: upper line, H_2O: lower line).

Concerning the analysis of the dielectric spectra of the samples, we have to consider that a rising amplitude of the first process leads to a higher accuracy of the fits with increasing surfactant concentration. On the other hand, some contributions from dipole relaxation

of oligo(ethylene glycol) chain segments of $C_{12}E_5$ may arise. However, due to the low dielectric constant of the pure surfactant ($\varepsilon \approx 6.5$ at 298.15 K), these are only small.
Figure 5.8 clearly indicates that the process (S_1, τ_1) shows no isotope effect. Additionally, no significant increase of the relaxation time τ_1 was found up to $w = 0.10$ and for a weight fraction of $w = 0.20$ the values are only slightly higher. Therefore we assume that the dynamics of the water molecules causing this relaxation process is governed by the hydrophilic surfactant headgroups. The (S_1, τ_1) process is characteristic for water at the micellar interface.
It is known from structural investigations by cryo-TEM[176], light[176] and neutron scattering[15,177], and also obvious from our investigation of the temperature dependence of the viscosity that aqueous $C_{12}E_5$ solutions undergo large changes of their topology, ranging from rather small isolated micelles of almost spherical geometry at low temperature and concentrations to networks of branched threadlike micelles.
No major concentration dependence of τ_1 was found. Furthermore, any changes of the relaxation mechanism should result in a different slope of the Arrhenius plot, $\log(\tau_1) = f(T^{-1})$. Fig. 5.8 clearly indicates that this is not the case here, and that similar energy barriers apply to both dielectric contributions. This means that the physical origin of the τ_1 relaxation mode has a lengthscale which is small compared with the size of a micelle. Thus, it can be used as an indicator for changes in the interactions of water with surfactant headgroups. It is unlikely that the τ_1 process is caused only by the presence of hydrophobic sites, as it was assumed for a similar process found for aqueous solutions of cationic surfactants[16,178]. There, the water molecules are characterized by relaxation times ~ 25 ps, whereas $\tau_1 > 50$ ps was found for non-ionic surfactant solutions. Additionally, quite different energy barriers of the (S_1, τ_1) process would be expected.
It has often been suggested in the literature that the phase behavior, especially clouding phenomena, are caused by dehydration of the ethylene oxide chain. In fact, only a few experimental techniques can provide further insights into the hydration behavior, mainly NMR spin-echo[12,179–182] and Raman spectroscopic[8] techniques. Methods comprising probe molecules, like chemical trapping[183] or ESR studies[184] also have been used but are flawed with some inherent problems which we do not want to discuss in detail here.
In any case, these investigations revealed quite conflicting pictures of the structural and dynamic features of oligo(ethylene glycol) alkyl ether surfactants[177]. The interplay of micellar growth, intermicellar attractive interactions and network entropy effects[185] does not allow a more direct investigation of water-headgroup interactions and of the cooperative structure of the bulk water domain from structural or thermodynamic data[176,177].
NMR methods, which were frequently used, can only reveal average water self-diffusion coefficients, and various assumptions are necessary to disentangle contributions from water characterized by different dynamic properties. By means of dielectric spectroscopy, the concentration of water incorporated in the cooperative relaxation mode of the bulk domain can be directly calculated from the analytical water concentration and the amplitude S_2. Assuming a water-rich region large compared to the relaxing cluster, there will be no change in the reaction field factor and effective dipole moment compared with pure liquid water, see Chap. 2.4.2. Using the Cavell equation, Eq. 2.79, and the temperature dependent amplitudes of the cooperative mode of pure water, S_W^0 (Appendix C), we can calculate

the concentration of bulk water, c_{S2}, present in a non-ionic surfactant solution of weight fraction w and density d by

$$c_{S2} = \frac{S_2}{S_{\mathrm{W}}^0} \frac{d_1^0}{M_1}, \tag{5.3}$$

where d_1^0 is the density and M_1 the molecular mass of pure water.
Furthermore, the ratio of water molecules not contributing to the bulk relaxation mode ($n_{\mathrm{W}}^{\mathrm{s}}$) per surfactant molecule of molecular mass M_2 can be obtained as

$$\frac{n_{\mathrm{W}}^{\mathrm{s}}}{n_2} = \left[\frac{(1-w)\,d}{M_1} - \frac{S_2}{S_{\mathrm{W}}^0} \frac{d_1^0}{M_1} \right] \frac{w\,d}{M_2}. \tag{5.4}$$

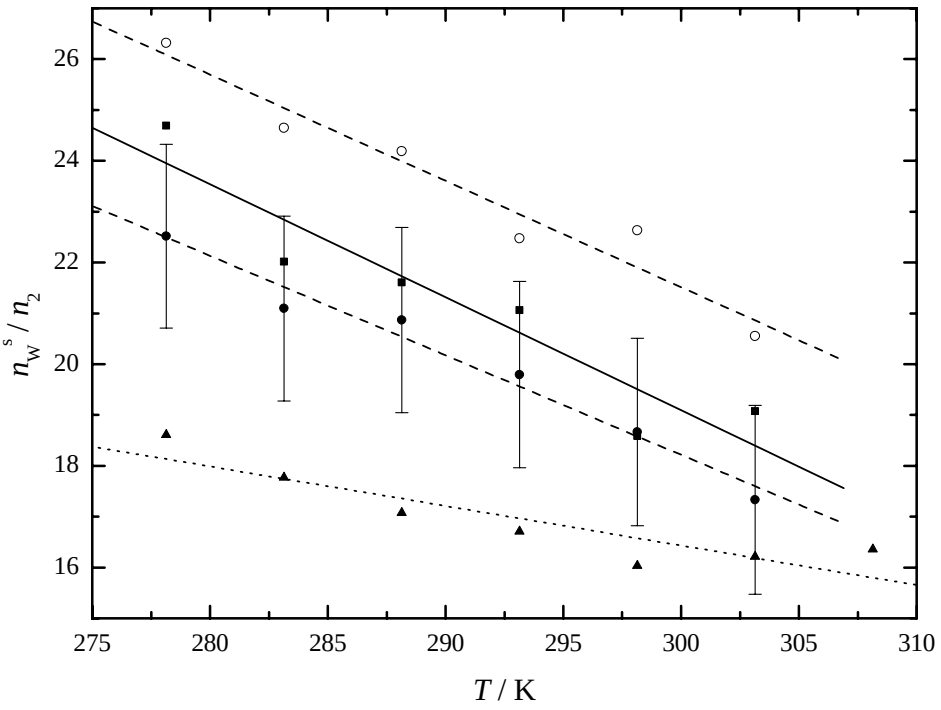

Figure 5.9: Molar amount of water per $C_{12}E_5$ molecule not incorporated in the bulk relaxation process of aqueous surfactant solutions of weight fraction w (■: $w = 0.05$, ●: $w = 0.10$, ○: $w = 0.10$ (D_2O), ▲: $w = 0.20$). Values were calculated from the analytical water concentration and the amplitude S_2 of a fit model comprising two Debye equations.

Figure 5.9 shows the results calculated from data of Tab. 5.1 and 5.2. The ratio of water molecules withdrawn from bulk water relaxation per surfactant molecule ('slow' water molecules) clearly decreases with increasing temperature, indicating a smaller number of water molecules interacting with surfactant headgroups at higher temperatures. This is a well known finding that generally applies to oligo(ethylene glycol) ether compounds, including those which do not form micellar aggregates[159].

From NMR (translational) self-diffusion studies, some information about water molecules moving with the micellar structure as a kinetic entity can be obtained and should result in similar absolute numbers. However, due to experimental difficulties, these data have a large uncertainty at low surfactant concentrations[179], $w \lesssim 0.20$, and can only be used for solutions containing D_2O. Moreover, the temperature dependence of the hydration numbers is not clear (given values are: 28 at 5.2 °C, 31 at 14.3 °C, and 23 at 24.8 °C). However, an average value of ~ 27 molecules is comparable to our findings ($\frac{n_W^s}{n_2} \approx 25$ when averaged over the corresponding temperatures).

Thus we finally conclude that τ_1 clearly indicates a preferred hydration of the end segments of the hydrophilic moieties of the surfactant and a significant number of remaining water-water H-bonds in the hydration layer of the micellar structure. Furthermore, the interaction strength is similar to that of pure water, otherwise an activation energy different from that of pure water would be observed from the Arrhenius plot, Fig. 5.8. The large number of slow water molecules per surfactant molecules can be explained by the size of a relaxation cluster, which is assumed to be in the order of tens of molecules[113]. From thermodynamic measurements[77] it was concluded that the O-CH_2-CH_2-OH segment of oligo(ethylene glycol) monomethyl ethers can be incorporated in water structure almost without excess heat capacity effects at lower concentrations. Additionally, we assume the micellar hydrocarbon core/water interface to be relatively densely packed[183] due to the high flexibility of oligo(ethylene glycol) chain and the weak water-ether oxygen interaction discussed for the oligo(ethylene glycol) dimethyl ethers. Thus the motions in the interfacial region are presumably highly cooperative, as changes of the hydrogen bond network structure or the conformation of the ether chain require a displacement of neighboring chains and water molecule reorientations, which are promoted further on by strong water-water interactions.

Using the concentration of slow water molecules discussed above, it is also possible to calculate the effective dipole moment relative to that of a water molecule in pure water from S_2. The Cavell equation was used and a similar geometric situation assumed. Fig. 5.10 shows the results obtained from data measured at various concentration and temperatures. Except for the lowest concentration, the ratio of the effective dipole moments were found rather constant, $\mu_1/\mu_2 \approx \sqrt{0.6} = 0.77$.

The small variation of this value supports the idea that the water-surfactant headgroup interaction is not much affected by the surfactant concentration and the temperature of the solution, and no specific behavior can be found when the phase separation boundary is approached. Thus, hydration phenomena cannot be the major driving force of phase separation of micellar non-ionic surfactant solutions, at least not in an direct way, as it was often discussed in literature[159,160]. There might be an effect of the anisotropic cavity field caused by surfactant headgroups on the dipole moment, and the assumption of similar geometric constraints is probably not fully hold in case of the slow water molecules. However, the much smaller absolute value of the effective dipole moment can only be explained by the incorporation of oligo(ethylene glycol) segments into the relaxation cluster, which is expected to perturb the propagation of dipole orientational correlations compared to pure water.

Theoretical investigations of non-ionic microemulsions revealed the importance of the in-

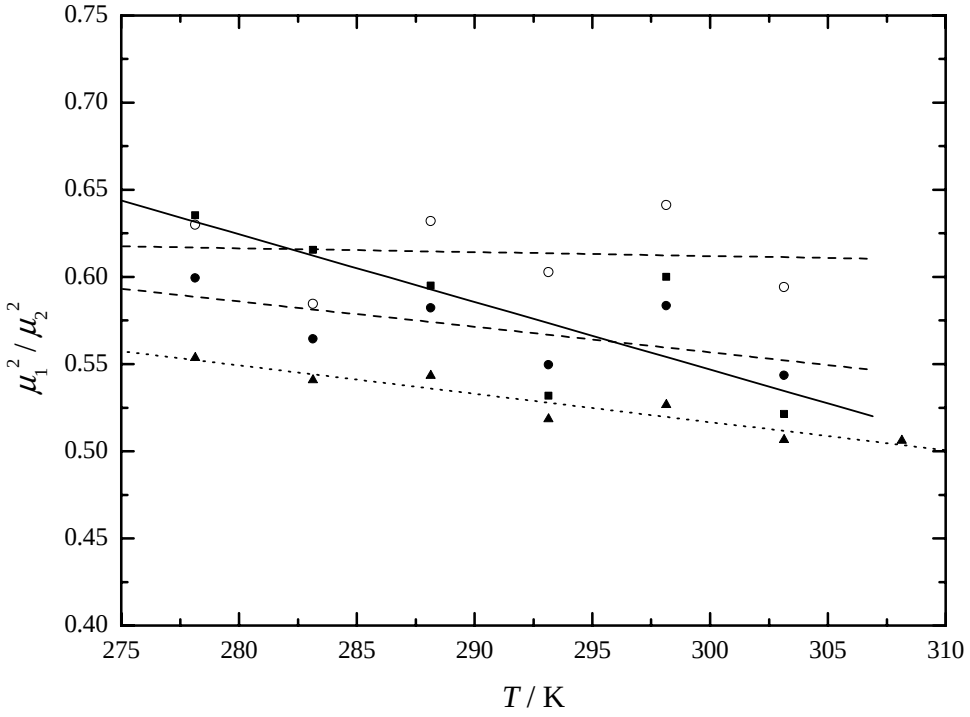

Figure 5.10: Ratio of the squares of the effective dipole moments of water molecules bound to the hydrophilic surfactant headgroups and the bulk water phase, at various surfactant weight fractions w (■: $w = 0.05$, solid line; ●: $w = 0.10$, ○: $w = 0.10$ (D_2O), both dashed line; ▲: $w = 0.20$, dotted line).

terplay of entropy and curvature energy, especially with regard to the network topology of these mixtures[185]. Thus, since we cannot observe any dramatic change of the hydration behavior of aqueous $C_{12}E_5$ solutions even at reasonably high surfactant concentrations ($w = 0.20$) or a change of the energy barriers governing the dynamics of water dipole reorientation at the micellar oil-water interface, other factors, like the existence of micellar networks causing entropy effects might be of importance here.

Let us now focus on the more concentrated samples studied, with $C_{12}E_5$ weight fractions of $w = 0.40$ and $w = 0.70$. For these solutions similar considerations apply as for the dilute ones, although the contribution from the water at the micellar interface shows a distribution of relaxation times. Thus, a Cole-Cole term was employed for the description of this part of the dielectric spectrum. Additionally, we have to take into account the phase behavior of these mixtures, Fig. 5.1, as the sample of $w = 0.40$ undergoes a phase transition from a hexagonal phase to the isotropic micellar phase at $\sim 290.5\,\mathrm{K}$[23]. The measurements of the sample of $w = 0.70$ are all located within a liquid crystalline lamellar region. It was already noted that the hexagonal and lamellar phases are characterized by macroscopic viscosities orders of magnitudes higher compared to the micellar solution. In contrast to this, the dielectric relaxation times, Fig. 5.11, do not show dramatic effects. This clearly supports the interpretation of these times as dynamical properties occurring on short lengthscales within the liquid mixture, whereas the high macroscopic viscosities

are governed by supramolecular processes, like the formation of three dimensional micellar networks and crystalline aggregates. Moreover, the Cole-Cole relaxation times τ_1 were found shorter at $w = 0.40$ than for the more diluted solutions. We can only speculate about the molecular origin of this observation, but it seems likely that the curvature of the micellar interface decreases with increasing concentration of the surfactant[159], which finally leads to the formation of the lamellar structure. Compared with a spherelike micelle, the energy barrier connected with the motions of the hydrophilic surfactant headgroups can be expected to be lower due to the more parallel orientation of these groups.

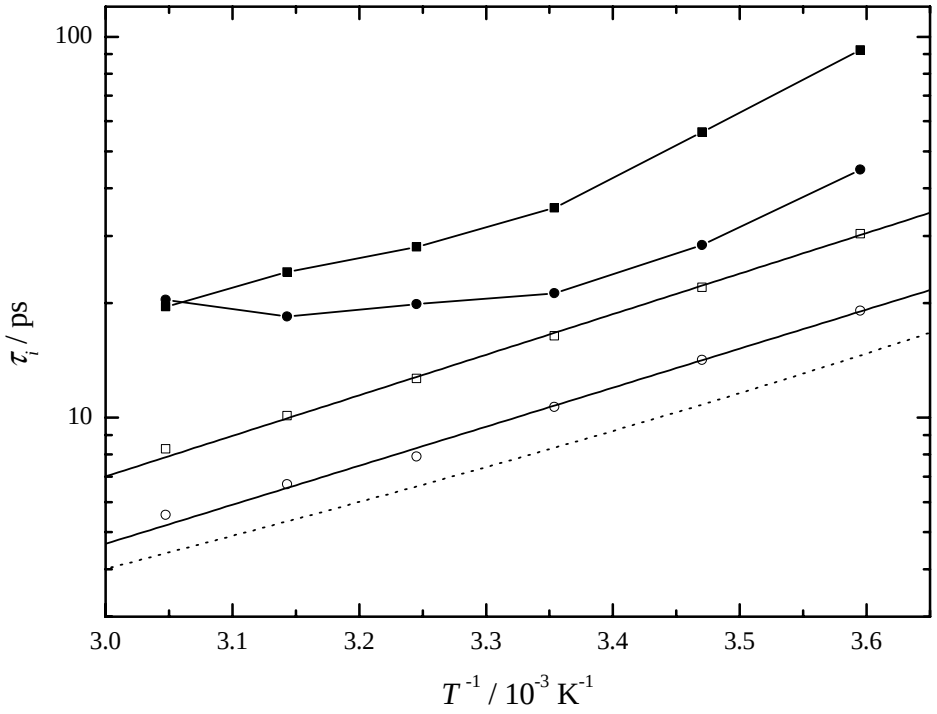

Figure 5.11: Arrhenius plot of the relaxation times of the Cole-Cole (full symbols) and the Debye (open symbols) contributions to the dielectric spectra of aqueous $C_{12}E_5$ solutions of weight fraction $w = 0.40$ (•) and $w = 0.70$ (■). Also shown are the relaxation time of the cooperative relaxation mode of pure water (dotted line).

Interestingly, when the phase boundary is crossed from the isotropic micellar L_1 phase to the lamellar L_α phase (at $T \approx 327\,\mathrm{K}$, $T^{-1} \approx 3.06 \cdot 10^{-3}\,\mathrm{K}$), see Fig. 5.1, the relaxation time τ_1 for a solution of $w = 0.40$ is found very similar to that of the higher concentrated one located in the same phase region (lamellar phase). This shows the large influence of geometric constraints and headgroup mobility on the relaxation times τ_1 of water incorporated in interfacial regions. Therefore, we only expect a moderate concentration dependence of the τ_1 relaxation time within the lamellar region at a given temperature.
The temperature dependence of the relative amplitudes of both relaxation processes found for non-ionic surfactant solutions, see Fig. 5.12, obeys the trend expected from the decrease of headgroup hydration also observed by other techniques. A quantitative evaluation of

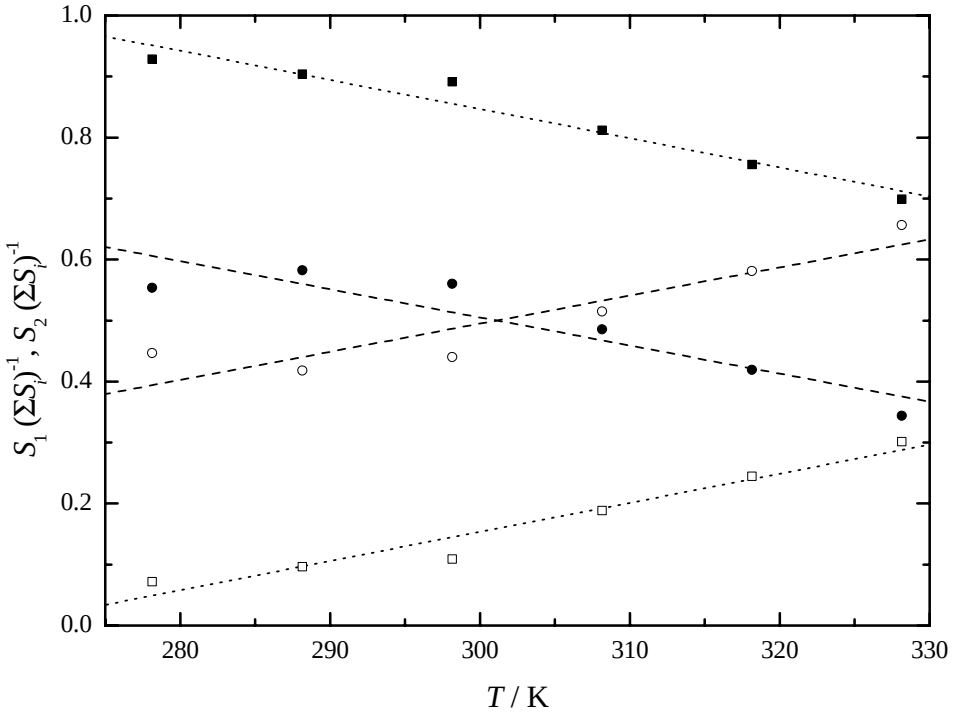

Figure 5.12: Temperature dependence of the relative amplitudes of the Cole-Cole (full symbols) and the Debye (open symbols) contributions to the dielectric spectra of aqueous $C_{12}E_5$ solutions of weight fraction $w = 0.40$ (●, dashed lines) and $w = 0.70$ (■, dotted lines).

the amplitudes in the highly concentrated regime is not straightforward, as the relaxation times found for the bulk water regions (τ_2) are significantly longer compared to pure liquid water, which indicates major alterations of the relaxation mechanism. Unfortunately, an estimation of the tentatively smaller effective dipole moment is difficult.
On the other hand, the increase of the relaxation times τ_2, Fig. 5.13, is inline with a limitation of the translational and rotational degrees of freedom of water molecules surrounded by rather stiff surfactant associates or even enclosed within lamellar, liquid crystalline regions. As already discussed for the case of water + 1,4-dioxane mixtures, this leads to a slowing down of the cooperative relaxation mode of water clusters. The similarity between the relaxation times found for water clusters in these mixtures is striking and points out the importance of confinement effects on the dynamic properties of water[186].

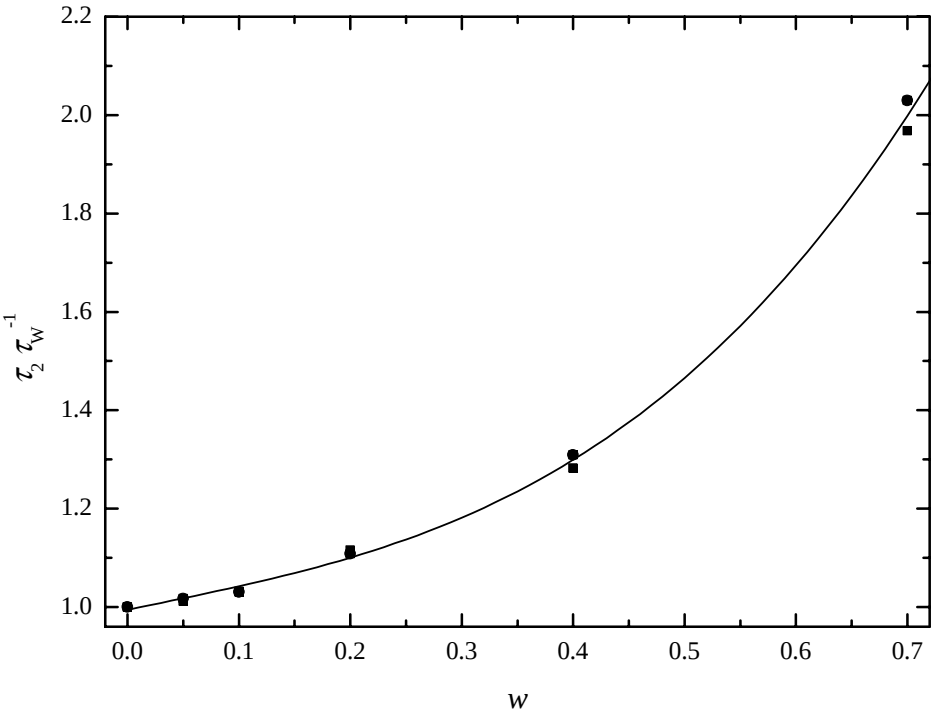

Figure 5.13: Ratio of the dielectric relaxation time of water-rich domains to the relaxation time found for the cooperative mode of pure liquid water. Values at 288.15 K (•) and 298.15 K (■).

Chapter 6

Dynamics of percolating microemulsions

6.1 Introduction

Microemulsions are thermodynamically stable, isotropic transparent fluids of two immiscible liquids and a surface active agent that have been thoroughly investigated over the last few decades not only with respect to possible industrial applications but also because of great theoretical interest.[187] On the oil rich side of the phase diagram reverse micelles are formed which, in a first approximation, can be described as spherical water droplets with typical diameters in the range of $\sim 10 - 60\,\mathrm{nm}$, separated from the continuous oil phase by a surfactant monolayer.[188] In recent years such water in oil (W/O) microemulsions with ionic surfactants (generally bis(2-ethylhexyl)sulfosuccinate, AOT) aroused considerable interest as model systems for the investigation of percolation transitions[20,189–194] and associated charge transport.[18,195] Investigations of the conductivity, κ, and the dielectric relaxation (via probing the total complex permittivity, $\hat{\eta}(\nu) = \varepsilon'(\nu) - \mathrm{i}[\varepsilon''(\nu) + \kappa/(2\pi\nu\varepsilon_0)]$ of the sample as a function of frequency ν; ε_0 is the electric field constant) of ionic W/O microemulsions not only revealed a marked rise of κ when the percolation limit of the reverse micelles is approached but also related maxima in the principle relaxation time τ (associated with the peak frequency of the dielectric loss, $\varepsilon''(\nu)$) and of the static permittivity, $\varepsilon = \lim_{\nu\to 0}\varepsilon'(\nu)$.[20,191,192,194,196] These effects are generally assigned to the exchange of charges between the reverse micelles which is strongly facilitated when the droplets start to aggregate to loose clusters that continue to grow until the percolation limit is reached. Charge carriers in these systems are the surfactant ion, like AOT^-, and the usually much smaller and more mobile counterion, e.g. Na^+.[197] Whereas conductivity measurements on ionic microemulsions are easily performed, the major problem of dielectric studies is the presence of other relaxation processes which prevent a proper determination of amplitude, relaxation time and bandshape of the dielectric dispersion associated with charge hopping. Especially the interfacial polarization, arising from fast tangential motions of adsorbed counterions in the oil/water interface, is large in amplitude and in a similar frequency range.[196]

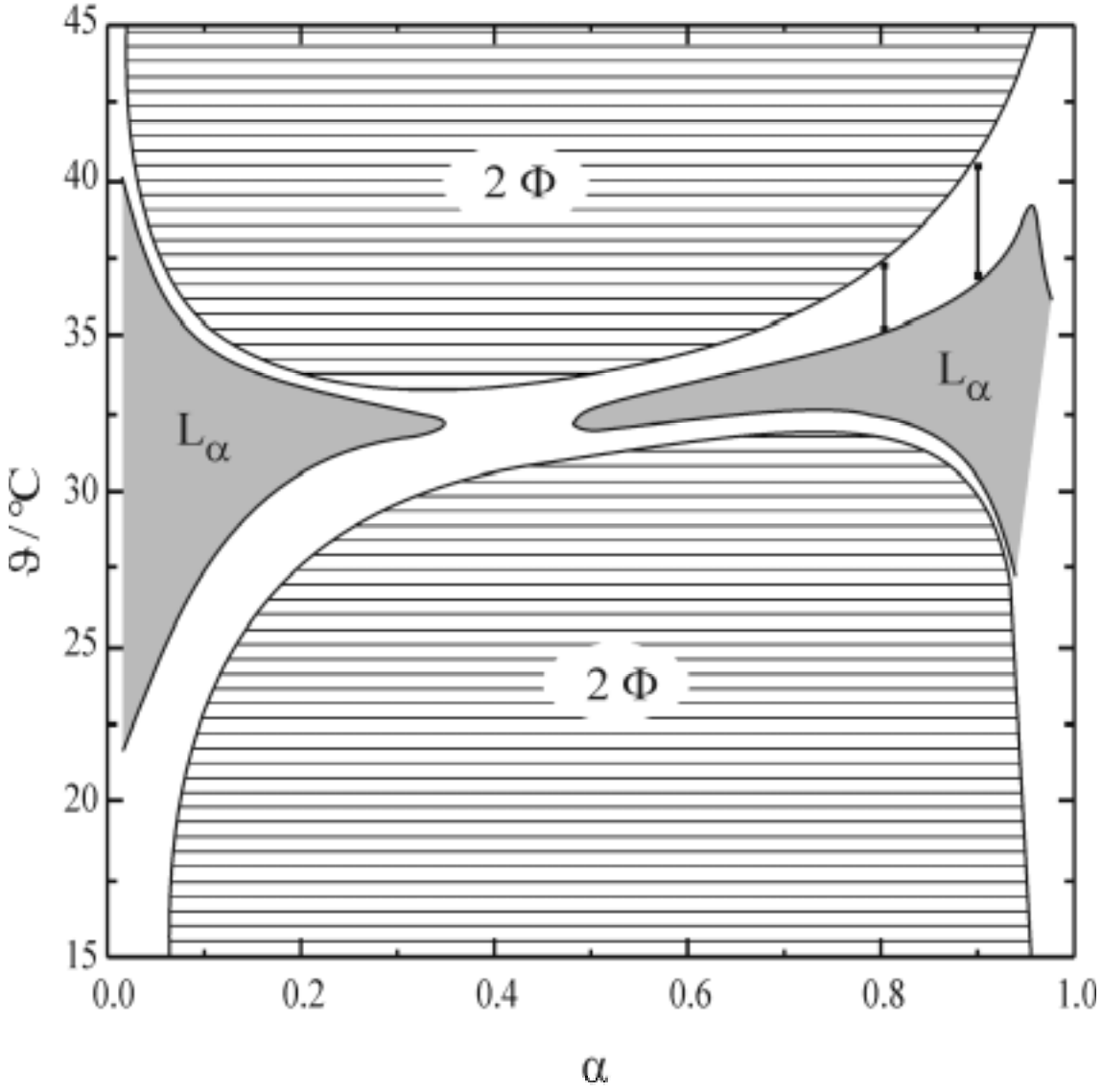

Figure 6.1: Phase diagram of the ternary water/*n*-octane/$C_{12}E_5$ system at $\gamma = 0.07$ (see text).

This is unfortunate because — at least in principle — dielectric relaxation studies should provide more and complementary information to measurements of κ.
The investigation of percolation phenomena in nonionic microemulsions is notoriously difficult due to the lack of appropriate probes. Conductivity studies are not possible and also attempts of dielectric studies failed to yield interpretable data.[22] However, it is possible to replace water by a dilute salt solution (e.g. $10^{-3}\,\mathrm{mol\,L^{-1}}$ KCl) which does not noticeably affect the phase behavior but provides sufficient charge carriers for a detectable signal. Several theoretical as well as experimental studies have been carried out on the conductivity of such 'doted' microemulsions and it was shown that the observed rise of conductivity by several orders of magnitude that occurs when the volume fraction of water or the temperature approach a critical value can be well explained on the basis of percolation theory.[18,19,195,198,199] To our knowledge dielectric studies of such systems have not been reported yet and it is the intention of this contribution to explore the feasability and possible merits of dielectric relaxation studies in this field.

6.2 Experimental section and data analysis

Microemulsions having a surfactant mass fraction of $\gamma = 0.07$ and α-values of $\alpha = 0.8$ and $\alpha = 0.9$ were prepared gravimetrically without buoyancy corrections. The chemicals used were pentaethylene glycol monododecyl ether, $C_{12}E_5$ (Nikko Chemicals, Japan; purity $\geq 99.7\,\%$) as the surfactant, *n*-Octane (p.a., Merck, Germany, used as received) as the oil phase, and $1\,\mathrm{mmol\,L^{-1}}$ aqueous potassium chloride. The latter was made from degassed water (deionized and purified with a Millipore Milli-Q system; specific conductivity $\approx 10^{-6}\,\mathrm{S\,m^{-1}}$) and potassium chloride (99.999 %, Suprapur, Merck, Germany; dried at 120 °C).
Both mixtures were kept at appropriate temperatures ($\alpha = 0.9$ at 313 K; $\alpha = 0.8$ at 309 K) in an air thermostat for at least 24 h to obtain stable single-phase solutions. The phase boundaries of the one-phase regions were determined by measuring the turbidity at 470 nm as a function of temperature using an automated apparatus described elsewhere.[23] Heating/cooling rates of $\leq 1\,\mathrm{K\,h^{-1}}$ were used to ensure thermodynamic equilibrium within the sample during the experiment. For $\alpha = 0.9$ the mixture is homogeneous in the temperature region of $309.94 \leq T/\mathrm{K} \leq 314.65$, for $\alpha = 0.8$ a single phase exists for $307.73 \leq T/\mathrm{K} \leq 310.27$, see Fig. 6.2.
Complex total permittivity spectra, $\hat{\eta}(\nu) = \varepsilon'(\nu) - \mathrm{i}[\varepsilon''(\nu) - \kappa/(2\pi\nu\varepsilon_0)]$, were recorded in the frequency range of $0.005 \leq \nu/\mathrm{MHz} \leq 10$ with a frequency-domain coaxial capacitor setup. This instrument consists of two signal sources (SMH & SMG01, Rohde&Schwarz, Germany) operated at $\approx 400\,\mathrm{mV}$ output power level, a switchable resistor and a vector voltmeter (ZPV with tuner E1, 10 Hz-50 MHz, Rohde&Schwarz, Germany). The coaxial cell, manufactured by WTW, Germany, is made from brass and gold plated. The cell temperature is controlled by a Julabo FP45 thermostat (stable to 0.01 K, RS232 serial interface) and measured with an ITS90 calibrated platinum resistance probe (10 mK traceability to NIST) connected to an ASL F250 precision thermometer (1 mK resolution, 15 mK accuracy). The entire setup is computer controlled via an IEEE-488 bus system, allowing

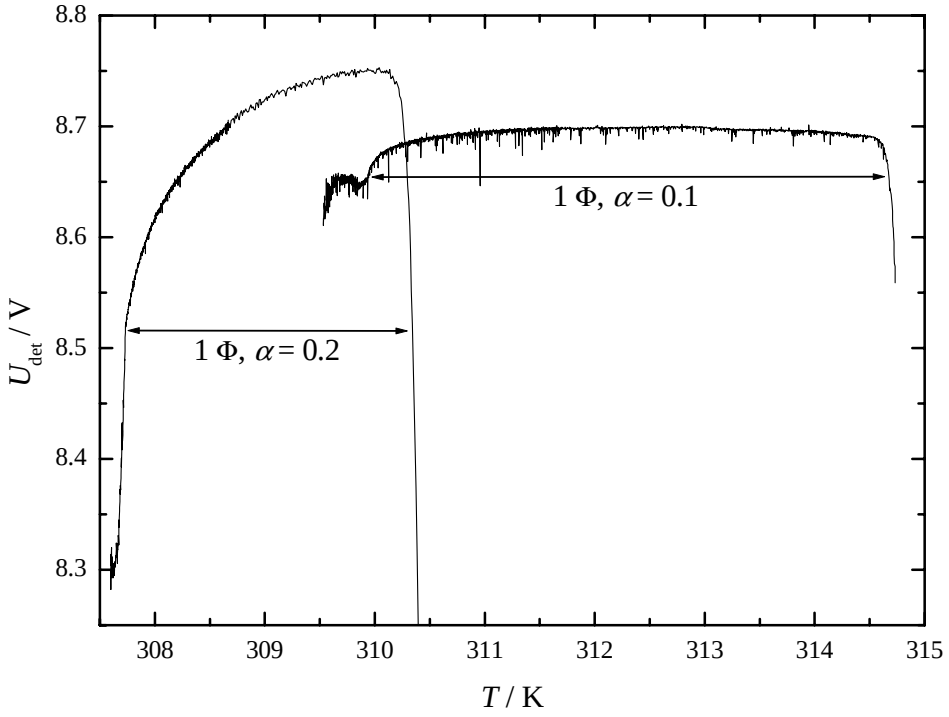

Figure 6.2: The temperature dependence of the turbidity, measured as a detector voltage, U_{det}, of the studied microemulsions at $\alpha = 0.8$ and $\alpha = 0.9$.

automated recording of $\hat{\eta}(\nu)$ for a preset temperature program. Before and after such a series of measurements the instrument was calibrated by measuring the admittance of the cell filled with standard liquids relative to the air-filled cell. For the cell a lumped element description of a capacitor in parallel with a resistor was used to calculate the dielectric properties of the sample.

Measurements were done within the one-phase region, starting at a temperature close to the upper phase boundary and lowering the temperature in steps of 0.1 K. After each temperature samples were equilibrated for 15 minutes before measurements of T and $\hat{\eta}(\nu)$ were triggered. Note that the low-frequency limit of the measurements is determined by the onset of electrode polarization effects and sample conductivity. In principle, measurements in the microwave range beyond the high-frequency limit of this investigation should provide information on the motions of water and $C_{12}E_5$ molecules.[17,139] Unfortunately, tests revealed that the amplitudes (relaxation strengths) associated with these modes were too small for a reliable analysis.

The total permittivity spectra, $\hat{\eta}(\nu)$, were fitted to the sum of a Cole-Cole equation for the dielectric part, $\hat{\varepsilon}(\nu) = \varepsilon'(\nu) - \mathrm{i}\varepsilon''(\nu)$, and a conductivity-loss term

$$\hat{\eta}\,(\nu) \;=\; \varepsilon_\infty + \frac{\Delta\varepsilon}{1 + (\mathrm{i}\cdot 2\pi\nu\tau)^{\,(1-\alpha_{\mathrm{CC}})}} - \mathrm{i}\cdot\frac{\kappa}{2\pi\nu\varepsilon_0} \tag{6.1}$$

to obtain the dispersion amplitude, $\Delta\varepsilon$, the principal relaxation time, τ, the (symmetrical) relaxation-time distribution parameter, α_{CC}, and the infinite-frequency permittivity, ε_∞,

describing $\hat{\varepsilon}(\nu)$ and the conductivity, κ. Typical complex permittivity spectra (conductivity contribution removed) and their fits with Eq. (6.1) are shown in Fig. 6.3. The obtained parameters, with the exception of $\varepsilon_\infty \approx 3.2$, are summarized in Fig. 6.4.

6.3 Results and discussion

In principle percolation phenomena in water-in-oil microemulsions can be studied in two different ways.[200] One of them is to work at constant temperature and to increase the amount of the dispersed phase until a critical composition is passed. However, this approach is very time consuming since each composition has to be prepared separately and settling of the thermodynamic equilibrium may require a long time. From an experimental point of view, the second route, that is changing the temperature of a filled, hermetically sealed measurement cell and determination of the percolation threshold temperature T_P, is more convenient. Therefore, we report in this contribution measurements of the total complex permittivity, $\hat{\eta}(\nu)$, as a function of temperature, T, for two different compositions of a water(KCl, $10^{-3}\,\mathrm{mol}\cdot\mathrm{L}^{-1}$)/*n*-octane/penta(ethylene glycol) dodecyl ether ($\mathrm{W/O/C_{12}E_5}$) microemulsion, a system which was extensively studied with other techniques.[24] The investigated samples are characterized by the same surfactant mass fraction $\gamma \equiv C/(A+B+C)$ of $\gamma = 0.07$ and oil contents of $\alpha = 0.8$ resp. $\alpha = 0.9$; $\alpha \equiv B/(A+B)$, where A, B and C refer to the masses of water, oil and surfactant, respectively. Note that according to Kahlweit *et al.*[24] α and γ together not only give a precise but also more convenient definition of the composition of ternary systems than the conventionally used ideal volume fractions of the components. Irrespective of T the dispersion of permittivity, $\varepsilon'(\nu)$, and the associated loss peak, $\varepsilon''(\nu)$, are symmetrical for both samples and well described by a Cole-Cole equation (see Experimental Section and Data Analysis, Eq. (6.1)). However, with decreasing temperature the conductivity increases by more than three orders of magnitude for the sample with $\alpha = 0.8$, see Figure 6.4a. A similar increase of κ, albeit only by a factor of 100 is observed for $\alpha = 0.9$. Simultaneously, the amplitude of the observed dispersion step, $\Delta\varepsilon$, and thus the static permittivity of the sample, $\varepsilon = \Delta\varepsilon + \varepsilon_\infty$, as well as the relaxation time, τ, and the Cole-Cole width parameter, α_CC, of the observed relaxation process pass through pronounced maxima, Fig. 6.4. These features are typical for percolation phenomena.[20,191,192,194,196]

For $\mathrm{W/O/C_{12}E_5}$ it is known that the reverse micelles in the homogeneous phase are spherical[24] and start to aggregate when the temperature is decreased,[19] opposite to AOT systems which percolate with rising T.[20] Measurements were therefore started close to the upper limit of phase separation, 310.27 K for $\alpha = 0.8$ and 314.65 K for $\alpha = 0.9$, and then the temperature subsequently lowered in 0.1 K steps (see Experimental Section). Figure 6.3 shows some $\hat{\varepsilon}(\nu)$ spectra of the sample with $\alpha = 0.8$ close to the percolation temperature as typical examples for the obtained data.

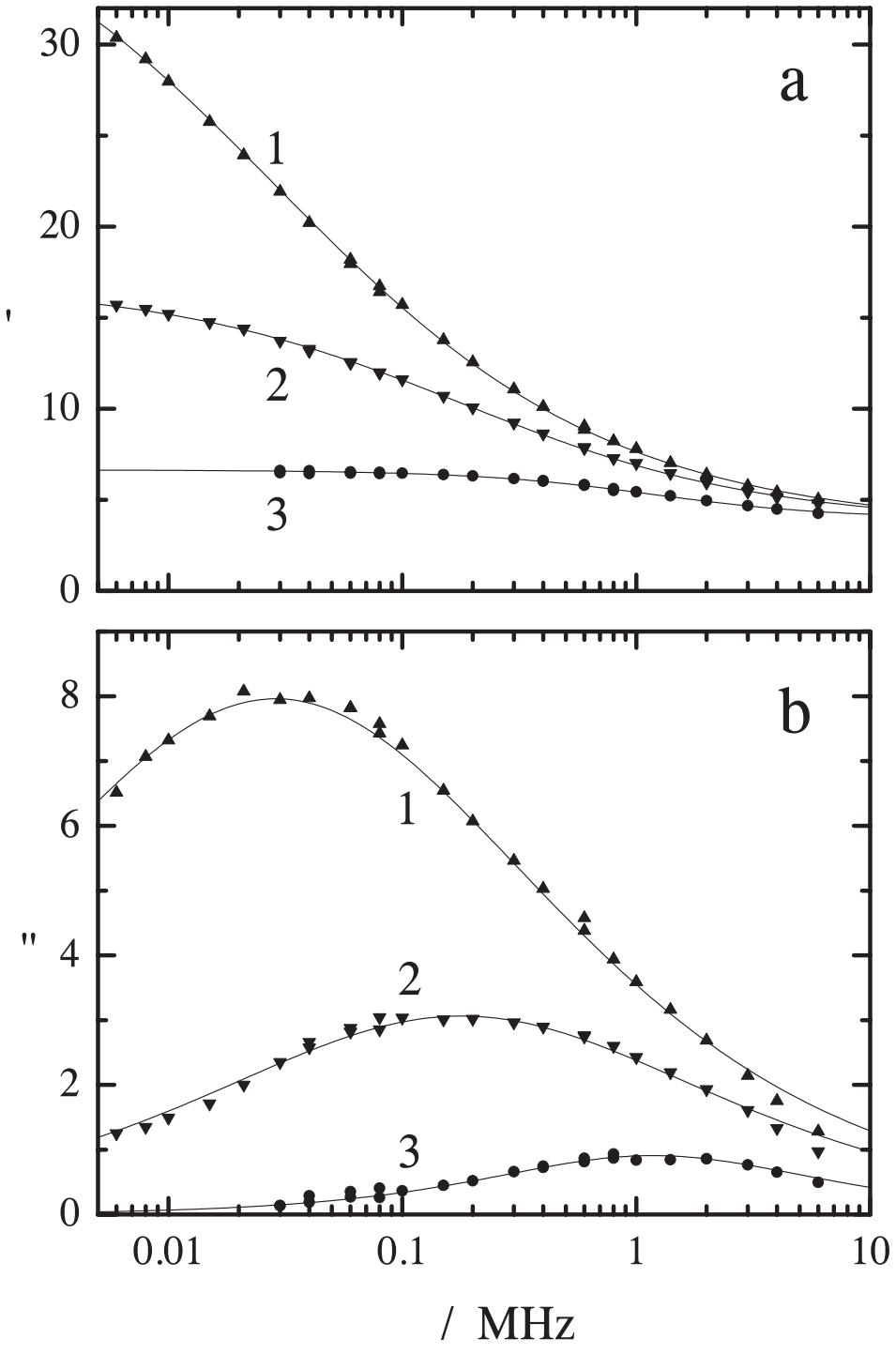

Figure 6.3: (a) The frequency-dependent permittivity, ε', and (b) the dielectric loss, ε'', of a microemulsion of water (doted with $10^{-3}\,\mathrm{mol}\cdot\mathrm{L}^{-1}$ KCl), *n*-octane and $C_{12}E_5$ (mass fraction $\alpha = 0.8$) at $T = 309.01\,\mathrm{K}$ (curve 1); $309.20\,\mathrm{K}$ (2); and $309.58\,\mathrm{K}$ (3). The lines represent fits to the data (symbols) with Eq. (6.1).

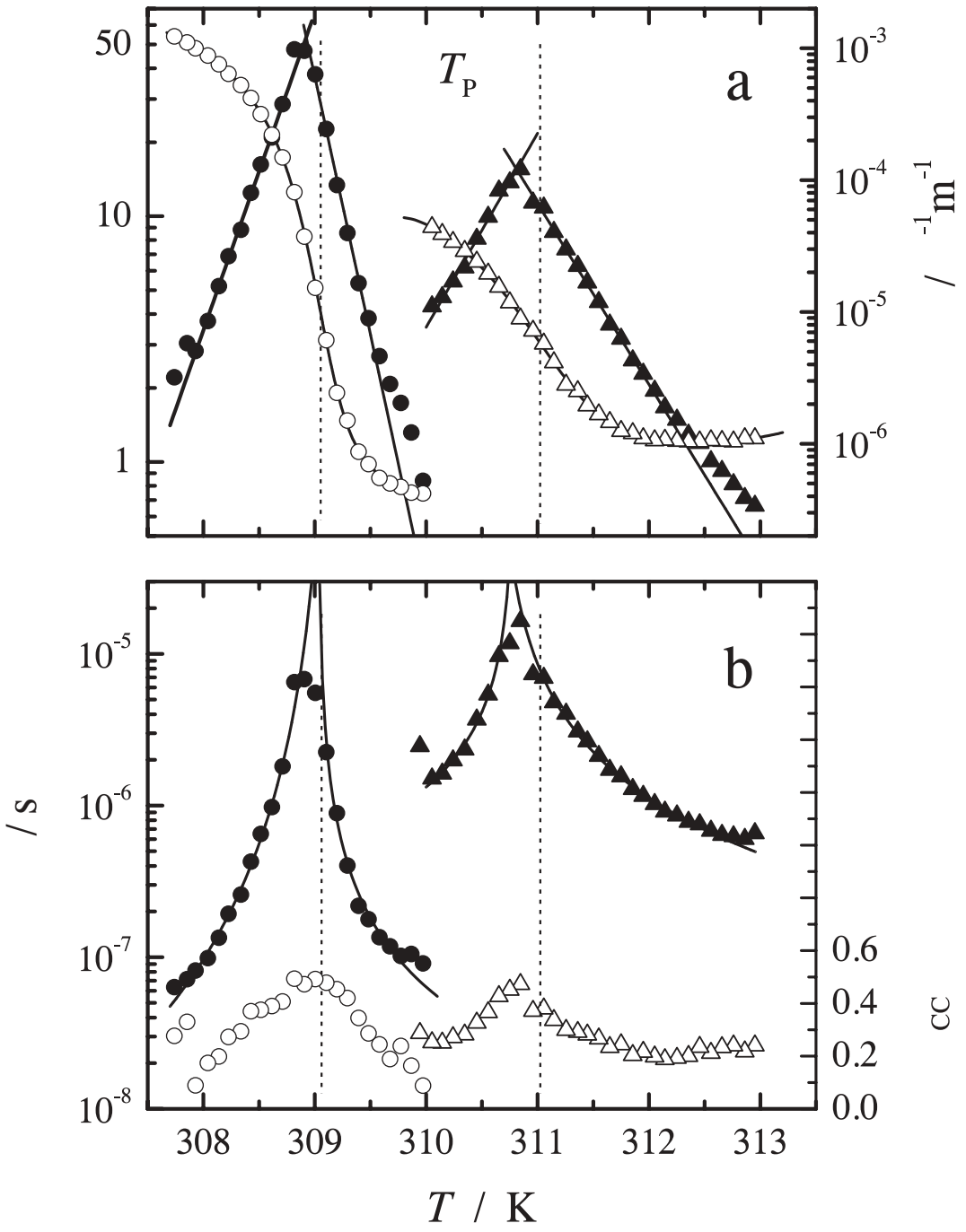

Figure 6.4: (a) Dispersion amplitudes, $\Delta\varepsilon$, and (b) relaxation times, τ, of microemulsions of water (doted with $10^{-3}\,\mathrm{mol}\cdot\mathrm{L}^{-1}$ KCl), *n*-octane and $C_{12}E_5$ at the mass fractions of $\alpha = 0.8$ (•) and $\alpha = 0.9$ (▲). Open symbols in (a) show the conductivity, κ, and in (b) the width parameter, α_{CC}; vertical broken lines indicate the percolation temperatures deduced from κ.

For 'doted' non-ionic microemulsions, where the ions essentially reside within the water droplets, the percolation-induced rise of conductivity was already reported previously.[195,201] Far below the percolation threshold isolated reverse micelles dominate in these systems. The non-zero conductivity arises from spontaneous fluctuations of the droplet charge, mediated by collisions, which leaves some of the droplets with a positive or negative excess charge so that they migrate in the electrical field.[202,203] On approaching T_P the reverse micelles agglomerate to growing clusters which facilitate charge transport by the increased probability for charge hopping between neighboring droplets. At the percolation temperature the increasingly larger ensemble of connected water droplets that can be visited by the ions becomes 'infinite'.[18,200,204] As a consequence, κ obeys a power-law divergence above and below the percolation temperature, T_P, according to

$$\kappa \sim (T - T_P)^{-s}, \quad T > T_P \tag{6.2}$$

and

$$\kappa \sim (T_P - T)^{t}, \quad T < T_P \tag{6.3}$$

For the investigated samples the percolation temperatures of $T_P = 309.05\,\mathrm{K}$ for $\alpha = 0.8$ and of $T_P = 311.02\,\mathrm{K}$ for $\alpha = 0.9$ could be determined from the data of Figure 6.4a by differentiating appropriate polynomial fits of $\log\kappa$ *vs.* T. Subsequently, the critical exponents $t = 1.63 \pm 0.02$ and $s = 1.21 \pm 0.06$ of Eqs. (6.2,6.3) were extracted for the sample with $\alpha = 0.8$ from log-log plots of κ *vs.* the reduced temperature $|T - T_P|/T_P$ (Figure 6.5).[205] The obtained values of both exponents are well within the range predicted by the dynamic percolation model.[196,206] Additionally, t and s are related to a further critical exponent, u, through the relation

$$u = \frac{t}{s + t} \tag{6.4}$$

From the above data $u = 0.57 \pm 0.01$ is obtained, which is in excellent agreement with the theoretical prediction of $u = 0.57$ for anomalous diffusion over percolation clusters.[207,208] For a material made of isolated conducting particles embedded in a non-conducting medium a dielectric relaxation process due to the accumulation of charges at the conductor/non-conductor interface is expected. The observed dispersion amplitudes and relaxation times of our samples (Fig. 6.4) far below the percolation limit, *i.e.* at $T \gg T_P$, are indeed of the magnitude predicted for such systems by e.g. Hanai's theory,[209] $\Delta\varepsilon \approx 0.3$ and $\tau \approx 0.8\,\mu\mathrm{s}$. On approaching the percolation threshold larger and larger clusters of reverse micelles are formed where some of the participating water droplets carry a net charge due to ion hopping. With growing cluster size these excess charges can explore a larger (fractal) space and thus build up larger effective dipole moments, see Fig. 6.6, which accordingly fluctuate on an increasingly longer timescale. This leads to a power-law divergence of the static permittivity (more exactly, of $\Delta\varepsilon$),

$$\varepsilon \sim (T_P - T)^{-s} \tag{6.5}$$

with the same universal exponent s as in Eq. (6.2) on approaching T_P from either side.[210,211] As a consequence, near the percolation threshold the complex permittivity, $\hat{\varepsilon}(\nu)$, should

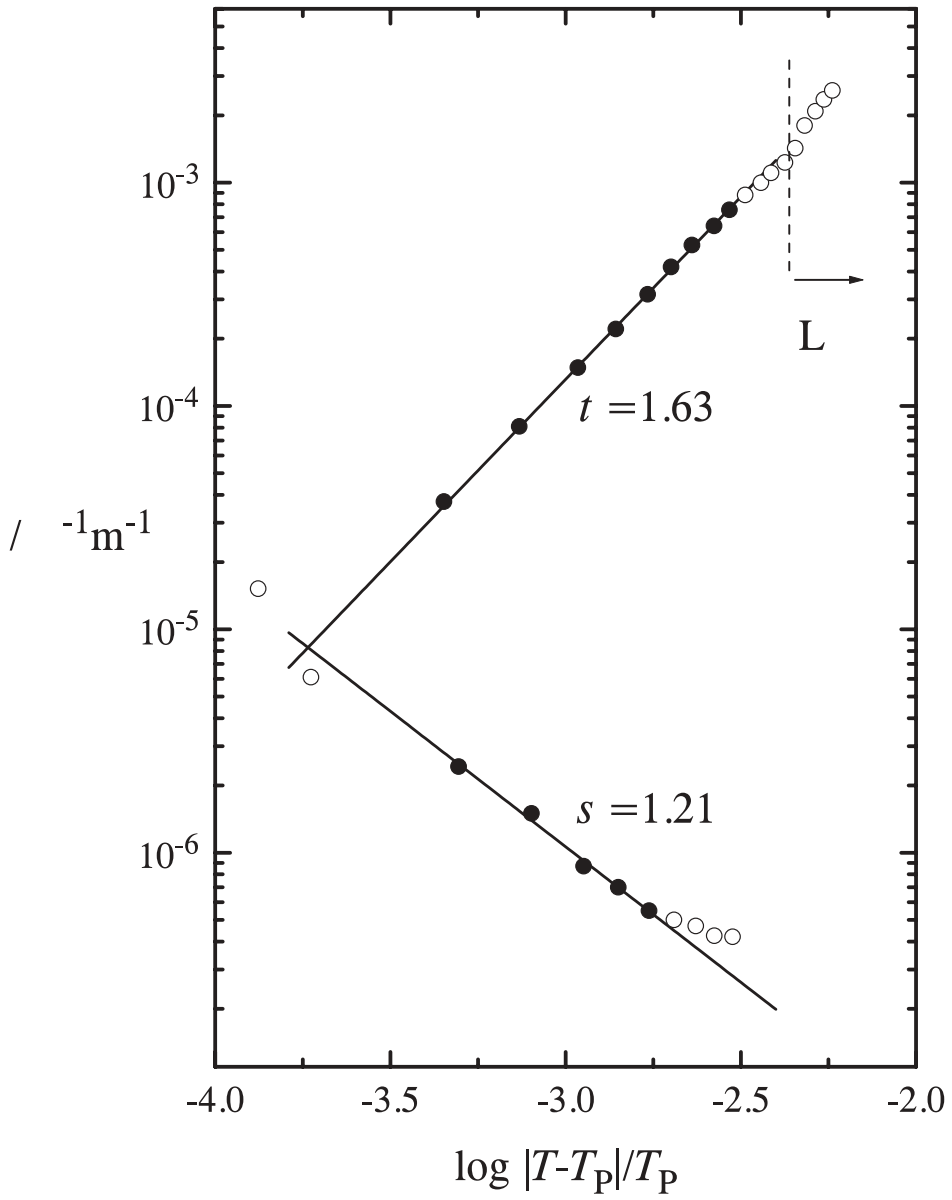

Figure 6.5: Log-log plot of conductivity, κ, *vs.* reduced temperature, $|T - T_{\mathrm{P}}|/T_{\mathrm{P}}$, at $\alpha = 0.8$. The vertical line denotes the phase transition from the isotropic microemulsion to a lamellar (L_α) phase. The data used for the determination of the critical exponents, t and s, are shown as full symbols.

follow the expression

$$\hat{\varepsilon}(\nu) = K \times \exp[\mathrm{i}\frac{\pi}{2}(1-u)] \times \nu^{u-1}. \tag{6.6}$$

between the characteristic frequencies $\nu_{\mathrm{B}} = \kappa_{\mathrm{B}}/(2\pi\varepsilon_0\varepsilon_{\mathrm{B}})$ and $\nu_{\mathrm{A}} = \kappa_{\mathrm{A}}/(2\pi\varepsilon_0\varepsilon_{\mathrm{A}})$ determined by the electric properties of the insulating oil (B) and conducting water phase (A).[189,200,206,210,211]

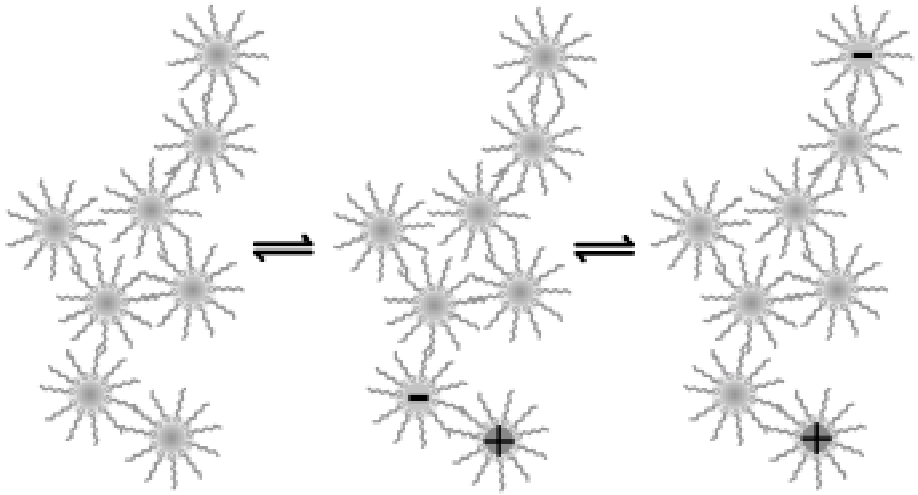

Figure 6.6: Dipole formation through charge hopping in aggregating micelles as a possible contribution to the large dielectric dispersion of percolating microemulsions of 10^{-3}M KCl(aq)/*n*-octane/$C_{12}E_5$.

Thus, a linear plot of $\log \varepsilon'$ *vs.* $\log \nu$ and a loss angle $\delta(\nu) = \arctan(\varepsilon''(\nu)/\varepsilon'(\nu))$ of

$$\delta(\nu) = \frac{1}{2}\pi(1-u) \tag{6.7}$$

are expected between ν_B and ν_A.

Figure 6.7a shows a linear decrease of $\log \varepsilon'$ over a significant frequency range. For $\alpha = 0.8$ the observed high-frequency limit agrees well with $\nu_A \approx 4\,\text{MHz}$ estimated from the conductivity and permittivity of $10^{-3}\,\text{M}$ KCl(aq).[212] For both samples the deviation at frequencies below $\nu_B \approx 20\,\text{kHz}$ arises from $\kappa > 0$ below the percolation threshold.[210] From Fig. 6.7a $\kappa_B \approx 10^{-6}\,\text{S m}^{-1}$ can be estimated, which is in good agreement with the conductivity data of both samples at $T \gg T_P$, see Fig. 6.4a. Not clear is the reduction of ν_A by an order of magnitude for the sample with $\alpha = 0.9$.

Although none of the samples exhibits the well defined plateau predicted for $\tan\delta$, see Fig. 6.4b, the critical exponents u obtained from the maxima of the loss angle with Eq. (6.7), $u = 0.68$ for $\alpha = 0.8$ and $u = 0.73$ for $\alpha = 0.9$, are in excellent agreement with the corresponding data from the slopes of $\log \varepsilon'$, Fig. 6.7a, namely $u = 0.68$ and $u = 0.72$. The slight difference in u between $\alpha = 0.8$ and $\alpha = 0.9$ may reflect a change in the structure of the percolation cluster. In any case, the data derived from the dielectric spectra are systematically larger than the value of $u = 0.57$ predicted by theory[207,208] and obtained from conductivity data discussed above.

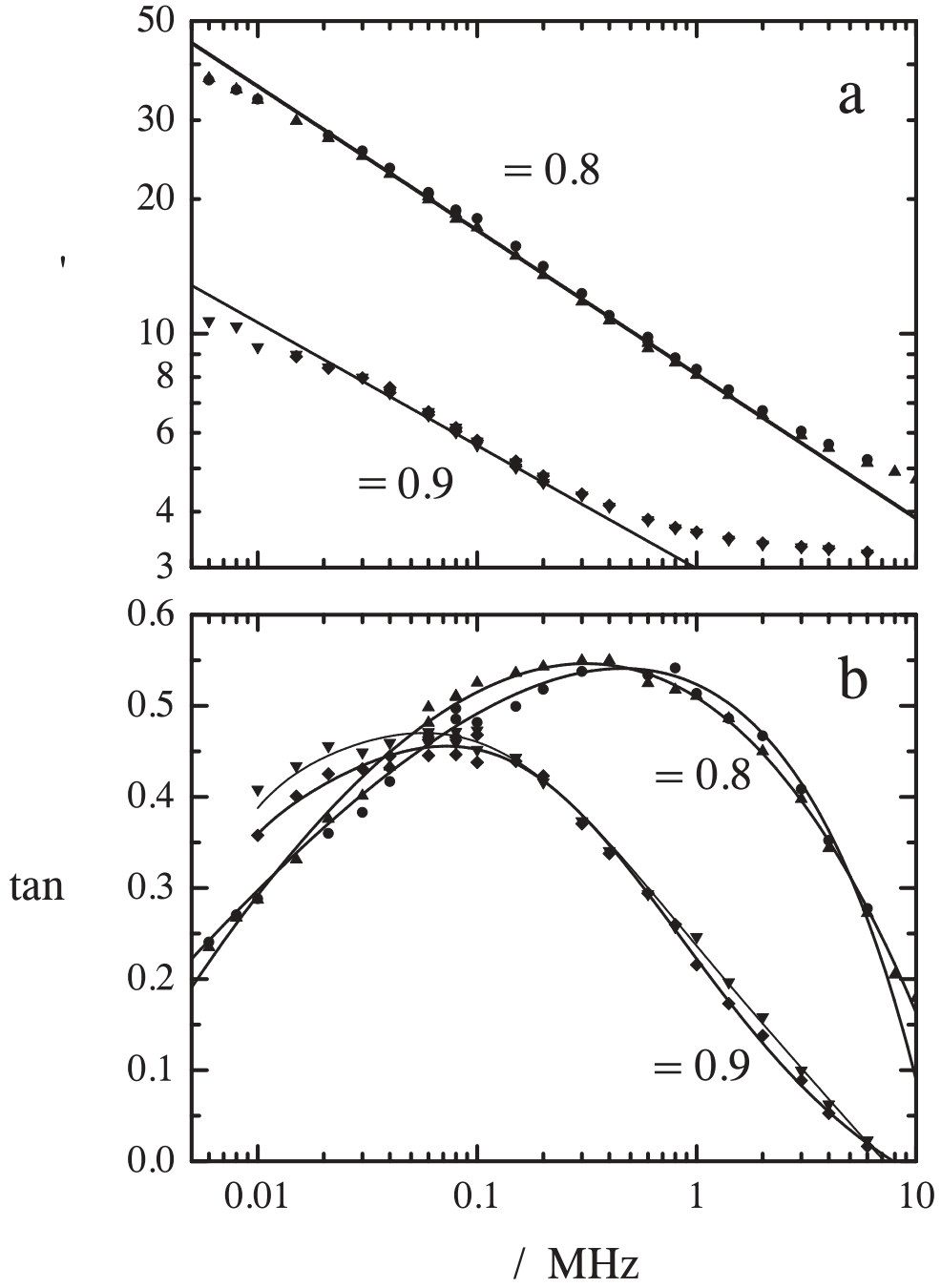

Figure 6.7: (a) The frequency dependence of permittivity, ε', and (b) loss angle, $\delta(\nu)$, for the mass fraction of $\alpha = 0.9$ at $T = 310.75\,\mathrm{K}$ (♦) and 310.85 K (▼), as well as for $\alpha = 0.8$ at $T = 308.82\,\mathrm{K}$ (●) and 308.91 K (▲). The straight lines in (a) represent the fits to the linear parts of $\log \varepsilon'$ (see text); lines in (b) as a guideline to the eye only.

At a first glance Figure 6.4 suggests maxima of the dispersion amplitude $\Delta\varepsilon$, of the relaxation time τ and of the width parameter α_{CC} at slightly lower temperatures T_c than the percolation threshold T_P obtained from conductivity data. τ apparently diverges according to

$$\tau \sim |T_c - T|^{-a} \tag{6.8}$$

whereas $\log \Delta\varepsilon$ varies linearly with T on both sides of this critical temperature T_c. Also, α_{CC} appears to stay finite at T_c. For $\alpha = 0.8$ the intersection of the linear branches of $\log \Delta\varepsilon$, Fig. 6.4a, yields $T_c = 308.93\,\mathrm{K}$, whereas from the relaxation times, Fig. 6.4b, values of 309.1 K for the data at $T < T_c$ and 309.0 K for those at $T > T_c$ are deduced. For $\alpha = 0.9$ the corresponding results are 310.82 K, 310.8 K and 310.6 K. Keeping in mind the limited accuracy of T_c and T_P their values agree for $\alpha = 0.8$. On the other hand for $\alpha = 0.9$ the difference of $T_P - T_c \approx 0.2\,\mathrm{K}$ seems to be genuine. This would be in line with the observations of Feldman *et al.*[196] for the AOT/water/decane system where $T_c > T_P$ and which percolates with increasing temperature.

According to Cametti *et al.*,[193] the width parameter α_{CC} of the dielectric relaxation process should relate to the universal exponent u of dynamical scaling as $\alpha_{CC} \approx 1 - u$ for temperatures close to T_P. For both samples peak values of $\alpha_{CC} \approx 0.45$ are observed, see Fig. 6.4b. Thus, the corresponding $u \approx 0.55$ is in good agreement with the theoretical prediction ($u = 0.57$).

For the static permittivity of ionic microemulsions the predicted power-law divergence, Eq. (6.5) was observed. However, the values obtained for the critical exponent vary considerably. Whereas Bhattacharja *et al.*[213] gave $s \approx 0.65$ for AOT/water/decane, and Peyrelasse *et al.*[214] $s \approx 1.65$, a value of $s \approx 1.1$, *i.e.* similar to the critical exponent from conductivity data, was reported by Feldman *et al.*[196] for the same system. Since the high-frequency permittivity does not depend markedly on temperature ($\varepsilon_\infty \approx 3.2$ is obtained for the spectra of this investigation) a relation similar to Eq. (6.5) should also hold for the amplitude $\Delta\varepsilon$ of the observed dispersion step. However, as seen from Fig. 6.4a, $\log \Delta\varepsilon$ is directly proportional to $|T_c - T|$ for the investigated nonionic W/O/$C_{12}E_5$ microemulsions. From the data slopes of $b = (1.29 \pm 0.02)\,\mathrm{K}^{-1}$ below T_c and $(2.10 \pm 0.06)\,\mathrm{K}^{-1}$ above can be extracted for the sample of composition $\alpha = 0.8$. For $\alpha = 0.9$ the corresponding data are $b = (0.79 \pm 0.04)\,\mathrm{K}^{-1}$ and $(0.74 \pm 0.01)\,\mathrm{K}^{-1}$, respectively. Apparently, the slopes are specific to the sample and to the direction from which the percolation threshold is approached.

According to Peyrelasse and Boned the scaling exponent of the relaxation time, a in Eq. (6.8), should be equal to the sum $s + t$ (here 2.84) of the conductivity parameters, Eqs. (6.2,6.3), when approaching T_P from either side.[215] From the present data for τ_{CC}, Fig. 6.4b, a value of $a = 1.6 \pm 0.1$ is obtained for both samples when T_c is approached from below the percolation threshold, *i.e.* for $T > T_c$. This is similar to $t = 1.63$ but definitely smaller than the expected value and may indicate that the probability of charge hopping between two reverse micelles in contact, which should not depend on α, is of importance for the investigated system. Beyond percolation ($T < T_c$) the exponents differ significantly ($\alpha = 0.8$: $a = 3.1 \pm 0.4$; $\alpha = 0.9$: $a = 1.1 \pm 0.2$) which possibly reflects different structures of the percolation clusters.

To summarize: For the investigated KCl-'doted' water/*n*-octane/$C_{12}E_5$ W/O microemulsions a dielectric relaxation behavior is observed which is reminiscent to the percolation-

induced relaxation process of ionic W/O microemulsions. From the conductivity data and the width parameter α_{CC} critical exponents are obtained that agree well with the universal parameters predicted by dynamic percolation theory. On the other hand, the exponents u derived from the loss tangent and the slope of $\log \varepsilon'(\nu)$, as well as the exponents a for the relaxation time differ from the predicted values, and $\Delta\varepsilon$ apparently does not follow a scaling law but is directly proportional to $|T_c - T|$ around T_c. Additionally, the parameters u, a and b depend on the composition of the sample. These observations suggest that for 'doted' nonionic microemulsions specific interactions are more important for the cooperative processes leading to percolation than for ionic systems. Possibly this hints to a partial fusion of the aggregated spheres and a gradual formation of a structure resembling the 'connected cylinders' discussed by Zemb.[216]

Compared with conventional conductivity measurements dielectric spectroscopy, which uses frequency as an independent variable, has major advantages in the investigation of percolating microemulsions: *i)* The technique allows the direct determination of the universal parameter u in two different ways, *viz.* via Eqs. (6.6, 6.7) and from the value of α_{CC} at T_P; *ii)* The exponent $a = s + t$ is accessible from the temperature dependence of the relaxation time; and *iii)* τ gives directly the timescale of the cluster dynamics relevant for the percolation process. Thus, in conjunction with other techniques, dielectric spectroscopy will help to disentangle universal behavior from features specific to the studied microemulsion.

This Chapter is part of a manuscript entitled "Percolating Microemulsions of Nonionic Surfactants probed by Dielectric Spectroscopy" , accepted for publication in ChemPhysChem in January 2005. (Authors: Simon Schrödle, Richard Buchner, and Werner Kunz)

Chapter 7

Conclusions

This study presents an investigation of the dynamics of aqueous non-ionic surfactant solutions and related systems. Various systems were studied, starting from water + 1,4-dioxane, which represents a simple binary mixture, up to non-ionic microemulsions featuring percolation transitions and a high degree of structuring.

Experimental techniques

To achieve the high accuracy which is necessary for a quantitative analysis of the complex dielectric spectra, the existing instruments and data processing techniques were modified for samples of high viscosity. Furthermore, the principle of operation of a commercially available VNA-reflectometry instrument was elucidated and a method for the correction of systematic errors is presented. As most of the materials of interest are only available in small amounts, a reduction of the sample volume almost by a factor of 10 could be achieved with regard to the VNA-R measurements.
In cooperation with the THz Group of Prof. Helm, University of Freiburg, a cell setup suitable for the determination of complex dielectric properties of liquids in the THz range was developed. The recently established THz-TDS method was successfully applied to water + 1,4-dioxane mixtures.
For the investigation of microemulsions, suitable experimental equipment was build for the measurement of the phase behavior and of the low-frequency dielectric properties.

Thermodynamic and dielectric properties of oligomeric models

For a better understanding of surfactant + water binary systems the present study was based on a set of oligomeric model compounds which allow the investigation of increasing degrees of internal freedom on the dynamics of hydrogen-bond networks. A careful evaluation of existing literature data showed major discrepancies and a quite incomplete coverage. Therefore, thermodynamic properties, especially the densities and heat capacities were determined and analyzed. The dielectric investigations revealed that compounds without H-bond donor groups like 1,4-dioxane and oligo(ethylene glycol) dimethyl ethers cause a quite pronounced microheterogenous structure and show cooperative relaxation

of water-rich domains even at high concentration of the organic solute. In contrast to this, compounds with groups acting as H-bond donors can be incorporated easily into the H-bond network and large effects on the relaxation times where found.
To get an estimation of the energy barriers connected with inter- and intramolecular motions of oligo(ethylene glycol)s, the temperature dependence of the complex dielectric spectra of triethylene glycol was measured and analyzed. The assignment of the relaxation modes to physical processes within the liquid was found in line with our previous investigation of the effect of chain length and provided additional information on the activation energies of these processes.
For mixtures of water + 1,4-dioxane the frequency range was extended up to 4000 GHz by combination of several experimental techniques. To our knowledge, the presented spectra are one of the first datasets of a polar mixture covering a band from MHz to THz frequencies. This provides close insights into cooperative and ultrafast relaxation processes. Furthermore, the dielectric properties of 1,4-dioxane and of the fully deuterated 1,4-dioxane-D_8 were determined and revealed a mode of resonance origin caused by collisional interactions which is important for the dynamics on a fs timescale.

Dielectric relaxation of non-ionic surfactant systems

The dielectric properties of $C_{12}E_5$ + water binary mixtures in the isotropic-micellar, lamellar and hexagonal phase were studied. Two dielectric dispersion steps were resolved and assigned to intermolecular cooperative dynamics of water at the micellar interface and in remaining bulk water domains. From the quantitative analysis of the bulk water response, which was further investigated by heavy water as a substitute for H_2O, the ratio of slow water molecules per mole surfactant was calculated. Additionally, the effective dipole moment of water dipoles incorporated in the relaxation process of water at the interface was determined and found considerably lower than that of pure water.
Special emphasis was put on the effect of hydration on the phase behavior. While the activation energies of the relaxation mode of interfacial water revealed no pronounced change of the water-surfactant interaction when approaching the cloud point, large deviations from the Arrhenius behavior were found for the relaxation times near the phase boundaries between isotropic and liquid crystalline phases.
With increasing surfactant content, confinement effects on the dynamics of bulk water domains within the binary mixture were found.
Further work was carried out on percolating KCl-'doted' water/*n*-octane/$C_{12}E_5$ W/O microemulsions, and critical exponents were obtained that agree well with the universal parameters predicted by dynamic percolation theory. Some properties do not follow a scaling law, a fact that points out the importance of specific interactions for non-ionic microemulsion.

Prospects for the future

This study clearly revealed the need of further improvements with regard to dielectric measurements in the GHz range. During the last few years, new instruments became available

which could provide a more rapid and accurate determination of complex dielectric permittivities, thus enabling a complete coverage of thermodynamic state points of binary and ternary surfactant systems. Also important is the exploration of more precise theoretical models for the reflectivity of the probe head used for the quite powerful reflectometric techniques.
Then, various other non-ionic surfactant systems characterized by different length and chemical composition of the headgroups could be studied, including salt effects on phase diagrams and liquid dynamics of these mixtures.
With respect to basic research, the THz-TDS method should be employed for the exploration of the fs relaxation dynamics of various polar mixtures. Within this time regime, predictions from molecular dynamics simulations are already feasible and therefore great success could be made filling the gaps between theory, simulation and experimentally accessible quantities.

Bibliography

[1] A. McPherson, *Methods Enzymol.* **1985**, *114*, 112.

[2] A. McPherson, *J. Cryst. Growth* **1991**, *110*, 1.

[3] B. Cudney and S. Patel, *Acta Crystallogr.* **1994**, *D50*, 414.

[4] J. M. Harris, *Poly(Ethylene Glycol) Chemistry: Biotechnical and Biomedical Applications*, Plenum Press, New York **1992**.

[5] W. C. K. Poon, A. D. Pirie, M. D. Haw, and P. N. Pusey, *Physica A* **1997**, *235*, 110.

[6] D. Zhao, Q. Huo, J. Feng, B. F. Chmelka, and G. D. Stucky, *J. Am. Chem. Soc.* **1998**, *120*, 6024.

[7] G. Olofsson, *J. Phys. Chem.* **1985**, *89*, 1473.

[8] V. S. Marinov, Z. S. Nickolov, and H. Matsuura, *J. Phys. Chem. B* **2001**, *105*, 9953.

[9] H. Christenson and S. E. Friberg *J. Coll. Interf. Sci.* **1980**, *75*, 276.

[10] L. Zheng, M. Suzuki, T. Inoue, and B. Lindman, *Langmuir* **2002**, *18*, 9204.

[11] K. Rendall and G. J. T. Tiddy, *J. Chem. Soc. Faraday Trans. 1* **1984**, *80*, 3339.

[12] P.-G. Nilsson and B. Lindman, *J. Phys. Chem.* **1984**, *88*, 5391.

[13] A. Tonegawa, K. Ohno, H. Matsuura, K. Yamada, and T. Okuda, *J. Phys. Chem. B* **2002**, *106*, 13211.

[14] M. Lesemann, A. Martín, L. Belkoura, D. Woermann, and E. Hoinkis, *Ber. Bunsenges. Phys. Chem.* **1997**, *101*, 228.

[15] J. Brunner-Popela, R. Mittelbach, R. Strey, K.-V. Schubert, E. W. Kaler, and O. Glatter, *J. Chem. Phys.* **1999**, *110*, 10623.

[16] C. Baar, R. Buchner, and W. Kunz, *J. Phys. Chem. B* **2001**, *105*, 2906.

[17] P. Fernandez, S. Schrödle, R. Buchner, and W. Kunz, *ChemPhysChem* **2003**, *4*, 1065.

[18] H.-F. Eicke, W. Meier, and H. Hammerich, *Coll. Surf. A* **1999**, *156*, 249.

[19] H.-F. Eicke and H. Hammerich, *Coll. Polym. Sci.* **2002**, *280*, 296.

[20] Y. Feldman, N. Kozlovich, Y. Alexandrov, R. Nigmatullin, and Y. Ryabov, *Phys. Rev. E* **1996**, *54*, 5420.

[21] A. Bernheim-Groswasser, T. Tlusty, S. A. Safran, and Y. Talmon, *Langmuir* **1999**, *15*, 5448.

[22] A. Dittrich, *PhD Thesis*, Georg-August-Universität, Göttingen **1985**.

[23] S. Schrödle, R. Buchner, and W. Kunz, *Fluid Phase Equilib.* **2004**, *216*, 175.

[24] M. Kahlweit, R. Strey, D. Haase, H. Kunieda, T. Schmeling, B. Faulhaber, M. Borkovec, H.-F. Eicke, G. Busse, F. Eggers, Th. Funck, H. Richmann, L. Magid, O. Söderman, P. Stilbs, J. Winkler, A. Dittrich, and W. Jahn, *J. Coll. Interf. Sci.* **1987**, *118*, 436.

[25] J. C. Maxwell, *A Treatise in Electricity and Magnetism*, Clarendon Press, Oxford **1881**.

[26] G. S. Greschner, *Maxwellgleichungen*, Hüthig, Basel **1981**.

[27] C. F. J. Böttcher, P. Bordewijk, *Theory of electric polarization*, Vol. 1 and 2, Elsevier, Amsterdam **1978**.

[28] H. Falkenhagen, *Theorie der Elektrolyte*, Hirzel, Leipzig **1971**.

[29] K. Ghowsi and R. J. Gale, *J. Electrochem. Soc.*, **1989**, *136*, 2806.

[30] J. Barthel and R. Buchner, *Chem. Soc. Rev.* , **1992**, *21* , 263.

[31] J. Barthel, R. Buchner, and H. Steger, *Wiss. Zeitschr. THLM* , **1989**, *31*, 409.

[32] R. H. Cole, *Annu. Rev. Phys. Chem.* , **1977**, *28*, 283.

[33] P. Debye, *Polar Molecules*, Dover Publ., New York **1930**.

[34] H. Pellat, *Ann. Chim. Phys.*, **1899**, *18*, 150.

[35] K. S. Cole and R. H. Cole, *J. Chem. Phys.*, **1941**, *9*, 341.

[36] K. S. Cole and R. H. Cole, *J. Chem. Phys.*, **1942**, *10*, 98.

[37] D. W. Davidson and R. H. Cole, *J. Chem. Phys.*, **1950**, *18*, 1417.

[38] D. W. Davidson and R. H. Cole, *J. Chem. Phys.*, **1951**, *19*, 1484.

[39] S. Havriliak and S. Negami, *J. Polym. Sci., Part C*, **1966**, *14*, 99.

[40] D.W. Marquardt, *J. Soc. Ind. Appl. Math.*, 1963, **11**, 431-441.

[41] L. Onsager, *J. Am. Chem. Soc.*, **1936**, *58*, 1486.

[42] J. G. Kirkwood, *J. Chem. Phys.*, **1939**, *7*, 911.

[43] H. Fröhlich, *Theory of dielectrics*, 2nd ed., Oxford University Press, Oxford **1965**.

[44] E. A. S. Cavell, P. C. Knight, and M. A. Sheikh, *J. Chem. Soc. Faraday Trans.*, **1971**, *67*, 2225.

[45] J. Barthel, H. Hetzenauer, and R. Buchner, *Ber. Bunsenges. Phys. Chem.*, **1992**, *96*, 1424.

[46] J. C. Dote, D. Kivelson, and R. N. Schwartz, *J. Chem. Phys.* , **1981**, *85*, 2169.

[47] P. Debye, *Polar molecules*, Dover Publ., New York **1929**.

[48] J. G. Powles, *J. Chem. Phys.*, **1953**, *21*, 633.

[49] S. H. Glarum, *J. Chem. Phys.*, **1960**, *33*, 639.

[50] T. F. Keynes and D. Kivelson, *J. Chem. Phys.*, **1971**, *56*, 1057.

[51] D. Kivelson and P. Madden, *Mol. Phys.*, **1975**, *30*, 1749.

[52] D. Kivelson and P. Madden, *J. Chem. Phys.*, **1984**, *88*, 6557.

[53] W. J. Moore and D. O. Hummel, *Physikalische Chemie*, de Gruyter, Berlin **1986**.

[54] R. Buchner, and J. Barthel, *Ber. Bunsenges. Phys. Chem.*, **1997**, *101*, 1509.

[55] R. H. Cole, *J. Phys. Chem.* **1975**, *79*, 1469.

[56] R. H. Cole, S. Mashimo, and P. Winsor, *J. Phys. Chem.* **1980**, *84*, 786.

[57] C. Hölzl, *PhD Thesis*, Universität Regensburg, Regensburg **1998**.

[58] J. Barthel, R. Buchner, P.-N. Eberspächer, M. Münsterer, J. Stauber, and B. Wurm, *J. Mol. Liq.*, **1998**, *78*, 83.

[59] T. Chen, G. Hefter, and R. Buchner, *J. Phys. Chem. A* **2003**, *107*, 4025.

[60] H. Levine and C. H. Papas, *J. Appl. Phys* **1951**, *22*, 29.

[61] D. V. Blackham, *IEEE Trans. Instr. Meas.* **1997**, *46*, 1093.

[62] J. Barthel, K. Bachhuber, R. Buchner, H. Hetzenauer, and M. Kleebauer, *Ber. Bunsenges. Phys. Chem.* **1991**, *95*, 853.

[63] D. R. Grischkowsky, C. Fattinger, M. van Exter, and S. R. Keiding, *J. Opt. Soc. Am. B* **1990**, *7*, 2006.

[64] M. Schall, J.-P. Helm, and S. R. Keiding, *Int. J. Infrared Millimeter Waves* **1999**, *20*, 595.

[65] J. R. Birch, J. D. Dromey, and J. Lesurf, *NPL Report DES 69*, NPL, Teddington, United Kingdom, **1981**.

[66] The International Association for the Properties of Water and Steam. *Release on the IAPWS Industrial Formulation 1997 for the Thermodynamic Properties of Water and Steam*; IAPWS Meeting, Erlangen, Germany, Sept. **1997**.

[67] CRC Handbook of Chemistry & Physics. 61st ed., CRC Press: Florida, 1980-1981.

[68] P. S. Nikam, T. R. Mahale, and M. Hasan, *J. Chem. Eng. Data* **1998**, *43*, 436.

[69] Z. Shan and A.-F. A. Asfour, *J. Chem. Eng. Data* **1999**, *44*, 118.

[70] M. C. F. Magalhães, E. Königsberger, P.M. May, and G. Hefter, *J. Chem. Eng. Data* **2002**, *47*, 590.

[71] J. E. Desnoyers, C. de Visser, G. Perron, and P. Picker, *J. Solution Chem.* **1976**, *5*, 605.

[72] The International Association for the Properties of Water and Steam. *Release on the IAPWS Formulation 1995 on the Thermodynamic Properties of Ordinary Water Substance for General and Scientific Use*; IAPWS Meeting, Fredericia, Denmark, Sept. **1996**.

[73] V. Roháč, M. Fulem, H.-G. Schmidt, V. Růžička, K. Růžička, and G. Wolf, *J. Therm. Anal. Cal.* **2002**, *70*, 455.

[74] M. Lipovská, H.-G. Schmidt, V. Roháč, V. Růžička, G. Wolf, and M. Zábranský, *J. Therm. Anal. Cal.* **2002**, *68*, 753.

[75] M. Zábranský, J. Růžička, V. Majer, and E. S. Domalski, *Heat Capacity of Liquids, Critical Review and Recommended Values*, Monograph No. 6, Vol I and Vol II, American Chemical Society, Washington D.C., USA **1996**.

[76] M. Čenský, M. Lipovská, H.-G. Schmidt, V. Růžička, and G. Wolf, *J. Therm. Anal. Cal.* **2001**, *63*, 879.

[77] S. Schrödle, G. Hefter, and R. Buchner, *J. Chem. Thermodyn.*, in press.

[78] G. Kortüm and V. Valent, *Ber. Bunsenges. Phys. Chem.* **1977**, *81*, 732.

[79] T. Takamuku, A. Yamaguchi, M. Tabata, N. Nishi, K. Yoshida, H. Wakita, and T. Yamaguchi, *J. Mol. Liq.* **1999**, *83*, 163.

[80] Y. Tominaga and S. M. Takeuchi, *J. Chem. Phys.* **1996**, *104*, 7377.

[81] V. A. Sirotkin, B. N. Solomonov, D. A. Faizullin, and V. D. Fedotov, *J. Struct. Chem.* **2000**, *41*, 997.

[82] S. Mashimo, N. Miura, T. Umehara, S. Yagihara, and K. Higasi, *J. Chem. Phys.* **1992**, *96*, 6358.

[83] C. J. Clemett, E. Forest, C. P. Smyth, *J. Chem. Phys.* **1964**, *40*, 2123.

[84] S. K. Garg and C. P. Smyth, *J. Chem. Phys.* **1965**, *43*, 2959.

[85] S. K. Garg, H. Kilp, C. P. Smyth, *J. Chem. Phys.* **1965**, *43*, 2341.

[86] D. R. Burfield, K.-H. Lee, and R. H. Smithers, *J. Org. Chem.* **1977**, *42*, 3060.

[87] M. Davies, G. W. F. Pardoe, J. Chamberlain, and H. A. Gebbie, *Trans. Faraday Soc.* **1970**, *66*, 273.

[88] P. L. Mercier and C. A. Kraus, *Proc. Natl. Acad. Sci. USA* **1955**, *41*, 1033.

[89] J. C. Justice and R. M. Fuoss, *J. Phys. Chem.* **1963**, *67*, 1707.

[90] R. W. Kunze and R. M. Fuoss, *J. Phys. Chem.* **1963**, *67*, 914.

[91] D. Büttner and H. Heydtmann, *Z. Phys. Chem. NF* **1969**, *63*, 316.

[92] C. F. Mattina and R. M. Fuoss, *J. Phys. Chem.* **1975**, *79*, 1604.

[93] M. Baron, P. Diaz de Vivar, and C. Henderson, *An. Asoc. Quim. Argent.* **1976**, *64*, 383.

[94] D. A. Jannakoudakis and D. K. Panopoulos, *Chem. Chron.* **1981**, *10*, 127.

[95] D. K. Panopoulos and D. A. Jannakoudakis, *Chem. Chron.* **1982**, *11*, 201.

[96] A. D'Aprano, F. Accascina, and R. M. Fuoss, *J. Sol. Chem.* **1990**, *19*, 65.

[97] M. C. Justice, J. C. Justice, and R. L. Key, *J. Sol. Chem.* **1994**, *23*, 703.

[98] M. Bester-Rogac, R. Neueder, and J. Barthel, *J. Sol. Chem.* **1999**, *28*, 1071.

[99] C. Rønne, *private communication*.

[100] C. Rønne, P.-O. Åstrand, and S. R. Keiding, *Phys. Rev. Lett.* **1999**, *82*, 2888.

[101] J. Crossley and C. P. Smyth, *J. Chem. Phys.* **1969**, *50*, 2259.

[102] J. R. Goates and R. J. Sullivan, *J. Phys. Chem.* **1958**, *62*, 188.

[103] H. Nakayama and K. Shinoda, *J. Chem. Thermodyn.* **1971**, *3*, 401.

[104] A. Inglese, I. Ferino, B. Marongiu, V. Solinas, and S. Torrazza, *Thermochim. Acta* **1983**, *65*, 169.

[105] K. W. Morcom and R. W. Smith, *Trans. Faraday Soc.* **1970**, *65*, 1073.

[106] M. Sakurai, *J. Chem. Eng. Data* **1992**, *37*, 492.

[107] J. A. Geddes, *J. Am. Chem. Soc.* **1933**, *55*, 4832.

[108] J. E. Lind, R. M. Fuoss, *J. Phys. Chem.* **1961**, *65*, 999.

[109] A. M. Shkodin, N. K. Levitskaya, and V. A. Lozhnikov, *Zh. Obshch. Khim.* **1968**, *38*, 1006.

[110] H. S. Frank and M. W. Evans, *J. Chem. Phys.* **1945**, *13*, 507.

[111] K. Arakawa and N. Takenaka, *Bull. Chem. Soc. Jap.* **1969**, *42*, 5.

[112] H. Tanaka and I. Ohmine, *J. Chem. Phys.* **1987**, *87*, 6128.

[113] I. Ohmine, H. Tanaka, and P. G. Wolynes, *J. Chem. Phys.* **1988**, *89*, 5852.

[114] O. Borodin, D. Bedrov, and G. D. Smith, *Macromolecules* **2002**, *35*, 2410.

[115] O. Borodin, D. Bedrov, and G. D. Smith, *J. Phys. Chem. B* **2002**, *106*, 5194.

[116] T. Tassaing, Y. Danten, M. Besnard, E. Zoidis, J. Yarwood, Y. Guissani, and B. Guillot, *Mol. Phys.* **1995**, *84*, 769.

[117] D. S. Venables and C. A. Schmuttenmaer, *J. Chem. Phys.* **1998**, *108*, 4935.

[118] D. M. Mittleman, M. C. Nuss, and V. L. Colvin, *Chem. Phys. Lett.* **1997**, *275*, 332.

[119] J. E. Boyd, A. Briskman, V. L. Colvin, and D. M. Mittleman, *Phys. Rev. Lett.* **2001**, *87*, 147401.

[120] G. J. Davies, J. Chamberlain, and M. Davies, *J. Chem. Soc. Faraday Trans. 2* **1973**, *7*, 1223.

[121] F. Hovorka, R. A. Schaefer, and D. Dreisbach, *J. Am. Chem. Soc.* **1936**, *58*, 2264.

[122] R. D. Stallard and E. S. Amis, *J. Am. Chem. Soc.* **1952**, *74*, 1781.

[123] H. Schott, *J. Chem. Eng. Data* **1961**, *6*, 19.

[124] D. Bedrov, M. Pekny, and G. D. Smith, *J. Phys. Chem. B* **1998**, *102*, 996.

[125] D. Bedrov and G. D. Smith, *J. Phys. Chem. B* **1999**, *103*, 3791.

[126] D. Bedrov and G. D. Smith, *J. Phys. Chem. B* **1999**, *103*, 10001.

[127] D. Bedrov, O. Borodin, G. D. Smith, F. Trouw, and C. Mayne, *J. Phys. Chem. B* **2000**, *104*, 5151.

[128] G. D. Smith and D. Bedrov, *J. Phys. Chem. A* **2001**, *105*, 1283.

[129] F. R. Trouw, O. Borodin, J. C. Cook, J. R. D. Copley, and G. D. Smith, *J. Phys. Chem. B* **2003**, *107*, 10446.

[130] U. Kaatze, V. Lönnecke-Gabel, and R. Pottel, *Z. Phys. Chem NF* **1992**, *175*, 165.

[131] U. Kaatze, R. Pottel, and A. Schumacher, *J. Phys. Chem.* **1992**, *96*, 6017.

[132] E. Habicht and R. Zubiani, *US patent* 3,235,461, **1966**.

[133] W. J. Wallace and A. L. Mathews, *J. Chem. Eng. Data* **1963**, *8*, 496.

[134] W. J. Wallace and A. L. Mathews, *J. Chem. Eng. Data* **1964**, *9*, 267.

[135] W. J. Wallace, C. S. Shephard, and C. Underwood, *J. Chem. Eng. Data* **1968**, *13*, 11.

[136] R. L. McGee, W. J. Wallace, and R. D. Ratalczak, *J. Chem. Eng. Data* **1983**, *28*, 305.

[137] S.-C. Ku and C.-H. Tu, *J. Chin. Chem. Soc. (Taipei)* **2002**, *49*, 651.

[138] J. N. Real, T. P. Iglesias, S. M. Pereira, and M. A. Rivas, *J. Chem. Thermodyn.* **2002**, *34*, 1029.

[139] S. Schrödle, W. Kunz, and R. Buchner, *J. Phys. Chem. B* **2004**, *108*, 6281.

[140] N. Goutev, K. Ohno, and H. Matsuura, *J. Phys. Chem. A* **2000**, *104*, 9226.

[141] G. Douhéret, M. I. Davis, M. E. Hernandez, and H. Flores, *J. Ind. Chem. Soc.* **1993**, *70*, 395.

[142] C. Dethlefsen and A. Hvidt, *J. Chem. Thermodyn.* **1985**, *17*, 193.

[143] J. Biroš, J. Pouchl'y, and A. Živn'y, *Makromol. Chem.* **1987**, *188*, 379.

[144] B. Das, M. N. Roy, and D. K. Hazra, *Indian J. Chem. Technol.* **1994**, *1*, 93.

[145] A. Pal and Y. P. Singh, *J. Chem. Eng. Data* **1996**, *41*, 1008.

[146] U. Kaatze, B. Gabriel, and R. Pottel, *Ber. Bunsenges. Phys. Chem.* **1994**, *98*, 9.

[147] R. Kjellander and E. Florin, *J. Chem. Soc. Faraday Trans. 1* **1981**, *77*, 2053.

[148] N. Goutev, Z. S. Nickolov, G. Georgiev, and H. Matsuura, *J. Chem. Soc. Faraday Trans.* **1997**, *93*, 3167.

[149] N. Goutev, Z. S. Nickolov, and H. Matsuura, *J. Mol. Liq.* **1998**, *76*, 117.

[150] H. Matsuura and K. Fukuhara, *J. Mol. Struct.* **1985**, *126*, 251.

[151] G. D. Smith, D. Bedrov, and O. Borodin, *Phys. Rev. Lett.* **2000**, *85*, 5583.

[152] S. Schrödle, *Diploma thesis*, Regensburg **2002**.

[153] N. Koizumi and T. Hanai, *J. Phys. Chem.* **1956**, *60*, 1496.

[154] Beilstein CrossFire, Beilstein Database, MDL Information Systems **2002**.

[155] A. F. Gallaugher and H. Hibbert, *J. Am. Chem. Soc.* **1936**, *58*, 813.

[156] A. F. Gallaugher and H. Hibbert, *J. Am. Chem. Soc.* **1937**, *59*, 2514.

[157] A. F. Gallaugher and H. Hibbert, *J. Am. Chem. Soc.* **1937**, *59*, 2521.

[158] K. J. Liu and R. Ullman, *J. Chem. Phys.* **1968**, *48*, 1158.

[159] M. J. Schick, *Nonionic Surfactants*, Dekker, New York **1987**.

[160] D. J. Mitchell, G. J. T. Tiddy, L. Waring, T. Bostock, and M. P. McDonald, *J. Chem. Soc., Faraday Trans. 1* **1983**, *79*, 975.

[161] R. Strey, R. Schomäcker, D. Roux, F. Nallet, and U. Olsson, *J. Chem. Soc. Faraday Trans.* **1990**, *86*, 2253.

[162] G. J. T. Tiddy, *Phys. Rep.* **1980**, *57*, 1.

[163] M. J. Schick, *Nonionic Surfactants (Vol. 2)*, Dekker, London **1967**.

[164] R. Strey, *Ber. Bunsenges. Phys. Chem.* **1996**, *100*, 182.

[165] D. Constantin, É. Freyssingeas, J.-F. Palierne, and P. Oswald, *Langmuir* **2003**, *19*, 2554.

[166] P.-G. Nilsson, H. Wennerström, and B. Lindman, *Chem. Script.* **1985**, *25*, 67.

[167] W. J. Ellison, K. Lamkaouchi, and J.-M. Moreau, *J. Mol. Liq.* **1996**, *68*, 171.

[168] Technical Datasheet, *HP 85070B High-Temperature Dielectric Probe Kit*, Hewlett Packard Company, **1993**.

[169] R. Buchner, G. T. Hefter, and P. M. May, *J. Phys. Chem. A* **1999**, *103*, 1.

[170] K. Asami, *HP Application Note 380-3*, Hewlett Packard Company.

[171] K. Asami, *Prog. Polym. Sci.* **2002**, *27*, 1617.

[172] N. Nandi, K. Bhattacharyya, and B. Bagchi, *Chem. Rev.* **2000**, *100*, 2013.

[173] G. Delbos, M. Keita, and T. K. Bose, *Can. J. Phys.* **2001**, *79*, 49.

[174] D. Mizuno, T. Nishino, Y. Kimura, and R. Hayakawa, *Phys. Rev. E* **2003**, *67*, 061505.

[175] S. Ezrahi, I. Nir, A. Aserin, N. Kozlovich, Y. Feldman, and N. Garti, *J. Disp. Sci. Tech.* **2002**, *23*, 351.

[176] A. Bernheim-Groswasser, E. Wachtel, and Y. Talmon, *Langmuir* **2000**, *16*, 4131.

[177] O. Glatter, G. Fritz, H. Lindner, J. Brunner-Popela, R. Mittelbach, R. Strey, and S. U. Egelhaaf, *Langmuir* **2000**, *16*, 8692.

[178] C. Baar, R. Buchner, and W. Kunz, *J. Phys. Chem. B* **2001**, *105*, 2914.

[179] P. G. Nilsson and B. Lindman, *J. Phys. Chem.* **1983**, *87*, 4756.

[180] P.-G. Nilsson, H. Wennerström, and B. Lindman, *J. Phys. Chem.* **1983**, *87*, 1377.

[181] W. Brown, Z. Pu, and R. Rymdén, *J. Phys. Chem.* **1988**, *92*, 6068.

[182] G. Briganti, A. L. Segre, D. Capitani, C. Casieri, and C. L. Mesa, *J. Phys. Chem. B* **1999**, *103*, 825.

[183] L. S. Romsted and J. Yao, *Langmuir* **1999**, *15*, 326.

[184] H. Caldararu, A. Caragheorgheopol, and S. Schlick, *Bull. Pol. Acad. Sci. Chem.* **2000**, *48*, 367.

[185] T. Tlusty, S. A. Safran, R. Menes, and R. Strey, *Phys. Rev. Lett* **1997**, *78*, 2616.

[186] F. Kremer, A. Huwe, M. Arndt, P. Behrens, and W. Schwieger, *J. Phys.: Condens. Matter* **1999**, *11*, A175.

[187] P. Kumar and K.L. Mittal, *Handbook of Microemulsion Science and Technology*, Marcel Dekker, New York **1999**.

[188] H.-D. Dörfler, *Grenzflächen und kolloid-disperse Systeme*, Springer, Berlin **2002**.

[189] M. A. van Dijk, *Phys. Rev. Lett.* **1985**, *55*, 1003.

[190] H.-F. Eicke, S. Geiger, F. A. Sauer, and H. Thomas, *Ber. Bunsenges. Phys. Chem.* **1986**, *90*, 872.

[191] M. A. van Dijk, G. Casteleijn, J. G. H. Joosten, and Y. K. Levin, *J. Chem. Phys.* **1986**, *85*, 626.

[192] M. W. Kim and J. S. Huang, *Phys. Rev. A* **1986**, *34*, 719.

[193] C. Cametti, P. Codastefano, P. Tartaglia, J. Rouch, and S. H. Chen, *Phys. Rev. Lett.* **1990**, *64*, 1461.

[194] A. Ponton, T. K. Bose, and G. Delbos, *J. Chem. Phys.* **1991**, *94*, 6879.

[195] F. Bordi, C. Cametti, P. Codastefano, F. Sciortino, P. Tartaglia, and J. Rouch, *Progr. Colloid Polym. Sci.* **1996**, *100*, 170.

[196] Y. Feldman, N. Kozlovich, I. Nir, and N. Garti, *Phys. Rev. E* **1995**, *51*, 478.

[197] C. Cametti, P. Codastefano, A. Di Biasio, T. Tartaglia, and S. H. Chen, *Phys. Rev. A* **1989**, *40*, 1962.

[198] D. G. Hall, *J. Chem. Phys.* **1990**, *94*, 429.

[199] H.-F. Eicke, W. Meier, and H. Hammerich, *Langmuir* **1994**, *10*, 2223.

[200] G. S. Grest, I. Webman, S. A. Safran, and A. L. R. Bug, *Phys. Rev. A* **1986**, *33*, 2842.

[201] H.-F. Eicke and H. Thomas, *Langmuir* **1999**, *15*, 400.

[202] H.-F. Eicke, M. Borkovec, and B. Das-Gupta, *J. Phys. Chem.* **1989**, *93*, 314.

[203] N. Kallay and A. Chitofratti, *J. Phys. Chem.* **1990**, *94*, 4755.

[204] Y. Feldman, N. Kozlovich, I. Nir, and N. Garti, *Coll. Surf. A* **1997**, *128*, 47.

[205] For $\alpha = 0.9$ the data are too noisy to extract meaningfull values of s and t.

[206] J. P. Clerk, G. Giraud, J. Laugier, and J. Luck, *Adv. Phys.* **1990**, *39*, 191.

[207] Y. Gefen, A. Aharony, and S. Alexander, *Phys. Rev. Lett.* **1983**, *50*, 77.

[208] D. Stauffer, *Phys. Rep.* **1979**, *54*, 3.

[209] T. Hanai, *Electrical Properties of Emulsions*, in: P. Sherman (ed.), *Emulsion Science*, Academic Press, London **1968**.

[210] A.L. Efros and B.I. Shkovskii, *Phys. Status Solidi (b)* **1976**, *76*, 475.

[211] J. M. Luck, *J. Phys. A* **1985**, *18*, 2061.

[212] J.O'M. Bockris and A.K.N. Reddy, *Modern Electrochemistry 1 — Ionics*, 2nd ed., Plenum, New York **1998**.

[213] S. Bhattacharya, J.P. Stokes, M.W. Kim, and J.S. Huang, *Phys. Rev. Lett.* **1985**, *55*, 1884.

[214] J. Peyrelasse, M. Moha-Ouchane, and C. Boned, *Phys. Rev. A* **1988**, *38*, 904.

[215] J. Peyrelasse and C. Boned, *Phys. Rev. A* **1990**, *40*, 938.

[216] T.N. Zemb, *Coll. Surf. A* **1997**, *129-130*, 435.

[217] C. G. Malmberg, *J. Res. Natl. Inst. Stand. Technol.* **1958**, *60*, 609.

Appendix A

Determination of phase diagrams

The following pages contain a reprint of the paper

S. Schrödle, R. Buchner, and W. Kunz,
Automated apparatus for the rapid determination of liquid-liquid and solid-liquid phase transitions,

which is part of this work.

The instrument described was used for the investigation of various binary mixtures, mainly aqueous solutions of propylene glycol ethers of industrial importance. For details please refer to

- P. Bauduin, L. Wattebled, D. Touraud, and W. Kunz,
  Hofmeister ion effects on the phase diagrams of water-propylene glycol propyl ethers.
  Z. Phys. Chem. NF **2004**, *218*, 631-641.

- P. Bauduin, L. Wattebled, S. Schrödle, D. Touraud, and W. Kunz,
  Temperature dependence of industrial propylene glycol alkyl ether/water mixtures.
  J. Mol. Liq. **2004**, *115*, 23-28.

Available online at www.sciencedirect.com
SCIENCE DIRECT®
Fluid Phase Equilibria 216 (2004) 175–182
FLUID PHASE EQUILIBRIA
www.elsevier.com/locate/fluid

Automated apparatus for the rapid determination of liquid–liquid and solid–liquid phase transitions

Simon Schrödle, Richard Buchner, Werner Kunz*

Institut für Physikalische und Theoretische Chemie, Universität Regensburg, Regensburg D-93040, Germany

Received 29 August 2003; accepted 31 October 2003

Abstract

An automated apparatus developed for the determination of liquid–liquid and solid–liquid equilibrium temperatures with a resolution of 1 mK and a traceable accuracy of 0.01 K is described. The amount of light transmitted through six sample cells placed in a computer controlled thermostat is recorded at heating or cooling rates from 0.075 to 15 K h^{-1}. The construction does not require expensive optic equipment like lasers, glass fibre optics or photomultipliers, but is based on light emitting diodes (LED) as light sources and light dependent resistors (LDR) or photodiodes as detectors. As shown by the discussed examples, the instrument has a wide range of possible applications from the investigation of simple one-component and binary systems to the study of the complicated phase behavior of surfactant solutions.

Keywords: Experimental method; Liquid–liquid equilibria; Solid–liquid equilibria; Phase diagram

1. Introduction

Liquid–vapor, liquid–liquid and liquid–solid equilibrium data are essential not only as a basis for other scientific investigations but also for the development of industrial processes and for theoretical purposes. Whereas quite a lot of well approved methods are known for the determination of liquid–vapor coexistence curves, liquid–liquid and liquid–solid phase transitions are usually still measured in a quite primitive way by visual observation of these systems at different temperatures [1,2]. To minimize the time demand, high heating and cooling rates (typ. 2 K h^{-1}) are generally used. As a result, even with very careful operation, phase-boundary compositions are generally only accurate to ±2 wt.% and transition temperatures to ±1 K [2].

Calorimetric methods employing the measurement of phase transition energies, like DSC, can be used in some cases instead of optical effects. But even with quite sophisticated instruments the required low heating rates in the range of 0.1–0.5 K h^{-1} needed for the precise determination of liquid/liquid transitions in surfactant systems (e.g. cloud or craft points) are not possible due to the small thermal signatures of these transitions. Additionally, these methods do not permit stirring of the sample which is essential for the investigation of two-phase/single-phase transitions.

For the measurement of mutual solubility curves of simple binary liquids a few semi-automated experimental setups are described in literature [3–5] but have always been applied for the determination of specific phase transitions or samples. To our knowledge an automated general-purpose instrument has not been described before. Thus we designed and constructed an improved instrument that is based on optical effects connected with phase transitions and is capable of high precision and accuracy.

2. Experimental setup

2.1. Apparatus

The apparatus for the automated determination of phase transitions takes advantage of the intensity changes in transmitted light which occur when the sample undergoes a phase change, see Fig. 1. The design of the central (thermostatted) unit is shown in Fig. 2, whereas Fig. 3 gives a block diagram of the entire setup with the required auxiliary instrumentation. Prerequisite for a high reproducibility and accuracy

* Corresponding author.
E-mail address: werner.kunz@chemie.uni-regensburg.de (W. Kunz).

0378-3812/$ – see front matter © 2003 Elsevier B.V. All rights reserved.
doi:10.1016/j.fluid.2003.10.015

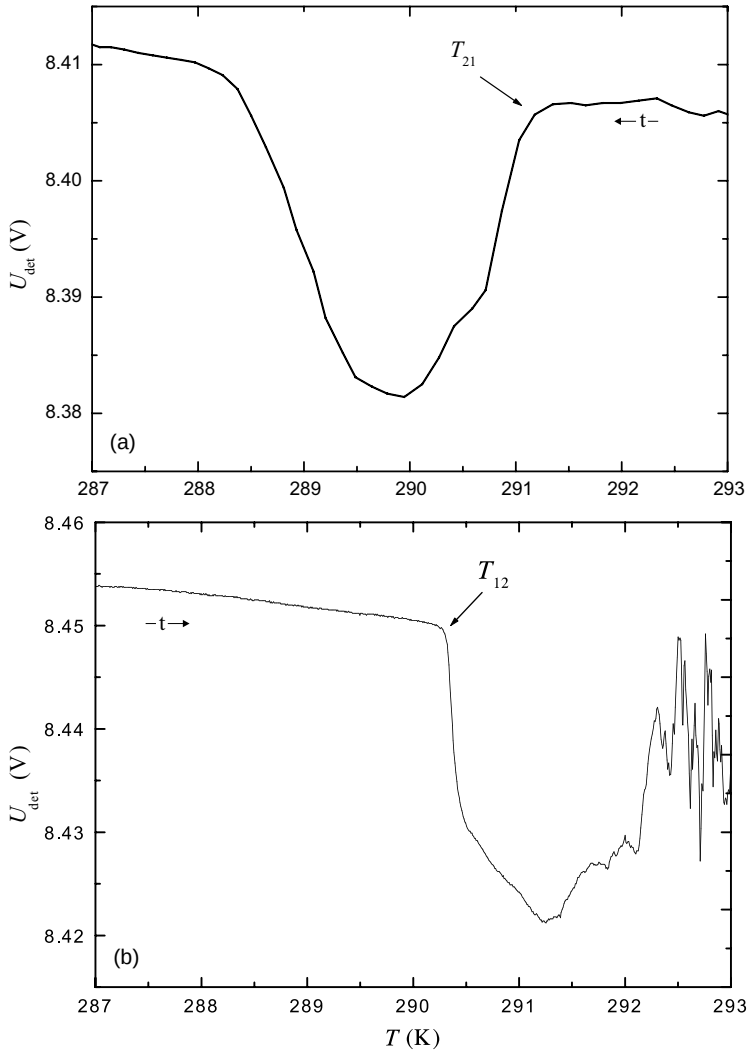

Fig. 1. Light detector voltage, U_{det}, as a function of absolute temperature, T, for the hexagonal (2) micellar isotropic (1) phase transitions of a pentaethylene glycol dodecyl ether/water binary mixture on cooling (a) and heating (b) with rate $|\dot{T}| = 1.7\,\mathrm{K\,h^{-1}}$.

of the determined transition temperatures is a strictly monotonous increase or decrease of temperature, T, as well as a reliable and traceable temperature measurement system. This was achieved by the special design of the oil bath (Fig. 2) and a stirrer (C) operated by a constant speed electric motor. Copper shields (F) are placed in a Dewar vessel (D) filled with silicone oil (Baysilone® M5) to control the oil flow, preventing thus local overheating and minimizing temperature fluctuations close to the sample cells (E). Because of the symmetrical construction of the sample cell holder (H), which is completely immersed in the oil bath, a single platinum resistance thermometer probe (B, RTD in Fig. 3) placed next to the sample cell holder is sufficient although up to six samples can be measured simultaneously. The temperature probe is traceable to the National Institute of Standards and Technology (NIST) with an accuracy of better than 0.01 K through an accredited calibration laboratory. It is connected to a precision thermometer (PRT in Fig. 3; Automatic Systems Laboratories F250-MKII, calibrated to an maximum resistance error $\leq 1\,\mathrm{m\Omega} \hat{=} 2.5\,\mathrm{mK}$) sending temperature values with a resolution of 1 mK to the controlling computer at a data rate of ~0.5 Hz via a serial (RS232) interface. The temperature of the sample cell can be controlled either automatically by a resistance heater (RH in Fig. 3) with a linear power amplifier (AMP) and a digital-to-analog converter (DAC) or manually via an external thermostat (ETC).

The appropriate light emitting diodes (LED) were carefully selected by measuring the optical properties of the emitted light with a diode array spectrometer (J&M TSPEC MCS16/1024/100-1) at a forward current of 20 mA and ambient temperature of 296 K. The data are summarized in Table 1. The luminous intensities, I_V, given are typical values published by the manufacturer. The light delivered by six LED, powered by a precision current source (CCS; Burster Digistant 6426), is fed into the cells and transmitted light picked up for the photodetectors (DET) with flexible light conductors (LC; Siemens Cupoflex K). The photodetectors (light dependent resistors (LDR) or photodiodes) are part

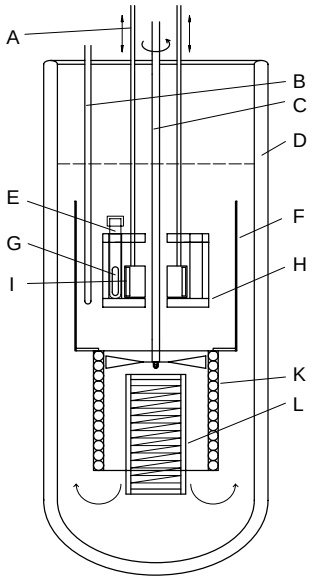

Fig. 2. Diagram of the thermostatted apparatus with solenoid rod (A); temperature sensor (B); stirrer (C); dewar vessel (D); sample cell (E); flow controller/heat conductor (F); magnetic follower (G); sample cell holder (H); magnet (I); heat exchanger (K); resistance heater (L).

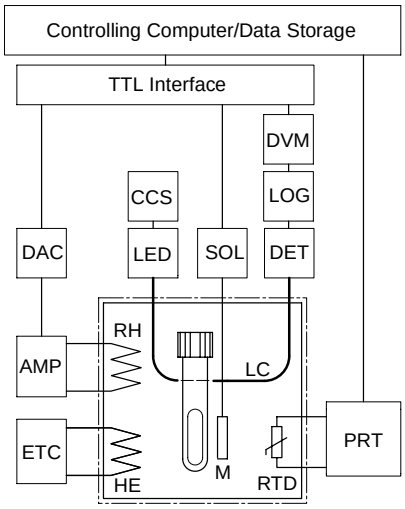

Fig. 3. Block diagram of the full instrument (see text).

of an electronic circuit (LOG) that converts the transmitted light flux to a voltage, which is subsequently measured by a precision integrating digital volt meter (DVM; Prema 5040 with 8-channel input multiplexer) and automatically recorded.

Table 1
Peak emission wavelengths, λ_{max}, spectral halfwidths, $\Delta\lambda_{1/2}$, and typical luminous intensities, I_V, of the light emitting diodes used in the apparatus

Manufacturer	Type	λ_{max} (nm)	$\Delta\lambda_{1/2}$ (nm)	I_V (mcd)
Oshino	ESB 44510	470	20	1800
Oshino	SPG 41510	525	35	4000
Hewlett-Packard	HLMP-DH08	637	17	8000

Thorough mixing of the sample is especially needed for two-phase systems. This is achieved by a PTFE (Teflon®) coated magnetic follower (G in Fig. 2) actuated by a magnet (I in Fig. 2; M in Fig. 3). One of those magnets is placed next to each sample vessel and operated through two rods by a directed current solenoid (SOL; Emessem R16 × 16). After each measurement of temperature and light intensity the solenoid is energized by the controlling computer for ≈200 ms followed by a ≈2 s break to allow settling of the photodetector response. This kind of sampled operation leads to a very high signal-to-noise level and is the major advantage compared with instruments previously described in the literature [3]. Sealed as well as screw-cap (PTFE sealing) vessels made of borosilicate glass can be used as cells. The required sample volume is 2.75 ml. Although all our measurements were performed near atmospheric pressure, the pressure limits of the apparatus can be easily extended with a different design of the sample cells.

2.2. Theory and features of operation

Ultimate aim of the instrument is the determination of phase transition temperatures from changes of the turbidity, τ, of the sample as a function of temperature, T. However, it is more convenient to measure T and τ simultaneously, but independently as a function of time, t, and to correlate both dependent variables in the subsequent data analysis. This allows the independent optimization of temperature control and turbidity measurement.

2.2.1. Temperature control and measurement

For the determination of phase transitions the bath temperature should be altered at rates $\dot{T} = dT/dt$ which are low enough to ensure thermal equilibrium between the apparatus and the studied sample. Measurements with temperature sensors placed at various positions within the oil bath revealed that values of $|\dot{T}| \lesssim 5\,K\,h^{-1}$ do not lead to significant errors. But especially for the determination of upper critical solution temperatures or for the detection of melting points very low rates must be applied to maintain thermodynamic equilibrium within the sample. Although such low rates are only needed close to the phase transition temperature, measurements would be too time-consuming if only one sample were studied and therefore the described instrument was designed for the simultaneous measurements of six samples.

Commercial precision thermostats are optimised to maintain a constant temperature in a bath or connected experimental equipment. Here a resolution of 1–10 mK in temperature measurement and control is generally sufficient. However, for such a very rapidly regulating thermostat with, e.g. 5 mK resolution a heating rate of $1\,K\,h^{-1}$ would result in a stepwise temperature rise with an equilibration time of about 18 s between two subsequent steps. In connection with other problems arising from the electronic temperature regulator, like overheating after a change of the temperature setting, such a mode of operation leads to a large noise contribution

to the time–temperature function and thus to a significant error in the determination of the phase transition temperature.

To avoid these problems it was decided to regulate the heating power in such a way that a constant $\dot{T}$ of the oil bath is achieved. For the setup $\dot{T}$ can be written as

$$\dot{T} = k_1(T_{\text{equ}} - T(t)) + \frac{U_{\text{h}}^2}{C_{\text{sys}} R_{\text{h}}} \tag{1}$$

where the first term describes the constant heating/cooling effect of the external thermostat or, if this is switched off, the heat transfer through the dewar vessel and insulation. The parameter k_1 characterizes the heat transfer and T_{equ} is the temperature of the external thermostat or the room temperature, respectively. The second term gives the rate of temperature increase induced in the setup of heat capacity C_{sys} by the immersed resistance heater (resistance R_{h}) set to the voltage U_{h} by the computer. The contribution from the stirrer is negligible.

With the instrument parameters k_1 and $k_2 = (C_{\text{sys}} R_{\text{h}})^{-1}$, determined from measurements of $\dot{T}$ as a function of U_{h}, the heater voltage necessary to maintain a constant heating rate is recalculated as

$$U_{\text{h}} = \sqrt{\frac{\dot{T} - k_1(T_{\text{equ}} - T(t))}{k_2}} \tag{2}$$

after each temperature measurement and reset by the controlling computer. Fig. 4 shows a typical example for such a temperature–time profile. Obviously, the linearity of the temperature increase is excellent. The deviations from perfect linear increase are at level of the thermometer's quantisation noise which has a resolution 1 mK. The described procedure can be used over the entire temperature range of the instrument, −20 to 80 °C, which is limited by the material of the light conductors.

2.2.2. Light source and detector characteristics

Assuming linear optical behavior of the light conductors, the luminous flux, I_0, of a light emitting diode passing through a sample medium of ideal transparency depends on the forward current generated by a constant current source. For the used LEDs this is quite accurately valid for currents in the range of 0.1–30 mA so that the behavior of the light source can be described by

$$I_0 = C_{\text{SRC}} I_{\text{LED}} \tag{3}$$

where C_{SRC} is an instrument constant. Depending on the optical properties of the sample, the LED current can be adjusted to fit the dynamic range of the photodetector. But for most studied systems a current of 10 mA was found to be appropriate.

The intensity of the transmitted light is given by $I = I_0 \exp[-\tau l]$, where l is the path length in the sample. Consequently, the turbidity τ is defined by the ratio of the transmitted luminous flux, I, to the luminous flux through a sample of ideal transparency, I_0, as

$$\tau = -l^{-1} \ln\left(\frac{I}{I_0}\right) \tag{4}$$

The photodetector—either a selected light dependent resistor or a photodiode, each in combination with an operational amplifier circuit for signal conditioning—shows logarithmic behavior, that is the detector output voltage, U_{det}, is given by

$$U_{\text{det}} = U^{\ominus} + C_{\text{det}} \ln\left(\frac{I}{I^{\ominus}}\right) \tag{5}$$

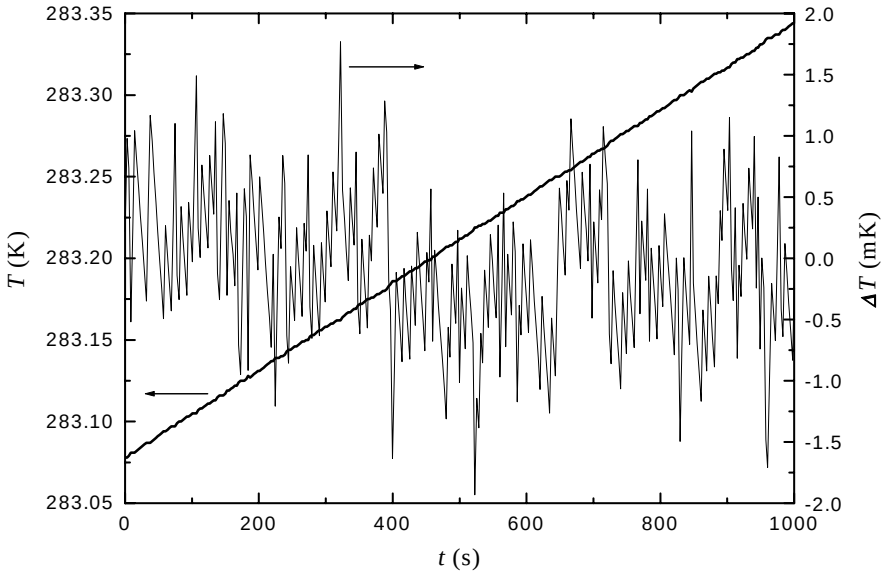

Fig. 4. Linearity and noise of the temperature rise in the thermostat: Kelvin temperature, T, and its deviation, ΔT, from linear increase as a function of time, t, for a heating rate of $\dot{T} = 1\,\text{K}\,\text{h}^{-1}$.

where $U^{\ominus}$ is the detector voltage at a reference luminous flux, $I^{\ominus}$, and C_{det} an instrument constant. Thus, the turbidity difference, $\Delta\tau$, between measurements at times t_1 and t_2 is given by

$$\Delta\tau = \tau(t_2) - \tau(t_1) = -A(U_{\mathrm{det}}(t_2) - U_{\mathrm{det}}(t_1)) \quad (6)$$

A subsumes the instrument constants. Prerequisite to the application of Eq. (6) is I_0 = constant for $t_1 \leq t \leq t_2$. Tests revealed that fluctuations of I_0 are negligible for the described instrument.

3. Evaluation of the instrument

The examples were not only selected due to the availability of accurate reference data but also to provide an overview over the range of applications possible with the instrument. For all experiments described below, Oshino ESB 44510 blue light emitting diodes, Table 1, were used together with selected Heimann A1060 light dependent resistors. This configuration gave very clear and stable signals, thus facilitating data analysis.

3.1. Materials

2,6-Lutidine (Fluka) with a GC purity of 99.2% and 410 ppm H_2O content (Karl Fischer titr.) was used as received. Ethylene carbonate (Merck, Selectipur® ≥99.9%, ∼19 ppm H_2O) was handled in a dry glove box filled with argon. Pentaethylene glycol dodecyl ether was obtained from Nikko, Japan with a purity better than 99%. Water was purified by a Millipore® Milli Q System and passed through a 0.22 μm particle filter. All mixtures were prepared gravimetrically without buoyancy correction. Compositions are thus accurate to four digits.

3.2. Lower critical solution temperatures: 2,6-lutidine/water

The binary system 2,6-lutidine/water is one of the best studied systems with a lower critical solution temperature, which makes it ideal to check the accuracy and reproducibility of the instrument. As the average of selected literature data a critical temperature of $\bar{T}_{\mathrm{c}} = 306.89 \pm 0.15$ K and a critical composition (mass fraction 2,6-lutidine) of $\bar{y}_{\mathrm{c}} = 0.2827$ is obtained [10–15]. The turbidity of a gravimetrically prepared mixture close to y_{c} was measured at low heating rates and typical τ versus T curves as shown in Fig. 5 were obtained.

For the turbidity of the solution near the critical temperature T_{c} scattering theory [16–18] yields the expression

$$\tau = \tau_0 T_{\mathrm{r}}^{-\gamma} f(a) \quad (7)$$

where $T_{\mathrm{r}} = (T_{\mathrm{c}} - T)/T$ is a reduced temperature. The function $f(a)$ depends on the wavelength of light in vacuum, λ_0, and the refractive index, n, of the solution

$$f(a) = \frac{(2a^2 + 2a + 1)\ln(1 + 2a)}{a^3} - \frac{2(1 + a)}{a^2} \quad (8)$$

where

$$a = 2\left(\frac{2\pi n\xi}{\lambda_0}\right)^2 \quad (9)$$

The correlation length, ξ, is related to the fluctuation amplitude, ξ_0, by

$$\xi = \xi_0 T_{\mathrm{r}}^{-\nu} \quad (10)$$

with ν as the critical exponent. Thus, the detector voltage, $U_{\mathrm{det}}(T)$ measured when approaching the critical point from the homogeneous part of the phase diagram can be

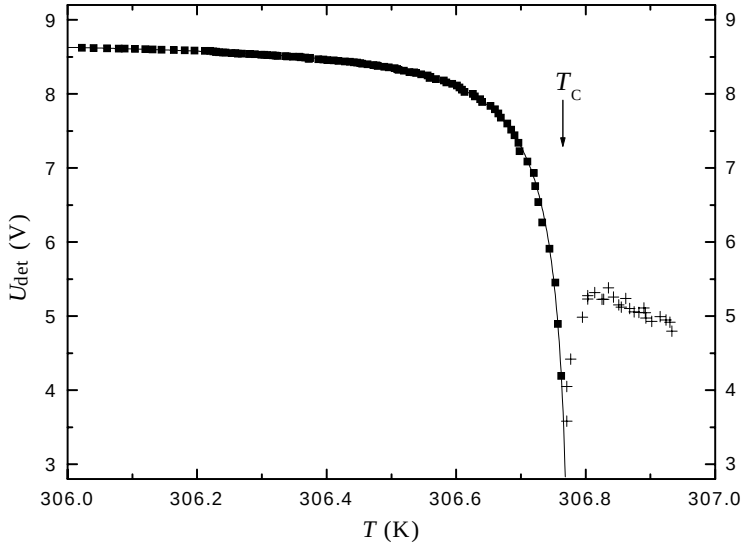

Fig. 5. Detector voltage, U_{det}, as a function of temperature, T for the phase separation of a homogenous solution of 2,6-lutidine in water ((■) single phase; (+) two phases).

Table 2
Comparison of data for the critical mass fraction of 2,6-lutidine, y_c, and the lower critical solution temperature, T_c, of 2,6-lutidine/water mixtures

Author	y_c	T_c (K)
Gutschick and Pings [10]	0.2926	306.72
Stein et al. [11]	0.2870	307.013
Kaatze and Woermann [12]	0.2533	306.76
Jungk et al. [13]	0.2913	306.92
Mayer and Woermann [14]	0.2857	306.926
Beckmann and Woermann [15]	0.2861	307.02
Average	0.2827	306.89 ± 0.15
This work	0.2760	306.780 ± 0.003

The quoted errors are maximum deviations from the corresponding mean.

written as

$$U_{\mathrm{det}} = C_1 - C_2 T_{\mathrm{r}}^{-\gamma} f(a) \quad \text{with } a = 2(C_3 T_{\mathrm{r}}^{-\nu})^2 \tag{11}$$

In the data analysis the instrument constants C_1 and C_2, the quantity $C_3 = 2\pi n \xi_0/\lambda_0$, as well as the critical temperature, T_c, were treated as adjustable parameters. The critical exponents were fixed to $\nu = 0.630$, and $\gamma = 1.241$, the theoretical values determined by renormalization group techniques [19,20]. For the investigated mixture with a 2,6-lutidine mass fraction of $y = 0.2760$, which is within the range of literature values for the critical composition, the average demixing temperature of six simultaneously investigated samples, $\bar{T}_c = 306.78$ K, determined with Eq. (11) were reproducible within ± 0.003 K and accurate to ± 0.01 K. A comparison with available literature data is given in Table 2. It is beyond the scope of this contribution to discuss all details here, but it can be seen from Fig. 5 that the theory describes the measured data very well.

3.3. Melting points: ethylene carbonate

Melting points, T_m, are usually obtained by DTA analysis or manually by different kinds of melting point apparatus. The accuracy and resolution of these methods is in most cases limited to ~0.5 K. Therefore, we investigated whether the variation of the light intensity transmitted through a melting sample is suitable the determination of melting points. Obviously, this will only work for a transparent or at least translucent sample and stirring is not possible. As the test substance ethylene carbonate was used due to its T_m in the range of our instrument and the high purity of the sample accessible to us. For these experiments two sample vials (a, b) were filled with liquid ethylene carbonate from the same batch in an argon-purged glovebox and sealed. Afterwards, the samples were cooled outside of the phase-diagram apparatus to achieve complete solidification, inserted into the instrument and heated with $\dot{T} = 0.094\,\mathrm{K\,h^{-1}}$ with the stirrer switched off. Fig. 6 shows typical experimental data for the detector voltage, $U_{\mathrm{det}}(t)$, and the corresponding temperature, $T(t)$. The sudden increase of $U_{\mathrm{det}}(t)$ at $t = 9170$ s indicates the melting point. Obviously, even a small amount of liquid forming at the grain boundaries of the solid crystalline sample leads to a significant change of its optical properties. The corresponding solid → liquid equilibrium temperature is calculated by linear regression of the time–temperature data near the melting point and a graphical determination of the time when $U_{\mathrm{det}}(t)$ changes. The melting points obtained for the same two samples (a, b) in two measurements (1, 2) performed a week apart are summarized in Table 3 together with literature data. The latter are limited to 0.1 K resolution but nevertheless in agreement with our results. The reproducibility of all our measurements was below the accuracy limits of the platinum resistance thermometer. For the

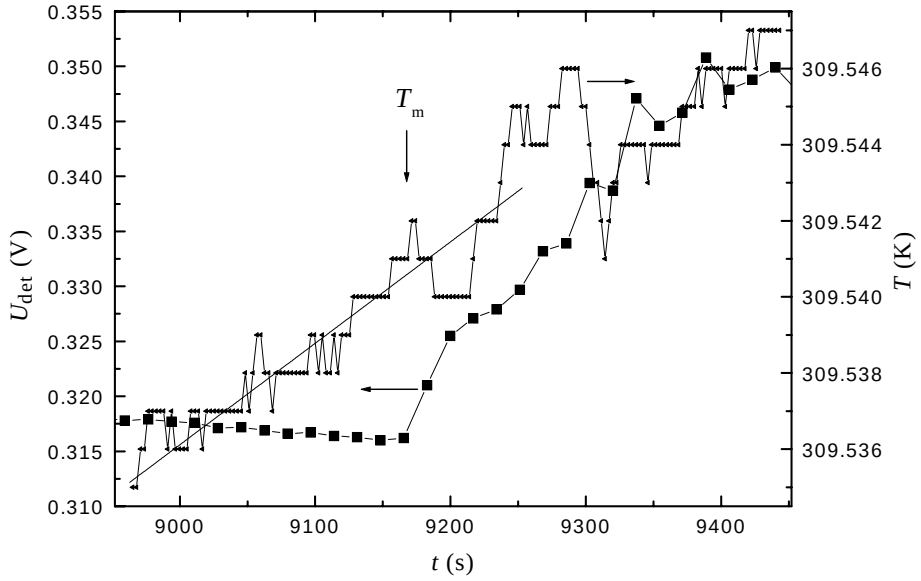

Fig. 6. Detector voltage, U_{det} (■), and temperature, T (◀), as a function of time, t for the melting of ethylene carbonate.

Table 3
Melting points, T_m, of ethylene carbonate from two independent measurements (1, 2) of two samples (a, b) at $\dot{T} = 0.094\,K\,h^{-1}$ compared with literature data.

Author	T_m (K)	This work	T_m (K)
Peppel [6]	309.55	1a	309.541
Annesini et al. [7]	309.55	1b	309.544
Ding et al. [8]	309.45	2a	309.553
Ding et al. [9]	309.55	2b	309.555
Average	309.53		309.548 ± 0.007

simultaneous measurement of the two samples (a, b) the difference in T_m never exceeded 5 mK and measurements with different heating rates below $0.25\,K\,h^{-1}$ showed no significant effect on the determined melting points. It might be that the small but systematic difference in the melting points of samples (a) and (b) arises from impurities ($\Delta T_m \approx 2.5$ mK corresponds to $\sim 5 \times 10^{-4}\,mol\,kg^{-1}$, equivalent to ~9 ppm water) introduced when filling cell (a).

3.4. Phase transitions in pentaethylene glycol dodecyl ether/water mixtures

Surfactant systems show a rich variety of phase transitions. In the case of pentaethylene glycol dodecyl ether ($C_{12}E_5$), the binary system with water shows a miscibility gap. Such behavior is well known for all kinds of nonionic surfactants and connected with large changes in the turbidity of the mixtures. In addition to this 'cloud point' transition, the system undergoes a structural transition in the liquid state that is connected with only a very small change of transmitted light. Below a temperature T_{12} the mixture has a hexagonal structure, whereas above a temperature T_{21} an isotropic micellar solution is formed. Between both temperatures the two phases coexist [1]. It should be noted that the detection of the onset of phase transition with the human eye is quite difficult in these mixtures because due to the high viscosity thermodynamic equilibrium is only slowly reached [1].

We investigated the transition from the isotropic to the hexagonal phase at a concentration of 40 wt.% of $C_{12}E_5$ in water. On cooling the isotropic micellar solution (Fig. 1a), the sample exhibits a sudden increase of the turbidity at $T_{21} = 291.11$ K due to the emergence of the second phase. Further cooling leads to a complete conversion (at ~288 K for the given $\dot{T} = -1.7\,K\,h^{-1}$) to the hexagonal phase and the photodetector response reaches the baseline level again, because the turbidities of the pure hexagonal and micellar phases are almost the same.

Fig. 1b shows U_{det} versus T for the same sample now heated with $1.7\,K\,h^{-1}$, starting from the pure hexagonal phase (obtained by keeping it at ~183 K for several days). Here the turbidity changes sharply at $T_{12} = 290.34$ K. Repeat experiments showed that with $|\dot{T}| < 5\,K\,h^{-1}$ transition temperatures can easily be obtained with an accuracy better than 0.1 K.

4. Conclusion

The automated apparatus described here can be applied for the determination of liquid/liquid and solid/liquid phase diagrams with high precision and traceable accuracy. In addition to the examples presented in this contribution the instrument was successfully used for the determination of the solubility curves of several binary glycol ether/water systems, the investigation of cloud and craft points, as well as of salting-out effects. Due to the automated, unattended operation and the simultaneous measurement of six samples the apparatus can produce high quality phase-diagram data in a reasonable time.

List of symbols

C_1, C_2, C_3	coefficients in Eq. (11)
C_{sys}	heat capacity (J/K)
C_{SRC}	instrument constant in Eq. (3)
$I, I_0, I^{\ominus}$	luminous flux (lm)
I_{LED}	diode current (I)
k_1, k_2	coefficients of Eqs. (1) and (2)
l	sample path length
n	refractive index
R_h	heater resistance (Ω)
t	time (s)
T	temperature (K)
$\dot{T}$	rate of temperature change ($K\,h^{-1}$)
T_c	critical temperature (K)
T_{equ}	temperature of external thermostate
T_m	melting point (K)
$U_{det}, U^{\ominus}$	detector voltage (V)
U_h	heater voltage (V)
y_c	critical mass fraction

Acronyms

LDR	light dependent resistor
LED	light emitting diode

Greek letters

γ, ν	critical exponents
λ_0	wavelength of light (m)
λ_{max}	peak emission wavelength
$\Delta\lambda_{1/2}$	spectral halfwidth
τ, τ_0	turbidity
ξ	correlation length (m)
ξ_0	fluctuation amplitude (m)

Acknowledgements

The authors thank H. Gores for providing the purified ethylene carbonate sample. S.S. appreciates the support of the Verband der Chemischen Industrie e.V. (VCI).

References

[1] R. Strey, R. Schomäcker, D. Roux, F. Nallet, U. Olsson, J. Chem. Soc., Faraday Trans. 86 (1990) 2253–2261.
[2] D.J. Mitchell, G.J.T. Tiddy, L. Waring, T. Bostock, M.P. McDonald, J. Chem. Soc., Faraday Trans. 179 (1983) 975–1000.
[3] G.T. Hefter, A.F.M. Barton, A. Chand, J. Chem. Soc., Faraday Trans. 87 (1991) 591–596.
[4] K. Ochi, M. Tada, K. Kojima, Fluid Phase Equilib. 56 (1990) 341–359.
[5] J. Szydlowski, L.P. Rebelo, W.A. Van Hook, Rev. Sci. Instrum. 63 (1992) 1717–1725.
[6] W.J. Peppel, Ind. Eng. Chem. 50 (1958) 767–770.
[7] M.C. Annesini, C. Capparucci, L. Marrelli, A.M. Vergara, Fluid Phase Equilib. 23 (1985) 293–302.
[8] M.S. Ding, K. Xu, T.R. Jow, J. Therm. Anal. Catal. 62 (2000) 177–186.
[9] M.S. Ding, K. Xu, S. Zhang, T.R. Jow, J. Electrochem. Soc. 148 (2001) A299–A304.
[10] V.P. Gutschick, C.J. Pings, J. Chem. Phys. 55 (1971) 3845–3850.
[11] A. Stein, S.J. Davidson, J.C. Allegra, G.F. Allen, J. Chem. Phys. 56 (1972) 6164–6168.
[12] U. Kaatze, D. Woermann, J. Phys. Chem. 88 (1984) 284–288.
[13] M. Jungk, L. Belkoura, D. Woermann, Ber. Bunsenges. Phys. Chem. 91 (1987) 507–516.
[14] W. Mayer, D. Woermann, J. Phys. Chem. 92 (1988) 2036–2039.
[15] V. Beckmann, D. Woermann, Z. Phys. Chem. NF 192 (1995) 141–153.
[16] V.G. Puglielli, N.C. Ford Jr., Phys. Rev. Lett. 25 (1970) 143–147.
[17] R.F. Chang, H. Burstyn, J.V. Sengers, Phys. Rev. A 19 (1979) 866–882.
[18] R.B. Kopelman, R.W. Gammon, Phys. Rev. A 29 (1984) 2048–2053.
[19] J. Zinn-Justin, in: M. Levy, J.C. Le Guillou, J. Zinn-Justin (Eds.), Phase Transitions, Cargese, 1980, Plenum Press, New York, 1981, pp. 349–370.
[20] J.C. Le Guillou, J. Zinn-Justin, Phys. Rev. B 21 (1980) 3976–3998.

Appendix B

Thermodynamic properties of glycol ether solutions

The following pages contain a reprint of the paper

S. Schrödle, G. Hefter, and R. Buchner,
Effects of hydration on the thermodynamic properties of aqueous glycol ether solutions,

which is part of this work.

The study provides a critical overview of the available literature and presents well-established excess molar volumes and heat capacities of various homologous series of ethylene glycol ether + water binary mixtures.

Available online at www.sciencedirect.com
SCIENCE DIRECT®
J. Chem. Thermodynamics 37 (2005) xxx–xxx
JCT
www.elsevier.com/locate/jct

Effects of hydration on the thermodynamic properties of aqueous ethylene glycol ether solutions

Simon Schrödle [a], Glenn Hefter [b], Richard Buchner [a,*]

[a] Institut für Physikalische und Theoretische Chemie, Universität Regensburg, D-93040 Regensburg, Germany
[b] Chemistry Department, DSE Murdoch University, Murdoch, WA 6150, Australia

Received 23 August 2004; accepted 8 October 2004

Abstract

The densities and isobaric specific heat capacities of binary mixtures of water with various open-chain and cyclic ethylene glycol ethers have been measured at 298.15 K using vibrating tube densimetry, and flow or differential scanning calorimetry, respectively. Excess molar volumes were derived over the whole composition range. Molar isobaric heat capacities and the relative apparent thermodynamic quantities were determined in the water-rich region. The data reflect the changes in the structure and hydrogen-bond dynamics of water caused by these non-ionic solutes. The observed effects are discussed in terms of the influence of hydrophobic hydration on the thermodynamic properties of aqueous solutions. Correlations are given that enable the prediction of the thermodynamic properties of open-chain and cyclic oligo(ethylene oxide) ethers in their pure liquid state and at infinite dilution in water.

Keywords: Hydrophobic hydration; Glycol ethers; Cyclic ethers; Apparent heat capacity; Excess volume

1. Introduction

Water shows distinctive properties relative to other solvents due to its strong intermolecular forces, which produce an extensive three-dimensional network of hydrogen (H) bonds. H-bonding in water is a highly cooperative phenomenon, mainly due to the small size of the water molecule and its considerable charge separation (high dipole moment) and its 1:1 ratio of donor to acceptor sites. The presence of non-ionic compounds in aqueous solutions typically results in significant changes to the local and long-range water structure. Particularly large thermodynamic effects occur in the presence of hydrophobic solutes. Such effects are of outstanding importance in understanding many biological processes and in polymer, surface and colloid science.

Straight chain oligo(ethylene glycol)s and their mono- and dimethyl ether analogues are miscible with water over the whole composition range, apparently without forming higher aggregates like micelles. As such, they provide a series of solutes with systematically varying characteristics, which can be used to probe the influences of hydrophobic hydration and the H-bond donor–acceptor ratio on the dynamics and structure of the H-bond network. Comparisons of the thermodynamic properties of aqueous solutions of open-chain oligo(ethylene glycol) ethers with those of related, but more rigid, cyclic ethers such as 1,4-dioxane and the crown ethers can in addition provide insights into the structural effects of organic solutes on water properties.

This investigation compares the molar excess volumes, V^E, and the relative apparent heat capacities, $\Delta C_{p,\Phi,2}$, of mixtures of water with oligo(ethylene glycol) monomethyl ethers, C_1E_nOH, and dimethyl ethers, $C_1E_nC_1$, of oligomerisation degree $1 \leqslant n \leqslant 5$. For some

* Corresponding author. Tel.: +49 9419434031.
E-mail address: richard.buchner@chemie.uni-regensburg.de (R. Buchner).

0021-9614/$ - see front matter © 2004 Elsevier Ltd. All rights reserved.
doi:10.1016/j.jct.2004.10.006

of the compounds, the volume properties have been reported for the aqueous solutions by other investigators. However, because of serious inconsistencies among the reported values, it was considered appropriate to measure them again systematically with samples of well-established purity.

2. Experimental

2.1. Materials

1,4-Dioxane (Merck, pro analysi) was purified by refluxing over solid calcium hydride (CaH_2) for several hours [1] and subsequently distilled over a 40 cm column at atmospheric pressure, resulting in a final purity of 0.9997 mole fraction (g.c.); $H_2O \leqslant 30$ ppm (Karl Fischer coulometric titration). Ethylene glycol monomethyl ether (C_1E_1OH; Fluka; 0.999 mole fraction; $H_2O \leqslant 300$ ppm), ethylene glycol dimethyl ether ($C_1E_1C_1$; Sigma; 0.9994 mole fraction; $H_2O \leqslant 80$ ppm) and triethylene glycol monomethyl ether (C_1E_3OH; Fluka; 0.997 mole fraction; $H_2O \leqslant 300$ ppm) were used as received. Diethylene glycol dimethyl ether (Merck, for synthesis) was heated with solid CaH_2, then fractionally distilled at atmospheric pressure using a 25 cm column, giving a product with a purity of 0.999 mole fraction; $H_2O \leqslant 60$ ppm. Triethylene glycol dimethyl ether ($C_1E_3C_1$; Merck, for synthesis) was distilled at ~1 mbar using a 65 cm column. The fraction used for measurements had a purity of 0.998 mole fraction; $H_2O \leqslant 500$ ppm.

Pentaethylene glycol monomethyl ether (C_1E_5OH) was prepared from diethylene glycol and 1-(2-chloroethoxy)-2-(2-methoxy-ethoxy)-ethane as follows. Using stirring throughout, a stochiometric amount of sodium metal (12.7 g) and 0.1 g of powdered, anhydrous sodium iodide (NaI) were added to 233.5 g diethylene glycol (dried by distillation). The mixture was heated to 120 °C until all the sodium dissolved. Then 100.5 g of 1-(2-chloro-ethoxy)-2-(2-methoxy-ethoxy)-ethane (prepared from triethylene glycol monomethyl ether and thionyl chloride [2], fractionated at ~0.1 mbar) was added dropwise and the resulting mixture heated (120 °C) for several hours. After standing overnight, sodium chloride was removed by filtration and washed with methanol. The filtrate was evaporated and the excess diethylene glycol removed by distillation at ~0.03 mbar using a 25 cm column. Phosphoric acid (~20% w/w, 25 mL) was added to the residue and the aqueous phase extracted with dichloromethane ($4 \cdot 100$ mL). The combined extracts were evaporated and the residue was fractionated at 0.02 mbar. The middle fraction was further purified using a short-path molecular distillation apparatus at $\sim 3 \cdot 10^{-5}$ mbar. Pentaethylene glycol monomethyl ether (58 g) with a final purity of 0.994 mole fraction ($H_2O \leqslant 500$ ppm, $n_D^{25} = 1.4481$) was collected.

Pentaethylene glycol dimethyl ether ($C_1E_5C_1$) was prepared in a similar way from ethylene glycol monomethyl ether and 1,2-bis-(2-chloro-ethoxy)-ethane: 69 g sodium was cut into small pieces and added under stirring to 500 g ethylene glycol monomethyl ether (C_1E_1OH; destilled from CaH_2). This mixture was heated to 100 °C until the sodium dissolved. Anhydrous NaI (1 g, finely powdered) and 281 g 1,2-bis-(2-chloroethoxy)-ethane (dropwise) were added, and heating (100 °C) continued for 3 days. After evaporation of excess C_1E_1OH the remainder was dissolved in water and extracted with dichloromethane ($4 \cdot 100$ mL). The organic layers were combined, dried over anhydrous sodium sulfate and evaporated. The residue was then distilled at 0.04 mbar. The fraction boiling between (95 and 119) °C was heated with 100 mL of ~5% hydrochloric acid for a few hours to decompose byproducts (acetals), washed with *n*-pentane (3.50 mL) and the water evaporated at atmospheric pressure. 300 mL dichloromethane was added to the residue. After stirring over anhydrous potassium carbonate for several hours the dichloromethane was removed under vacuum. The raw product was fractionated over a 40 cm column at 0.03 mbar and the center fraction (b.p. ~105 °C) was further distilled at ~0.008 mbar using a Fischer Spaltrohr apparatus (60 theoretical plates at 1013 mbar). The pentaethylene glycol dimethyl ether (73 g) so obtained had a purity of 0.997 mole fraction ($H_2O \leqslant 500$ ppm; $n_D^{25} = 1.4376$).

The structures of the pentaethylene glycol ethers were confirmed by n.m.r. spectroscopy (^1H, ^{13}C and ^{13}C DEPT 135°).

Note that all reactions were carried out with anhydrous reagents under a dry nitrogen atmosphere. All distillation employed vacuum-jacketed Vigreux colums.

Aqueous mixtures were prepared gravimetrically on an analytical balance without buoyancy corrections. Concentrations are thus accurate to four significant figures. Water, deionized and purified with a Millipore Milli-Q system (with a final pass through a 0.22 μm filter) was used throughout. All pure liquids were carefully degassed at low pressure prior to mixture preparation.

2.2. Apparatus and procedure

Solution densities, ρ, were determined by vibrating tube densimetry (Anton Paar DMA602/mPDS4000 system) and are accurate to $\sim 5 \cdot 10^{-3}$ kg · m^{-3}. The temperature was kept constant to ±4 mK with a circulating thermostat (Julabo F33 SD). The densimeter was calibrated using water and air as references. The density of water at 298.15 K was taken as 997.047 kg · m^{-3} consistent with the IAPWS-IF97 value [3], and that of air was calculated from generally accepted equations [4].

At least two independent density measurements were performed with each solution.

Isobaric volumetric heat capacities were measured relative to water using a Picker flow calorimeter (Sodev, Sherbrooke, Canada), consisting of a specific heat unit, model CP-Cpr, a thermal detector, model DT-C, and a temperature control/program unit, model CT-L. A peristaltic pump (Gilson Minipulse 3) was used to control the flow rate (~0.5 $mL \cdot min^{-1}$). The output voltage from the detector was digitized by a voltmeter (Agilent 34401A) connected to a computer. From each measurement, two independent values were determined for the relative volumetric heat capacity $\Delta\sigma/\sigma^\circ = (\sigma - \sigma^\circ)/\sigma^\circ$, where σ and σ° are the heat capacities per unit volume of the sample and reference liquid, respectively [5]. The values of c_p, the isobaric specific heat capacity, were calculated from these values using the following expression [6]:

$$c_p = c_p^\circ \cdot (1 + \Delta\sigma/\sigma^\circ) \cdot \rho^\circ/\rho. \quad (1)$$

The calorimeter was calibrated electrically at the end of each series of measurements. Water was used as a reference liquid, assuming $c_p^\circ = 4181.3\ J \cdot K^{-1} \cdot kg^{-1}$ according to the IAPWS-95 formulation [7]. No correction was made for heat losses [5].

A Tian-Calvet type heat-conduction microcalorimeter (MicroDSC II, Setaram, France) was utilized to measure the heat capacities of the pure organic materials with an accuracy sufficient for the determination of thermodynamic excess quantities. Specially designed batch cells (sample volume ~0.8 mL) made from stainless steel with a perfluoroelastomer O-ring seal (Kalrez 4079) were used. A discontinuous step method was employed with heating/cooling rates of 0.1 K/min and an isothermal delay of 3600 s [8,9]. The power difference needed to heat or cool the reference and sample cells between (297.65 and 298.65) K (1 K step) were determined by integration of the heat flow signals. An internal reference (*n*-heptane; $c_p = 2244.4\ J \cdot K^{-1} \cdot kg^{-1}$ [10]) was used. Heat capacities were calculated from two independent experiments, each consisting of several heating and cooling cycles. The reproducibility of the c_p values was usually better than 0.1%, the overall uncertainty of the measurement estimated from calibration and test experiments is assumed to be ~0.3%. No allowances were made for sample vaporization and gas phase corrections as the vapor volume was kept below 10% of the total cell volume and all substances have quite low vapor pressures at the measurement temperature [11].

3. Data treatment

Experimental results for the densities, ρ, and specific heat capacities, c_p, of the pure compounds are given in table 1; those of the mixtures of the various ethers with water are summarized in tables 2 to 4. From these data, apparent thermodynamic quantities relative to the pure liquid state of the solute,. $\Delta Y_{\Phi,2}$, were obtained by the following equation:

$$\Delta Y_{\Phi,2} = \frac{Y - x_1 \cdot Y_1^\circ}{x_2} - Y_2^\circ. \quad (2)$$

Here, Y denotes the molar quantities of the mixtures, and Y° the corresponding properties of the pure substances. For the systems studied, the relative apparent quantities are more helpful than the absolute quantities for comparison of compounds of different chain length.

TABLE 1
Densities, ρ, and isobaric specific heat capacities, c_p, of the pure liquid ethers, obtained in this work along with the literature values, all at 298.15 K

Compound	M	$\rho/(kg \cdot m^{-3})$		$c_p/(J \cdot K^{-1} \cdot kg^{-1})$	
	$10^{-3}\ kg \cdot mol^{-1}$	This work	Literature	This work	Literature
1,4-Dioxane	88.11	1028.043	1027.92 [12] 1027.98 [13] 1028.07 [15]	1719.9	1713.2 [10] 1696.7 [14]
C_1E_1OH	76.10	960.164	960.34 [16] 960.16 [18] 960.101 [19]	2295.3	2304.9 [17] 2289.8 [19]
$C_1E_1C_1$	90.12	861.199	861.506 [20] 861.32 [21] 861.48 [23]	2124.8	2144.4 [17] 2121.0 [22] 2121.8 [24]
$C_1E_2C_1$	134.17	938.529	938.73 [25] 938.4 [26]		2083.8 [25] 2079.8[27]
C_1E_3OH	164.20	1042.965	1043.0 [28]	2174.5	
$C_1E_3C_1$	178.23	981.686	980.82 [29] 981.17 [30] 980.01 [33]	2074.6	2069.2 [17] 2073.3 [32] 2071.4 [29]
C_1E_5OH	252.30	1069.437		2128.8	
$C_1E_5C_1$	266.33	1024.793		2055.4	

TABLE 2
Densities, ρ, and isobaric specific heat capacities, c_p, of {water (1) + 1,4-dioxane (2)} mixtures at 298.15 K

x_2	$x_{O,2}$	ρ / kg · m^{-3}	c_p / J · K^{-1} · kg^{-1}	x_2	$x_{O,2}$	ρ / kg · m^{-3}	c_p / J · K^{-1} · kg^{-1}
			{Water (1) + 1,4-dioxane(2)}				
0	0	997.05	4181.3	0.2000	0.3333	1034.98	2979.3
0.00990	0.01961	1000.99	4102.4	0.2857	0.4444	1036.85	2709.2
0.01639	0.03226	1003.44	4050.7	0.4000	0.5714	1036.18	
0.03226	0.06250	1009.01	3925.2	0.5000	0.6667	1034.66	
0.06250	0.1177	1017.66	3702.3	0.6667	0.8000	1031.91	
0.09091	0.1667	1023.79	3507.9	0.8000	0.8889	1029.87	
0.1111	0.2000	1027.12	3388.0	0.8889	0.9412	1028.76	
0.1429	0.2500	1030.99	3222.6	1	1	1028.04	1719.9

TABLE 3
Densities, ρ, and isobaric specific heat capacities, c_p, of {water (1) + oligoethylene glycol monomethyl ethers (2)} mixtures at 298.15 K

x_2	$x_{O,2}$	ρ / kg · m^{-3}	c_p / J · K^{-1} · kg^{-1}	x_2	$x_{O,2}$	ρ / kg · m^{-3}	c_p / J · K^{-1} · kg^{-1}
			{Water (1) + ethylene glycol monomethyl ether (2)}				
0	0	997.05	4181.3	0.1111	0.2000	1006.32	3811.2
0.01316	0.02597	998.08	4157.0	0.1429	0.2500	1006.98	3680.8
0.01961	0.03846	998.70	4142.6	0.2000	0.3333	1005.88	3456.0
0.03846	0.07407	1000.68	4090.9	0.3333	0.5000	997.80	3073.8
0.04762	0.09091	1001.65	4061.0	0.5000	0.6667	985.96	
0.06250	0.1176	1003.11	4008.0	0.6667	0.8000	975.40	
0.07692	0.1429	1004.34	3952.0	0.8000	0.8889	968.51	
0.09091	0.1667	1005.32	3894.8	1	1	960.17	2295.3
			{Water (1) + triethylene glycol monomethyl ether (2)}				
0	0	997.05	4181.3	0.1111	0.3333	1049.55	3413.8
0.01316	0.05063	1007.68	4082.0	0.1429	0.4000	1053.42	3265.7
0.01961	0.07407	1012.43	4031.6	0.2000	0.5000	1055.74	
0.03846	0.1379	1024.71	3883.0	0.3333	0.6667	1053.92	
0.04762	0.1667	1029.57	3812.9	0.5000	0.8000	1050.27	
0.06250	0.2105	1036.38	3704.7	0.6667	0.8889	1047.07	
0.07692	0.2500	1041.50	3607.5	0.8000	0.9412	1045.27	
0.09091	0.2857	1045.55	3519.1	1	1	1042.97	2174.5
			{Water (1) + pentaethylene glycol monomethyl ether (2)}				
0	0	997.05	4181.3	0.09091	0.3750	1068.43	3324.1
0.00662	0.03846	1007.31	4097.2	0.1667	0.5455	1076.08	2976.3
0.00990	0.05660	1012.04	4056.2	0.3333	0.7500	1075.06	
0.01961	0.10714	1024.63	3937.7	0.5000	0.8571	1072.73	
0.03846	0.1936	1043.39	3731.4	0.6667	0.9231	1071.22	
0.06250	0.2857	1058.63	3517.5	1	1	1069.44	2128.8

As mole fraction is not fully satisfactory as a measure of composition for oligomeric systems, the mole fraction of oxygen atoms from the non-ionic solute

$$x_{O,2} = \frac{n_{O,2} \cdot x_2}{n_{O,2} \cdot x_2 + x_1} = \frac{n_{O,2} \cdot x_2}{1 + x_2 \cdot (n_{O,2} - 1)} \quad (3)$$

was used, where (1) denotes water and (2) the ether compound containing $n_{O,2}$ oxygen atoms.

Excess molar volumes (figures 1 to 3) were derived from the density values by the equation

$$V^E = V - V^{id} = \frac{x_1 M_1 + x_2 M_2}{\rho} - \sum_i x_i V_i^\circ, \quad (4)$$

where M_i is the molar mass of the pure liquid component i.

4. Results

4.1. Volumes

The densities for the pure compounds are mostly in good agreement (better than 50 ppm, table 1) with the literature data. The only exceptions are $C_1E_1C_1$ for which the present result is 240 ppm lower and $C_1E_3C_1$ where it is 1000 ppm higher than the average of the reported values, although both values are still within 3σ of the literature means. The source of these differences is unknown but purity is probably the most critical factor. All the glycol ethers are sensitive to oxygen and readily absorb significant amounts of water from air. Special

TABLE 4
Densities, ρ, and isobaric specific heat capacities, c_p, of {water (1) + oligoethylene glycol dimethyl ethers (2)} mixtures at 298.15 K

x_2	$x_{O,2}$	ρ / kg · m^{-3}	c_p / J · K^{-1} · kg^{-1}	x_2	$x_{O,2}$	ρ / kg · m^{-3}	c_p / J · K^{-1} · kg^{-1}
{Water (1) + ethylene glycol dimethyl ether (2)}							
0	0	997.05	4181.3	0.1111	0.2000	979.24	3864.4
0.01316	0.02597	993.84	4177.4	0.1429	0.2500	972.59	3726.8
0.01961	0.03846	992.67	4171.4	0.2000	0.3333	958.93	3474.8
0.03846	0.07407	989.98	4137.6	0.3333	0.5000	929.51	3042.5
0.04762	0.09091	988.87	4113.0	0.5000	0.6667	903.35	
0.06250	0.1177	987.00	4064.6	0.6667	0.8000	885.19	
0.07692	0.1429	985.05	4010.6	0.8000	0.8889	873.97	
0.09091	0.1667	982.88	3953.1	1	1	861.20	2124.8
{Water (1) + triethylene glycol dimethyl ether (2)}							
0	0	997.05	4181.3	0.1111	0.3333	1024.83	3462.3
0.01316	0.05063	1003.92	4102.0	0.1429	0.4000	1022.94	3292.3
0.01961	0.07407	1007.09	4060.4	0.2000	0.5000	1017.20	3054.9
0.03846	0.1379	1015.26	3928.5	0.3333	0.6667	1005.21	
0.04762	0.1667	1018.21	3862.1	0.5000	0.8000	995.86	
0.06250	0.2105	1021.75	3757.5	0.6667	0.8889	989.62	
0.07692	0.2500	1023.84	3661.3	0.7936	0.9389	986.18	
0.09091	0.2857	1024.79	3575.8	1	1	981.69	2074.6
{Water (1) + pentaethylene glycol dimethyl ether (2)}							
0	0	997.05	4181.3	0.09091	0.3750	1048.94	3324.2
0.00662	0.03846	1005.40	4107.3	0.1667	0.5455	1046.87	
0.00990	0.05660	1009.29	4071.1	0.3333	0.7500	1037.64	
0.01961	0.1071	1019.64	3963.5	0.5000	0.8571	1031.91	
0.03846	0.1936	1034.39	3770.1	0.6667	0.9231	1028.40	
0.06250	0.2857	1044.63	3546.0	1	1	1024.79	2055.4

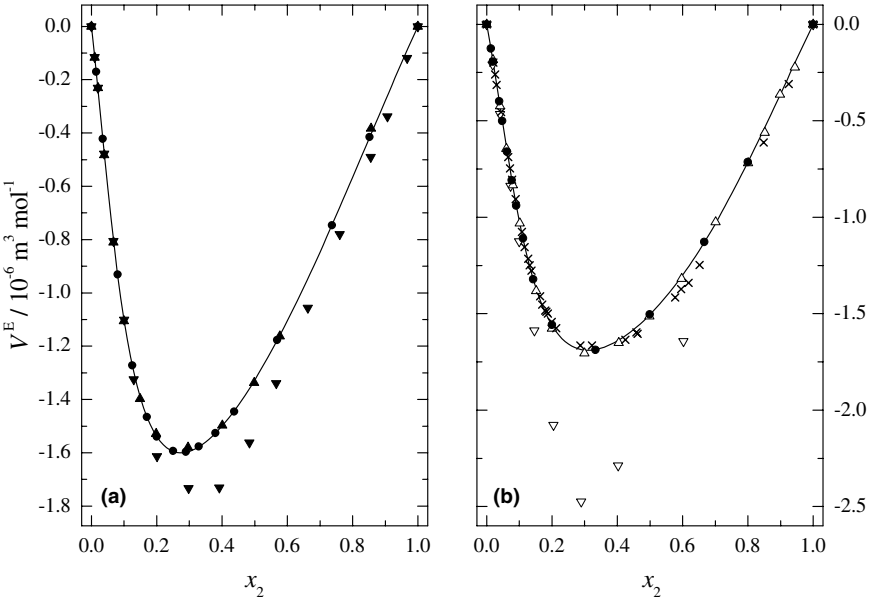

FIGURE 1. Molar excess volumes, V^E, of mixtures of water (1) + $C_1E_2C_1$ (2) (a) and $C_1E_1C_1$ (2) (b). The markers represent the experimental values: (●) this work, (▲) reference [26], (▼) reference [30], (×) reference [36], (△) reference [37] and (▽) reference [38].

care therefore needs to be taken with regard to purification and storage (see section 2). No densities appear to have been reported previously for C_1E_5OH and $C_1E_5C_1$.

Given the generally good agreement among the literature (and present) densities of the pure compounds (table 1), it is surprising to find that major discrepancies exist in the densities (and related excess molar volumes) of their mixtures with water. This is illustrated in figure 1 for mono- and diethylene glycol dimethyl ether, $C_1E_1C_1$ and $C_1E_2C_1$. The present data clearly

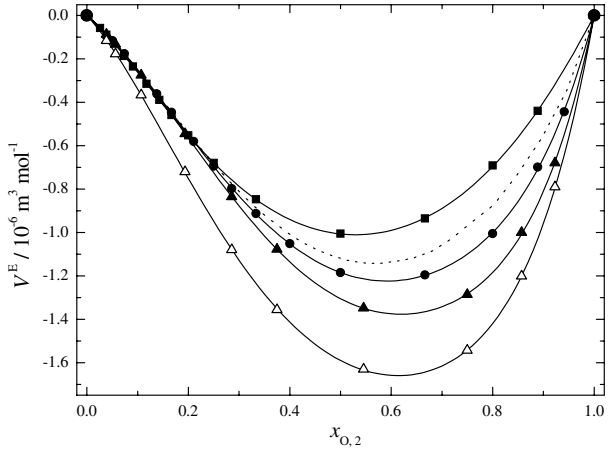

FIGURE 2. Molar excess volumes, V^E, of mixtures of water (1) + C_1E_1OH (■), C_1E_2OH [43] (dotted line), C_1E_3OH (●), C_1E_5OH (▲) and $C_1E_5C_1$ (△).

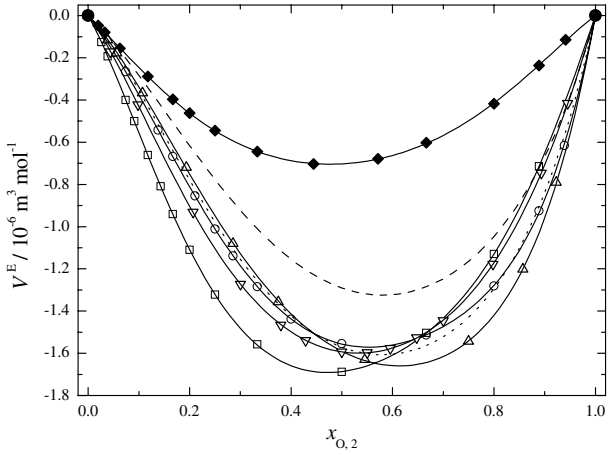

FIGURE 3. Molar excess volumes, V^E, of mixtures water (1) + 1,4-dioxane (♦), 12-crown-4 [36] (dashed line), $C_1E_1C_1$ (□), $C_1E_2C_1$ (▽), $C_1E_3C_1$ (○), $C_1E_4C_1$ [30] (dotted line) and $C_1E_5C_1$ (△).

support the older determinations by Wallace and Mathews [26,37] rather than the more recent vibrating tube study by Dethlefsen and Hvidt [30] and Marchetti *et al.* [38], even though the former was obtained by the less accurate [31] pycnometric method. The source of this discrepancy is unknown but it is noted that Wallace and Mathews distilled their ethers from sodium immediately prior to use whereas Dethlefsen and Hvidt used an untreated commercial sample with a stated purity of only 0.98 mole fraction. The lithium aluminium hydride method employed by Marchetti *et al.* [38] for purification of ethers is known to be ineffective [1]. It is of concern that the less accurate data for $C_1E_2C_1$ [30] have been utilized in several other investigations [36,39]. Similar considerations apply to the mixtures of water with $C_1E_1C_1$. In each case the present results (tables 4 and 5) confirm the older values and it is disturbing that none of the more recent papers cite the earlier work.

TABLE 5
Densities, ρ, of {water (1) + diethylene glycol dimethyl ether (2)} mixtures at 298.15 K

x_2	$x_{O,2}$	ρ / kg · m^{-3}
{Water (1) + diethylene glycol dimethyl ether (2)}		
0	0	997.05
0.01495	0.04355	999.33
0.03497	0.09806	1002.88
0.08002	0.2069	1006.59
0.1251	0.3002	1003.91
0.1696	0.3800	998.18
0.2001	0.4287	993.70
0.2501	0.5002	986.48
0.2897	0.5502	981.26
0.3293	0.5956	976.53
0.3798	0.6476	971.16
0.4375	0.7000	965.91
0.5689	0.7984	956.27
0.7366	0.8935	947.49
0.8522	0.9453	942.93
1	1	938.53

Figures 2 and 3 show the excess molar volumes derived from the present density data for mixtures of water with the compounds of interest, along with selected literature values for related compounds. All V^E values are negative across the entire composition range. Their minima, V^E_{min}, are shifted to higher $x_{O,2}$ values with increasing degree of polymerisation, n, figure 4. Simultaneously, V^E_{min}, decreases from (−1.0 to −1.4) cm^3 · mol^{-1} for the monomethyl ethers, whereas only moderate changes were observed for the dimethyl ethers. For the cyclic ethers, where only limited data are available, there is some evidence that they behave

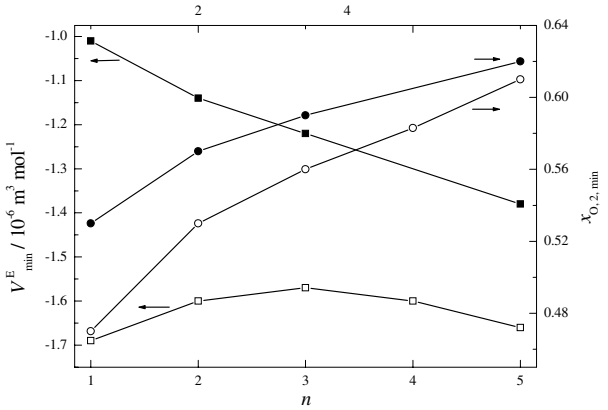

FIGURE 4. Shift of the minimum value of the molar excess volumes, V^E_{min} (□), and the minimum position, $x_{O,2,min}$ (○) of mixtures of water (1) + homologous series of oligo(ethylene glycol) monomethyl ethers (full symbols) and dimethyl ethers (open symbols) at 298.15 K.

more like the monomethyl ethers [36]. Apparently, the V^{E}_{min} of C_1E_nOH and $C_1E_nC_1$ as a function of n are approximately parallel for $n \geqslant 3$. The comparison of ethylene glycol monomethyl ether, C_1E_1OH, with its dimethyl analogue, $C_1E_nC_1$, shows, that the terminal –CH_2–OMe groups give rise to a strong negative volume contribution.

The relative apparent molar volumes, $\Delta V_{\Phi,2}$, show distinct minima at $x_{O,2} \approx 0.12$ to 0.15, figure 5. It is striking that at higher dilution the volume effects of the $C_1E_nC_1$ compounds almost coincide with those of their $C_1E_{n+2}OH$ homologues, especially for the higher members. From the extrapolation of the $\Delta V_{\Phi,2}$, values of the molar volume at infinite dilution, $\Delta V^{\circ}_{\Phi,2}$, can be obtained (table 6). Close agreement of our data with the available literature values was found. The present results appear to be the first estimates for the pentaethylene glycol derivatives. Their estimated accuracy is $\sim 0.15 \cdot 10^{-6}$ m$^3 \cdot$ mol^{-1}.

4.2. Heat capacities

The isobaric specific heat capacities of the pure compounds are given in table 1. Where comparison is possible, the present data are in good agreement (better than 5 J $\cdot$ K$^{-1} \cdot$ kg^{-1}) with the means of the literature values, with the partial exception of 1,4-dioxane which differs slightly (<2%). Interestingly, the available literature heat capacities have been classified as having an accuracy of only 2% [10,17].

The molar excess heat capacities, C^{E}_{p}, calculated from the present data are positive over the composition range studied, so are the relative apparent quantities, $\Delta C_{p,\Phi,2}$, figure 6. As for the volumes (figure 5), aqueous solutions of the $C_1E_nC_1$ compounds have relative apparent heat capacities that are very close to their $C_1E_{n+2}OH$ homologues at $x_{O,2} \approx 0.15$.

Heat capacities at infinite dilution in water, $\Delta C^{\circ}_{p,\Phi,2}$, were determined by extrapolation. The values so ob-

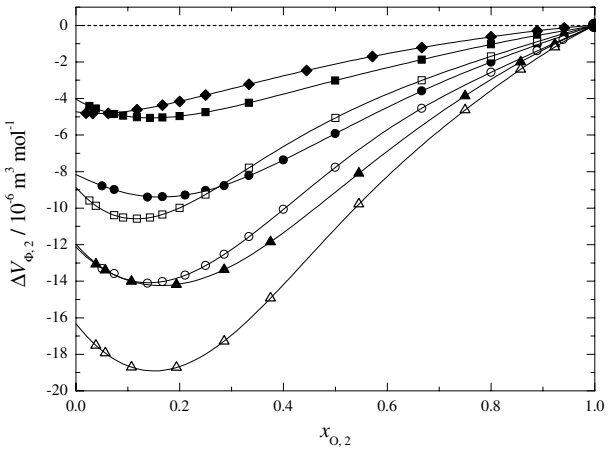

FIGURE 5. Relative apparent molar volumes, $\Delta V_{\Phi,2}$, of mixtures of water (1) + 1,4-dioxane (♦), C_1E_1OH (■), $C_1E_1C_1$ (□), C_1E_3OH (●), $C_1E_3C_1$ (○), C_1E_5OH (▲) and $C_1E_5C_1$ (△) at 298.15 K.

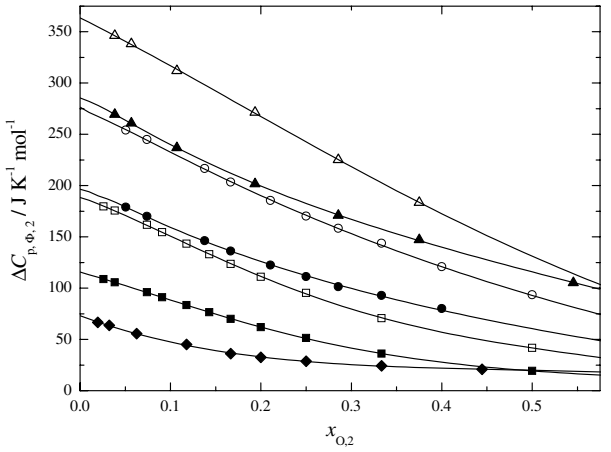

FIGURE 6. Relative apparent molar heat capacities, $\Delta C_{p,\Phi,2}$, of mixtures of water (1) + 1,4-dioxane (♦), C_1E_1OH (■), $C_1E_1C_1$ (□), C_1E_3OH (●), $C_1E_3C_1$ (○), C_1E_5OH (▲) and $C_1E_5C_1$ (△) at 298.15 K.

TABLE 6
Relative apparent molar volumes and heat capacities of various ethers at infinite dilution in water at 298.15 K

Compound	$n_{O,2}$	$\Delta V_{\Phi,2\circ}$/(10^{-6} m$^3 \cdot$ mol^{-1})		$\Delta C_{p,\Phi,2}{}^{\circ}$/(J $\cdot$ K$^{-1} \cdot$ mol^{-1})	
		This work	Literature	This work	Literature
1,4-Dioxane	2	−4.73	−4.77 [40]	71.9	70.9 [40]
			−4.75 [41]		
C_1E_1OH	2	−4.04	−4.14 [18]	115.9	116.3 [16]
			−4.08 [16]		112.0 [18]
					115.3 [45]
$C_1E_1C_1$	2	−8.87	−8.75 [34]	188.4	188.5 [45]
C_1E_3OH	4	−8.17	−8.02 [43]	196.4	
$C_1E_3C_1$	4	−11.97	−11.85 [35]	276.5	
			−11.65 [44]		
			−11.72 [42]		
C_1E_5OH	6	−12.13		285.4	
$C_1E_5C_1$	6	−16.33		365.3	

tained are in close agreement with the literature estimates where these are available (table 6).

4.3. Ethylene oxide group increments

The molar volumes, V_i°, and isobaric molar heat capacities, $C_{p,i}^\circ$, of the pure compounds increase virtually linearly within the various homologous series, figure 7(a) and (b). Thus, the increments V_i° in 10^{-6} $m^3 \cdot mol^{-1}$ upon addition of one E (–CH_2CH_2O–) group are 39.2, 38.9 and 37.5, whereas for $C_{p,i}^\circ$ the corresponding values are 90.9, 89.2 and 87.3 $J \cdot K^{-1} \cdot mol^{-1}$ (omitting 1,4-dioxane) to, respectively, the mono-, di- (present work) and cyclic-ethers [46].

Similar linear correlations were found between chain length and the relative apparent quantities of oligo(ethylene glycol) monomethyl and dimethyl ethers at infinite dilution in water, figure 7(c) and (d). The average increments of $\Delta V_{\Phi,2}^\circ$ per E group found for the C_1E_nOH and $C_1E_nC_1$ compounds were (-2.04 and $-2.07 \cdot 10^{-6}$) $m^3 \cdot mol^{-1}$.

For the corresponding $\Delta C_{p,\Phi,2}^\circ$ values, increments of (42.4 and 44.2) $J \cdot mol^{-1} \cdot K^{-1}$ were obtained. The value of $\Delta C_{p,\Phi,2}^\circ$ for $C_1E_1C_1$, which deviates from the linear trend because of its two –OMe groups, was not used for the fit.

With the increments given above it should be possible to predict volumetric properties and heat capacities of

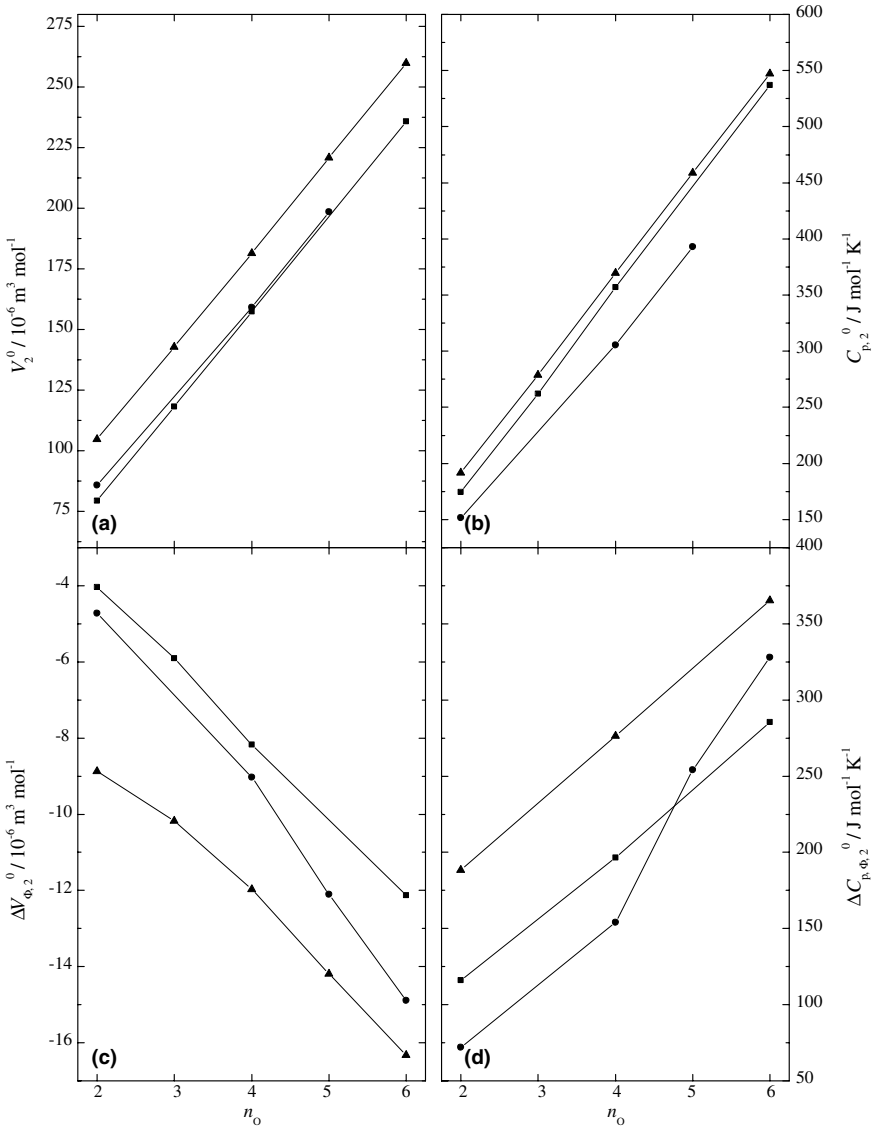

FIGURE 7. (a) Molar volumes, V_2°, and (b) molar heat capacities, $C_{p,2}^\circ$, for various homologous series of pure liquid cyclic ethers (●), oligo(ethylene glycol) monomethyl ethers (■) and dimethyl ethers (▲). (c) Relative apparent molar volumes, $\Delta V_{\Phi,2}^\circ$, and (d) relative apparent heat capacities, $\Delta C_{p,\Phi,2}^\circ$, at infinite dilution in water, for the same ethers. n_O denotes the number of oxygen atoms per molecule of the organic compound [43,44,46]; all values at 298.15 K.

other ethylene glycol ethers, including those of polydisperse industrial mixtures.

5. Discussion

It is always problematic to draw structural conclusions from thermodynamic data. However, in this case the volume defects observed are consistent with a contraction of the water structure near the hydrophobic surfaces of the –OMe or –O–CH_2CH_2–O– groups. As V^E_{min} is located close to the 1:1 ratio of water molecules to H-bond acceptor sites on the solutes, the formation of a packed collection of water with oligo(ethylene glycol) dimethyl ether molecules can be proposed. Because of the highly flexible nature of the open-chain ethers, these groupings are probably not strongly associated. Dielectric relaxation studies indicate that, although the dynamics of these systems slow down significantly, they are still governed by rapidly fluctuating H-bond networks [47].

At high dilution in water, the effects of non-ionic compounds on the thermodynamic properties of the mixtures cannot be easily extracted from molar excess quantities. In this region it is more helpful to discuss the relative apparent molar values. Such quantities can be interpreted as the molar volumes of the fully hydrated, non-associated solute.

From the very similar behavior of the $C_1E_nC_1$ compounds and their $C_1E_{n+2}OH$ homologues, it would seem that at high dilution the –CH_2–O–CH_2CH_2–OH moiety can be incorporated into the water structure almost without thermodynamic excess effects. The relative apparent molar heat capacities, $\Delta C_{p,\Phi,2}$, of these related ethers are parallel up to $x_{O,2} \approx 0.15$. As indicated by the minima in $\Delta V_{\Phi,2}$, figure 5, at higher concentrations the structure of water already starts to get heavily disturbed and association of the monomethyl ethers becomes more important.

1,4-Dioxane is the smallest member of the cyclic ethers series. It cannot be considered as a rigid molecule, but it has a lower degree of conformational freedom than its open chain counterpart, ethylene glycol dimethyl ether. This results in a less negative relative apparent volume and a lower relative apparent heat capacity at high dilution which can be ascribed to its smaller hydrophobic area exposed to the surrounding water. With increasing size of the cyclic ethers, the molecules become more flexible, with their thermodynamic properties at high dilution approaching those of the dimethyl ethers, see figure 7.

6. Conclusions

The number of ethylene oxide units within one class of compounds can be correlated with their thermodynamic properties, both in the pure liquid state and at infinite dilution in water. For the pure compounds, the molar volume and heat capacity increment is almost independent of the molecular structure. The trend of the thermodynamic properties of the fully hydrated monomeric molecules is strongly dependent on their molecular shape and flexibility.

The effects observed can be well explained by the assumption of a strengthening of the water structure in the vicinity of non-ionic solutes. This is clearly revealed by the measured heat capacity data. Volume effects are less easy to interpret, but show some distinct features that support the general picture.

Acknowledgements

The authors thank Dr. Jürgen Seidel and Prof. Gerd Wolf (Institut für Physikalische Chemie, TU Bergakademie Freiberg, Freiberg, Germany) for providing access to their MicroDSC II calorimeter. S.S. appreciates the support of the Verband der Chemischen Industrie e.V. (VCI). We gratefully acknowledge experimental assistance from Dr. Josef Duschl (Regensburg), Thomas Rowland (Murdoch) and Ethan See (Murdoch).

References

[1] D.R. Burfield, K.-H. Lee, R.H. Smithers, J. Org. Chem. 42 (1977) 3060.
[2] E. Habicht, R. Zubiani, US patent 3,235,461, February 1966.
[3] The International Association for the Properties of Water and Steam. Release on the IAPWS Industrial Formulation 1997 for the Thermodynamic Properties of Water and Steam; IAPWS Meeting, Erlangen, Germany, September 1997.
[4] CRC Handbook of Chemistry and Physics, 61st ed., CRC Press, Boca Raton, FL, 1980–1981.
[5] M.C.F. Magalhães, E. Königsberger, P.M. May, G. Hefter, J. Chem. Eng. Data 47 (2002) 590.
[6] J.E. Desnoyers, C. de Visser, G. Perron, P. Picker, J. Solution Chem. 5 (1976) 605.
[7] The International Association for the Properties of Water and Steam. Release on the IAPWS Formulation 1995 on the Thermodynamic Properties of Ordinary Water Substance for General and Scientific Use; IAPWS Meeting, Fredericia, Denmark, September 1996.
[8] V. Roháč, M. Fulem, H.-G. Schmidt, V. Růžička, K. Růžička, G. Wolf, J. Therm. Anal. Calorim. 70 (2002) 455.
[9] M. Lipovská, H.-G. Schmidt, V. Roháč, V. Růžička, G. Wolf, M. Zábranský, J. Therm. Anal. Calorim. 68 (2002) 753.
[10] M. Zábranský, J. Růžička, V. Majer, E.S. Domalski, in: Heat Capacity of Liquids Critical Review and Recommended ValuesMonograph No. 6, vols. I and II, American Chemical Society, Washington, DC, 1996.
[11] M. Čenský, M. Lipovská, H.-G. Schmidt, V. Růžička, G. Wolf, J. Therm. Anal. Calorim. 63 (2001) 879.
[12] A. Inglese, J.-P.E. Grolier, E. Wilhelm, J. Chem. Eng. Data 28 (1983) 124.
[13] R. Francesconi, F. Comelli, J. Chem. Eng. Data 40 (1995) 31.
[14] L. Barta, Z.S. Kooner, L.G. Hepler, G. Roux-Desgranges, J.-P.E. Grolier, Can. J. Chem. 67 (1989) 1225.

[15] R. Francesconi, F. Comelli, J. Chem. Eng. Data 39 (1994) 106.
[16] M. Pagé, J.-Y. Huot, C. Jolicoeur, J. Chem. Thermodyn. 25 (1993) 139.
[17] M. Zábranský, J. Růžička, E.S. Domalski, J. Phys. Chem. Ref. Data 30 (2002) 1199.
[18] G. Roux, G. Perron, J.E. Desnoyers, J. Solution Chem. 7 (1978) 639.
[19] K. Tamura, T. Yamasawa, J. Therm. Anal. Calorim. 73 (2003) 143.
[20] P. Baraldi, G.C. Franchini, A. Marchetti, G. Sanna, L. Tassi, A. Ulrici, G. Vaccari, J. Solution Chem. 29 (2000) 489.
[21] B. Das, M.N. Roy, D.K. Hazra, Indian J. Chem. Technol. 1 (1994) 93.
[22] L.M. Trejo, M. Costas, D. Patterson, J. Chem. Soc., Faraday Trans. 87 (1991) 3001.
[23] S.-C. Ku, C.-H. Tu, J. Chem. Eng. Data 49 (2004) 357.
[24] G.C. Benson, L.L. Wang, B.C.-Y. Lu, J. Chem. Thermodyn. 30 (1998) 1533.
[25] C.A. Tovar, E. Carballo, C.A. Cerdeiriña, L. Romaní, J. Chem. Eng. Data 42 (1997) 1085.
[26] W.J. Wallace, A.L. Mathews, J. Chem. Eng. Data 9 (1964) 267.
[27] F. Kimura, P.J. D'Arcy, M.E. Sugamori, G.C. Benson, Thermochim. Acta 64 (1983) 149.
[28] A. Pal, S. Sharma, J. Chem. Eng. Data 44 (1999) 212.
[29] C.A. Tovar, E. Carballo, C.A. Cerdeiriña, L. Romaní, J. Chem. Thermodyn. 29 (1997) 1353.
[30] C. Dethlefsen, A. Hvidt, J. Chem. Thermodyn. 17 (1985) 193.
[31] W. Wagner, R. Kleinrahm, H.W. Lösch, J.T.R. Watson, in: Measurement of the Thermodynamic Properties of Single Phases Experimental Thermodynamics, vol. VI, Elsevier, Amsterdam, 2003, pp. 127–149.
[32] C.A. Tovar, E. Carballo, C.A. Cerdeiriña, I.P. Andrade, L. Romaní, J. Chem. Soc., Faraday Trans. 93 (1997) 3505.
[33] T. Treszczanowicz, Thermochim. Acta 160 (1990) 253.
[34] S. Cabani, L. Lepori, E. Matteoli, Chim. Ind. 58 (1976) 221.
[35] L. Lepori, E. Matteoli, V. Mollica, Chim. Ind. 58 (1976) 882.
[36] G. Douhéret, M.I. Davis, M.E. Hernandez, H. Flores, J. Ind. Chem. Soc. 70 (1993) 395.
[37] W.J. Wallace, A.L. Mathews, J. Chem. Eng. Data 8 (1963) 496.
[38] A. Marchetti, L. Tassi, A. Ulrici, Bull. Chem. Soc. Jpn. 70 (1997) 987.
[39] G. Douhéret, J.C.R. Reis, M.I. Davis, I.J. Fjellanger, H. Høiland, Phys. Chem. Chem. Phys. 6 (2004) 784.
[40] O. Kiyohara, G. Perron, J.E. Desnoyers, Can. J. Chem. 53 (1975) 2591.
[41] S. Cabani, G. Conti, L. Lepori, J. Phys. Chem. 76 (1972) 1338.
[42] S. Harada, T. Nakajima, T. Komatsu, T. Nakagawa, J. Solution Chem. 7 (1978) 463.
[43] G. Douhéret, P. Lajoie, M.I. Davis, J.L. Ratli., J. Ulloa, H. Høiland, J. Chem. Soc., Faraday Trans. 91 (1995) 2291.
[44] P. Bernal, A. Bunn, J. Logan, J. McCluan, J. Solution Chem. 29 (2000) 651.
[45] K. Kusano, J. Suurkuusk, I. Wadsö, J. Chem. Thermodyn. 5 (1973) 757.
[46] L.-E. Briggner, I. Wadsö, J. Chem. Thermodyn. 22 (1990) 143.
[47] S. Schrödle, B. Fischer, G. Hefter, W. Kunz, R. Buchner, in preparation.

JCT 04-177

Appendix C

Dielectric relaxation parameters of water

Tables C.1 and C.2 contain the dielectric relaxation parameter of pure water, calculated from data of Hölzl[57]. These were extended by complex dielectric spectra in the THz range, determined by Rønne[99] using THz-TDS techniques, carefully selected and interpolated to the temperatures of the IF and TDR experiments.

Table C.1: Relaxation parameters, ε_j, τ_j (in ps), and reduced error function χ^2_r of light water. Superposition of two Debye terms. Also given are literature values of the static dielectric constant, ε[167].

T/K	ε	ε_1	τ_1	ε_2	τ_2	ε_∞	$10^3\,\chi^2_\mathrm{r}$
273.35	87.773	87.63	17.2	6.27	0.628	4.03	187.2
278.15	85.868	85.77	14.6	6.24	0.498	3.95	104.0
283.15	83.929	83.85	12.5	6.21	0.439	3.85	103.9
288.15	82.033	81.90	10.8	5.98	0.330	3.66	55.5
293.15	80.179	80.08	9.43	5.89	0.293	3.53	63.7
298.15	78.368	78.17	8.32	5.87	0.264	3.48	48.5
303.15	76.598	76.48	7.37	5.57	0.202	3.25	86.7
308.15	74.867	74.42	6.53	5.46	0.183	3.06	87.2
313.15	73.176	73.05	5.97	5.54	0.189	2.98	79.2
318.15	71.523	71.29	5.31	5.33	0.153	2.68	79.0
323.15	69.907	69.80	4.81	5.30	0.149	2.60	61.9
328.15	68.328	67.99	4.38	5.30	0.155	2.59	122.6
333.15	66.784	66.78	4.03	5.33	0.139	2.60	102.3
338.15	65.276	65.32	3.70	5.29	0.132	2.62	108.9

Table C.2: Relaxation parameters, ε_j, τ_j (in ps), and reduced error function χ^2_r of heavy water. Superposition of two Debye terms. Also given are literature values of the static dielectric constant, ε[217].

T/K	ε	ε_1	τ_1	ε_2	τ_2	ε_∞	$10^3\,\chi^2_\mathrm{r}$
278.15	85.480	85.68	19.5	5.92	0.380	3.40	124.1
283.15	83.526	83.75	16.4	5.85	0.353	3.32	79.1
288.15	81.618	81.71	13.8	5.67	0.335	3.23	113.5
293.15	79.755	79.77	12.1	5.69	0.322	3.18	70.3
298.15	77.936	78.01	10.6	5.54	0.299	3.13	68.9
303.15	76.161	76.63	9.37	5.53	0.296	3.14	115.9
308.15	74.427	74.33	8.17	5.44	0.283	2.95	135.7
313.15	72.735	73.11	7.34	5.35	0.271	2.80	113.6
318.15	71.083	71.09	6.63	5.20	0.269	2.70	104.6
323.15	69.470	69.57	6.01	5.33	0.263	2.64	100.0
328.15	67.896	68.12	5.49	5.35	0.253	2.46	144.8
333.15	66.358	66.57	4.95	5.36	0.266	2.36	104.8
338.15	64.857	65.02	4.61	5.87	0.257	2.25	42.8